ABSTRACT

Title of Document:	ACTIVE JET ACOUSTIC CONTROL OF LOW FREQUENCY, IN-PLANE HELICOPTER HARMONIC NOISE
	D. Caleb Sargent, Doctor of Philosophy, 2012
Directed By:	Professor Fredric H. Schmitz Department of Aerospace Engineering

A new approach to reducing low frequency, in-plane harmonic noise of helicopter rotors is explored theoretically and experimentally in this dissertation. The active jet acoustic control methodology employs on-blade, tip located unsteady air blowing to produce an acoustic anti-noise waveform that reduces or cancels the observed noise at targeted positions in the acoustic far-field of the rotor system. This effectively reduces the distance at which the helicopter rotor can be aurally detected. An extended theoretical model of the subsonic air jet, which is modeled as both a source of mass and momentum, is presented. The model is applied to a baseline, full-scale, medium weight helicopter rotor for both steady and unsteady blowing. Significant reductions in low frequency, in-plane harmonic noise are shown to be possible for the theoretical rotor system by using physically reasonable unsteady jet velocities. A new model-scale active jet acoustic control experimental test rotor system is described in detail. Experimental measurements conducted in the University

of Maryland Acoustic Chamber for the ~1/7th rotor, operated at a full-scale hover tip Mach number of M_H = 0.661, indicate that active jet acoustic control is a viable option for reducing low frequency, in-plane harmonic noise. Good correlation between theoretical predictions and measured data for four valve control cases are observed in both the time and frequency domains. Model-scale limitations of the tip-jet blowing experiment limited the peak noise level reductions to 30%. However, theory suggests that if the limitations of the model-scale controller are mitigated, much larger noise reductions are possible.

ACTIVE JET ACOUSTIC CONTROL OF LOW FREQUENCY, IN-PLANE HELICOPTER HARMONIC NOISE

By

D. Caleb Sargent

Dissertation submitted to the Faculty of the Graduate School of the
University of Maryland, College Park, in partial fulfillment
of the requirements for the degree of
Doctor of Philosophy
2012

Advisory Committee:
Professor James D. Baeder, Chair/Advisor
Professor Fredric H. Schmitz, Advisor
Professor Alison B. Flatau
Professor Christopher P. Cadou
Professor Inderjit Chopra
Professor Balakumar Balachandran (Dean's Representative)

Dedication

To my family: Alec, Lee, Laura and Kathryn.

Acknowledgements

This dissertation could not have been completed without the help of a great number of people. Without their combined knowledge, patience, and unwavering support, I could not possibly have done this on my own. I would first like to thank the members of my dissertation. Special thanks Dr. Baeder for acting as chair of my dissertation committee. He has provided invaluable advice and support and words cannot accurately express how thankful I am. Dr. Chopra was one of the first faculty members I met here at Maryland and my admiration and respect for the research that he does continues to grow. I am immensely grateful for Dr. Flatau's continued interest in my work and for serving on my committee. Drs. Cadou and Balachandran have both been tremendously supportive and encouraging throughout this exhausting process and I thank them both. I would also like to thank the rest of the faculty at Maryland, especially Dr. V.T. Nagaraj for his enthusiasm, friendship, and never-ending support.

I would also like to thank the good people at Sikorsky, Army, NASA and DARPA that I have had the opportunity to work with for the past few year in an attempt to build an active jet acoustic control system for a real life helicopter. Special thanks goes to Mark Scott whose enduring support has made this process incredibly enjoyable and interesting. Thanks are also in order for Dr. Ben Sim for the many discussion and laughs that we have shared.

Making it through graduate school in one piece would be borderline impossible without considerable help from friends who are, or have gone through the same, sometimes painful, process. A great number of friends have made me think, laugh, shout and cry (not really). Thanks to all of them and I wish them all continued success. I would like to especially thank the members of Team Schmitz: Rick Sickenberger, Dr. Eric Greenwood, Joel Feinerman, Ben May and Chris Sutton. Your willingness to help run experiments (i.e. provide free labor) or discuss new ideas (i.e. provide free consulting) has been invaluable. Thanks also to my former office mates from JMP 2108: Ondrej, John, Kumar and Monica.

It goes without saying that I owe a great deal of gratitude to Dr. Sudarshan Koushik and Dr. Gaurav Gopalan. Sud taught everything there is to know about running the rotor stand and the acoustic chamber and I would still be untangling cable if it weren't for his help. On a sadder note, Gaurav was in many ways the driving force behind this research, and his untimely death near the end of its completion has been difficult for all who knew him. I take tremendous pride in the fact that I knew Gaurav and that he was proud of the work that I was doing. He will be forever missed.

On a more personal level, I would like to thank all of my family and friends outside of the University. My parents, Lee and Alec, have provided unwavering love, support and an expectation of excellence throughout my life that has made me what I am today. Quite simply, I could not have accomplished this without them. The same goes for my sister, Laura, whose brilliance and uncanny ability to simultaneously keep me on my toes and make me laugh have pushed me to do and be better. Thanks

also to my grandfather and uncle for instilling a deeply rooted love for all things that fly. Finally, I owe a great deal of thanks and respect to the love of my life, Kathryn. Without her everlasting love, support, kindness, and perhaps most importantly, patience, I would not have succeeded in this pursuit. I am sure that the completion of this dissertation is as much a relief for her as it is for me.

Lastly, I would like to express my immense gratitude and respect for my advisor of six years, Dr. Fredric H. Schmitz. The idea behind this research has been rattling around in the back of his mind for nearly three decades and I cannot be more honored than to have had the opportunity to work with him and bring it to fruition. If I accomplish even half of what he has done over the course of his life, both professionally and personally, I will consider myself successful. He has made me a better engineer and become a close friend.

Table of Contents

List of Tables

List of Figures

List of Symbols

A	rotor disk area, ft^2 (m^2)
AJAX	Active Jet Acoustic Control
A_{jet}	jet exit area , ft^2 (m^2)
a_0	ambient speed of sound, ft/sec (m/sec)
AoA	angle of attack, deg
BVI	Blade Vortex Interaction noise
c	blade chord, ft (m)
$C_{l\alpha}$	section lift-curve slope
C_{d0}	section zero-lift drag coefficient
C_μ	blowing momentum coefficient, $\dot{m}_{jet} V_{jet} \Big/ \left(0.5\rho(\Omega R)^2 S\right)$
D	distance between hub and observer, ft (m)
dB	decibel
dC_P	sectional power coefficient, $dP/\rho A(\Omega R)^3$
dC_T	sectional power coefficient, $dT/\rho A(\Omega R)^2$
dF_x	sectional in-plane force, lbf (N)
dF_z	section out-of-plane force, lbf (N)
DL	disk loading, T/A
dS	element surface area, ft^2 (m^2)
ETR	Experimental Test Rotor
$\vec{F}$	acoustic momentum source vector in blade fixed coord., lbf (N)
F	Prandtl tip-loss function
$f = 0$	radiation source surface
H	Heavyside function
HSI	High Speed Impulsive noise
l_r	section blade load in observer direction, lbf (N)
LF-IPH	Low Frequency In-Plane Harmonic Noise
M	Mach number
$\dot{m}_{jet}$	jet mass flow, lb/sec (kg/sec)

M_r	Mach number in radiation direction
N_b	number of blades
n	element/panel normal vector
$\hat{n}_{jet}$	jet normal vector pointing in positive flow direction
p'	acoustic pressure, lbf/ft^2 (Pa)
p'_{AN}	acoustic pressure due to active jet acoustic control, lbf/ft^2 (Pa)
P_{ij}	compressive stress tensor acting on fluid, lbf/ft^2 (Pa)
p'_F	acoustic pressure due to AJAX momentum source, lbf/ft^2 (Pa)
p'_L	acoustic pressure due to blade loading, lbf/ft^2 (Pa)
p'_M	acoustic pressure due to AJAX mass source, lbf/ft^2 (Pa)
p'_{ROTOR}	acoustic pressure due to blade loading and thickness, lbf/ft^2 (Pa)
p'_T	acoustic pressure due to blade thickness, lbf/ft^2 (Pa)
p	surface pressure, lbf/ft^2 (Pa)
Q	acoustic mass source strength, ft^3/sec (m^3/sec)
R	blade radius, ft (m)
r	radial location, ft (m)
$\hat{r}$	radial unit vector in blade fixed coordinate system
$\vec{r}_{jet}$	jet location relative to hub, ft (m)
r_{obs}	radiation distance between acoustic source and observer, ft (m)
S	blade panform area
SPL	sound pressure level, dB
T_{ij}	Lighthill stress tensor
t	observer time, sec
TPP	Tip Path Plane
U	blade element resultant velocity, ft/sec (m/sec)
u	fluid velocity, ft/sec (m/sec)
UMAC	University of Maryland Acoustic Chamber
v	body velocity, ft/sec (m/sec)
$\overline{V}_{jet}$	jet velocity ratio, $\left\|V_{jet}\right\| / \Omega R$
$\vec{V}_{jet}$	jet velocity relative to blade, ft/sec (m/sec)

$\vec{V}_{tip-jet}$	jet source location velocity due to blade rotation, ft/sec (m/sec)
V_∞	rotor forward velocity, ft/sec (m/sec)
$\vec{x}$	observer location relative to hub, ft (m)
$\hat{x}_{rot}$	unit vector pointing along ¼ chord axis
$\hat{y}_{rot}$	unit vector pointing along chord axis, perpendicular to $\hat{x}_{rot}$
α_{jet}	jet angle relative to ¼ chord axis, deg
α_{TPP}	tip path plane angle, deg
δ	Dirac delta function
θ	sectional twist, deg
$\hat{\theta}$	chord-wise unit vector in blade fixed coordinate system
λ	rotor inflow
μ	advance ratio, $V_\infty \cos\alpha_{TPP} / \Omega R$
ρ_0	ambient density of air, lb/ft^3 (kg/m^3)
σ	rotor solidity, $N_b c/\pi R$
ψ	rotor azimuth angle, deg
ϕ	relative inflow angle, deg
Ω	rotor rotational rate, deg/sec
∂	partial derivative operator
$\Box^2$	d'alembertian wave operator

Chapter 1: Introduction

The ability to operate rotorcraft in a discreet fashion is paramount to their expanded use in the modern aviation world. The inability to do so results in an aircraft with not only a significantly diminished military operational effectiveness, but also a reduction in utility for civilian application. Low frequency rotor harmonic noise, which is loudest near the plane of the rotor, is of particular concern. It can propagate over long distances without being substantially attenuated by the atmosphere or obstacles. As such, it is this low frequency in-plane harmonic noise (LF-IPH) that dictates how and when a particular rotorcraft will be noticed or detected [1].

Over the past twenty years, helicopter manufacturers have improved their designs in order to mitigate the extremes of LF-IPH noise by reducing rotor blade operational tip Mach numbers, sweeping and thinning blade tips. Though this has reduced the noise to some extent, manufacturers have not yet been able to completely eliminate it. In most cases, helicopters still emit a considerable amount of LF-IPH that is both annoying and can alert enemy combatants of a helicopter's approach.

This dissertation presents a new method of actively reducing LF-IPH noise using on-blade, tip located, unsteady air blowing. This new approach expands on the active acoustic control work previously conducted by Gopalan and Schmitz at the University of Maryland [2-4].

The methodology for the on-blade active acoustic control of LF-IPH is shown below in Figure 1-1. The basic philosophy of the underlying active noise control research is to first identify the physical and motion-related mechanisms that are responsible for

generating low frequency harmonic noise. These mechanisms are then exploited to produce "anti-noise" that is of similar shape, but opposite in amplitude, to the characteristic negative acoustic pulse associated with LF-IPH; reducing the noise heard at a specific observer location. A single or distributed time varying in-plane force or mass source is applied at some point along the blade. The control source strength needed to cancel or reduce the LF-IPH to the desired level at a specified observer location can then be analytically or numerically determined. Theoretical work has shown that a high rate of change in the source strength on the advancing side of the rotor (for a target ahead of the helicopter in the direction of flight) results in an "anti-noise" waveform of the required shape and amplitude [2-4].

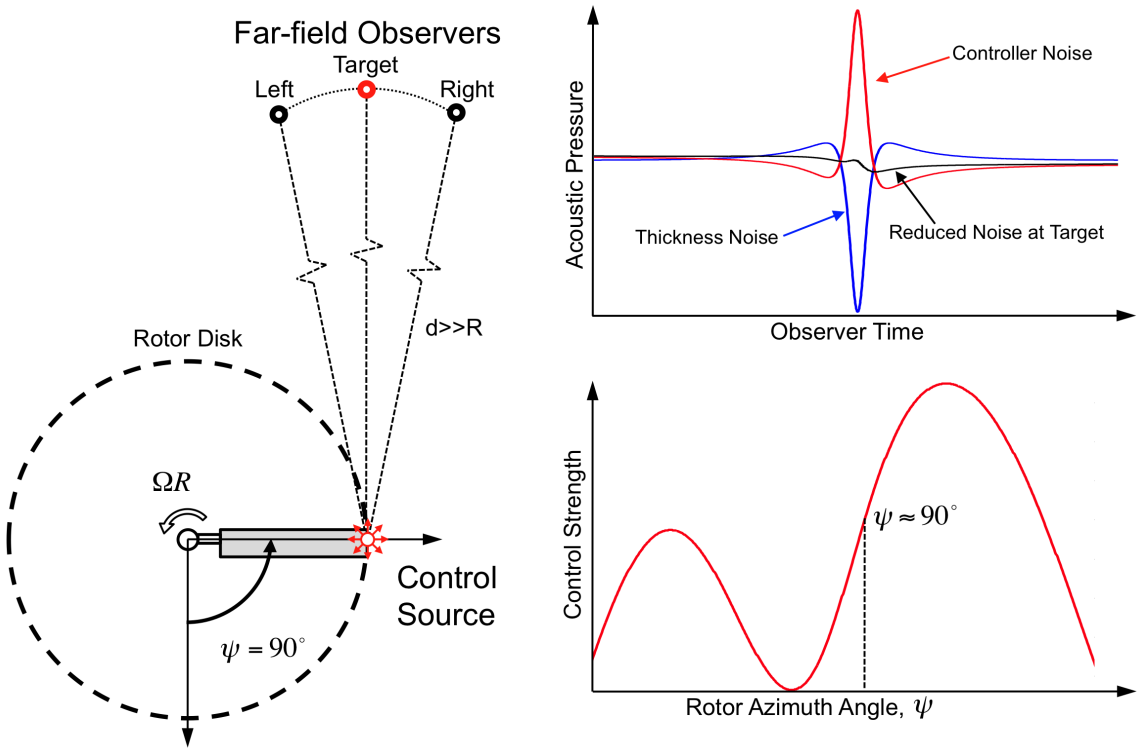

Figure 1-1: Active acoustic control using acoustic tip jet blowing.

Recently, the use of active moment flaps to reduce LF-IPH in forward flight has been demonstrated experimentally using a modern five-bladed rotor system, the Boeing SMART rotor [5,6]. Findings at the U.S. Army Aeroflightdynamics Directorate (AFDD), at Ames Research Center, have identified the use of active on-blade flaps as a means of producing the necessary anti-noise [6]. This joint DARPA/Boeing/NASA/Army test in the 40 foot by 80 foot National Full-Scale Aerodynamic Complex showed that by varying the flap deflections of their SMART rotor system, reduced noise levels could be achieved at certain observer locations. The flaps effectively twisted the torsionally soft rotor blades such that the tilt of the blade lift vector was altered – resulting in changes in in-plane drag. When oscillated at the correct phase, they found that this drag force produced an acoustic pulse of positive amplitude (opposite to the IPH pulse) and similar shape to that associated with the rotor LF-IPH. When this pulse was added to the IPH pulse, significant IPH noise level reductions were observed. This experiment showed that the physical phenomenon that governs on-blade noise reduction is, in fact, fundamentally correct. It also showed the importance of the proper selection of a noise generation method, as the active flap system used on the SMART rotor causes a significant change in rotor blade lift distribution which can result in increased levels of noise at off-target observer locations. As noted in references [2-4], a preferable method of acoustic control should have a small effect on the overall lift distribution of the rotor, and subsequently, the noise levels at off-target locations.

Operating quietly is paramount to the helicopters ability to perform well on current and future battlefields. Between October 2001 and September 2009, approximately 31% of the rotorcraft lost during Operation Iraqi Freedom were due to

small arms and automatic weapon fire [8]. One of the key factors in reducing these mishaps is improvement of the helicopters aural detection characteristics.

Specifically addressing this problem, the reduction of in-plane harmonic noise is a relatively new area of research. As such, very little theoretical and experimental work has been conducted. This dissertation presents an alternate method of actively reducing LF-IPH using on-blade, tip located, unsteady air blowing. By controlling the air jet mass flow rate, a pulse is produced that has positive amplitude and is in phase with the LF-IPH noise to reduce the negative amplitude IPH noise. Due to the inherent coupling between the jets mass source and momentum source mechanisms, both the mass flow rate, and the jet momentum govern the shape and amplitude of the resultant acoustic pulse. A theoretical acoustic model of the active air jet is developed and a parametric study of the jet characteristics, as applied to a full-scale helicopter rotor, is explored. Using experimental data from a carefully controlled model-scale rotor experiment conducted in the University of Maryland Acoustic Chamber (UMAC), the theory is then validated. The new Active Jet Acoustic Control Experimental Test Rotor (AJAX ETR), which was designed and constructed for specifically this work, is discussed in detail. Finally, a direct comparison between theoretical predictions and experiment acoustic measurements shows that the modeling is capturing the primary physical effect of on-blade blowing acoustic control and validates the active jet acoustic control concept for LF-IPH noise reduction.

1.1 Sources of Helicopter Noise

Whereas fixed wing aircraft suffer predominantly from engine and airframe noise, rotorcraft are plagued by the noise generated by the main and tail rotor, transmission

system, and any number of broadband sources (see Figure 1-2). The problems associated with reducing the overall noise profile of a helicopter are further exacerbated by the fact that the noise emanating from these sources becomes more or less important to a human observer based upon their location with respect to the helicopter, the nature of the medium between the observer and the particular noise source, and the helicopter's configuration and flight condition.

Rotorcraft noise covers a wide range of frequencies. A typical frequency spectrum of the in-plane noise radiated by a helicopter in forward flight is shown in Figure 1-3. The lower frequencies (0-500 Hz) are generally dominated by the main rotor harmonic noise. The mid-frequencies (500-1000 Hz) are dominated by tail rotor or other main rotor noise phenomena like blade vortex interaction noise or high speed impulsive noise. Higher frequency noise is generally dominated by broadband noise as well as transmission and engine related noise.

Figure 1-2: Sources of helicopter noise.

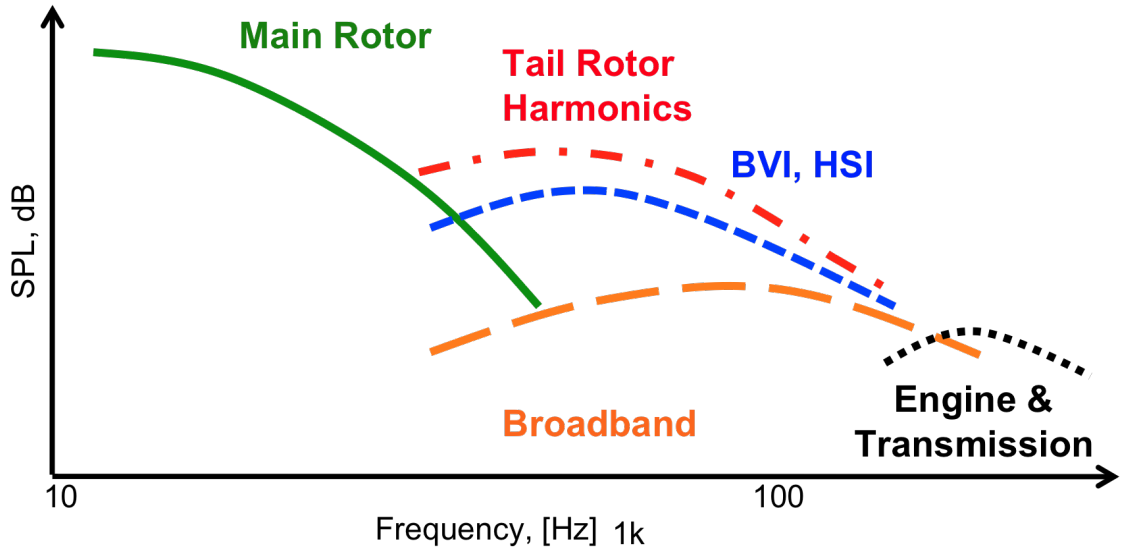

Figure 1-3: Representative frequency distribution for helicopter in forward flight.

An important problem for helicopters today is the detection or audibility problem. Namely, how and when a human observer first hears a helicopter. Helicopters often operate at relatively low altitude and with a slight downward tilt of the main rotor tip path plane (TPP), as shown in Figure 1-4. Combined with the fact that low and mid frequency noise, which is generated largely by the main and tail rotor systems, propagate further than high frequency noise, the main and tail rotor harmonic noise is the key factor in determining how and when a helicopter will be detected.

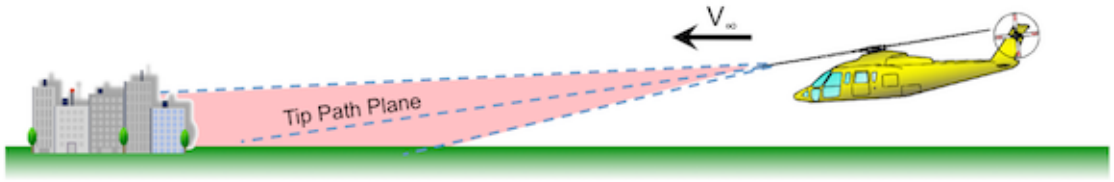

Figure 1-4: Helicopter detection or audibility problem.

Rotor harmonic noise can be broadly classified into four source mechanisms: thickness noise, loading noise, high-speed impulsive noise (HSI) and blade vortex interaction noise (BVI).

- **Thickness Noise:** Thickness noise is a direct result of the displacement of the fluid in which the rotor is operating (in this case, air) by the blade. Thickness noise is present in all operating conditions. It can be modeled using monopole sources and is characterized by a large negative pulse shape that is loudest in the plane of the rotor. Figure 1-5 shows a typical thickness noise time history for a four bladed medium weight helicopter. Thickness noise is often the dominant source of noise for LF-IPH.

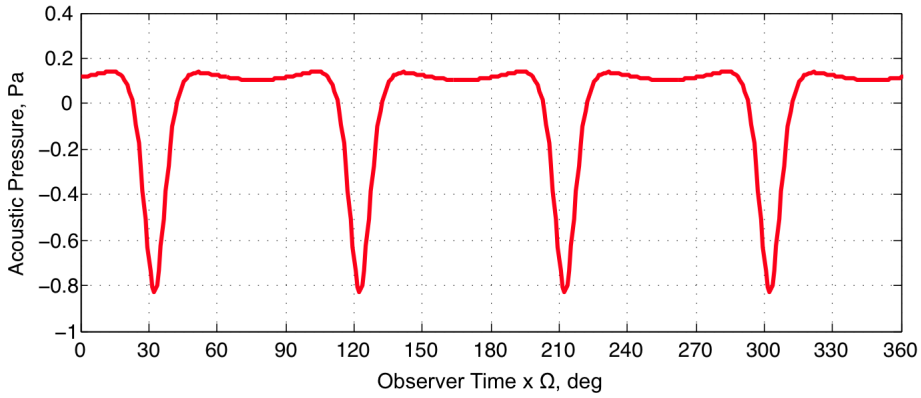

Figure 1-5: Typical representative acoustic pressure for thickness noise.

- **Loading Noise:** This noise is due to the steady and unsteady aerodynamic forces acting on the medium due to blade loading, and it is highly dependent on the flight condition of the helicopter. Loading noise is generally modeled by using dipole sources, with the lift component radiating predominantly below the plane of the rotor and the smaller drag (torque) component radiating closer to the tip path plane (Figure 1-6). Due to its low-frequency content, the in-plane loading noise can be important in determining a helicopters' likelihood of detection. The out-of-plane loading noise (lift) is of greater concern for annoyance.

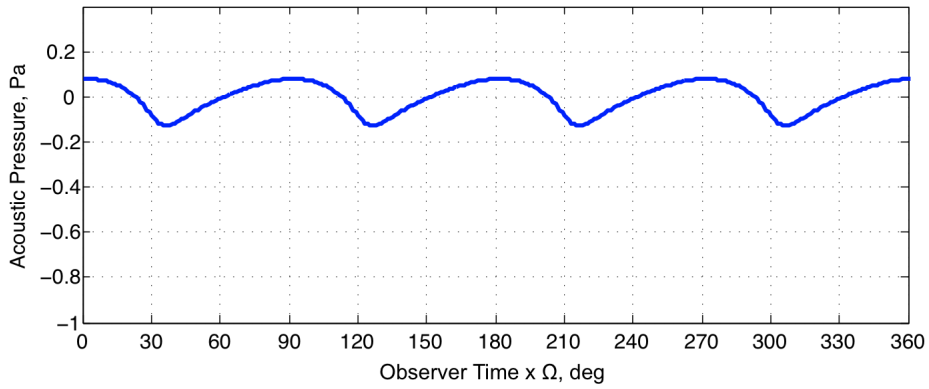

Figure 1-6: Typical representative acoustic pressure for in-plane loading noise.

- **Low Frequency In-Plane Harmonic (LF-IPH) Noise:** Low Frequency In-plane harmonic noise (LF-IPH) is simply the combined summation of low frequency thickness and loading noise near the rotor tip path plane (+/- 30 degrees). In this region, thickness noise is generally dominant but the in-plane loading noise can also have a significant contribution to the lower frequency content of the total noise. Because LF-IPH is the summation of two independent sources of noise, phase plays an important role. The distribution and time varying nature of the blade loading can result in an increased or diminished importance of the loading noise. A typical profile of the noise directly in the tip path plane is shown below in Figure 1-7. The thickness noise (red) clearly dominates the total in-plane harmonic noise (black). However, the loading noise (blue) does have significant contributions to the lower frequency spectra. It is therefore important to include both loading and thickness noise when determining a helicopters likelihood of detection. The reduction of low-frequency in-plane harmonic noise is the focus of this dissertation.

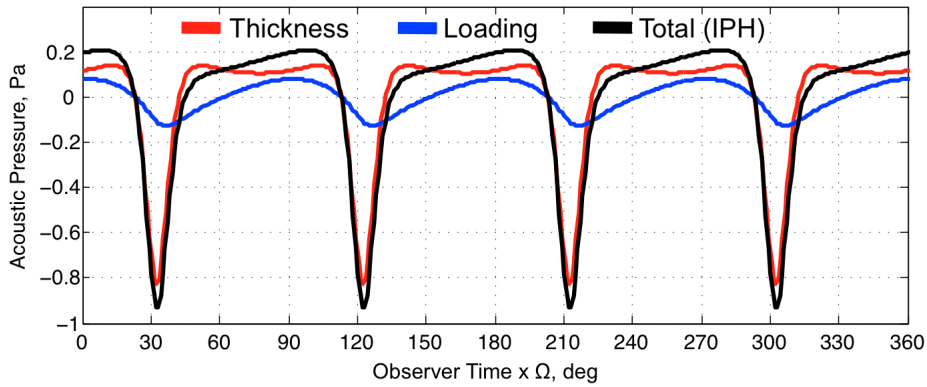

Figure 1-7: Typical representative acoustic pressure for in-plane harmonic noise.

- **High Speed Impulsive (HSI) Noise:** HSI noise is an extreme case of thickness noise and is characterized by a large sharp negative pulse (Figure 1-8) that is strongly influenced by the transonic effects on the blade surface when operated at high advancing tip Mach numbers. This results in the formation of a shock on the blade surface that can extend past the tip of the blade into the acoustic far field (known as "delocalization") [9,10]. This type of noise is typically observed on older Vietnam era helicopters like the Bell UH-1 Huey and it can be mitigated to some extent by reducing the rotor tip speed and thinning, or sweeping the blade tips. When it does occur, HSI is mostly focused in or slightly below the rotor TPP and can be important for the detection problem. Numerous flight tests [10] and pioneering experiments in wind tunnels and hover chambers [9-11] have been conducted to better understand this source of noise. The resultant body of knowledge ultimately has led to various passive design changes to rotors systems that have made HSI less of a concern for modern helicopters [13].

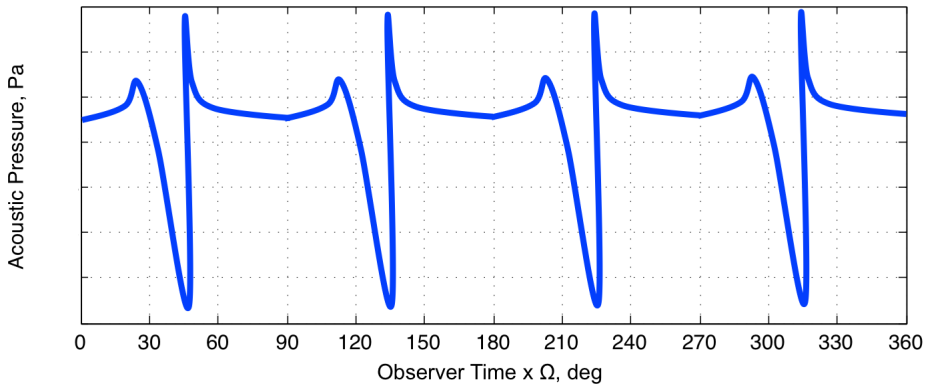

Figure 1-8: Typical acoustic pressure for High Speed Impulsive Noise (HSI)

- **Blade Vortex Interaction (BVI) Noise:** This noise is perhaps the most heavily investigated main rotor noise phenomenon and is characterized by the typical "slapping" noise heard in the acoustic far-field, in front of many helicopters. It is the result of the interaction between the wake and trailed vortices of a preceding blade and an oncoming blade, as shown in Figure 1-9. This interaction results in a rapid change in blade loading and a resulting high frequency, high energy, acoustic wave (Figure 1-10). Because BVI occurs when the rotor wake is aligned with the tip path plane, as is the case when a helicopter is descending, BVI is particularly important in determining how and when a helicopter can be operated in urban environments. It is primarily radiated in front of or below the rotor system. Due to its high frequency content and the fact that it can be avoided to some extent by careful flight planning, BVI is generally considered less of a concern for detection.

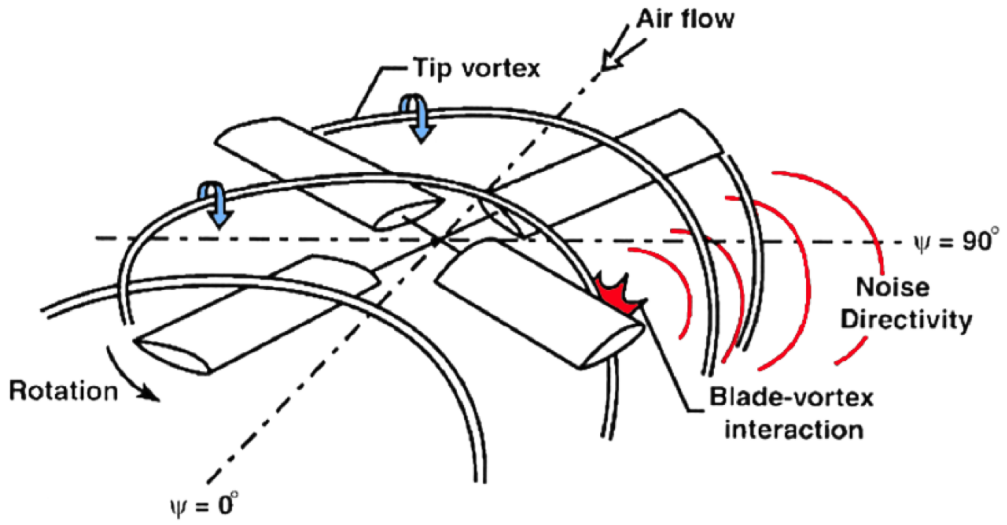

Figure 1-9: Schematic of Blade Vortex Interaction noise.

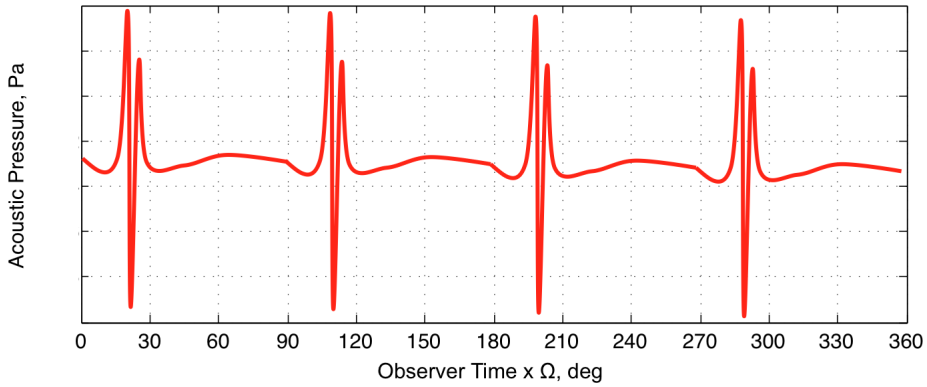

Figure 1-10: Typical acoustic pressure for Blade Vortex Interaction (BVI) noise.

- **Tail Rotor Harmonic Noise:** Tail rotor harmonic noise can also radiate in the horizon plane of the aircraft and contribute to IPH noise. Therefore it can adversely affect the detection distance of a single rotor helicopter. Because the fundamental frequency of the tail rotor is higher than the main rotor, the harmonic noise is also higher in frequency. However, on the first few harmonics of tail rotor noise are typically considered because of atmospheric absorption and attenuation. That said, tail rotor noise is an important determinant in a helicopters' likelihood of detection.

In many respects, the low frequency noise generated by a tail rotor is quite similar to the main rotor. For that reason, and although it is not considered in this dissertation, an active jet acoustic control system to reduce tail rotor IPH may be another application for this novel control method.

1.2 Previous Work

1.2.1 Active Noise Control

Any investigation into the use of a noise source to suppress or reduce another must begin with a brief look at the origins of the science of noise control, anti-noise, and the superposition of linear acoustic waves.

The idea that sound pressure can be reduced by introducing a secondary noise source that is in exact phase with, but of opposite amplitude to the primary source was originally conceived by the German Physicist, Paul Lueg in his 1933 German Patent [14] (or the corresponding U.S Patent in 1936 [15]). Though unable to experimentally replicate his idea of active noise control at the time, Lueg proposed that a noise source (A), inside an infinite pipe domain (T), could be recorded with a microphone (M). This signal could then be processed by some unknown means (V) and a sinusoidal wave of the opposite amplitude would be produced using a noise source (L) at another location in the pipe. The superposition of these sinusoids (S_1 and S_2) then cancel each other at all points in the pipe. A diagram from Lueg's patent is shown in Figure 1-11. Also introduced in Lueg's early work were the concepts of cancellation by interference at points in space and the creation of protected "quiet zones".

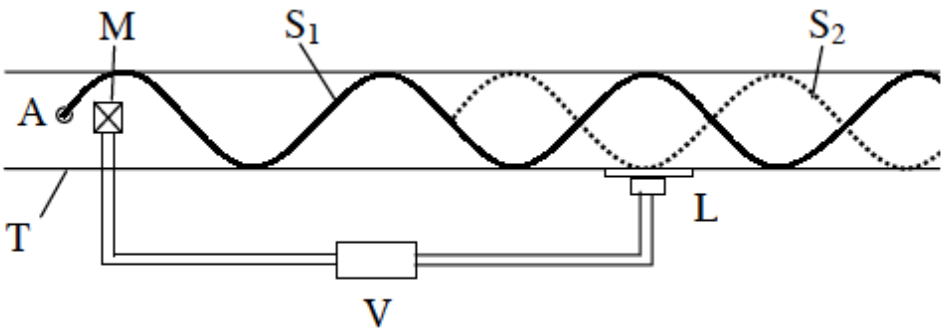

Figure 1-11: Diagram of 1-D active noise cancellation [15].

Lueg's ideas quickly developed into the field of active noise control and throughout the 1950s and beyond, countless works were published on the topic. Each of these works ultimately dealt with the mitigation of noise using one of three different control mechanisms [16].

The first mechanism is sound field cancelation. Critically important to the applicability of this mechanism is the fact that human beings live in a three dimensional world. Because of this, and the fact that multiple sound sources cannot occupy the exact same physical space, the use of anti-phase noise as a means of control not only results in localized areas of cancellation and/or reduction, but also areas of reinforcement. The most widely recognized modern application of this mechanism is the noise cancelling headphones first developed by W.F. Meeker of RCA and now widely distributed by Bose Corporation [14]. These headphones take advantage of the small distance between the ear canal and headphone speaker to observe external noise using a headphone-mounted microphone. This sound heard by the ear is then reduced by playing an equal but opposite waveform through the speaker.

The second mechanism, referred to as the suppression of sound generation, involves making an entire control sound field 180° of out phase with the original field.

This alters the radiation impedance of the original source so that it radiates less acoustic energy. To achieve this type of suppression an extremely large control source is required that must be located in such a way that it is able to provide the necessary impedance. The implementation of this mechanism is visible in the vibration control units used on large machinery in modern manufacturing plants. The controllers actively suppress the vibration between the plant floor and machine that is the primary source of noise.

The third mechanism of active noise control is absorption. In this mechanism, the primary sound field energy is absorbed and driven by the control source, resulting in a reduced acoustic field beyond the control source. Generally additional energy is required to drive the source with the required amplitude and phase to enable proper absorption of the primary sound energy. First developed by Harry Olsen in the 1950s [14] (though less effectively due in part to the available materials), a modern application of this method is the use of Smart material actuated panels embedded in the walls of helicopter fuselages to reduce the interior cabin noise [17]. When properly driven, these panels effectively absorb a given primary noise source and provide a more comfortable environment for passengers.

The active jet acoustic control methodology developed in this dissertation is most closely aligned with the first mechanism. By constricting the focus to the low frequency, main rotor in-plane noise at a fixed observer distance in the acoustic far-field, and using knowledge of the radiated rotor noise for a given flight condition (using common computational predictive methods instead of a microphone), a control noise on the rotor that will significantly reduce the observed noise is produced. Taking advantage of the rotor's rotation, which in forward flight results in an amplification of the noise directly

ahead of the advancing side of the rotor, a noise source can be designed that is not only efficient but also physically realizable. Before exploring the theoretical modeling and real-world implementation of this concept, it is useful to examine some of the previous work that has been done to reduce rotor related noise using other means as well as the previous attempts that have been made to incorporate jet or jet like devices into rotor systems.

1.2.2 Active Control of Rotor Noise Sources

Most of the work done in the early years of rotorcraft acoustic research was aimed at better understanding the noise mechanisms and the passive design of helicopter components that might mitigate the noise. For example, early helicopters, operating with high tip speeds and relatively thick airfoils near the tip, suffered from high levels of HSI. By simply lowering tip speeds and thinning blade tips these extremely high levels of noise were reduced. Eventually, tapered, swept rotor designs resulted in further reductions of this noise as the acoustic "delocalization" associated with HSI noise was delayed. These passive design trades are thoroughly discussed in many other works but they are not the primary focus of this research [13,18-22]. Because of the limitations of these passive designs, it was perhaps inevitable that efforts would eventually be made to actively reduce rotor noise. The most common approach has been to manipulate the tip vortex, as evidenced in the visual summary of previous attempts to do so in Figure 1-12.

As the understanding of the various noise mechanisms of helicopter evolved and improved, so too did the effort to reduce other sources of main rotor noise. One of the most widely studied and annoying of these sources has been BVI. Considered by many to be the most annoying source of noise for residential communities, the reduction of BVI

was and is considered critical to the expanded utility of helicopters in urban and civilian environments. BVI is generated predominantly from the unsteady pressure fluctuations on a blade due to the trailed vortices from other blades as is particularly prevalent in fast transient maneuvers or landing/take-off flight conditions. This phenomenon is very complex but it was long ago established that one of the main parameters in controlling BVI was the careful control of the rotor wake and vortex structure.

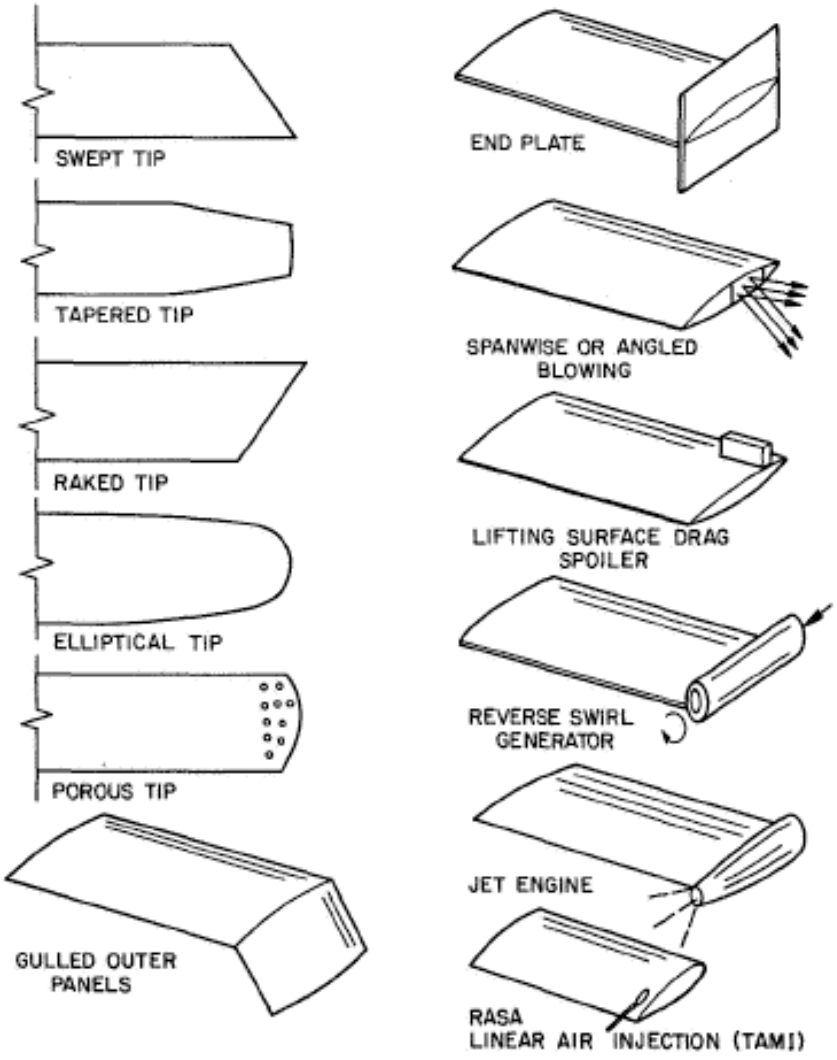

Figure 1-12: Configurations for BVI reduction [23].

Higher harmonic control (HHC), individual blade control (IBC), trailing edge flap (TEF), actively twisting or blowing on or near the rotor blade have all been explored as potential means of disrupting or changing the wake structure [24]. Changes in tip vortex strength, core size, intersection angle, and miss distance can all be affected to varying degrees by these methods.

Originally developed with the goal of reducing rotor born vibrations, HHC was suggested as a potential means of reducing BVI in the late 1980s [25] but it was determined that when using fixed frame control, as is the case for HHC, fuselage vibration levels were increased significantly when the control was driven at frequencies required for low BVI noise [26,27]. Higher levels of vibration could however be avoided in part if the blades were individually driven at high frequencies. This ultimately led to the development of the IBC concept, conceived in Germany [28] in the early 1990s. Subsequent cooperative testing between NASA, the U.S. Army, and Germany showed that significant simultaneous reductions in both BVI noise and hub vibrations could be achieved [29,30]. Despite this early success, the cost and complexity of these systems has hindered their widespread use. Careful flight planning or alteration of the fuselage drag (X-Force Control [31]), have also hampered their use as both are more affordable. As of today, no operational helicopters exist that use either HHC or IBC, though there is still considerable development and research in the area.

1.2.3 Flight Path and Rotor Wake Control

Another method of control that has been proposed for BVI reduction is to control the tip path plane angle of the rotor relative to the rotor wake. In flight conditions where the inflow through the rotor becomes nearly zero, the rotor wake and tip vortices remain

in the tip path plane resulting in strong and plentiful blade vortex interactions and an increase in BVI is observed. Early studies of the flight conditions that were associated with increases in BVI by Hawles [32] found that by changing the helicopters rate of descent or flight speed, the relative position of the rotor plane and wake was altered and a reduction in the radiated BVI could be achieved.

Schmitz suggested a similar approach in reference [31]. Instead of altering the helicopter's flight condition, he proposed that increasing the fuselage X-force (through the use of deployable drag devices, etc.) could be used to manipulate the tip path plane angle such that the strength and likelihood of vortex impact was reduced. As a result, the radiated BVI noise would be reduced. A schematic of one of the proposed X-force controllers is shown in Figure 1-13.

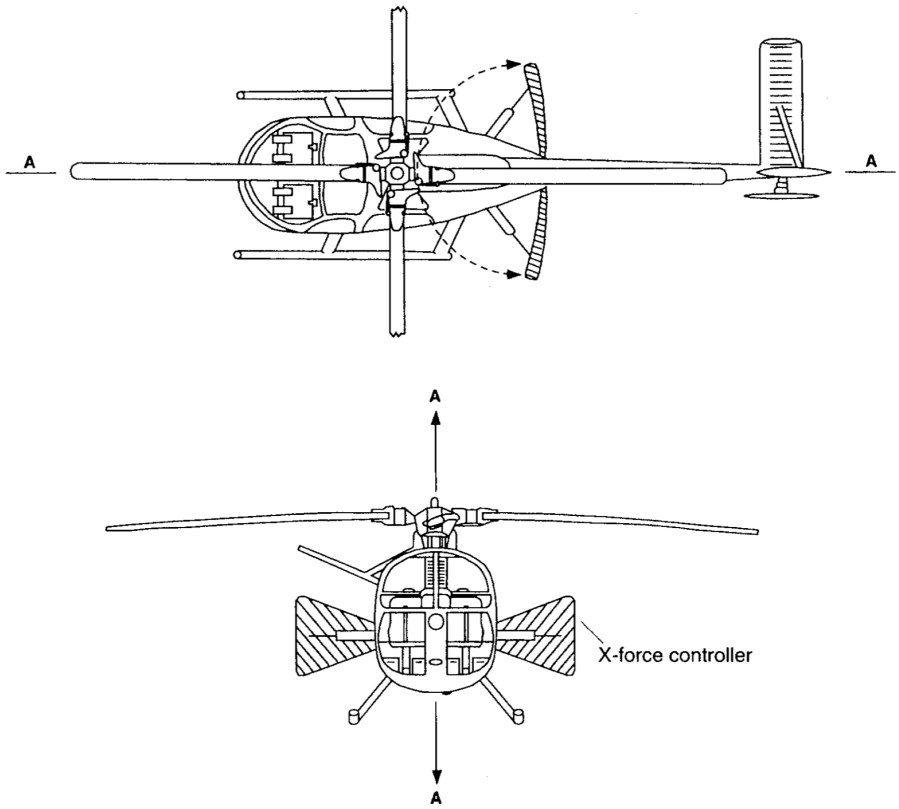

Figure 1-13: X-Force control schematic for BVI noise reduction [31].

1.2.4 Active Blowing Concepts

Another concept in the active control of BVI is the use of steady jet blowing at, or near, the blade tip to displace or weaken the tip vortex. In the early 1970s a joint experimental research program between the United States Navy, Army and NASA [33-36] resulted in the Tip Air Mass Injection system (TAMI). In one phase of this program a full scale UH-1D rotor system was tested on the Helicopter Rotor Test Facility at NASA Langley [35]. The results of these tests were inconclusive because a BVI flight condition could not be obtained (resulting in later scale testing in the University of Maryland Wind Tunnel [36]). However, the test did serve as a validation method for their predictive codes. The testing also ultimately showed that by using a span wise TAMI system, the vortex structure could be changed and moved further outboard of the tip. This body of work also serves as a useful reference for how an air jet type system might be integrated into a helicopter rotor blade. In the full-scale testing, air was supplied to the rotor hub through a rotary union, transferred to the blade through a connector hose, and to the blade tips through the blade D-spar. The air was the steadily ejected through a nozzle embedded in the blade tip whose orifice was flush with the blades upper surface (Figure 1-14). Under certain laboratory conditions, the system was able to dissipate the vortex strength to some extent. However the added complexity of a fully articulated rotor in flight, and the accompanying unsteadiness of the wake, limited TAMI's capabilities. Though the TAMI testing did ultimately result in some significant reductions in BVI noise, the somewhat modest reductions (~4-6 dB), large increase in power requirement (~14%), and sensitivity to missing the vortex central axis led to its eventual demise.

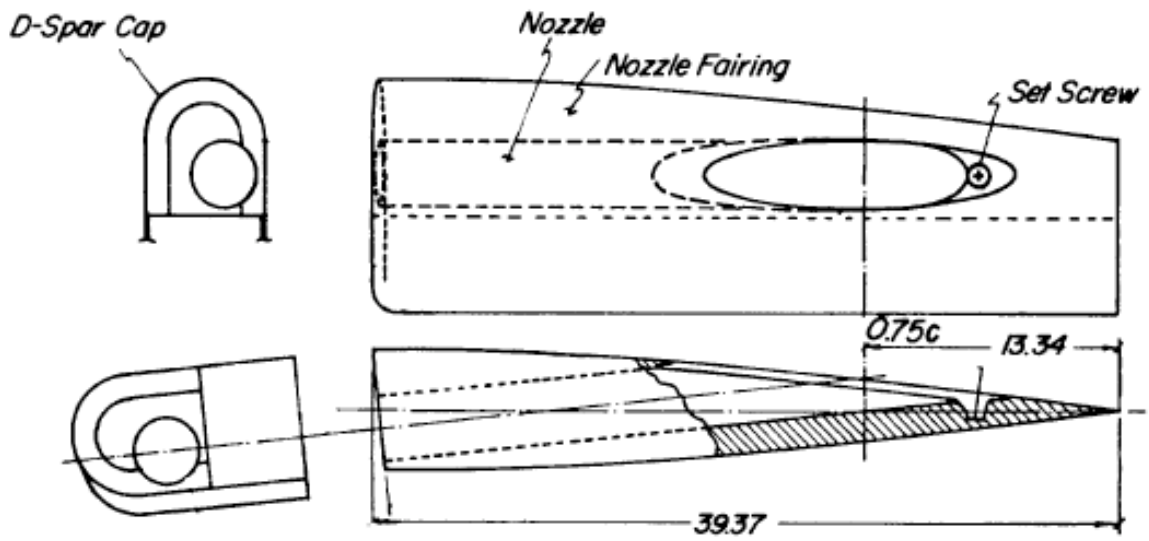

Figure 1-14: Schematic of nozzle and tip extension for TAMI [35].

Steady tip blowing was also conceived as a method to improve the lift generated by fixed wing aircraft. By using a single long slot, Lee *et al.* [37] showed that a span wise jet sheet could be created by using large mass flows that effectively modified the lift distribution in a fashion similar to an increase in aspect ratio. This however did not change the structure of the vortex itself. In order to achieve this, Wu and Vakili investigated the concept of using discrete wingtip jets to disperse the wake vortex by introducing multiple vortices into the tip flow region thereby increasing the instability of the tip vortex and reducing its strength [38]. Work by Gowanlock and Matthewson [39] later extended this method to rotorcraft, building a two bladed 25.25" radius rotor. A blade was designed with three discrete jets that were supplied with air from an external pressure source (Figure 1-15). They then used hot-wire anemometry and flow visualization to show that the vortices path could be altered using this method.

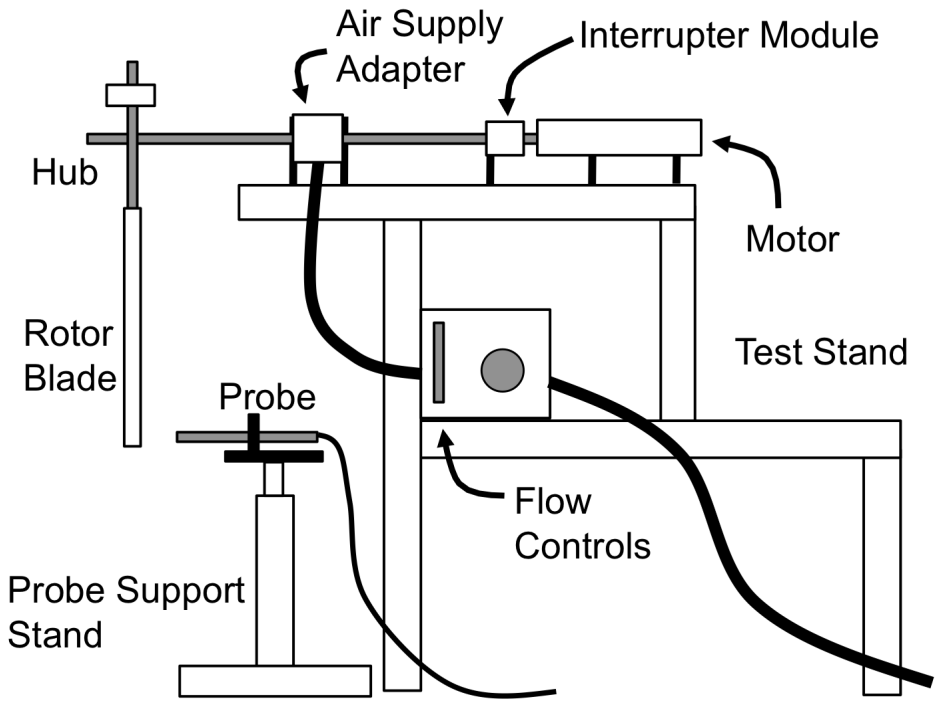

Figure 1-15: Rotor Test Stand used by Gowanlock and Mattheweson [39].

In an effort to mitigate some of the problems associated with complicated hub ducting and the additional power required for blowing, Han and Leishman [40,41] developed a system that used four ducts from the leading edge of the blade to the tip side, as shown in Figure 1-16. A reduction of the tip vortex's peak swirl velocity value of up to 60% and corresponding core radii of up to two or three times the baseline un-slotted blade was observed. This method also represents a promising concept for an active control methodology. By using the dynamic head at the inlet (a time varying function around the rotor azimuth), a time varying mass flow could be generated in conjunction with centrifugal pumping. Investigation of this system is still underway as of 2012. Additionally, several numerical studies on the tip blowing topic have been conducted [42,43]. These studies have generally been focused on the behavior of the tip vortex as a function of blowing and none have addressed the acoustic implications of these jets.

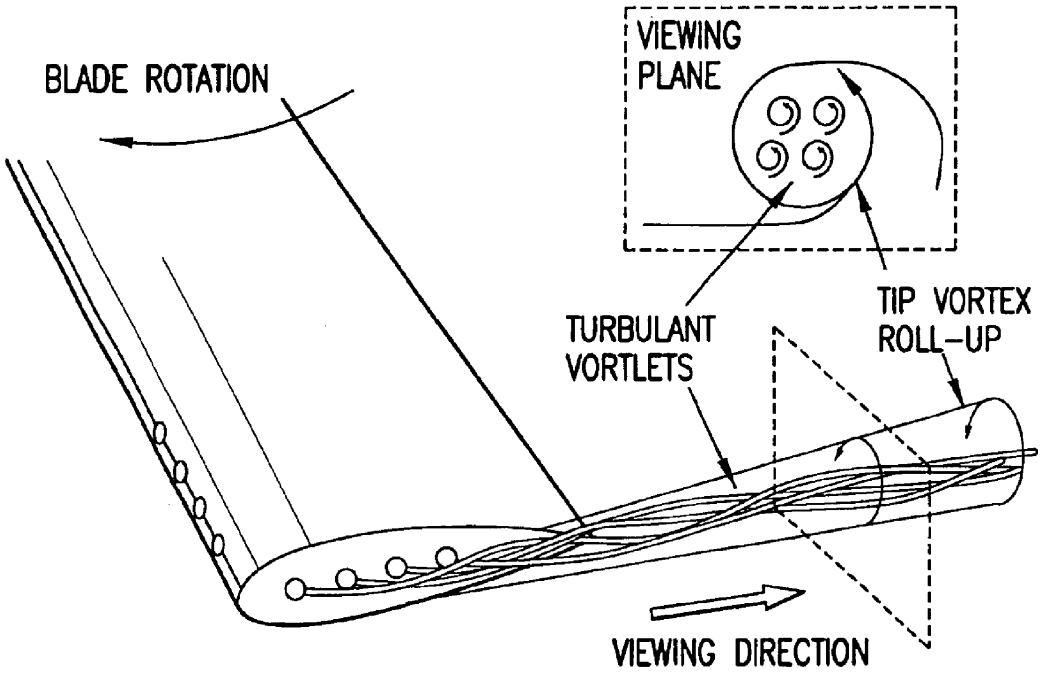

Figure 1-16: Schematic of slotted tip blade from Han, Leishman [41].

In addition to the steady blowing concepts already described, many attempts have also been made to employ unsteady blowing. With regard to BVI, the goal in using unsteady blowing is to induce high rates of vortex diffusion or even bursting of the vortex through actuation of specific vortex instability frequencies. Concepts such as synthetic jets (zero-net-mass jets) have shown promise for the control of flow separation and alleviating retreating blade stall [44,45] but inadequate for the suppression of BVI. More promising was the development of modulated positive net mass jets, which have been under investigation since the early 1960s in the form of reaction drive and circulation control (CC) wings and rotors.

1.2.5 Reaction Drive and Circulation Control Rotors

In the past few decades, one of the most widely researched uses of pumped air as a means of manipulating noise or aerodynamic performance has been the circulation

controlled wing or rotor. Though this concept was not originally aimed at reducing rotor noise (to the contrary, many were plagued by extreme levels of "jet noise"), the methods and lessons learned as they apply to embedding air jet technology into rotor systems are useful.

Reaction drive rotor concepts have been around since the early days of rotorcraft development due to their relative simplicity, alleviated anti-torque requirements, and potential for high-speed flight. Generally, compressed air is supplied to the rotor tip via ducting from a high-pressure source (usually a shaft driven compressor fan). The temperature of the exhaust (cold, warm or hot) dictates the materials and design for the system. Thrust can also be supplied via a tip jet of some type, such as the ramjets used on the McDonnel Helicopter Model 38 in the 1940s. In this case, propane fuel was supplied via piping to the tip where it was then ignited in the tip-mounted ramjet. Later iterations of this concept involved using very hot air pumped down the span of the blade into a combustion chamber where it was mixed with fuel and ignited, such as the XV-1 rotor [46]. Though these concepts provided important analysis tools and implementation ideas, they were plagued by a plethora of problems and failed to evolve into a practical rotorcraft design (as evidenced by the fact that no commercial or military aircraft use this technology). The pressure jet rotor did however open the door for a lower velocity, lower temperature solution in the circulation control rotor.

Circulation control (CC) rotors use the Coanda effect to induce an increase in sectional lift independent of angle of attack. By blowing tangential to the leading or trailing edge of an airfoil, the fluid will remain close to the surface thereby displacing the airfoil separation and stagnation points and thus altering the circulation (Figure 1-17).

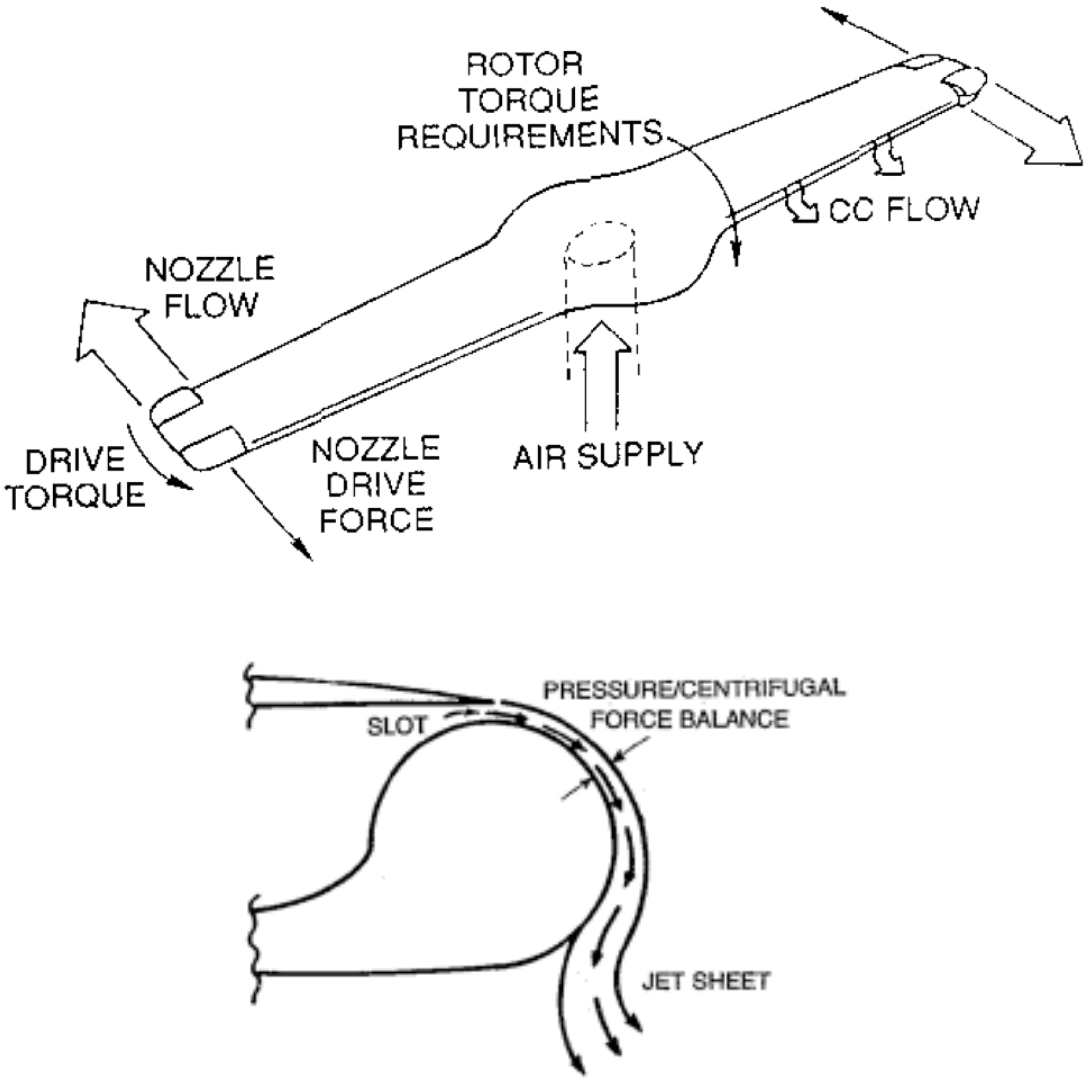

Figure 1-17: Schematic of Coanda effect rotor and forces on an airfoil.

Though originally investigated for fixed wing aircraft, Cheeseman and Seed [47] were the first to apply this technology to rotorcraft. The majority of the work done in the United States was conducted in the 1970s at the David Taylor Research Center (DTRC), a summary of which is provided by Englar and Applegate [48]. In the early 1980s Kaman built and tested a circulation controlled rotor on the HH-2D Seasprite. It was also around this time that the X-wing rotor concept came about.

The X-wing program was sponsored by NASA, the Defense Advanced Research Projects Agency (DARPA), the Army and Sikorsky Aircraft and was not aimed at designing a replacement for either rotorcraft or fixed-wing aircraft but rather an aircraft with special enhanced capabilities [49,50]. By using a 4-bladed, stoppable, circulation control rotor/wing, the program began in 1983 using aircraft developed during the Rotor System Research Aircraft (RSRA) program begun in the 1970s. The system was designed to use tip, trailing edge and/or leading edge blowing at any point around the rotor azimuth in either rotary wing, conversion, or fixed wing flight mode. After several wind tunnel and flight tests, the program ultimately ended in 1988, largely due to the systems complexity, cost, and stability problems in transitional flight. Despite the programs cancellation, a good deal was learned regarding the problems associated with flow in pneumatic rotor systems. A large number of complications were attributed to the extremely complex hub valve system (Figure 1-18) that was plagued by leaks and valve seizures. This emphasizes the need for a robust and simple valve system in the active jet acoustic control system design.

The acoustic ramifications of using a circulation control rotor were not fully realized or understood during the X-Wing program [51,52]. Recent work at the Georgia Institute of Technology in conjunction with NASA Langley has shown that circulation control can be used to not only reduce airframe noise on fixed wing aircraft by reducing slow separation, high angle of attack operation, and large exposed complex mechanisms, but also the location and formation of tip vortices on both fixed wing and rotor aircraft [53-56]. This of course would have a considerable effect on BVI noise and is under continued investigation.

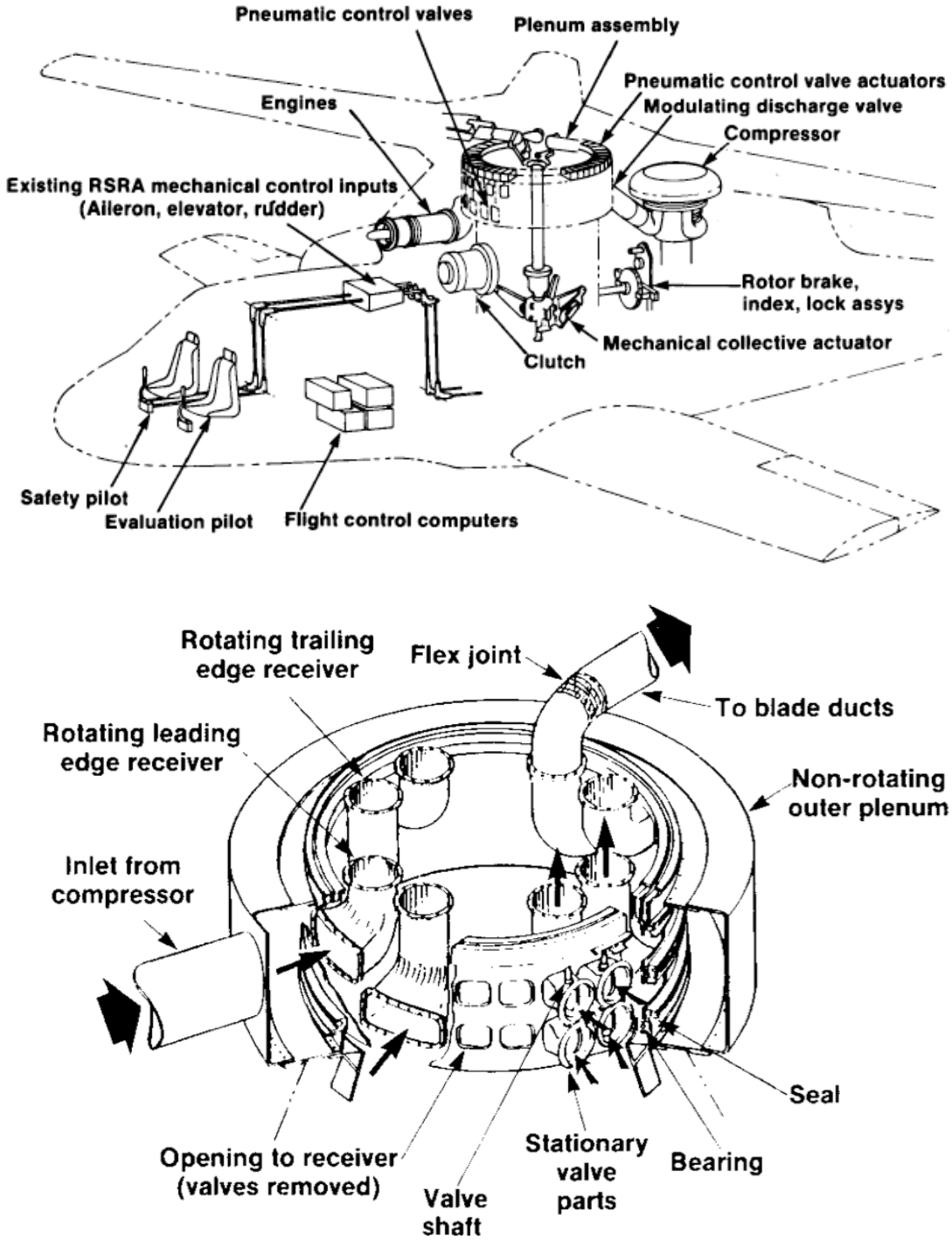

Figure 1-18: RSRA/X-Wing Schematic [49].

Another more recent effort in reaction driven rotorcraft has been in the development of the Canard rotor wing concept. An increase in demand for high-speed rotorcraft in the late 1990's rejuvenated interest in the rotor/wing concept at McDonnell Douglas (soon to be Boeing). Having been involved with the XV-9A, XH-17 and X-Wing program, Boeing understood that many of the problems faced by rotor/wing concepts were related to the transition between rotary wing and fixed wing flight. To alleviate some of these problems, the Canard wing concept aimed to offload the rotor almost entirely during transition mode, with the lift being generated by the canard and horizontal tail wings. The resultant design included a warm cycle, reaction driven rotor that, in forward flight would remain fixed and vector its thrust backwards, providing the additional thrust needed for high-speed flight [57]. Because other high-speed concepts often included large and heavy proprotors, the weight (compared to conventional rotorcraft) and relative inefficiency associated with reaction-drive systems were deemed to be a justifiable sacrifice given the systems reduced complexity and versatility. Using a single engine for both rotary and fixed wing flight meant that a new engine design wasn't necessary. The UAV concept that Boeing has developed with funding from DARPA, the X-50A Dragonfly, is shown in Figure 1-19.

Several interesting design features can be seen in the CRW concept. The two-bladed teetering rotor allows for easy transfer of the engine exhaust to blade ducts in the rotating frame. The flow was controlled not by a complicated series of hub valves as in the X-Wing demonstrator, but rather by varying the orifice area of a single mast valve (ball valve) and conventional jet thrust nozzles located in the rear of the aircraft [57]. Unlike the X-Wing, the Dragonfly also used conventional collective and cyclic controls

to control the rotor and used the tip jets only to drive the rotor. After several wind tunnel testing efforts, the X-50A program resulted in two demonstrator aircraft, both of which resulted in crashes after successful hover flights (the first in March 2004 and the second in April 2006) [58]. This ultimately led to the projects cancellation.

Figure 1-19: Boeing X-50A Canard Rotor Wing concept [57].

Though many of the efforts to use reaction control rotors have not specifically focused on noise reduction, it is important to consider why these technologies have all failed to find acceptance as the standard for rotor design. The goal in doing this is to avoid these same mistakes in later designing an active jet acoustic control system. Several important differences between the multitude of designs and the current design should be pointed out. First, the active jet acoustic control is not being used as a method of rotor primary or vibratory control. Though an acoustic controller will affect these characteristics, the active jet acoustic controller is something that would ideally only be

activated during specific missions and is not likely to be flight critical. As such, this system does not have to be as reliable as other primary control jet rotors and can be turned off when desired.

Secondly, many reaction drive rotors have suffered from extreme levels of noise radiating in every direction. In many cases this was determined to be the biggest problem with these designs. The active jet acoustic controller is very different in that cyclic control of the mass flow can instead be used to reduce noise. Duct and valve problems associated with reaction control designs have thus far proven insurmountable. The use of centrifugal pumping to generate the flow, with valve control near the blade tip should be explored in the future as a means of providing sufficient blowing profiles. This concept has been presented before for the design of a retreating side blowing concept, developed by United Technologies Corporation [59]. A schematic of this type of design is shown in Figure 1-20.

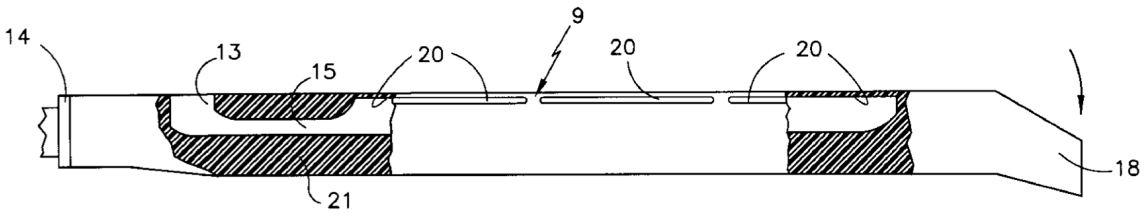

Figure 1-20: Centrifugal air flow control [59].

Despite the considerable research that has gone into reaction drive and other tip jet rotors to control rotor systems or actively mitigate BVI, there were no significant efforts to actively reduce other sources of rotor noise, including LF-IPH, until quite recently. Starting in 2007, several works on the subject were presented by Gopalan and Schmitz from the University of Maryland. A different approach was used to examine the rotor noise problem as an ideal far field noise reduction problem. This theoretical work

serves as the basis for the active jet acoustic control system. As mentioned previously, wind tunnel testing of the Boeing SMART rotor has also generated further interest in the idea of using on-blade active acoustic sources to control noise [6].

1.2.6 Theoretical Active Acoustic Control of IPH Noise

In the five theoretical works [2-4,60,61] that originally explored the noise reduction possibilities of on-blade acoustic controllers for the reduction of LF-IPH, the control was modeled as either a simple source of mass (monopole) or momentum (dipole). Gopalan and Schmitz investigated how ideal acoustic monopole or dipole sources placed on the rotor blade could be used to mitigate LF-IPH. The types of control that were examined include: monopole sink/source pairs in forward flight [2,61]; single monopole sources in hover [3] and forward flight [2,4,61]; single dipole sources in hover [3] and forward flight [2,4,61]; and distributed dipole sources in forward flight [60].

In order to calculate the noise reductions that could be obtained using these various sources, linear acoustic theory, in the form of the Ffowcs Williams and Hawkings equation [62] for surfaces in motion as applied to rotorcraft [63] was used to first predict the near in-plane target acoustic pressure. For the majority of this work, it was assumed that the near in-plane rotor thickness noise was dominant and that contributions from in-plane loading were small (though an analytical approximation to the loading noise in hover was used in [3]). The resultant governing equation then is,

$$4\pi p'(\vec{x},t) \approx \underbrace{\frac{\partial}{\partial t}\iint\left[\frac{\rho_0 v_n}{|\vec{x}-\vec{y}\|1-M_r|}\right]_\tau dS(\vec{y})}_{\text{Rotor Term 1: Blade Thickness Noise}} - \underbrace{\frac{\partial}{\partial x_i}\iint\left[\frac{p_{ij}n_j}{|\vec{x}-\vec{y}\|1-M_r|}\right]_\tau dS(\vec{y})}_{\text{Rotor Term 2: Blade Loading Noise}}$$
$$+\underbrace{\frac{\partial}{\partial t}\sum_j\left[\frac{\rho_0 v_{C,j,n}\Delta S(\vec{y}_{C,j})}{|\vec{x}-\vec{y}\|1-M_r|}\right]_\tau}_{\text{Control Term 1: Monopole Noise}} - \underbrace{\frac{\partial}{\partial x_i}\sum_k\left[\frac{F_{C,k,i}(\vec{y}_{C,j})}{|\vec{x}-\vec{y}\|1-M_r|}\right]_\tau}_{\text{Control Term 2: Dipole Noise}} \quad (1.1)$$

In this equation, the acoustic pressure p' observed at a location x and time t is approximated as the sum of the rotor thickness and loading noise and the monopole and dipole control noise. For the blade thickness the density (ρ_0) is multiplied by the velocity of the fluid normal to the blade surface (v_n) and divided by the distance between the source and observer |x-y| and Doppler amplification $|1-M_r|$. These are integrated at the correct retarded time for the entire blade surface (with panel area dS) and the derivative is taken. The blade loading noise requires knowledge of the blade surface pressure and is similar to the thickness calculation with the exception that a spatial derivative is taken (though this can and often is reformulated as a temporal derivative [64]). The control noise terms are in many ways similar to the rotor terms in that the monopole source is treated as an incompressible source of mass and the dipole term as a simple in-plane drag force, both located on and rotating with the blade.

Using a reformulated, simplified representation of these governing equations (or some parts of it), in which assumptions relevant to modern rotors were made, the effectiveness of the aforementioned controllers were explored using three methods: solving the governing differential equations numerically to obtain the required control time history for a desired noise reduction; using a prescribed multiple harmonic control

time history and calculating the effective noise reduction; and using a prescribed single frequency harmonic control time history.

In addition to the mathematical formulation of this problem it is also instructive to review the basic physics of the rotor noise mechanism in order to understand why this cancellation is possible. For this purpose the case of a rotor blade with a single source/sink pair located near the blade tip is examined.

1.2.6.1 Monopole Source and Sink Pair

In the first paper, presented in late 2007 to the International Forum on Rotorcraft Multidisciplinary Technology in Korea, the possibility of complete ("null") acoustic control for thickness/HSI noise was explored [2]. The required control strengths were calculated for a single source (located near the tip trailing edge) and a single sink (located near the tip leading edge) (Figure 1-21).

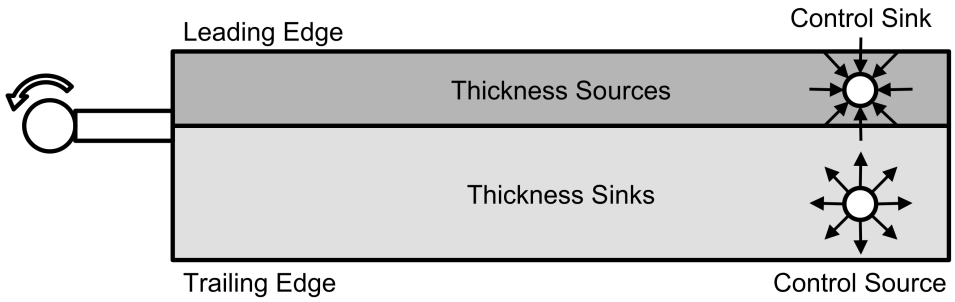

Figure 1-21: Sink/Source Acoustic control for approximate null solution.

As a rotor blade passes through the air, the volume of air equivalent to the volume of the rotor blade (the "apparent mass") is continuously "blown away" and "sucked in" resulting in radiated acoustic waves. Consider, for example, a hovering helicopter. Ignore the aerodynamic forces and focus on a fixed azimuth and radial location in the rotor plane. As the blade approaches, air is initially displaced outwards as the blade began to occupy the space. The blade continues to pass through this point in space and after the

maximum thickness has passed, air is then sucked back inwards (as a vacuum is clearly not left in the wake of a helicopter blade). Because these events occur at different times, the radiated acoustic energy perceived by the observer also arrives at slightly delayed times. The time rate of change of the combined source contributions then results in thickness noise. In effect, the rotor blade is acting as a series of sources (ahead of the maximum thickness) and sinks (behind the maximum thickness). A similar explanation can be made for the noise associated with in-plane loading with the exception that there is a directivity to the pushing and pulling of the free medium which can be modeled instead using dipoles.

By adding ideal sources and sinks near the tip of the rotor of opposite pressure amplitude to those associated with the blade thickness, one can choose a time varying control source strength profile that produces acoustic waves that approximately cancel the rotor noise. Because only one (or a few) sink/source pair is used, the control is most effective at a single point in space, tapering off to the sides and out of the rotor plane. This method was shown to require enormous mass flows (~40 kg/sec and $M_{JET} = 14.3$ for a UH-60 like rotor) and is physically unrealizable.

1.2.6.2 Single Mass Source (Monopole) Controller

The use of a single source located near the blade tip (Figure 1-22) was also explored and showed a reduced "zone of effectiveness" compared with the sink/source pair. However, localizing the mass flow solution to the advancing side of the rotor (which is where it is most efficiently radiated), the required source strength (mass flow rate) could be reduced significantly when high mass flow rates of change were used.

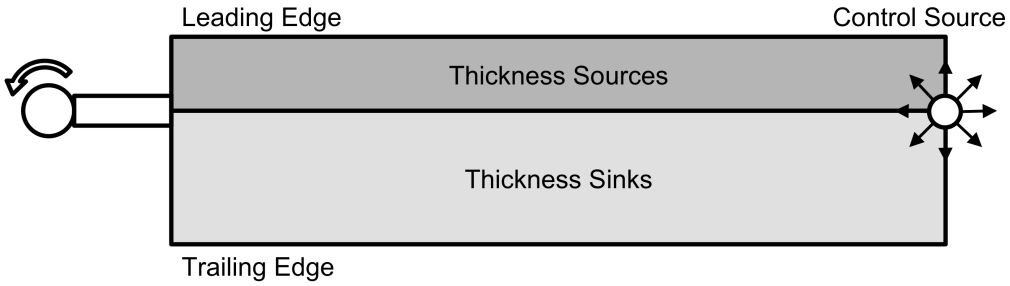

Figure 1-22: Single monopole (mass) source controller.

Solving the governing differential equation associated with the FW-H equation with an additional control source term, a mass flow profile was calculated that significantly reduced the peak-to-peak pressure amplitude of the rotor noise. This technique was then used to evaluate sources located at a variety of span-wise locations and it was concluded that the source strength requirements increase as the control source was moved in-board and that for the simple rectangular blade, the dominant feature of the source strength profile was a positive rate of change near the 90°rotor azimuth position (Figure 1-1). The solution was also shown to be composed largely of low and mid frequency harmonics (1 – 4/REV) and so these frequencies were determined to be most efficient at reducing the level of thickness noise. It was then shown that lower single-frequency controllers (2/REV) required larger mass flow rates for a set noise reduction while providing good cancellation over a wide observer angle range. Higher frequency controllers (3/REV) were shown to require smaller mass flow rates but suffer from more focused zones of effectiveness. These higher frequency controllers were also shown to be more likely to result in increased noise levels at off-target locations.

1.2.6.3 Single Force (Dipole) Controllers

The use of dipole (force) controllers for reduction of near in-plane rotor noise was also explored. Because of the ongoing, widespread research being conducted on on-blade

force controllers (flaps, slats, etc.) a physically realizable controller was figured to be closer at hand. For this method a pure in-plane drag controller was analyzed.

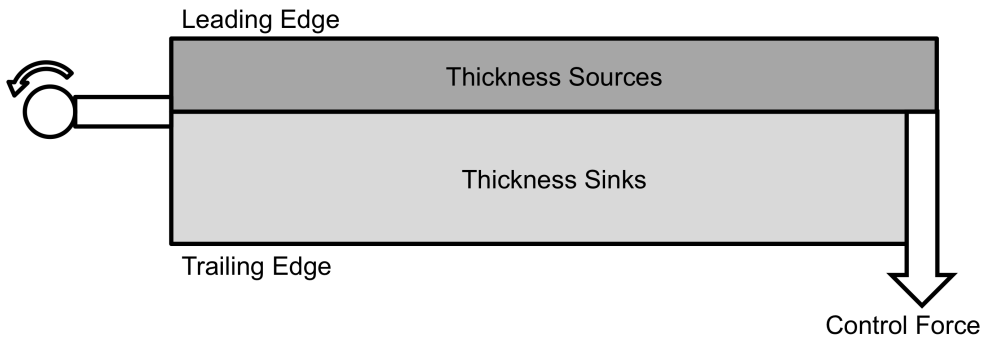

Figure 1-23: Single dipole (force) acoustic controller.

It was shown that significant noise reductions could be obtained using this type of pure dipole controller. For example, a 2/REV control with amplitude of 3.3% of rotor thrust resulted in a 20 dB reduction. The investigation also determined that the harmonic content of the control force requirement (calculated by solving the governing differential equation) was quite different from the monopole source requirements. While the monopole controller was dominated by the 1/REV and 2/REV content, the dipole control was dominated heavily by the 1/REV frequency content.

1.2.6.4 Distributed Force (Dipole) Controller

In an effort to improve the acoustic controller zone of effectiveness and explore the solution that most closely approximates on-blade flaps, the utility of distributed force (dipole) sources was also investigated (Figure 1-24). This method was found to be quite effective as it reduced the magnitude of the required drag force at any particular span-wise location. However, the distributed forces, if acting in unison, still had a relatively narrow zone of effectiveness.

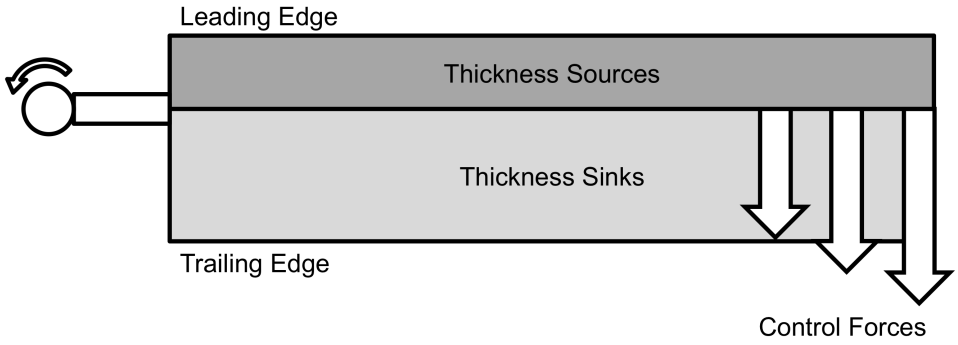

Figure 1-24: Distributed dipole (force) acoustic controller.

It was determined that by introducing multiple independent distributed sources, as would be the case for a rotor equipped with multiple flaps, the zone of effectiveness could be improved considerably. Using this method a solution was shown to reduce in-plane thickness noise by 6 dB over an azimuth zone of ±30° above and below the plane of the rotor.

1.2.6.5 Combined Monopole/Dipole Controllers

Missing from the previous body of work is an investigation of the utility of a combined mass and momentum source. This is the case most closely associated with an active subsonic air jet and is the focus of Chapter 2. In earlier work, an analytical approximation was used to help gain an understanding of how the time derivative terms of the acoustic equations could be controlled to produce the ideal on-blade controller to eliminate IPH (mostly thickness) noise. The approximation was validated for high aspect ratio rotor operating at advancing tip Mach numbers below 0.85 – becoming less accurate at higher advancing tip Mach numbers. For legacy helicopters operating at moderate advancing tip Mach numbers, the dominance of thickness noise is a good assumption. However, for higher aspect ratio, tapered, swept, and/or flexible modern rotors operating at lower tip speeds, the in-plane loading noise can alter the total rotor noise enough to

warrant its inclusion in the design process for any acoustic controller. Further, it can be particularly important in determining the LF-IPH. For more information on this topic, a parametric study of how some rotor variables influence loading noise and LF-IPH is explored in reference [65].

The combined monopole and dipole controller is similar in many ways to the other types of control that have been discussed. The LF-IPH produced by a rotor can be thought of as the result of a distribution of steady and unsteady sources rotating about a central axis in space. For thickness noise, the strength of these sources ($\rho_0 v_n$) is relatively steady for an observer sitting on the blade (in forward flight this is not strictly true). The noise that is generated is mostly due to the fact that the sources themselves are rotating at high speeds and the resultant acoustic waves omitted by the different sources arrive at the observer at slightly delayed times. Without the blade rotation, the same rotor blade would not generate much noise at all. A non-lifting blade section in free stream flow (say a low speed wind tunnel) does not produce significant levels of thickness noise.

At moderate tip Mach numbers, the thickness noise mechanism is capable of producing large amount of radiated acoustic energy using what are essentially steady acoustic sources. The active jet acoustic control and active acoustic control mechanisms in general are different. Steady acoustic controllers require large amounts of localized or distributed source strength in order to reduce LF-IPH. Instead, the unsteady component of the noise can be exploited, which, along with the amplifying mechanisms due to blade rotation, allow large levels of noise to be generated using modest amounts of source strength. In this sense, it is the time rate of change of the acoustic sources that dictate the shape and amplitude of the acoustic control anti-noise. Using two mechanisms of similar

shape and amplitude makes the combined mass/momentum controller an appealing solution for LF-IPH reduction. The addition of both mass and momentum to the quiescent medium allow significant levels of noise to be radiated.

1.2.7 Experimental Active Acoustic Control of IPH Noise

To date, only program has been conducted specifically addressing the reduction of in-plane harmonic helicopter rotor noise using active acoustic control. The joint DARPA/Boeing/NASA/Army test conducted in the National Full-Scale Aerodynamic Complex's 40 foot by 80 foot wind tunnel (NFAC) demonstrated that it is possible to reduce the low frequency IPH of the Boeing-SMART rotor (Figure 1-25) using active trailing edge flaps [5,6]. This work was part of Phase 1b of the DARPA Helicopter Quieting Program [7].

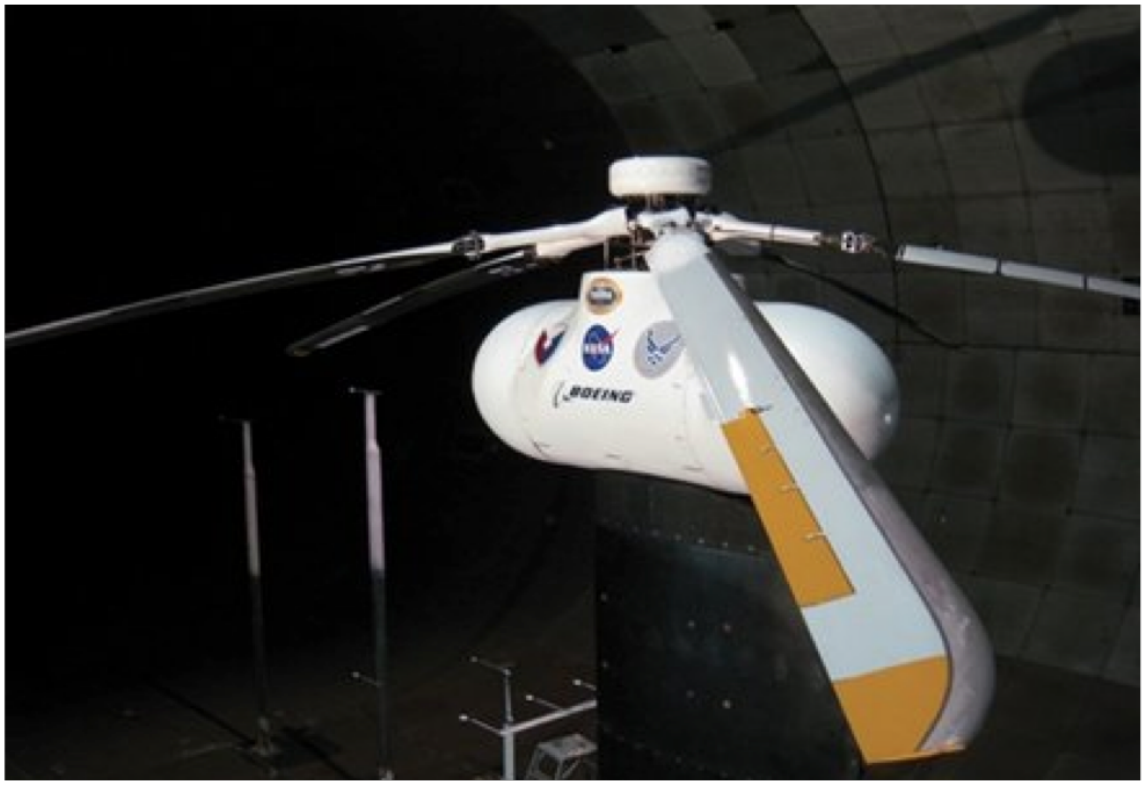

Figure 1-25: Boeing-SMART rotor with trailing edge flaps in NFAC [6].

Sim *et al.* showed that harmonic single trailing edge flap deflections could reduce the LF-IPH by up to 6 dB in steady level flight (advance ratio of 0.3). The deflections that resulted in the best noise reductions also corresponded with cases in which the in-plane force was increasing on the advancing side of the rotor. Though the experiment lacked on-blade pressure measurements for full validation, it was surmised that the governing mechanism of noise reduction was related to the change in magnitude and orientation of the lift vector due to flap deflection. These conclusions were in alignment with those made by Gopalan and Schmitz regarding the use of point and/or distributed dipoles sources on a rotor blade for LF-IPH reduction.

Though this work served as the first experimental validation of the active acoustic control methodology, it was not without its problems. The use of flaps as a means of generating the required in-plane noise for significant LF-IPH reduction has some fundamental limitations.

One such limitation is that flaps are not a pure in-plane force generator. Instead, they generate a pitching motion of the blade that results in a change in the lift distribution and orientation of the lift vector, as shown in Figure 1-26. Though the in-plane component of this lift vector can provide reduction in LF-IPH, the out-of-plane component can also result in large increases in out-of-plane noise. Sim showed that these increases could be as high as 12 dB 30° below the rotor plane for a target reduction of 4 dB. The use of flaps also presents vibration and performance issues. Sim et al reported that increases of 300% were found in the vibratory hub shear lateral and longitudinal modes (5/REV) when the flaps were actuated so as to provide the maximum noise reduction. It was also found that there was some degradation in performance though this was not quantified.

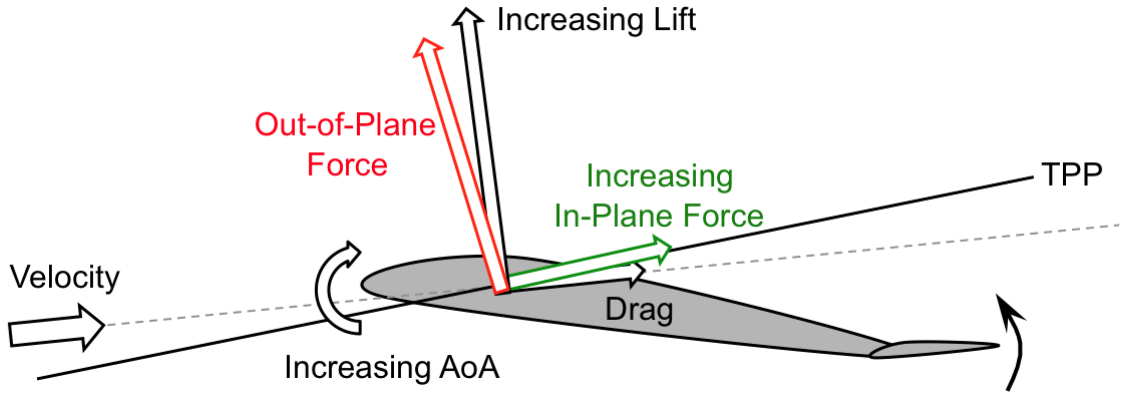

Figure 1-26: Effect of active flap on blade aerodynamic force.

The final issue with the data obtained during the SMART rotor program is with the size of the rotor and the tunnel in which it was tested. Subsequent studies of the acoustic reflections in the 40 by 80 foot NFAC facility found that the acoustic treatment, which was originally intended for rotors with a diameter of 10 feet, was insufficient for noise below 100 Hz [66]. The full-scale SMART rotor has a blade passage frequency of 32.7 Hz. Therefore, the first three harmonics of the rotor noise were likely corrupted to some extent by acoustic reflections. Though this does not diminish the significance of the results obtained during this testing, it does highlight the importance of using a properly treated acoustic environment with an appropriately sized rotor.

1.3 Objectives of Current Research

Specifically addressing this problem, the reduction of low frequency in-plane harmonic noise is a relatively new area of research. As such, very little theoretical and experimental work has been conducted in this area. The primary objective of this study is to develop a completely new method of actively reducing the low frequency in-plane harmonic noise of a helicopter rotor.

The new method entails using a time varying subsonic air jet ($M_{jet} < 0.6$) located at or near the tip of the rotor blade to generate the "anti-noise" required to reduce LF-IPH. As a first step in developing the Active Jet Acoustic Control, a theoretical acoustic model of the jet will be presented using linear acoustic theory (Chapter 2). This model will be applied to a baseline full-scale rotor, representative of modern helicopter rotors, and a parametric study examining the effect of varying jet size, angle, position and prescribed jet velocity will be conducted.

The second objective of this dissertation is to validate the theoretical model using a carefully controlled acoustic experiment. This experiment involves the design and use of a completely new Active Jet Acoustic Control Experimental Test Rotor (AJAX ETR) installed in the University of Maryland Acoustic Chamber. The single bladed, sub-scale rotor, which will be described in detail in Chapter 3, is appropriately sized for the acoustic treatment in this facility and can be run at full-scale tip Mach numbers. A fixed frame pneumatic system has been integrated with the rotor system so as to provide time varying airflow at the blade tip jet exit. This system is synchronized with the rotor encoder so that a phase lock can be maintained between the rotor angular position and valve flow rate.

In Chapter 4, the quality of the acoustic measurements of the uncontrolled AJAX ETR will be evaluated and compared to theoretical predictions. The ability to produce good quality and repeatable low frequency in-plane harmonic noise is a critical step in establishing the potential capabilities of the AJAX methodology.

Finally, in Chapter 5, the AJAX ETR will provide a unique opportunity to generate a dataset that can be used to validate the Active Jet Acoustic Control theoretical

model and ultimately, to show that the AJAX methodology is worth further pursuit. Several jet velocity control profiles will be evaluated in both the frequency and time domains.

Chapter 2: Theoretical Modeling

Since the emergence of the jet engine in the 1950s and the enormous growth of air transportation in the 1960s, countless efforts have been made to reveal and understand the noise generation mechanisms associated with air jets [67]. The most critical deficiency in the early understanding of these mechanisms stemmed from the inability to uniquely determine the location and relative strength of the noise generating sources. The inherent non-uniqueness of the source location and strength resulted in a multitude of claims and hypotheses over the past several decades. Despite this, no theory has yet been widely and readily accepted for subsonic jets, though modern sensing techniques have certainly made this closer at hand [68].

Lighthill was the one of the first to propose a mechanism of jet noise in his 1952 work on what is now referred to as the *acoustic analogy* [69] (this also ultimately led to the development of the Ffowcs-Williams and Hawking equations). Lighthill represented the aerodynamic sources in the jet shear layer between the jet and ambient medium as a distribution of quadrupoles. This theory has since been applied to countless sets of jet-noise data to show that the far-field sound pressure level scales with the 8^{th} power of the jet velocity. While this theory was able to capture many of the important features of jet mixing noise for moderate jet velocities, significant discrepancies between subsonic jet acoustic testing and Lighthill's model exist.

Due to the lack of knowledge regarding the exact nature of the noise mechanisms that dominate the far-field acoustic spectrum for low subsonic air jets, a simple model has been used in the design and analysis of an air jet acoustic controller. By constraining the

acoustic controller to low jet Mach numbers (M_{jet} < 0.6), the jet can reasonably be modeled as a combined source of mass and momentum. The quadrupole source contributions that dominate at moderate and high jet Mach numbers are then be assumed small. Further justification of this assumption comes from an examination of the governing equations for compressible fluid dynamics, which show that the monopole (mass), dipole (force) and quadrupole (stress) acoustic levels are roughly proportional to M^2, M^3, and M^4 [70]. This assumption was used by Crighton in his work on subsonic jets [71], who concluded that much of the difference between measurement and Lighthill's theory for low Mach number jets could be accounted for by the mass flow and momentum also associated with them.

2.1 Modeling Low Frequency In-Plane Harmonic Noise

As discussed in Chapter 1, low frequency in-plane harmonic noise (LF-IPH) is the summation of thickness and low frequency, loading noise near the rotor tip path plane. LF-IPH can be modeled using Farassat's Formulation 1A [63,64] of the Ffowcs Williams and Hawkings (FW-H) equation (Eq. 1.1) and neglecting the non-linear quadrupole term.

Formulation 1A is the retarded time formulation of the FW-H equations and is convenient in that it moves the time derivative of the sources inside the integral. This allows one to calculate the acoustic pressure at the observer location by simply repeatedly evaluating the integrand for each discrete source and adding them at the correct retarded time over the blade surface (for thickness noise, p'_T) or span-wise blade elements (for low frequency loading noise, p'_L). The equation then is,

$$p'_{ROTOR}(\vec{x},t) = p'_T(\vec{x},t) + p'_L(\vec{x},t) \tag{2.1}$$

where the thickness and loading noise produced by the rotor are,

$$4\pi p'_T(\vec{x},t) = \underbrace{\int_{f=0}\left[\frac{\rho_0\left(\dot{v}_n + v_{\dot{n}}\right)}{r\left|1-M_r\right|^2}\right]_{ret} dS + \int_{f=0}\left[\frac{\rho_0 v_n \dot{M}_r}{r\left|1-M_r\right|^3}\right]_{ret} dS}_{\text{far-field}} + \underbrace{\int_{f=0}\left[\frac{\rho_0 v_n a_0\left(M_r - M^2\right)}{r^2\left|1-M_r\right|^3}\right]_{ret} dS}_{\text{near-field}} \tag{2.2}$$

$$4\pi p'_L(\vec{x},t) = \frac{1}{a_0}\underbrace{\int_{f=0}\left[\frac{\dot{l}_r}{r\left|1-M_r\right|^2} + \frac{l_r \dot{M}_r}{r\left|1-M_r\right|^3}\right]_{ret} dS}_{\text{far-field}} + \underbrace{\int_{f=0}\left[\frac{l_r - l_M}{r^2\left|1-M_r\right|^2}\right]_{ret} dS + \int_{f=0}\left[\frac{l_r\left(M_r - M^2\right)}{r^2\left|1-M_r\right|^3}\right]_{ret} dS}_{\text{near-field}} \tag{2.3}$$

In equations (2.2) and (2.3), ρ_0 is the ambient density, v is the body velocity, n is panel normal vector, r is the distance between the source and observer, M_r is the relative Mach number of the source and l is the sectional blade load vector. The dots denote a derivative with respect to source time, subscripts represent when the dot product of two vectors is to be calculated, and the integrands are bracketed $[\ldots]_{ret}$ within to reinforce that the terms must be evaluated at the correct retarded time.

The thickness noise calculation is quite straightforward as it is dictated by the rotor geometry and flight condition. Blade geometric surfaces are modeled and discretized using CATIA software (which allows for non-traditional blade geometries to be imported) after which all normal and position vectors are computed.

Because it is the low-frequency noise that is of particular interest for this work, a compact acoustic source approximation is used for loading noise prediction. The loads, which are predicted using either UMARC for the theoretical analysis in this chapter or

Blade Element Momentum Theory for the experimental predictions in chapters three and four, are then calculated at discrete span-wise locations along the blade. The in and out of plane time varying loads are then used to calculate the loading noise.

Both thickness and loading noise are computed using a self-written acoustics code in MATLAB. This allows the rotor acoustics to be calculated and stored before computing the active jet acoustic control noise.

2.2 Modeling Active Jet Acoustic Control Noise

The Ffowcs Williams and Hawkings equations are widely used in the prediction of helicopter rotor noise. They are a rearrangement of the exact Navier-Stokes equations, using generalized function mathematical theory, into an inhomogeneous wave equation with quadrupole sources distributed throughout the volume surrounding the body, and monopole and dipole sources distributed on the surface of the body. In this respect they are a generalization of Lighthill's acoustic analogy so as to include the acoustic energy that is radiated by very general types of sources in motion. In differential form, the full permeable formulation of the governing aeroacoustic equation is,

$$\Box^2 p' = \frac{\partial}{\partial t}\left[\rho_0 v_n + \rho\left(u_n - v_n\right)\right]\delta(f) \qquad \text{(Monopole/Mass)} \tag{2.4}$$

$$-\frac{\partial}{\partial x_i}\left[\left(P_{ij} n_j + \rho u_i\left(u_n - v_n\right)\right)\delta(f)\right] \qquad \text{(Dipole/Momentum)}$$

$$+\frac{\partial^2}{\partial x_i \partial x_j}\left[T_{ij} H(f)\right] \qquad \text{(Quadrupole/Non-Linear Stresses)}$$

where v_n is the velocity of the moving body normal to the body surface, u_n is the velocity of the fluid with respect to the medium, p is the pressure acting on the body surface, and T_{ij} is the Lighthill stress tensor

The FW-H equations are directly applicable and valid for the prediction of the low frequency in-plane harmonic noise generated by solid rotor blades operating at low subsonic Mach numbers. In this case, the local transonic aerodynamics are neglected and the blade is modeled as an impermeable body using a surface distribution of monopole and dipole sources to represent the blade thickness and loading. In Equation (2.4), the fluid and body velocity normal to the surface are assumed to be equivalent ($u_n = v_n$) so that fluid cannot pass through the surface. The resultant impermeable surface formulation, neglecting the quarupole term is, in differential form,

$$\Box^2 p' = \frac{\partial}{\partial t}\left[\rho_0 v_n\right]\delta(f) \qquad \text{(Thickness Noise)} \tag{2.5}$$

$$-\frac{\partial}{\partial x_i}\left[\left(P_{ij} n_j\right)\delta(f)\right] \qquad \text{(Loading Noise)}$$

As the tip Mach number is increased into the transonic regime, the FW-H equation can once again be used if the transonic aerodynamic effects surrounding the blade are included in the modeling. This requires knowledge of the local transonic pressures on the blade surface as well as the inclusion of quadrupole sources surrounding the blade. Modern computational fluid dynamics has made gathering this necessary information easier and the permeable surface formulation of the FW-H equation (2.4) has seen considerable use. In these problems the surface of the blade is no longer specifically included in the FW-H equation. Instead, a permeable surface off of the blade surface and enclosing all, or most of the non-linear aerodynamic effects is used. The CFD solution within this volume then includes both the thickness, loading and other non-linear effects and can be used to calculate the perturbations on the permeable surface itself, and subsequently the acoustic energy propagated to the far-field.

The permeable and impermeable FW-H equations are based upon a free-space solution to the three-dimensional linear wave equation in an unbounded homogenous space. When additional mass or energy is added to the flow at a physical surface of the solid body, the problem becomes a more complex two-phase flow problem that has no known simple wave equation solution. However, by interpreting the mass and energy sources as alterations to the surface boundary conditions in the FW-H equations, an analogy can be made that can be used to model the active jet acoustic control.

In the simplest sense, the active jet acoustic control explored for this work is both a source of mass and momentum that is directly injected into the quiescent medium. Several simplifying assumption regarding the nature of the air jet boundary conditions are made in order to facilitate the ability to model these processes within the framework of the FW-H equations.

The jet is first idealized as a perturbation monopole point source ejecting mass into the free medium at a rate of,

$$\dot{m}_{jet} = \rho_{jet} A_{jet} V_{jet} \tag{2.6}$$

and moving with respect to the quiescent medium at a speed of,

$$\vec{V}_{\text{source}} = \vec{\Omega} \times \vec{r}_{jet} + \vec{V}_{\infty} \tag{2.7}$$

A diagram of the source and respective velocity vectors is shown in Figure 2-1.

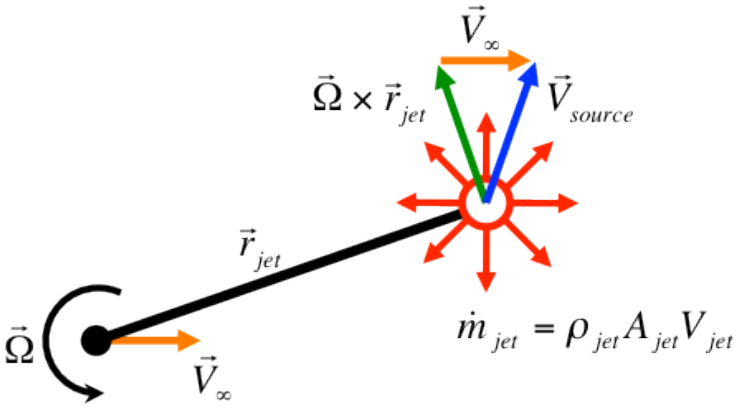

Figure 2-1: Monopole point mass source moving through quiescent medium.

An important assumption that is made is that the amount of mass injected into the medium by the air jet is small with respect to the entire fluid domain for an observer that is very far away from the source.

Since a real air jet is not omnidirectional but instead ejects air in a direction normal to the jet orifice surface, the injected air particles have a velocity greater than zero, which is the velocity of the quiescent medium by definition. In reality, air passing from the blade jet duct (non-inertial frame) to the free medium (inertial frame) will experience some degree of impedance associated with the interface between the jet and the surrounding flow. An acoustic wave traversing this interface will experience an impedance change due to viscous mixing, pressure gradients, and density changes. Ultimately the impedance of the boundary would result in the partial reflection of the radiated acoustic energy and a reduced level of noise radiated into the acoustic far-field.

Determining the impedance of this interface is very complex, particularly for a time-varying air jet on the tip of a rotor blade. Accurately predicted the flow field near the tip of a solid rotor blade is complicated in itself. Adding a source of time varying mass and momentum makes the problem even more difficult. In lieu of any knowledge of

the boundary condition, it is therefore assumed that there is no impedance across the interface between the jet and the surrounding medium. All of the momentum of the air released at the blade tip is therefore converted directly, and fully, into radiated acoustic energy. Furthermore, the pressure and density of the ejected air are assumed to be the same as the ambient medium and so,

(2.8) $\rho_{\text{jet}} = \rho_0$ and $\left(\text{P}_{\text{ij}}\right)_{jet} = 0$

Since there is no impedance across the jet boundary, the momentum flux of the mass injected into the free medium is then the product of the mass flow rate of the injected fluid and the fluid injection velocity with respect to free medium.

(2.9) $\vec{F}_{jet} = \dot{m}_{jet}\left(\vec{V}_{jet} + \vec{V}_{source}\right) = \dot{m}_{jet}\left(\vec{V}_{jet} + \vec{\Omega} \times \vec{r}_{jet} + \vec{V}_{\infty}\right)$

Note that the jet velocity $\vec{V}_{jet}$ is defined with respect to an observer on the blade moving with the jet (the non-inertial reference frame). A diagram of the air jet mass momentum before and after injection into the free medium is shown in Figure 2-2. Since it is assumed that there is no impedance across the boundary, the velocity just before and after release are effectively the same. The momentum is injected instantaneously at the current jet location. Also embedded in this assumption is that the jet flow itself does not affect the surrounding pressures, including the pressures on the surface of the blade. This decouples the jet from the rotor blade.

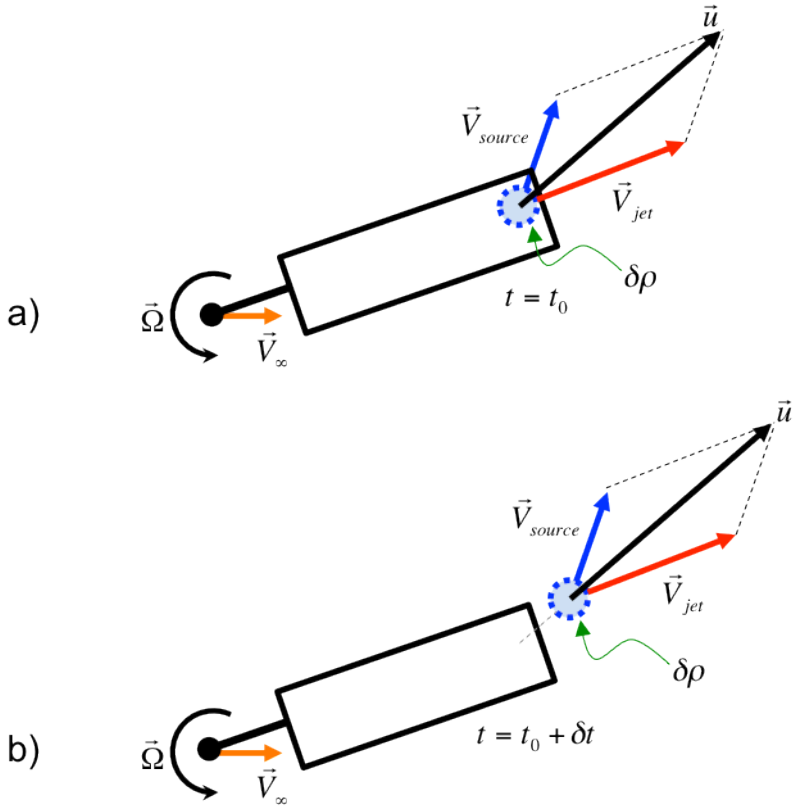

Figure 2-2: Jet momentum transfer from blade (a) to free medium (b).

Using these definitions of mass (2.6) and momentum (2.9) flux, the analogy to the generalized source terms that appear in the permeable FW-H equation can be made. If a similar approach is taken using the permeable mass and momentum injection terms from equation 2.4 then,

(2.10) $Q = \rho A\left(u_n - v_n\right)$ (Mass Injection)

(2.11) $\vec{F} = \rho A\vec{u}\left(u_n - v_n\right)$ (Momentum Injection)

Remembering that u and v are defined as the fluid and body velocities with respect to the free medium, the corresponding velocities for the idealized tip jet are,

(2.12) $\vec{u} = \vec{V}_{\text{jet}} + \vec{V}_{\text{source}}$

(2.13) $\vec{v} = \vec{V}_{\text{source}}$

The analogous mass injection source term for the jet is then, for $\rho = \rho_0$,

$$(2.14) \quad Q = \rho A\left(\vec{u}\cdot\hat{n} - \vec{v}\cdot\hat{n}\right) = \rho_0 A_{jet}\left(\vec{V}_{jet}\cdot\hat{n}\right) = \rho_0 A_{jet} V_{jet} = \dot{m}_{jet}$$

Similarly, the momentum injection for the jet contains the same mass flux multiplied by the jet fluid velocity.

$$(2.15) \quad \vec{F} = \rho A\left(u_n - v_n\right)\vec{u} = \dot{m}_{jet}\vec{u} = \dot{m}_{jet}\left(\vec{V}_{jet} + \vec{V}_{source}\right)$$

This exercise highlights that the permeable FW-H source terms in (2.14) and (2.15) are identical to the perturbation source strengths derived for the air jet in (2.6) and (2.9). Using this analogy and the aforementioned assumptions for the jet, which are listed here for convenience, Formulation 1A of the FW-H equation is used to calculate the noise radiated by the time-varying tip jet. Though the jet model used for this analysis is imperfect, it should model all of the first order acoustic effects.

Idealized Tip Jet Assumptions

1. The fluid impedance across the jet boundary is zero.
2. The fluid is inviscid (no mixing) and incompressible ($\rho_{jet} = \rho_0$).
3. The pressure of the jet fluid injected into the medium across the boundary is equal to the ambient pressure, $(P_{ij})_{jet} = 0$.
4. The air jet does not affect the blade surface pressures and vice versa.
5. The additional mass injected into the medium is very small compared to the surrounding fluid mass for an observer far away.

This retarded time formulation allows all time derivatives to be taken in source time. Formulation 1A for the new jet source terms is then,

(2.16) $$p'_{AN}(\vec{x},t) = p'_{M}(\vec{x},t) + p'_{F}(\vec{x},t)$$

(2.17) $$4\pi p'_{M}(\vec{x},t) = \underbrace{\sum\left[\frac{\dot{Q}_n}{r\left|1-M_r\right|^2}\right]_{ret}}_{\text{far-field}} + \underbrace{\sum\left[\frac{Q_n\left(r\dot{M}_r\right)}{r\left|1-M_r\right|^3}\right]_{ret}}_{\text{far-field}} + \underbrace{\sum\left[\frac{Q_n\left(a_0 M_r - a_0 M^2\right)}{r^2\left|1-M_r\right|^3}\right]_{ret}}_{\text{near-field}}$$

where $Q_n = \rho_0 A_{jet}\left(\vec{V}_{jet}\cdot\hat{n}\right) = \dot{m}_{jet}$, $\dot{Q}_n = \rho_0 A_{jet}\left(\frac{\partial\left(\vec{V}_{jet}\cdot\hat{n}_{jet}\right)}{\partial\tau}\right)$ and $\vec{\mathrm{M}} = \frac{\vec{\mathrm{V}}_{\text{source}}}{\mathrm{a}_0}$

(2.18) $$4\pi p'_{F}(\vec{x},t) = \frac{1}{a_0}\underbrace{\sum\left[\frac{\dot{F}_r}{r\left|1-M_r\right|^2}\right]_{ret}}_{\text{far-field}} + \frac{1}{a_0}\underbrace{\sum\left[\frac{F_r\left(\dot{M}_r\right)}{r\left|1-M_r\right|^3}\right]_{ret}}_{\text{far-field}} + \underbrace{\sum\left[\frac{F_r - F_M}{r^2\left|1-M_r\right|^2}\right]_{ret}}_{\text{near-field}} + \underbrace{\sum\left[\frac{F_r\left(M_r - M^2\right)}{r^2\left|1-M_r\right|^3}\right]_{ret}}_{\text{near-field}}$$

where $\vec{F} = \dot{m}_{jet}\left(\vec{V}_{jet} + \vec{V}_{source}\right)$

Subscripts r and M denote the component of a vector in the radiation of body velocity Mach number direction (i.e. $F_r = \vec{F}\cdot\frac{\vec{r}}{|\vec{r}|}$). The square brackets denote that the source contribution from all quantities must be added at the correct retarded time.

The solution to this equation is calculated using a prescribed jet velocity based on either theoretical or experimentally obtained values. The total controlled noise is then predicted at a given time and observer position by adding the rotor noise and "anti-noise" at the correct retarded time,

(2.19) $$p'_{TOT}(\vec{x},t) = p'_{ROTOR}(\vec{x},t) + p'_{AN}(\vec{x},t)$$

One of the more interesting results of the aforementioned mass and momentum injection source terms can be seen for the most simple jet configuration. A jet located at the blade tip and the elastic axis and pointed in the radial direction on a hovering rotor.

The mass flux source term is a scalar quantity and so it is independent of the jet direction or location in the free medium. Realistically, a steady jet mass flow rate would require a time-varying backpressure to compensate for the time varying exit boundary pressure condition. However, the mechanisms required to generate the jet velocity are not considered in this work and so we assumed that the desired flow velocity and mass flux rate are provided.

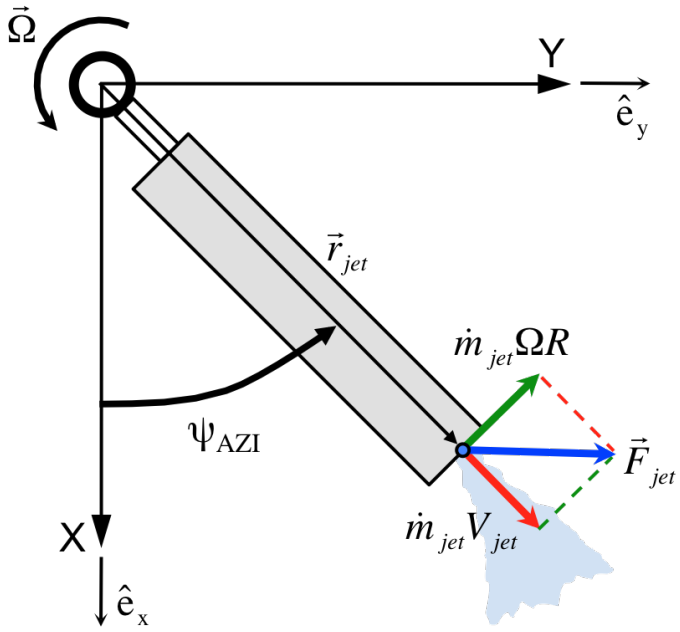

Figure 2-3: Schematic of momentum injection for radial tip jet in hover.

Though the mass term is an efficient acoustic source and accounts for the majority of the radiated noise, the momentum term is perhaps more interesting. For the hovering tip jet, as shown in Figure 2-3, the jet velocity and source vectors with respect to the quiescent medium are,

(2.20) $$\vec{V}_{jet} = \left(V_{jet}\cos\psi\right)\hat{e}_x + \left(V_{jet}\sin\psi\right)\hat{e}_y$$

(2.21) $$\vec{V}_{source} = \left(-\Omega R\sin\psi\right)\hat{e}_x + \left(\Omega R\cos\psi\right)\hat{e}_y$$

where $\hat{e}_x$ and $\hat{e}_y$ are unit vector pointing along the fixed frame x and y axes. The momentum flux injected into the free medium is then,

(2.22) $$\vec{F} = \dot{m}_{jet}\left(V_{jet}\cos\psi - \Omega R\sin\psi\right)\hat{e}_x + \dot{m}_{jet}\left(V_{jet}\sin\psi + \Omega R\cos\psi\right)\hat{e}_y$$

From equation (2.22), evaluated at $\psi = 0°$, the momentum injection is then,

(2.23) $$\vec{F} = \dot{m}_{jet}\left(V_{jet}\right)\hat{e}_x + \dot{m}_{jet}\left(\Omega R\right)\hat{e}_y$$

This represents an introduction of momentum not only along the jet axis, as would be the case for a traditional jet, but also perpendicular to the jet axis, in the blade chord-wise direction. The magnitude of this momentum is equal to the product of the jet mass flow rate and rotor tip speed, and thus not insignificant. This injected momentum is similar to a dipole drag source but it not necessarily manifested as an actual drag force exerted on the rotor since energy is actually being added to the free medium. What this means acoustically will become apparent in the coming sections.

Though the physical explanation of these jet control cases are interesting, it is the acoustic implications of these source strengths that are most relevant to this body of work. The phase, amplitude and directivity of the acoustic waves associated with the mass flow and momentum produced by these jets dictate how successfully the active acoustic control is at reducing LF-IPH. To evaluate a control's effectiveness, a baseline acoustic signature that is to be reduced must first be defined.

2.3 Baseline Rotor and Active Jet Acoustic Control Definition

To explore and understand the potential effectiveness of an active jet acoustic control system, a parametric design study is conducted. Baseline rotor, flight condition, and AJAX parameters typical of modern rotor systems and "low-noise" flight conditions are defined in this section. A parametric sweep of jet angle, radial location, chord-wise location, peak velocity, and jet area will then be conducted for both steady and unsteady blowing.

2.3.1 Rotor Configuration

A survey of five modern medium lift helicopters is used to choose the major rotor design parameters for this study. In addition to the quantities defined in Table 2.1, the baseline rotor also has a constant chord NACA 0009 airfoil and has no sweep, anhedral, or taper. Though this is not representative of many modern rotors, a simple rectangular blade planform has been chosen to focus on the active control design as opposed to passive acoustic control. It is important to note though that these design attributes can and will change the LF-IPH of a helicopter (generally reducing the levels) and can be used to the active acoustic control designers advantage.

Table 2.1: Typical Medium Lift Helicopter Rotor Parameters

Helicopter	GW(lb)	N_b	R (ft)	c_{AVG} (ft)	AR	V_{TIP} (ft/s)	M_H	DL (lb/ft^2)	θ_{TW}
UH-60	22,972	4	26.75	1.730	15.46	725	0.649	10.22	-16°
S-92	26,500	4	26.84	1.937	13.85	725	0.649	11.71	NA
AH-64	23,500	4	24.00	1.750	13.71	726	0.650	12.99	-9°
AS-332L1	18,960	4	25.59	1.970	12.99	710	0.636	9.22	-12°
AS-332L2	20,944	4	26.58	1.970	13.49	737	0.660	9.44	-12°
MEAN	22,575	4	25.95	1.871	13.87	725	0.649	10.67	-12°
BASELINE	**22,000**	**4**	**26.00**	**1.857**	**14.00**	**725**	**0.649**	**10.36**	**-12°**

2.3.2 Low Noise Flight Condition

A single flight speed has been chosen to represent speeds often associated with low noise approach/loiter type missions, 85 knots (μ = 0.2, M_{AT} = 0.779). The target observer (1) is established 1000 feet ahead of the rotor, directly in the rotors' tip path plane. Control effectiveness is also be examined at 15° deviations from this location (observers 2 through 5) when appropriate. A diagram of the flight condition and observers is shown in Figure 2-4.

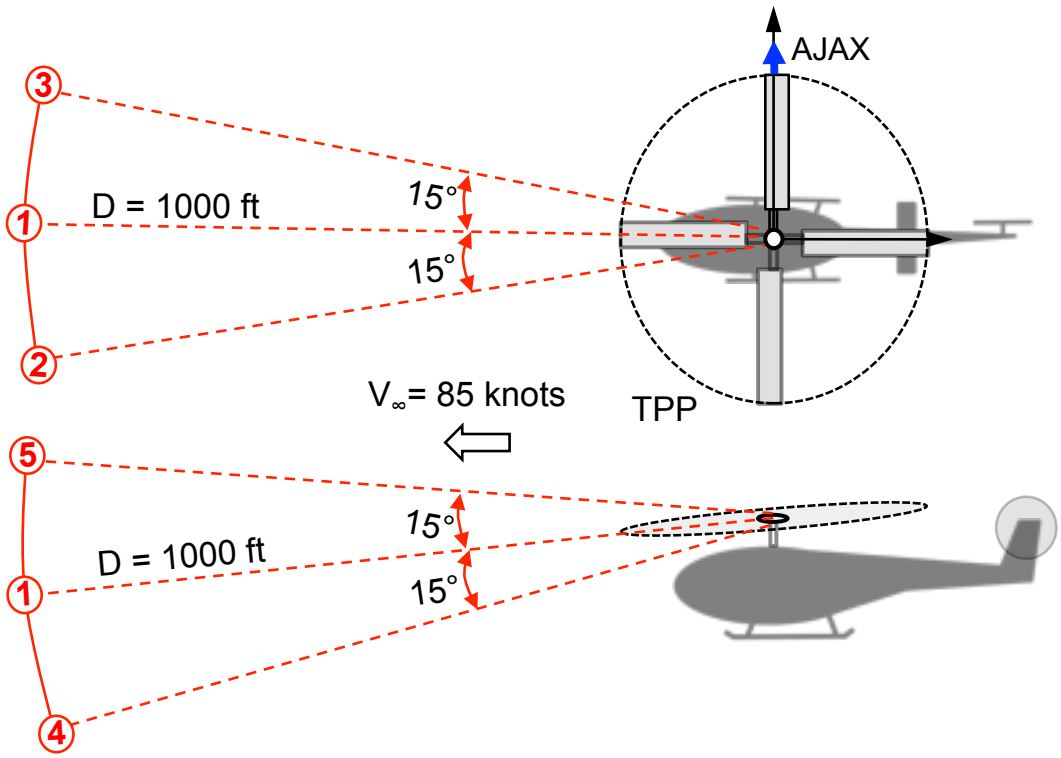

Figure 2-4: Low noise flight condition observer locations.

2.3.3 Active Jet Exit Configuration

To establish baseline parameters for the AJAX exit, conservative estimates of the available space at the tip have been made based on modern blade construction and the baseline blades' cross-sectional area.

Air jet blowing strength and velocity are traditionally quantified using two non-dimensional terms, the blowing coefficient and jet velocity ratio defined respectively as,

$$C_\mu = \frac{\dot{m}_{jet} V_{jet}}{\frac{1}{2}\rho(\Omega R)^2 S} \tag{2.24}$$

$$\overline{V}_{\text{jet}} = \frac{V_{jet}}{\Omega R} \tag{2.25}$$

where S is the blade planform area. Assuming incompressible flow, the mass flow is $\dot{m}_{jet} = \rho_0 A_{jet} V_{jet}$. The jet area can then be expressed in terms of the blowing coefficient and jet velocity ratio as,

$$A_{jet} = \frac{C_\mu S}{2\left(\overline{V}_{jet}\right)^2} \tag{2.26}$$

To limit the investigation of the acoustics associated with jets to physically practical levels, bounds on both the jet Mach number and jet orifice area are imposed. In order to avoid the complications associated with modeling jets that are approaching sonic velocities, the maximum jet Mach number is limited to 0.6. Similarly, the size of the jet orifice is restricted by the available cross sectional area of the rotor blade itself. Assuming an elliptical duct area that fits within a symmetric airfoil (Figure 2-5) of thickness (t) and chord (c), the maximum duct area is defined as [75],

$$A_{jet} = \pi\left(\frac{t}{2}\right)\left(\frac{0.74c}{2}\right) \tag{2.27}$$

For a NACA 0009 airfoil then with a chord of 1.857 ft, the maximum orifice area is 0.183 ft^2 and the maximum mass flow rate, assuming standard atmospheric values of density and speed of sound, is then 9.17 lb/sec.

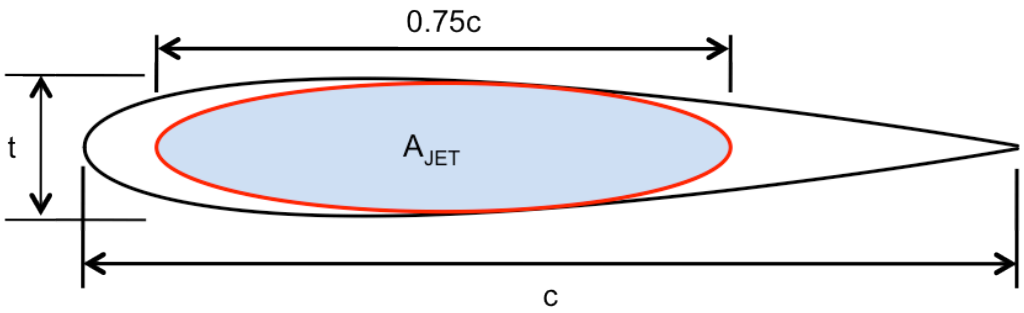

Figure 2-5: Maximum jet exit geometry.

The baseline jet is defined as being located at the blade elastic axis, at the tip with a radial jet angle of 0°. The baseline jet exit area is defined as half of the maximum value, $A_{JET} = 0.0915$ ft^2, and the baseline jet velocity is defined as 103.25 m/s ($M_{JET} = 0.3$). All of the baseline jet parameters are summarized in Table 2.2

Table 2.2: Active Jet Baseline Configuration

Parameter	Value
A_{jet}	0.0915 ft^2
A_{jet}/A_{BLADE}	43%
r_{jet}	< R, 0, 0 >
c_{jet}	0
α_{jet}	0°
$\overline{V}_{jet}$	0.4672
C_μ	0.000827

2.3.4 Baseline Rotor Acoustic Signature

The thickness noise produced by the baseline rotor is a function of blade geometry, rotational speed, flight speed, and tip path plane orientation. These parameters are used to calculate the baseline rotor thickness noise using Farassat's Formulation 1A of the FW-H equation as described in section 2.1. Figure 2-6 shows the resultant time history and frequency content (Figure 2-7) at the target observer, position 1.

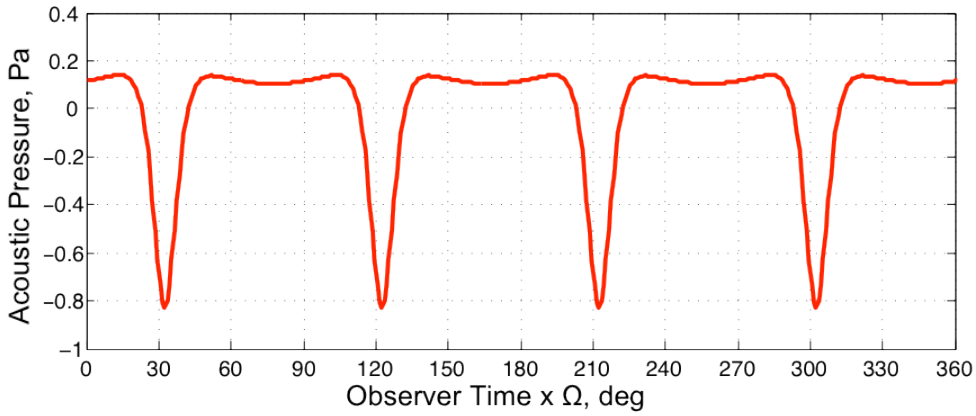

Figure 2-6: Baseline rotor thickness acoustic pressure at observer 1

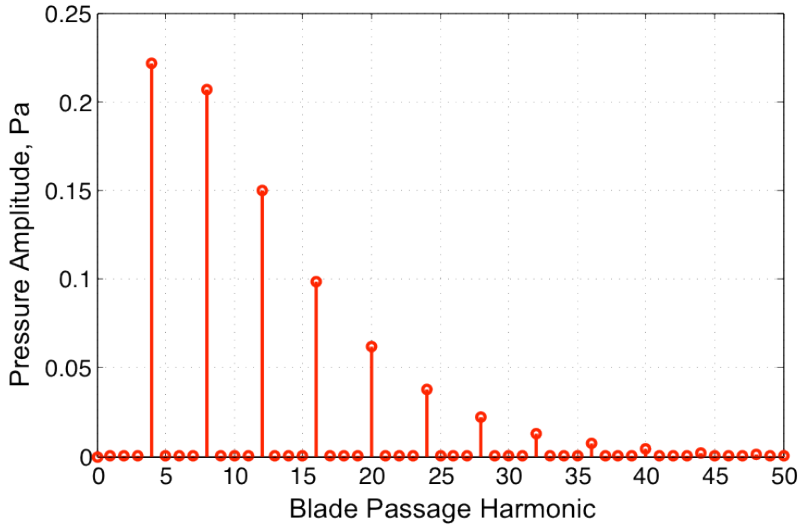

Figure 2-7: Baseline rotor thickness frequency content at observer 1.

The loading noise produced by the baseline rotor is a function of blade geometry, rotational speed, flight speed, tip path plane orientation, and most importantly, rotor loads. For the baseline rotor, the blade loads have been predicted using the University of Maryland comprehensive rotorcraft code, UMARC for an isolated rotor in "wind tunnel" trimmed conditions. The rotor is trimmed to near zero pitching and rolling moments about the hub, which ensures that the rotor plane is normal to the shaft. The blade structural properties have been selected to keep the elastic deformations to a minimum. Because in-plane loads are the primary concern for this study, UMARC was run using

unsteady aerodynamics and Drees linear inflow. Figure 2-8 shows the non-dimensional in-plane ($C_{D,TPP}M^2$) and out-of-plane ($C_{N,TPP}M^2$) loads for the baseline rotor and aforementioned UMARC settings. A compact chord assumption for the loading has been made for acoustic calculation of the loading noise. Since the low frequency content of the harmonic noise is of primary interest, a compact chord assumption is sufficient.

The resultant loading noise time history and frequency content calculated using these loads is shown in Figure 2-9 and Figure 2-10. The amplitude is significantly lower that the thickness noise. However, in the rotor TPP, some low-frequency energy in the first few blade harmonics that can be important for detection is observed.

In addition to the thickness and loading noise amplitude levels and frequency content, the phase relationship between the two plays an important role in the radiated low-frequency noise emitted by a helicopter. The total noise of the baseline rotor at all five observer positions is shown in Figure 2-11. The in-plane loading (blue) mostly affects the positive peaks of the thickness (red) but also slightly increases the peak negative amplitude of the total noise (black). The loading noise is phased such that it does increase the low-frequency content of the total radiated noise.

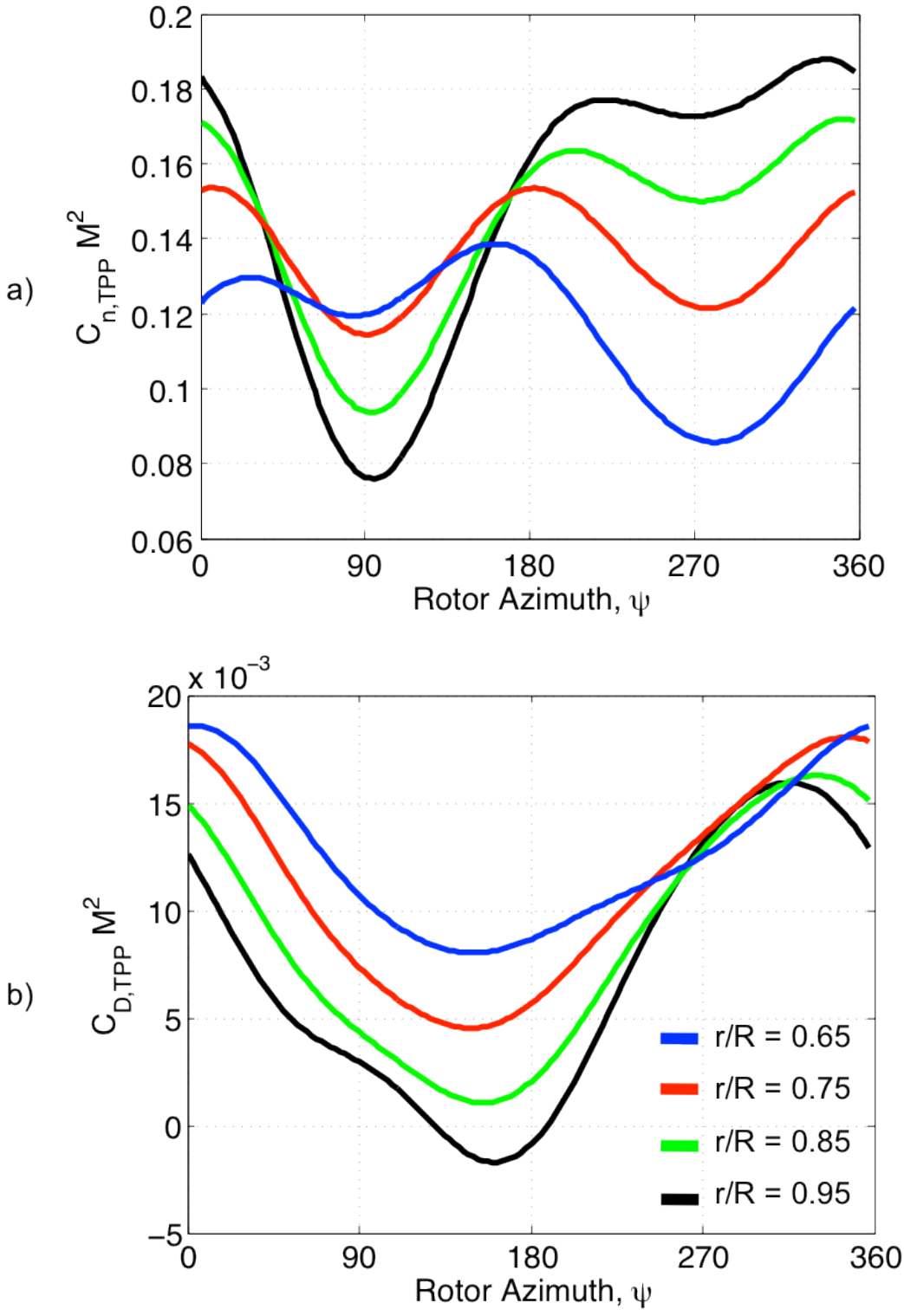

Figure 2-8: In and out-of-plane loads for baseline rotor generated using UMARC.

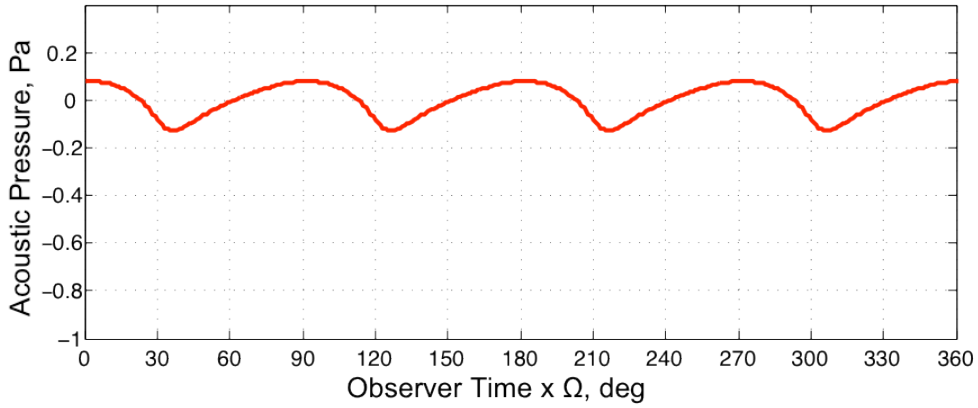

Figure 2-9: Baseline rotor loading noise acoustic pressure at observer 1.

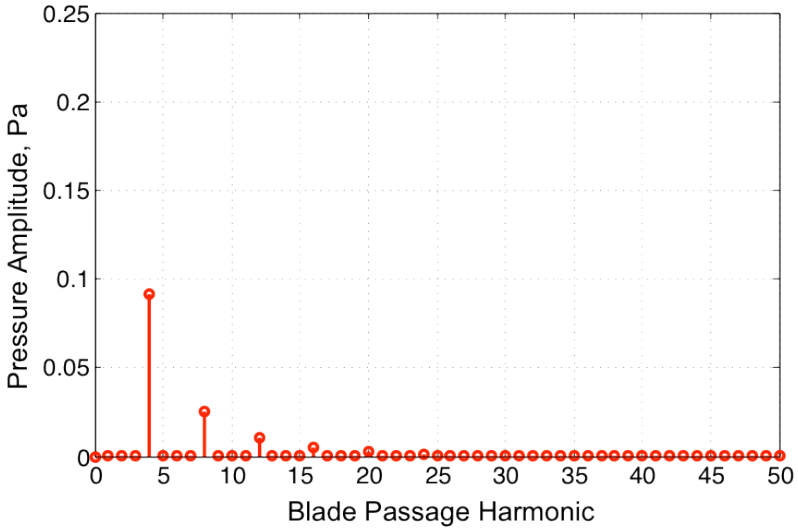

Figure 2-10: Baseline rotor loading noise frequency spectra at observer 1.

The degree to which a particular controller affects out-of-plane noise is also important in determining its acoustic performance. In order to visualize this effect, peak-to-peak sound pressure level contours maps can be used. These maps represent a spherical surface projected onto a flat plane, as viewed from the cockpit of the helicopter. A schematic of this view is shown in Figure 2-12. The center point on these maps

represents a point 1000 ft away from the rotor hub directly in the tip path plane. The dashed black lines represent 15-degree deviations from the center point.

The contour maps for the thickness, loading and total peak-to-peak sound pressure levels are shown in Figure 2-13. Thickness noise is loudest near the tip path plane directly in front of the aircraft. Loading noise is quite low near-plane but also has a low level below and to the right of the target. This is due to the phase of the blade loads, as hotspots are apparent above and to the right, and below to the left of the target.

In the total SPL contour plot the thickness noise dominates near the plane and that the highest levels occur within 15 degrees of the tip path plane. The region of most concern for detection is between 15° above and below the rotor tip path plane.

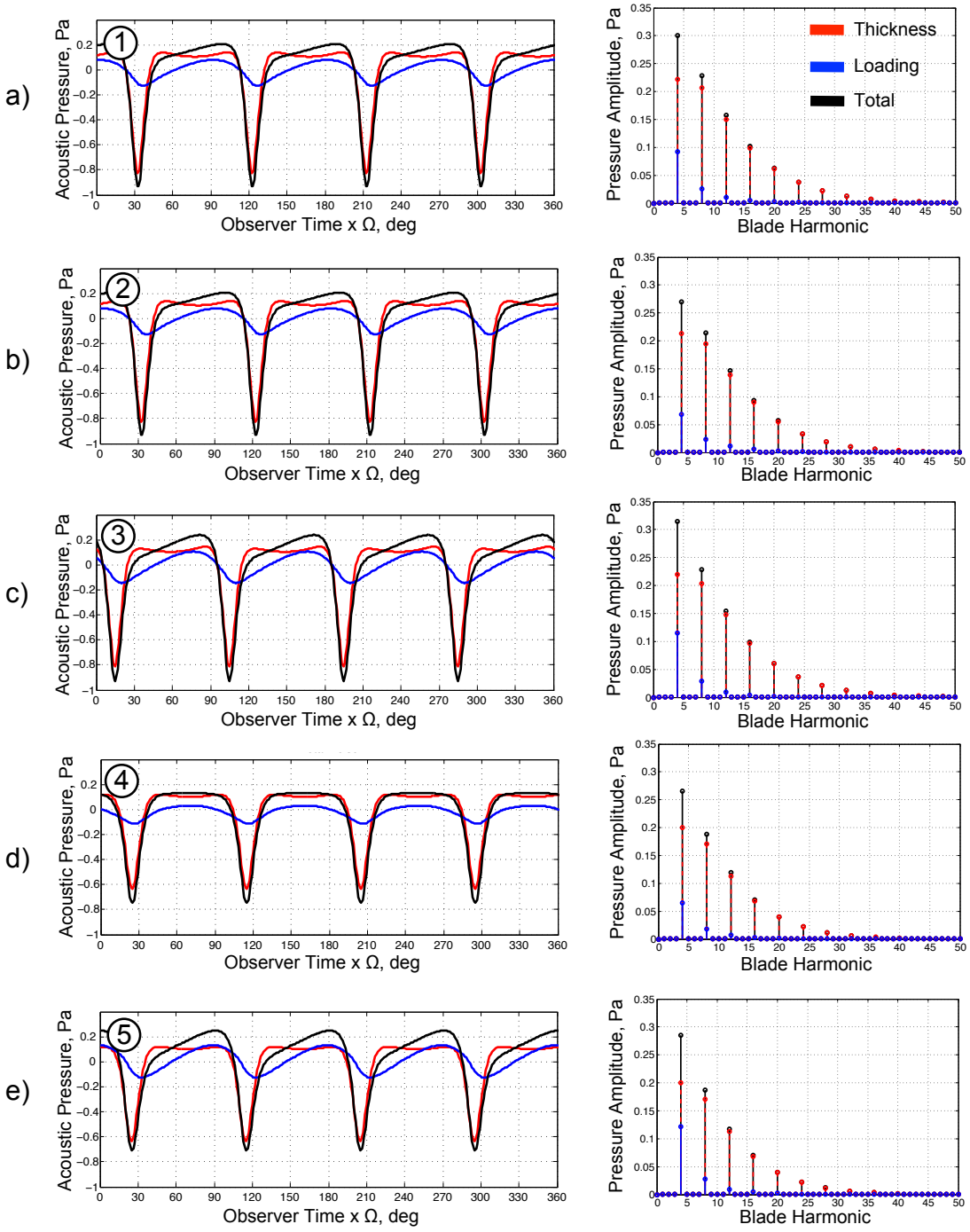

Figure 2-11: Baseline rotor noise (thickness and loading) at observers 1-5.

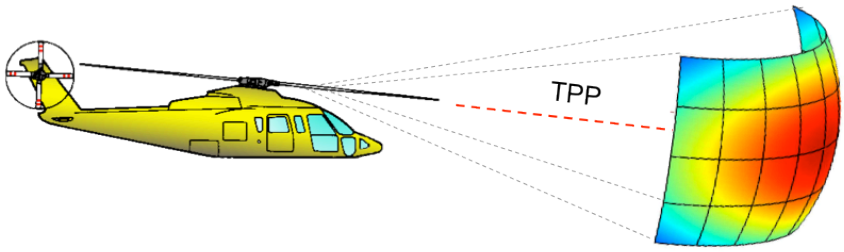

Figure 2-12: Sound pressure level contour map schematic.

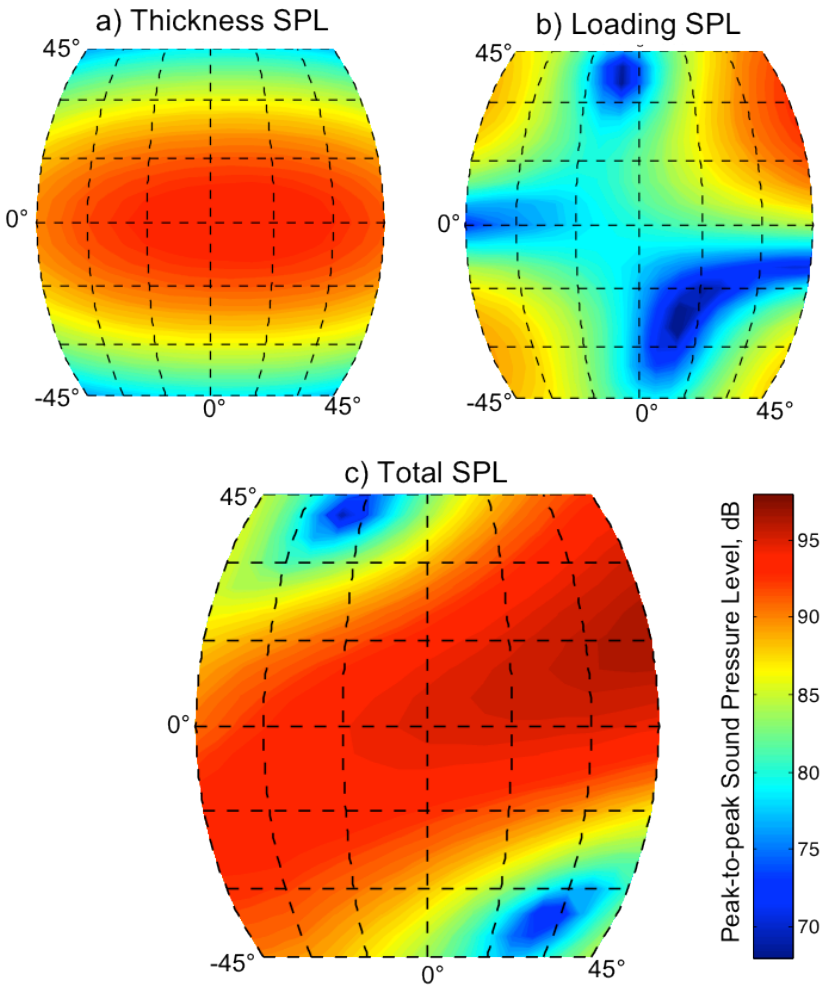

Figure 2-13: Peak-to-peak sound pressure level contour maps for baseline rotor.

2.4 Steady blowing (Constant Jet Velocity)

Now that a baseline rotor and acoustic signature have been established, a parametric sweep of the main active jet design variables is conducted. Jet angle, location, velocity, and jet exit area are all varied under steady blowing conditions in an effort to better understand the phase and relative magnitudes of the mass and momentum acoustic source contributions to the anti-noise pulse. Steady blowing (constant jet velocity) is examined first in order to simplify the problem from that of an unsteady jet. Note that though the mass flow term is steady for a constant jet velocity, the momentum term in forward flight is not. It is also a function of the aircraft forward velocity (V_∞) as seen in Equation (2.16). The calculated jet momentum source strength for the baseline constant velocity jet is shown in Figure 2-14. Fig. (a) shows the jet velocity, fig. (b) shows the radial momentum for three different jet angles and fig. (c) shows the chord wise momentum. Note that momentum is being injected into the fluid medium and that a force need not necessarily be exerted on the rotor system itself.

The magnitude of the chord-wise and radial momentum source terms for all three angles are very small compared to the baseline helicopter gross weight of 22,000 lb. As expected from equations 2.22-2.24, the forward pointing jet (α_{jet} = 90°) has the largest magnitude of chord-wise momentum, the radial jet (α_{jet} = 0°) has the second largest magnitude due to the transfer of momentum between the rotating and fixed frame, and the aft facing jet (α_{jet}= -90°) produces the least amount of momentum in the chord-wise direction. The acoustic ramifications of this will become clear in the coming discussion of varying jet angle. The radial momentum is largest for the radial jet as expected but still very small for all cases

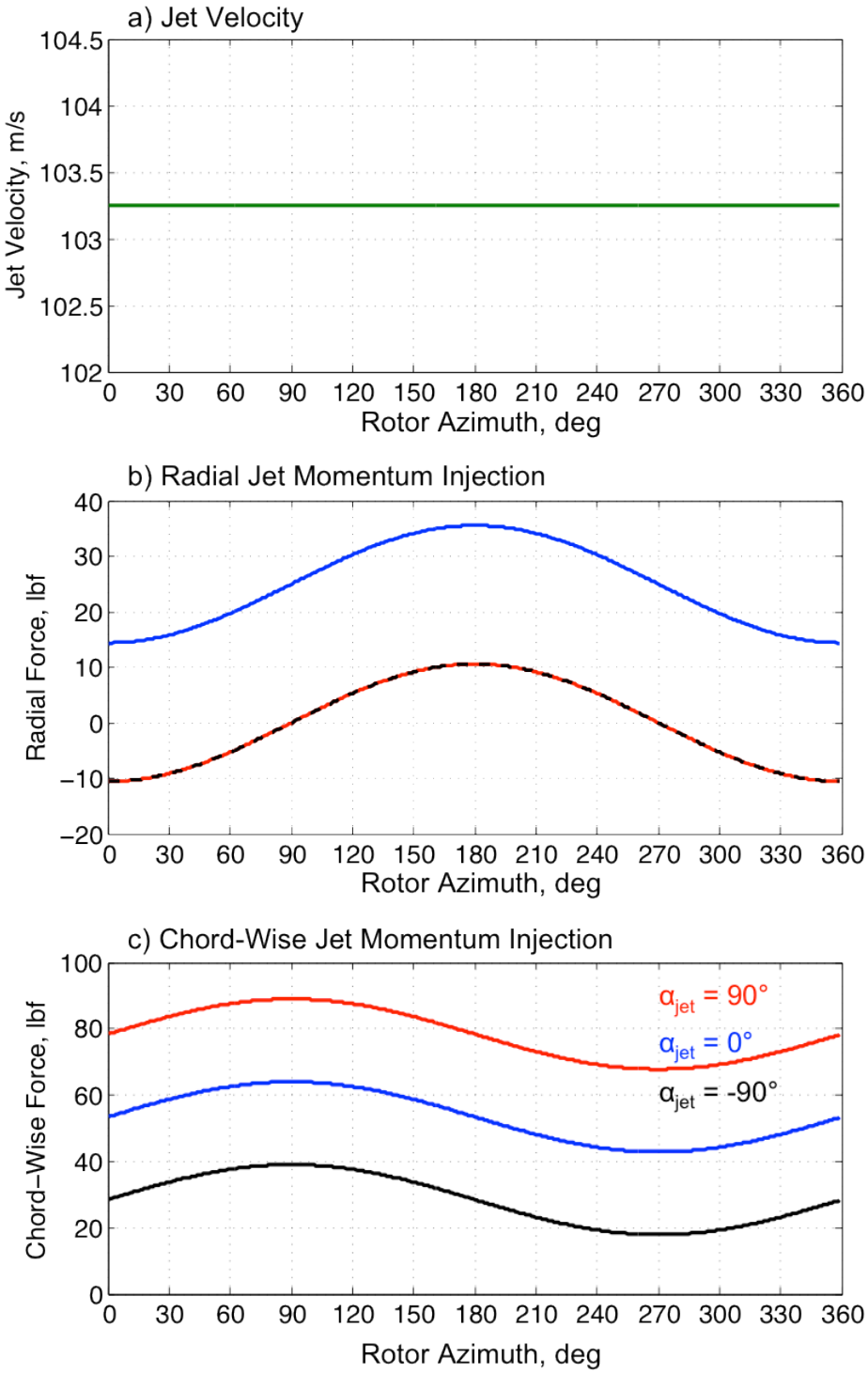

Figure 2-14: Constant jet velocity momentum source strength.

In Figure 2-15, the result of steady blowing with a constant jet velocity (M_{JET} = 0.3) at the baseline location and size, with a corresponding blowing coefficient and jet velocity of C_μ = 0.0008273 and $V_{jet}/\Omega R$ = 0.4672, is shown. The steady jet increases the peak-to-peak sound pressure level slightly. This is due to the acoustic phasing that is naturally associated with the baseline jet configuration though this phase relationship can be manipulated for steady blowing by relocating the jet exit.

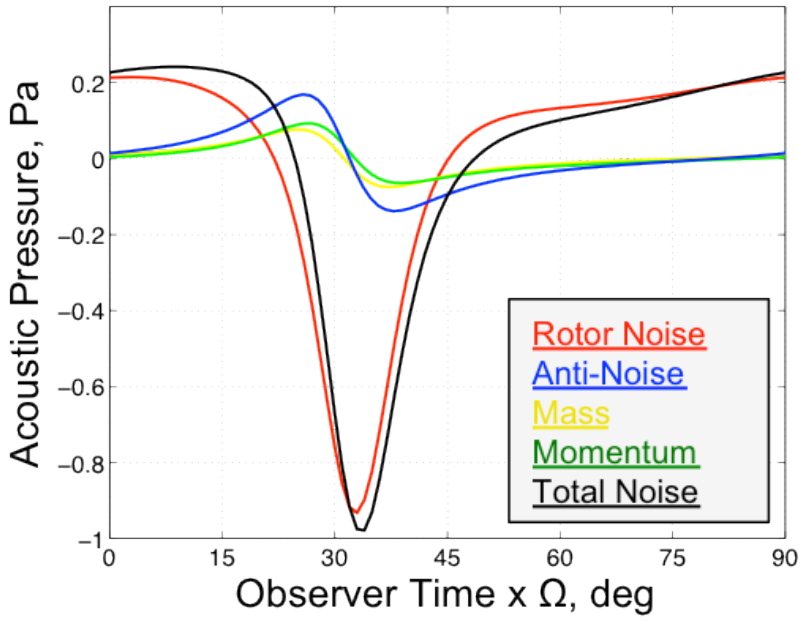

Figure 2-15: Steady blowing applied to baseline rotor with baseline jet parameters.

2.4.1 Jet Angle

The jet angle is altered for a fixed steady jet. The resultant acoustic pressure time history for jet angles between -90° (aft facing jet) and 90° (forward facing jet) at 45° intervals are shown in Figure 2-16. Also shown is the change in peak-to-peak pressure as a function of changing jet angle. The volume source term is independent of angle as expected, and the momentum source term becomes larger as the angle is increased (pointed further forward). Pointing the jet forwards increases the magnitude of chord-

wise momentum on the fluid as shown in Figure 2-14. Pointing the jet as far forwards as possible, neglecting the effect on rotor performance, is preferable from an acousticians perspective. However, the direction of the jet will affect the performance of not only the pneumatic system providing jet flow (which is not considered at present) and the rotor aerodynamic performance.

2.4.2 Jet Radial Location

The jet radial location is altered for a fixed steady jet velocity ($M_{jet} = 0.3$) at the baseline chord-wise location and size, with a corresponding blowing coefficient and jet velocity of $C_\mu = 0.0008273$ and $V_{jet}/\Omega R = 0.4672$. The resultant acoustic pressure time history for radial distances of 0.9R, 0.95R and R are shown below in Figure 2-17. Also shown is the change in peak-to-peak pressure as a function of increased radial location. Both the volume and momentum source terms grow in magnitude quickly as the jet is moved outwards. This is expected as the sources relative velocity and accompanying Doppler amplification grow considerably at the tip of a rotor. This means that a jet placed at the tip will yield the largest acoustic magnitude for a given jet strength.

2.4.3 Jet Chord-Wise Location

One potentially useful parameter that can be varied is the chord-wise position of the active jet. By moving its position towards the trailing or leading edge, one can effectively manipulate it's acoustic phase with respect to the noise produced by the rotor system. In Figure 2-18, the acoustic pressure is shown for cases in which the jet is placed at the leading edge, elastic axis (baseline), mid-chord, and trailing edge. The magnitude is

relatively unchanged. In fact the change is only due to the slight increase in radial distance from the axis of rotation as the jet is moved along the chord at the tip.

As the jet is moved further towards the trailing edge, the peak positive amplitude of the steady blowing noise moves in phase to the negative peak of the rotor noise, eventually resulting in a small reduction in peak-to-peak amplitude. This indicates that some additional gain in acoustic effectiveness can be gained for steady blowing when the jet is placed as close to, or even beyond, the trailing edge.

2.4.4 Jet Velocity

The most useful jet parameter that can be varied for a steady jet, the velocity is directly tied to the source strength of both the volume (V_{jet}) and momentum (V_{jet}^2) source terms governing the acoustic strength of the active jet acoustic controller. In Figure 2-19, the jet velocity is varied from 51.63 m/s up to 206.52 m/s (0.15 to 0.6 M_{JET}). Note that in doing this, the blowing coefficient and jet velocity also change as summarized in Table 2.3. Increasing the velocity yields larger amplitudes. Of course this modeling does not include any non-linear compressibility effects that might begin to become important at high jet velocities.

Table 2.3: Jet velocity parameters

M_{JET}	V_{jet}	C_μ	$V_{jet}/\Omega R$
0.15	51.63 m/s	0.000207	0.234
0.30	103.26 m/s	0.000827	0.467
0.45	154.89 m/s	0.001861	0.701
0.60	206.52 m/s	0.003309	0.934

2.4.5 Jet Area

The final jet parameter that is varied for this study is the jet area. The acoustic pressures are shown for an increase and decrease in area. Once again, changing the jet area will change the blowing coefficient, as shown in Table 2.4. Whereas changing jet velocity altered both the momentum and volume coefficients, changing area only affects the blowing coefficient. As shown in Figure 2-20, increasing the jet area increases the peak-to-peak amplitude of the anti-noise waveform. This mechanism is however slightly less efficient in increasing the amplitude than changes in jet velocity, as a doubling of both results in a larger peak-to-peak level for the increasing velocity.

Table 2.4: Jet area parameters

A_{jet}/A_{BASE}	M_{JET}	V_{jet}	C_{μ}	$V_{jet}/\Omega R$
0.50	0.3	103.26 m/s	0.000414	0.467
1.00	0.3	103.26 m/s	0.000827	0.467
1.50	0.3	103.26 m/s	0.001241	0.467

2.4.6 Sound Pressure Level Reduction

When steady blowing is used, the phase relationship between the anti-noise and rotor noise is determined by its position on the blade. In Figure 2-16 to Figure 2-20, it is apparent the baseline jet results in an increase in peak-to-peak pressure level. This is confirmed again in Figure 2-21, which shows that variation in controlled SPL as each parameter is varied. One interesting result is that as chord-wise location is changed (Figure 2-21 (c)), a reduction in noise can be achieved if the jet is moved towards the trailing edge of the blade. This changes the steady jet phase and moves the positive peak of the anti-noise into alignment with the negative peak of the rotor noise. This result should be considered when designing an active jet acoustic control system.

In general, the steady blowing active acoustic control is not ideal for significant reductions of LF-IPH. The values of flow required are simply too high. In order to obtain greater benefit from the control, time-varying flow should instead be used.

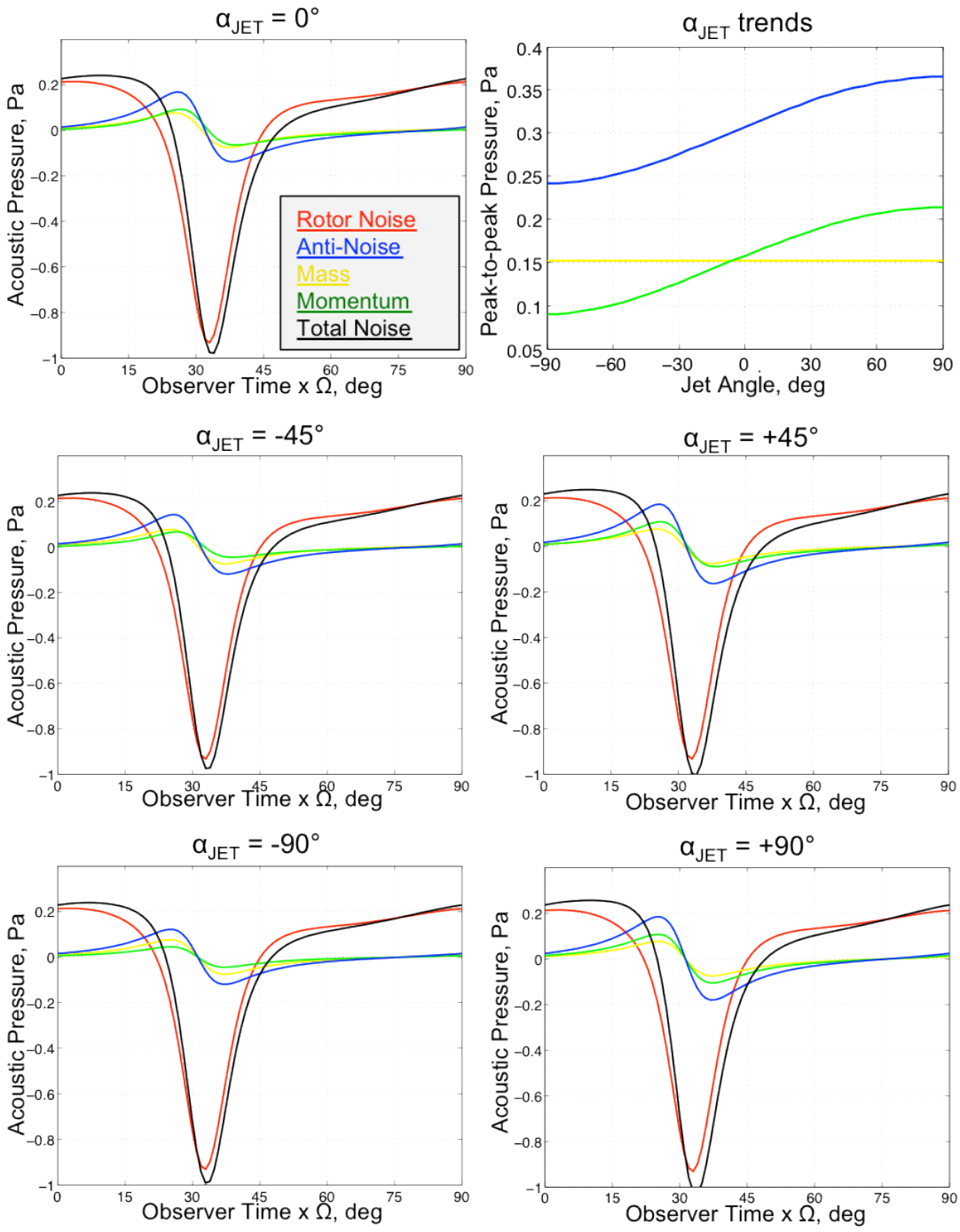

Figure 2-16: Steady Blowing with varying jet angle.

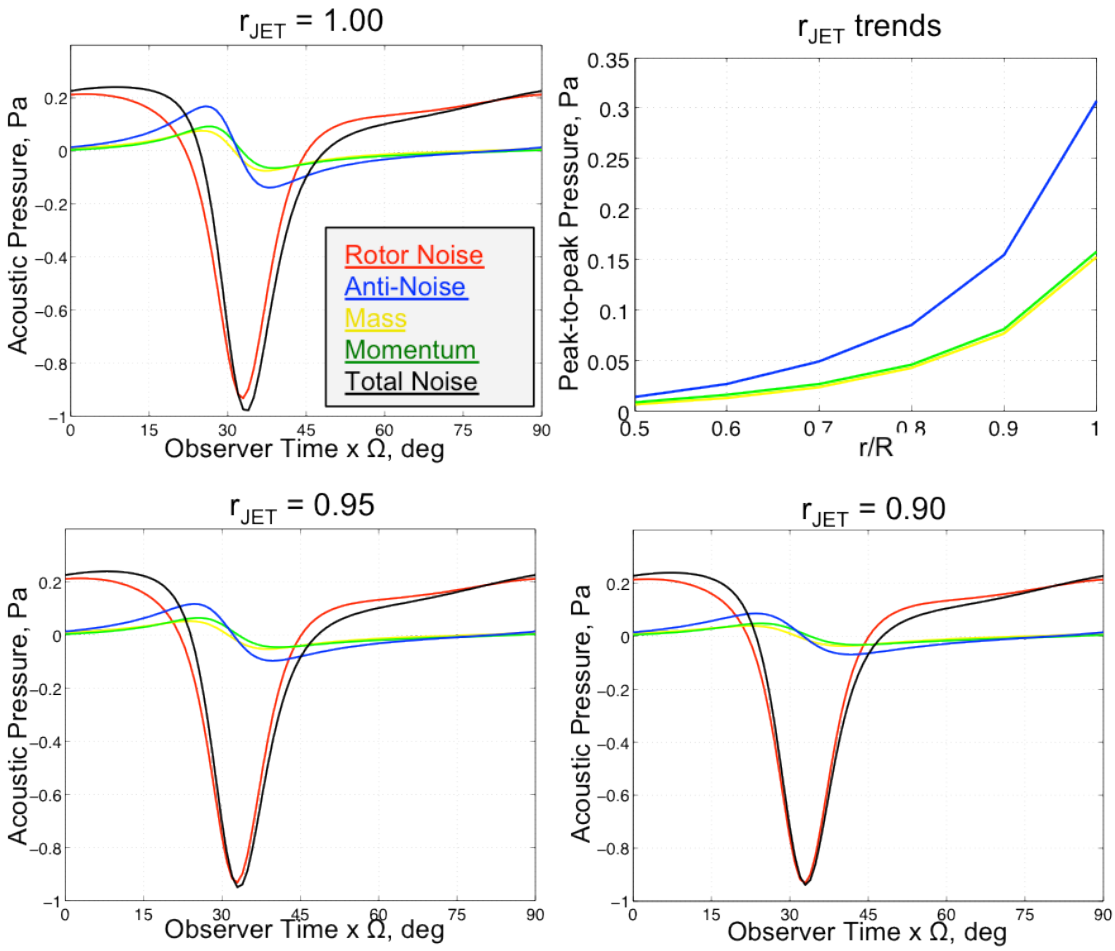

Figure 2-17: Steady blowing with varying jet radial location.

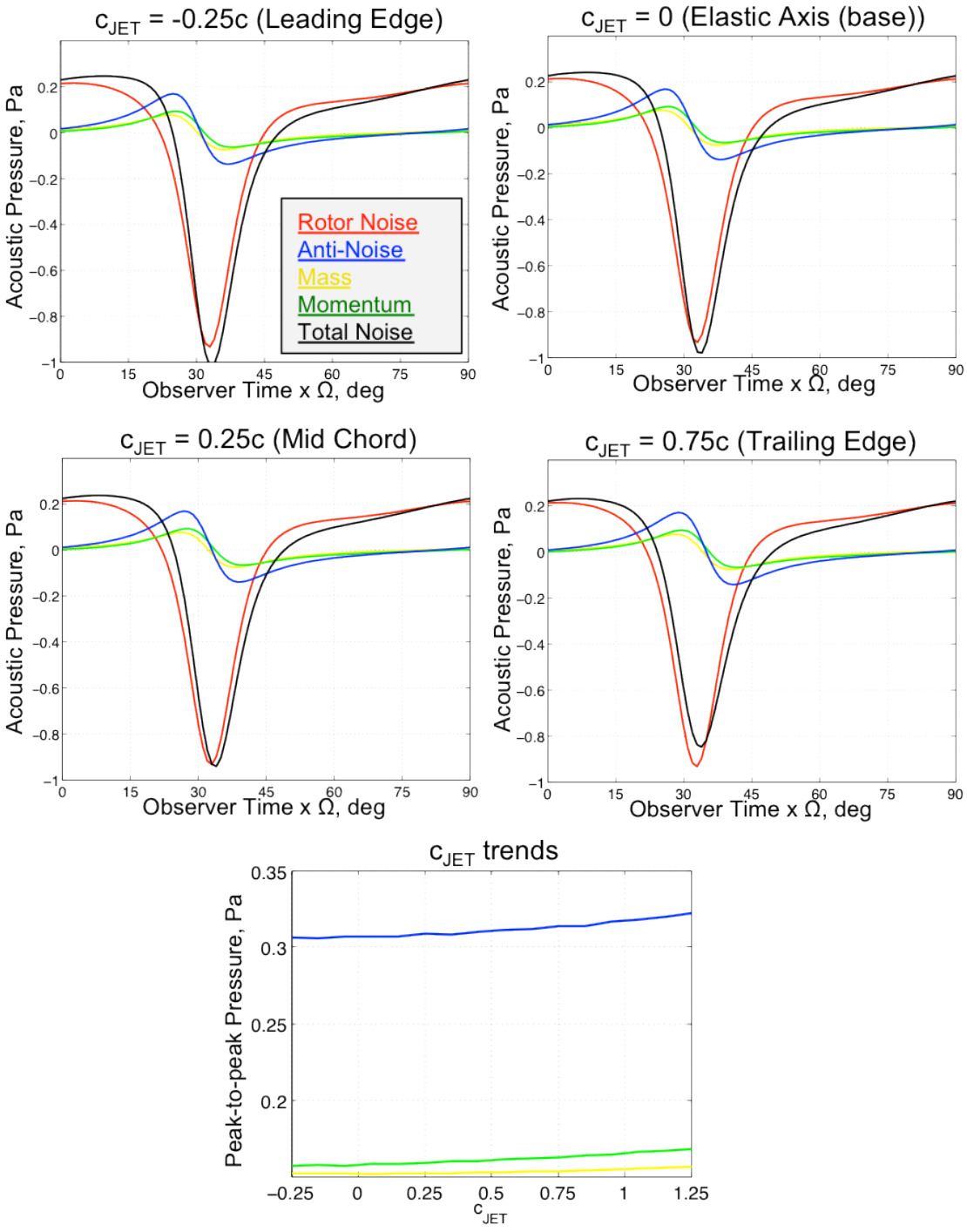

Figure 2-18: Steady blowing with varying chord-wise location.

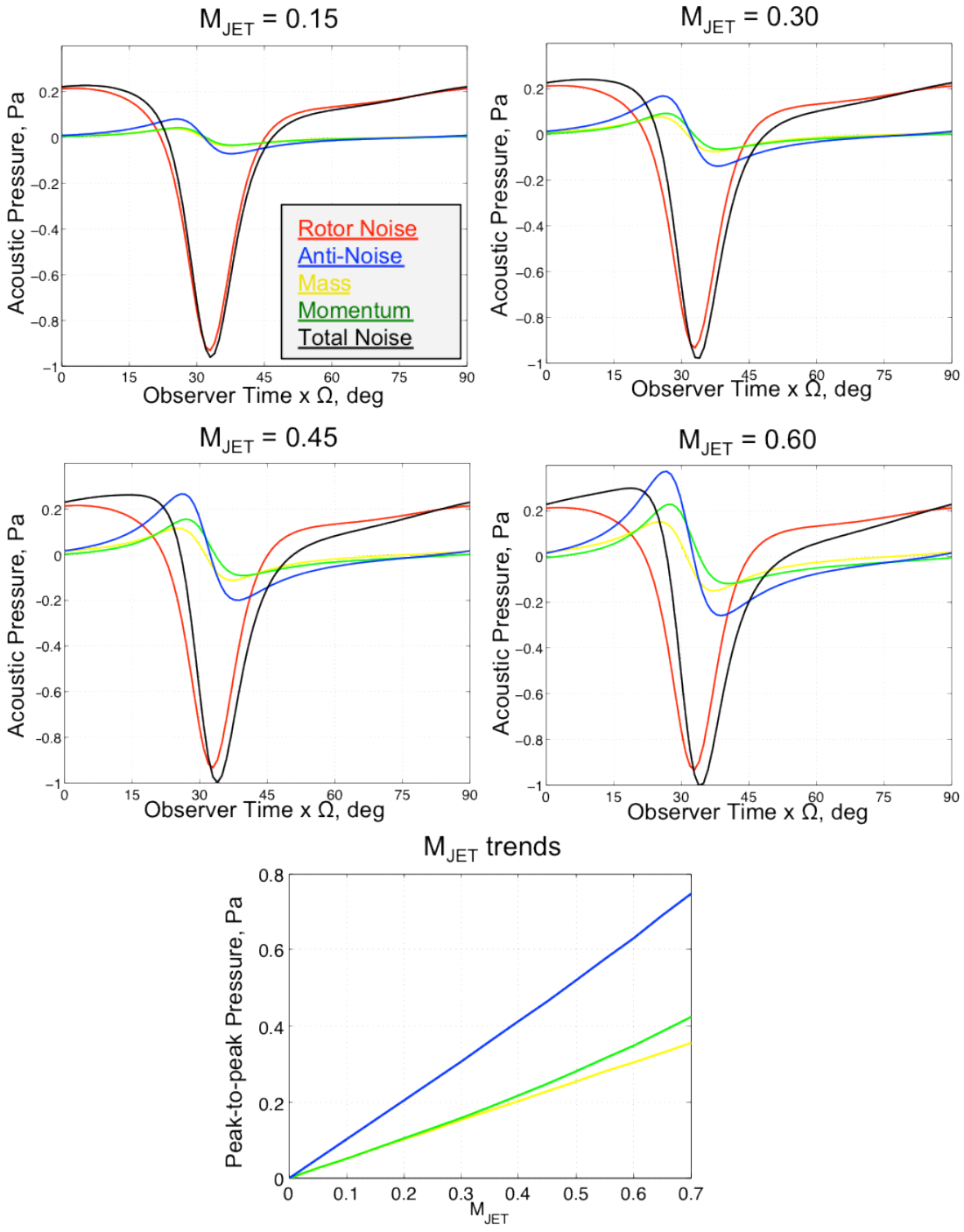

Figure 2-19: Steady blowing with varying jet velocity.

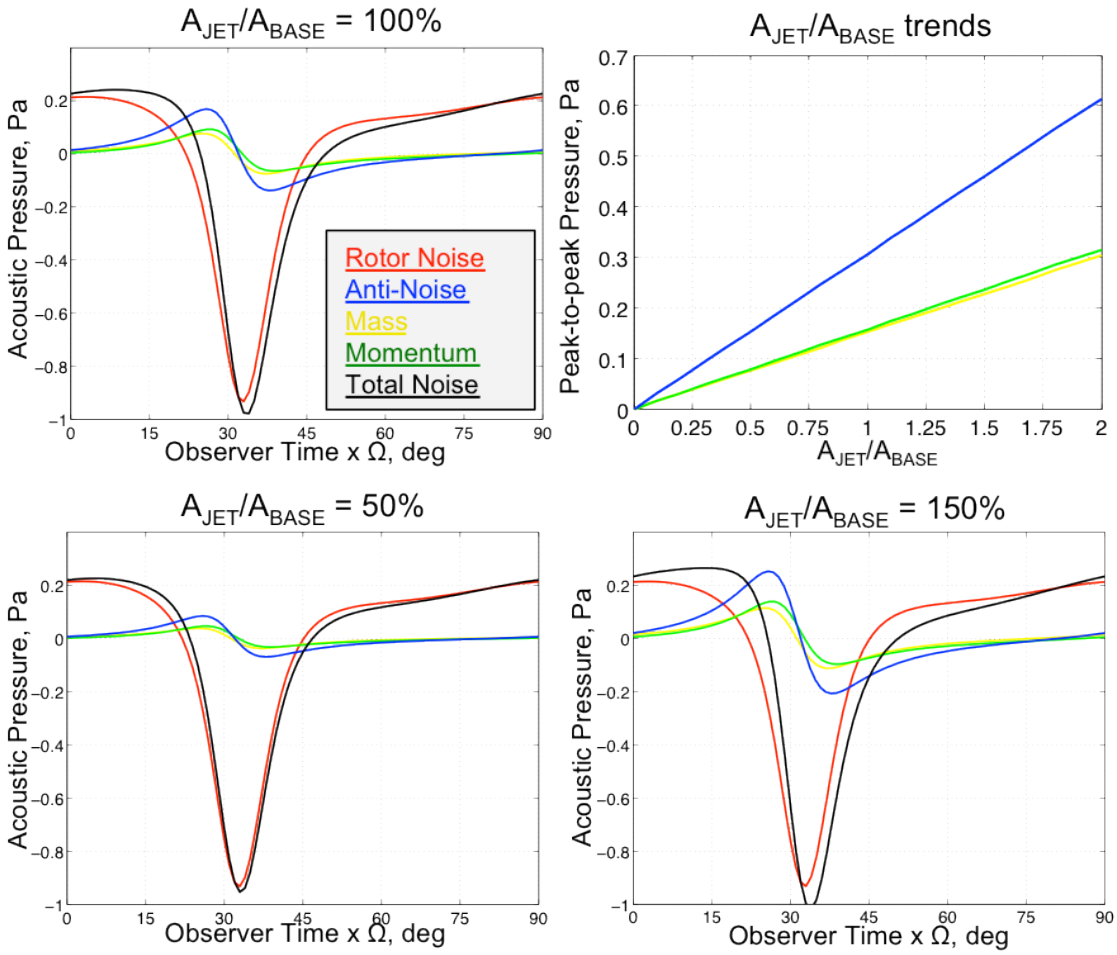

Figure 2-20: Steady blowing with varying jet area.

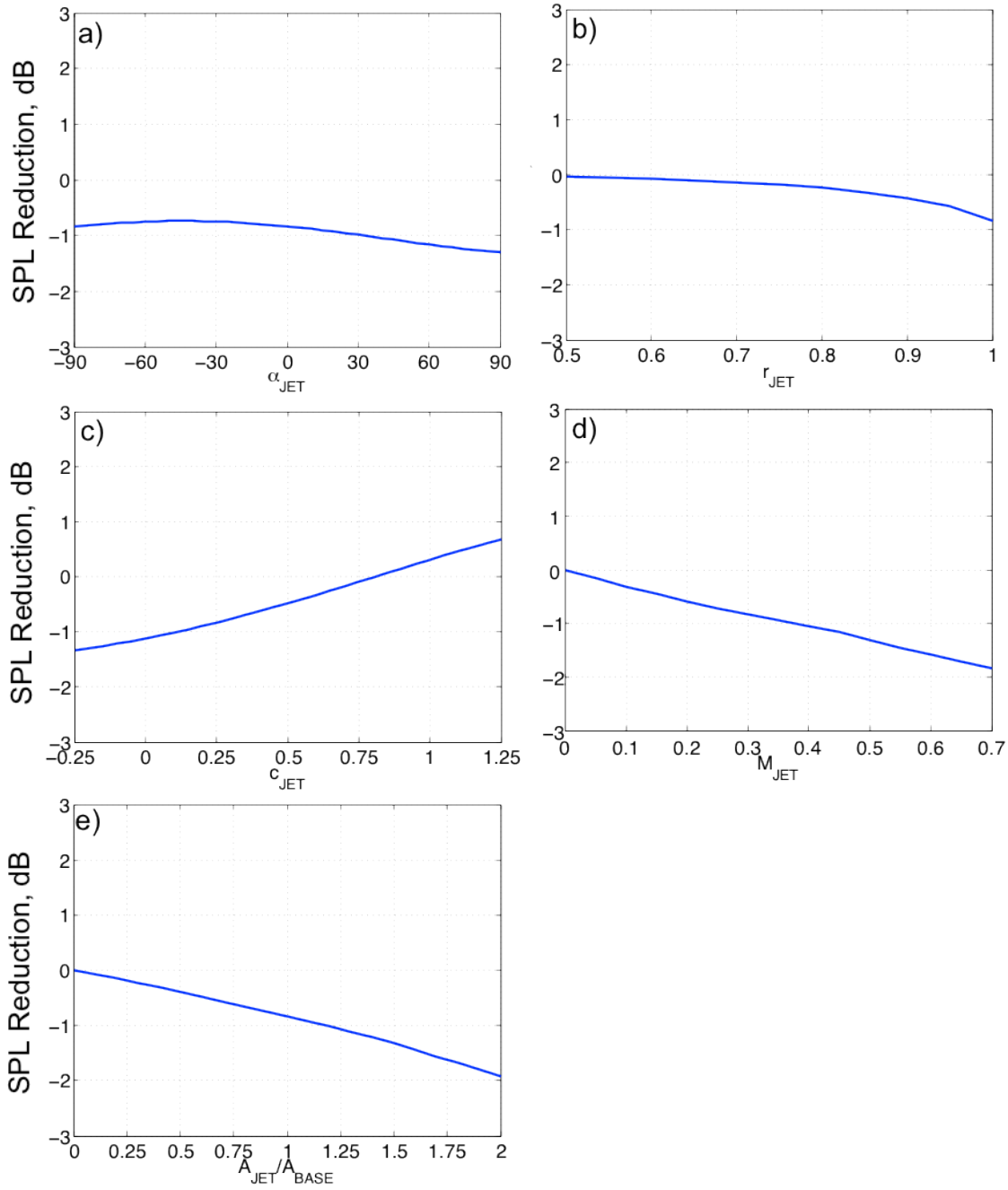

Figure 2-21: SPL reduction trends for steady blowing parametric sweep.

2.5 Unsteady Blowing (Time-Varying Jet Velocity)

Early theoretical work conducted by Gopalan and Schmitz concluded that for single monopole and/or dipole controllers, unsteady variation of the source strength was a

more efficient means of reducing the in-plane harmonic rotor noise. Generally speaking, the solutions that yielded the best results shared a key feature, a large time rate of change in source strength when the radiation direction vector was tangential to the rotor disk. Analysis of active acoustic control using tip jets has shown that this general trend remains true.

In this section, the same geometry and flight condition are used for the analysis of time varying jet flows. Pure sinusoidal, single pulse, and tailored jet controllers will be explored. Note that the controls described are for a single control on each blade. Each blade is equipped with its own active jet control and $\psi_{azi} = 0°$ is the same point around the rotor azimuth for each blade (i.e. when the blade is over the tail boom).

2.5.1 Harmonic Sinusoidal Blowing

One method of unsteady blowing that has been explored for either monopole or dipole sources in the past, is the use of purely sinusoidal variation of the jet velocity. For this study, the acoustic profiles, frequency content and directivity patterns associated with several harmonic controllers are explored.

The pure harmonic controller is defined such that all mass flow is positive and the maximum time rate of change occurs at a rotor azimuth of 90°, though this phase can be adjusted. The prescribed jet velocity for each blades jet control then is,

$$V_{jet}(\psi) = \frac{1}{2} V_{MAX} \left[1 - \cos\left(n(\psi - \Delta\psi) - (n-1)\frac{\pi}{2} \right) \right] \qquad \text{for n} = 1,2,3... \tag{2.28}$$

A 3/REV controller is shown below in Figure 2-22 with the baseline represented by the solid line and a phase-adjusted waveform represented as the dashed line.

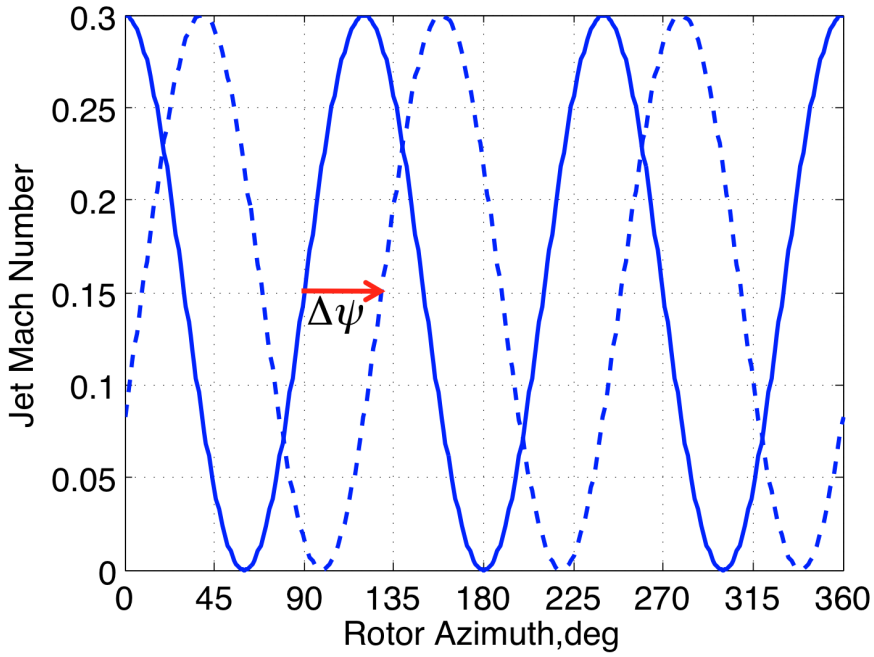

Figure 2-22: Jet velocity for a 3/REV sinusoidal variation.

Because of the small phase differences between the mass and momentum source acoustic pressures, a phase adjustment is necessary to achieve a maximum peak-to-peak sound pressure level reduction for a given observer location, flow profile, and jet position.

As with the steady jet, it is instructive to examine the momentum source strengths once again for the time-varying jet. The 3/REV case is shown in Figure 2-23 (a)-(c). The radial component is once again very small for all cases though larger for the radial jet. The chord-wise momentum, shown in fig. (c) exhibits the same trends for each of the three jet angles as the steady jet. However, there is also a steep rate of change on the advancing side of the rotor that generates a larger amplitude anti-noise waveform than the steady blowing. This is despite the fact that the steady jet actually generates less net momentum over a rotor single revolution but comes at the expense of a more localized acoustic controller.

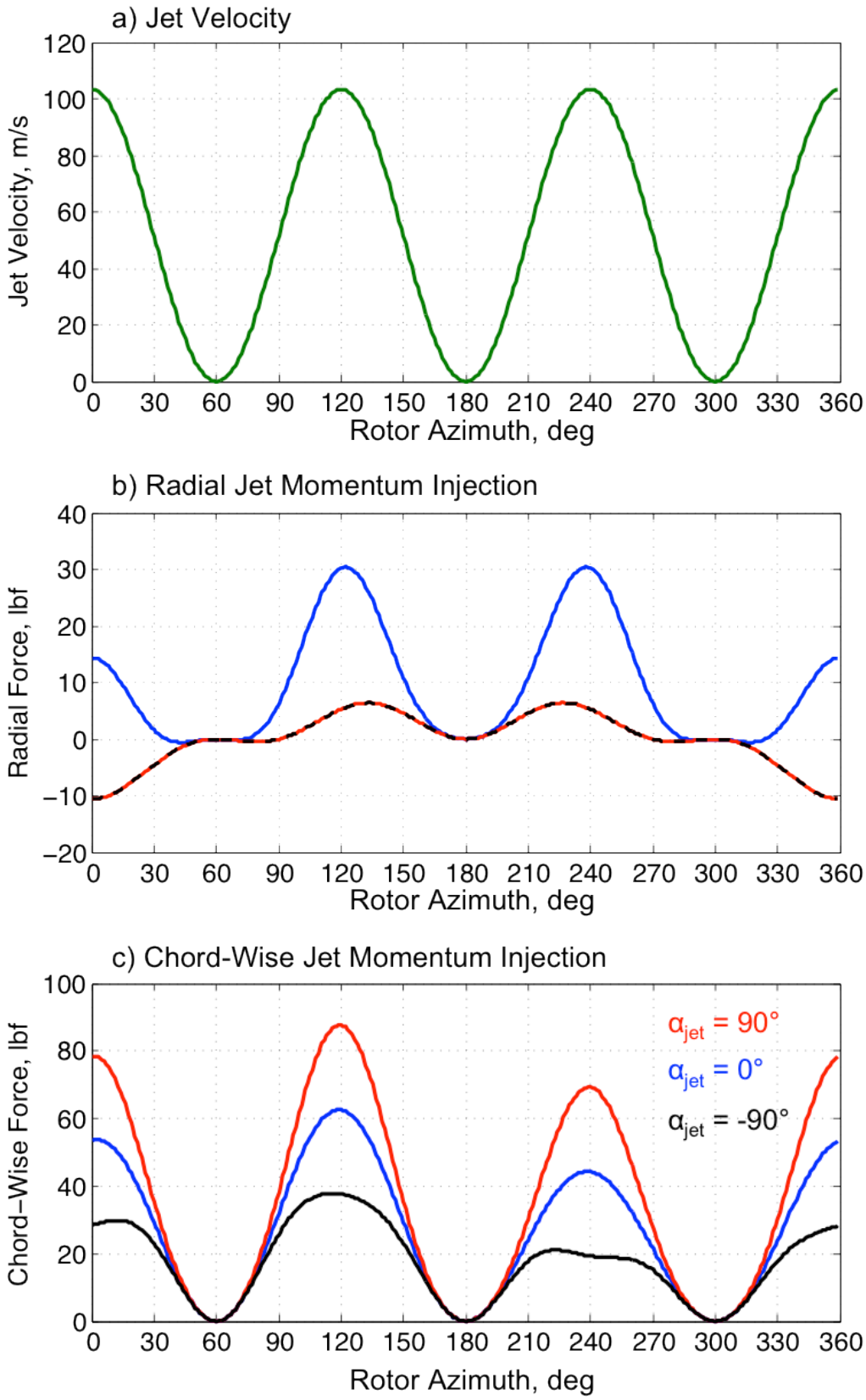

Figure 2-23: Time varying jet velocity momentum source strength (3/REV).

In each of the following cases the phase has been adjusted so as to maximize the sound pressure level reduction at the baseline target observer location (1). The corresponding phase adjustment for 1/REV to 5/REV controllers are summarized in Figure 2-24. Not that the higher harmonics are more sensitive to non-optimal phase and that there is a point at which increasing the frequency no longer yields a larger reduction in SPL (above 4/REV).

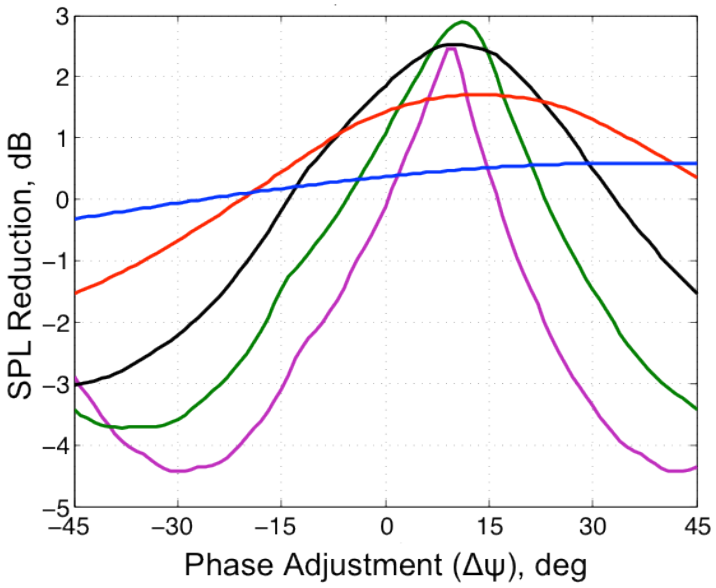

Harm.	Δψ	ΔSPL
1	38°	0.57 dB
2	14°	1.71 dB
3	10°	2.52 dB
4	11°	2.90 dB
5	10°	2.46 dB

Figure 2-24: Phase adjustment for harmonic unsteady blowing.

The following plots show the resultant acoustic pressure time history (a), frequency content (b) and frequency specific SPL reduction (c) for five different harmonic controllers. The red line indicates the uncontrolled rotor noise at the target observer (1), the blue indicates the anti-noise, which is composed of the mass (yellow) and momentum (green) source terms, and the black represents the controlled noise. The frequency information is plotted versus rotor harmonic where the fundamental blade rotational frequency is 4.4 Hz. The first 12 rotor harmonics (~220 Hz) are shown as they are of most concern when considering helicopter detection.

Remember also that each individual blade is equipped with an identical controller generating the same jet velocity as the blade passes a particular rotor azimuth position. Each blades jet control is therefore responsible for minimizing the blade on which it resides LF-IPH.

The results for 1/REV blowing (Figure 2-25) show that this controller is not particularly efficient at reducing the SPL. In fact it is almost as effective as steady blowing. It does however influence the 1st and second harmonic. As the frequency of the controller is increased to 2/REV (Figure 2-26), the peak level of the anti-noise increases and a larger reduction is achieved. The peak harmonic reduction is also shifted from the 2nd rotor harmonic to the 3rd.

Increasing the control frequency further to a 3/REV (Figure 2-27), the controller now results in a 2.5 dB reduction in noise for peak-to-peak SPL. However, reductions of up to 6 dB in the higher frequencies (3 – 8 Rotor Harmonic) are now achieved. Applying a 4/REV controller (Figure 2-28), the higher frequencies are now almost completely reduced. The lowest harmonic has however been slightly increased in this case. That said, for this rotor, the 4/REV reduces the peak-to-peak level most.

As the control frequency is increased even further to 5/REV (Figure 2-29), the frequency of the anti-noise has now surpassed that of the rotor noise. The result of this is that the controller is less effective as reducing the peak level despite having a higher peak to peak pressure amplitude than the 4/REV. This then increases the higher frequency content of the total controlled noise.

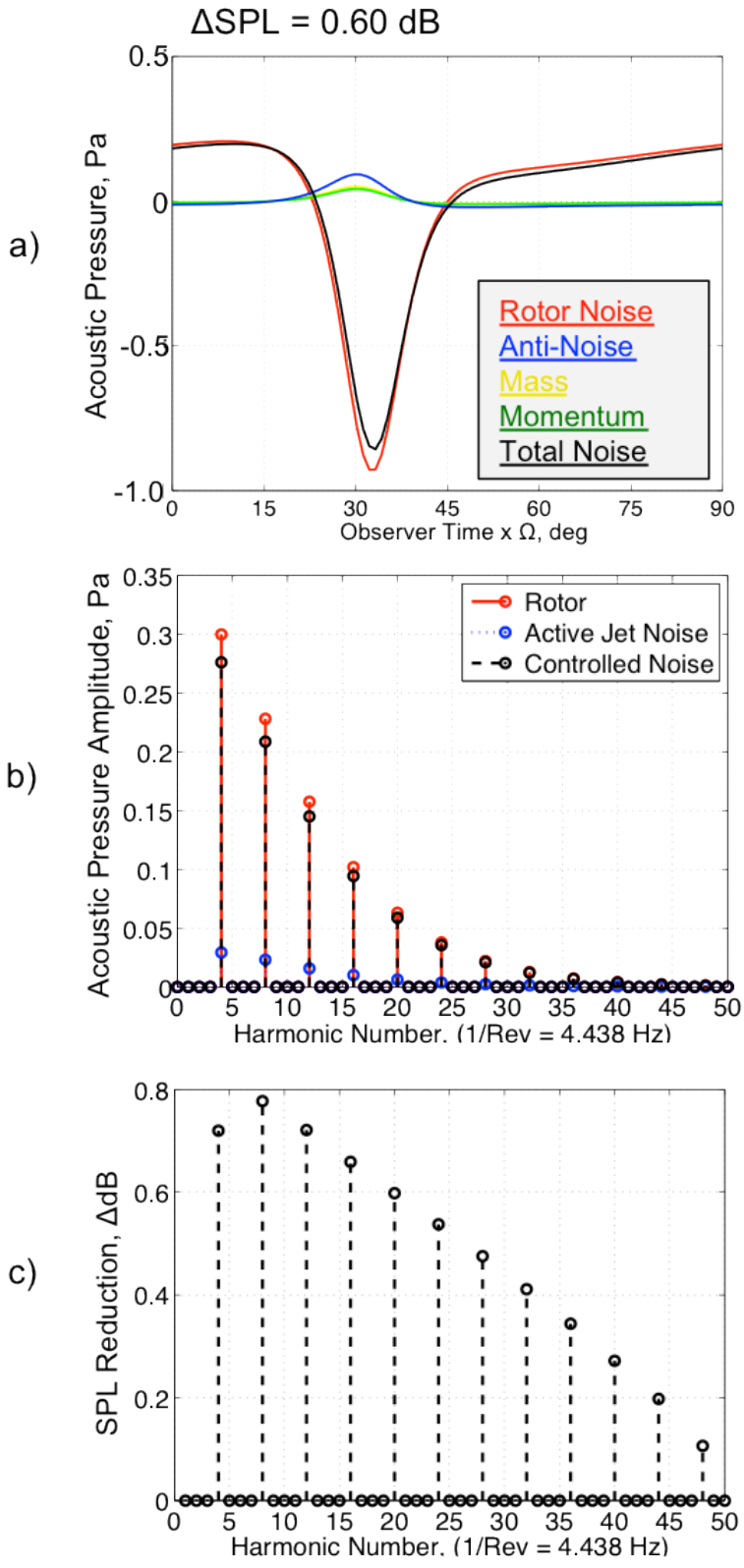

Figure 2-25: 1/REV control a) pressure, b) frequency, and c) ΔSPL.

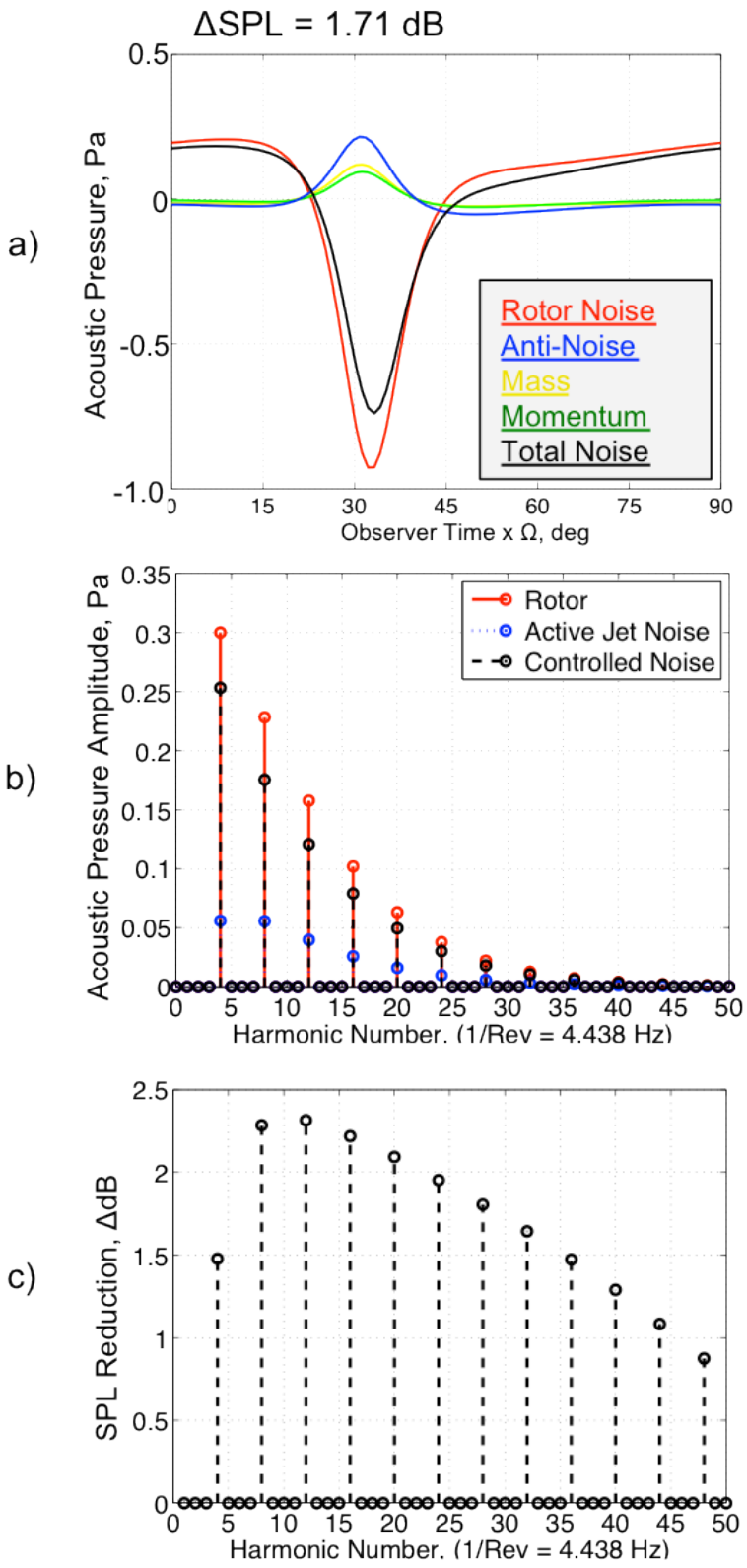

Figure 2-26: 2/REV control a) pressure, b) frequency, and c) ΔSPL.

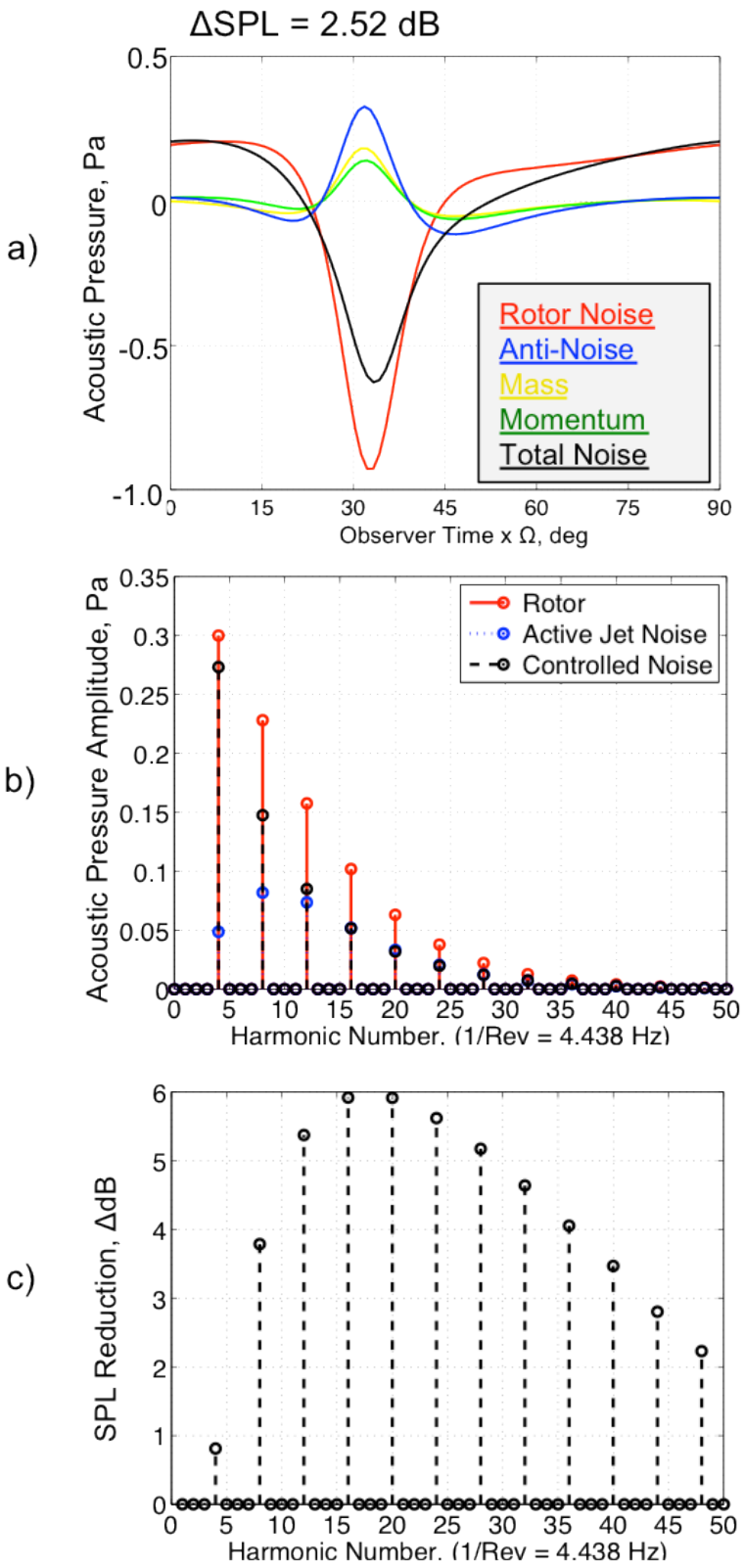

Figure 2-27: 3/REV control a) pressure, b) frequency, and c) ΔSPL.

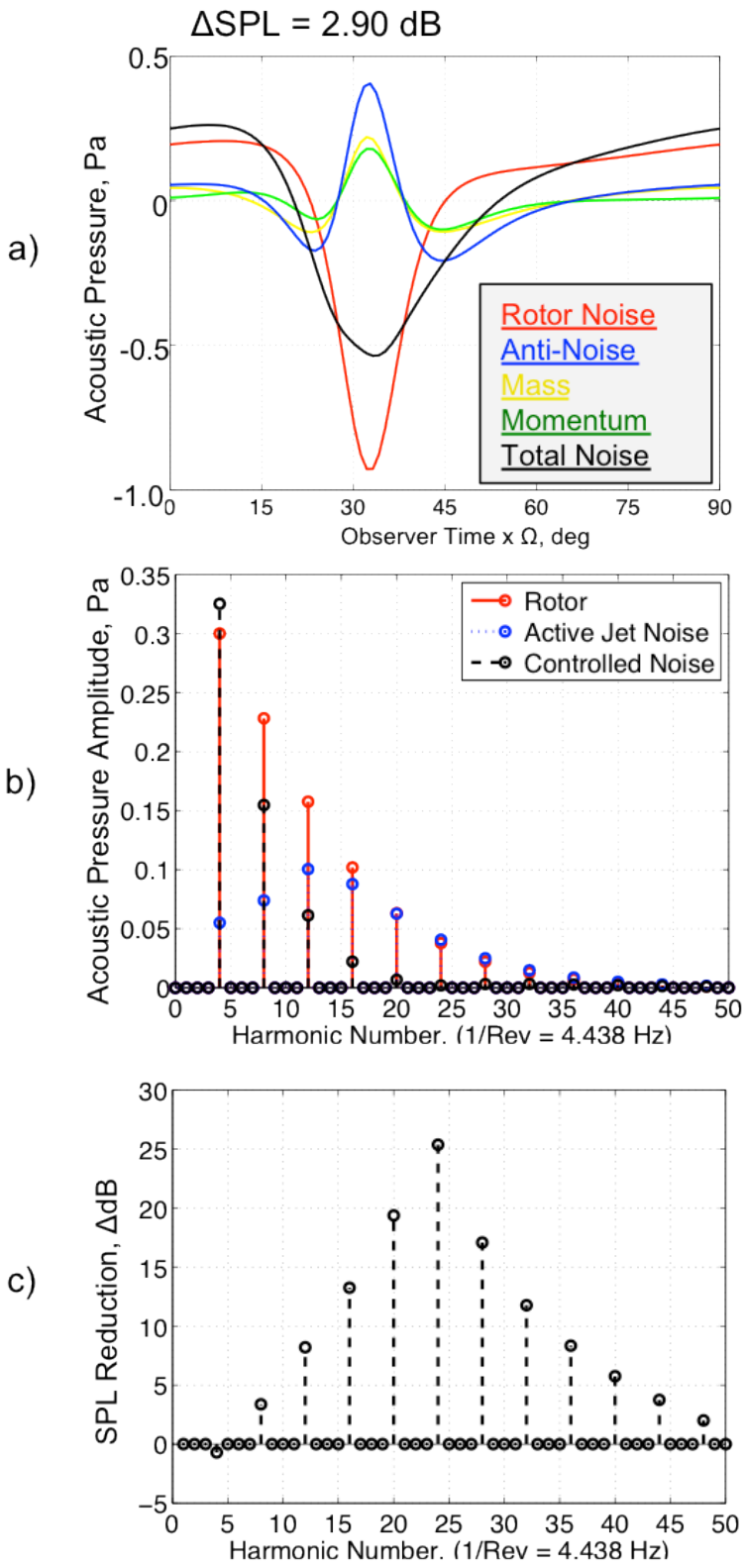

Figure 2-28: 4/REV control a) pressure, b) frequency, and c) ΔSPL.

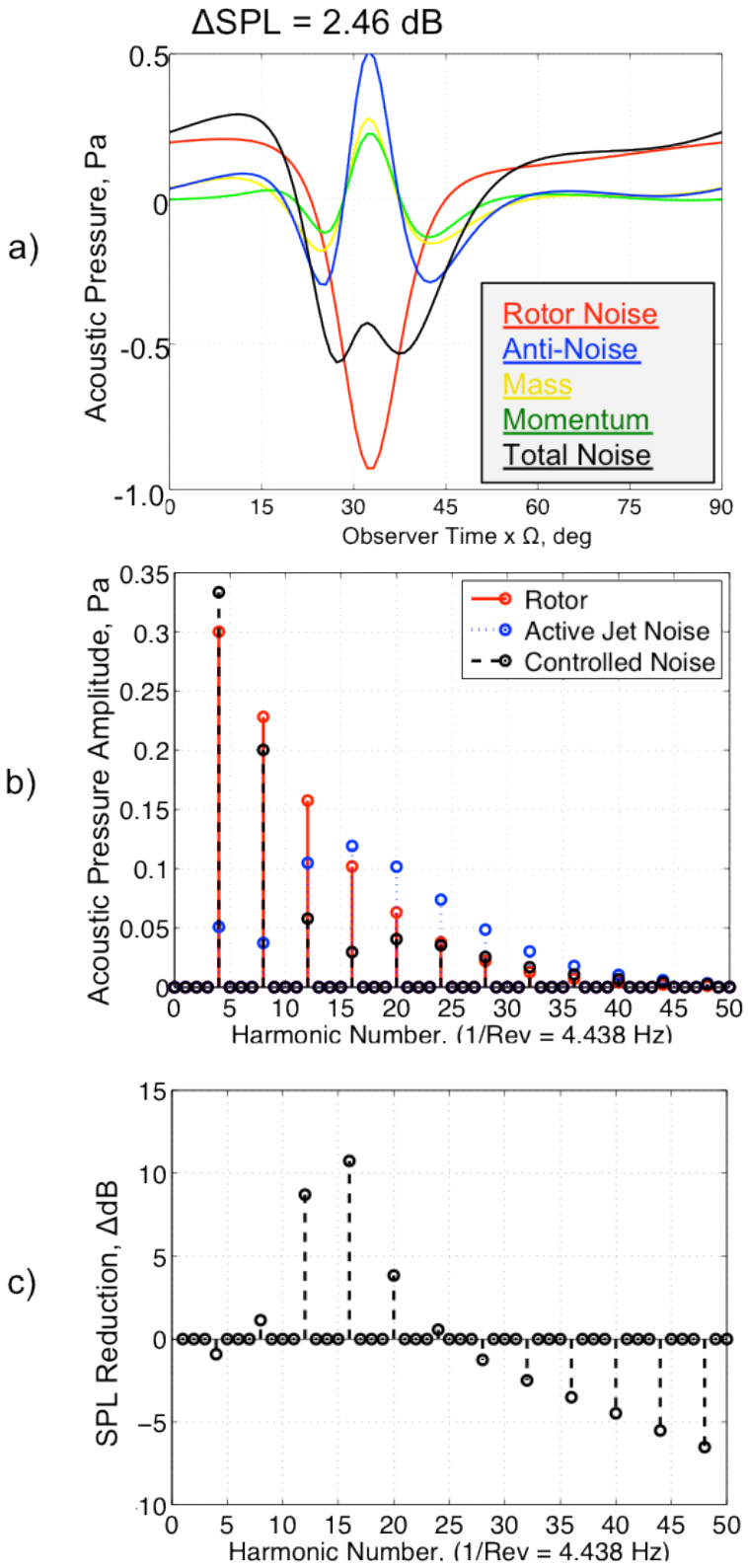

Figure 2-29: 5/REV control a) pressure, b) frequency, and c) ΔSPL.

The acoustic time histories and frequency content at the target observer provide useful information regarding how effective a controller is at reducing the noise at a single point in space. However, they provide no information regarding what the control does at off-target observer locations. In order to visualize their off-target effectiveness, contour plots can be used. Figure 2-30 shows the peak-to-peak sound pressure level on a spherical surface 1000 ft from the rotor hub. The contour shows a window of +/- 45 degrees to the left and right of the target and +/- 15 above and below the target. The target lies directly in the rotor tip path plane, straight ahead of the hub in the direction of flight. Also shown, on the right column of Figure 2-30, is the reduction in SPL, with positive values indicating a reduction in noise, and negative values an increase in noise.

Once again the 4/REV controller yields the largest reduction at the target observer. It is also clear that the higher harmonic controller yields a more narrowly focused zone of noise reduction. The noise actually increases at off-target observers, indicated by the red regions in the SPL reduction plots, for the high frequency controllers. This is expected given the trends in control phase seen in Figure 2-24. Higher frequency controllers are simply more sensitive to phase, and so, when considering off-target locations, the noise reduction benefit should be expected to fall off more rapidly. This is one of the consequences of using a pure harmonic control. In an attempt to alleviate these off-target noise reductions, focus is shifted to controllers that remain off for large portion of the rotor azimuth.

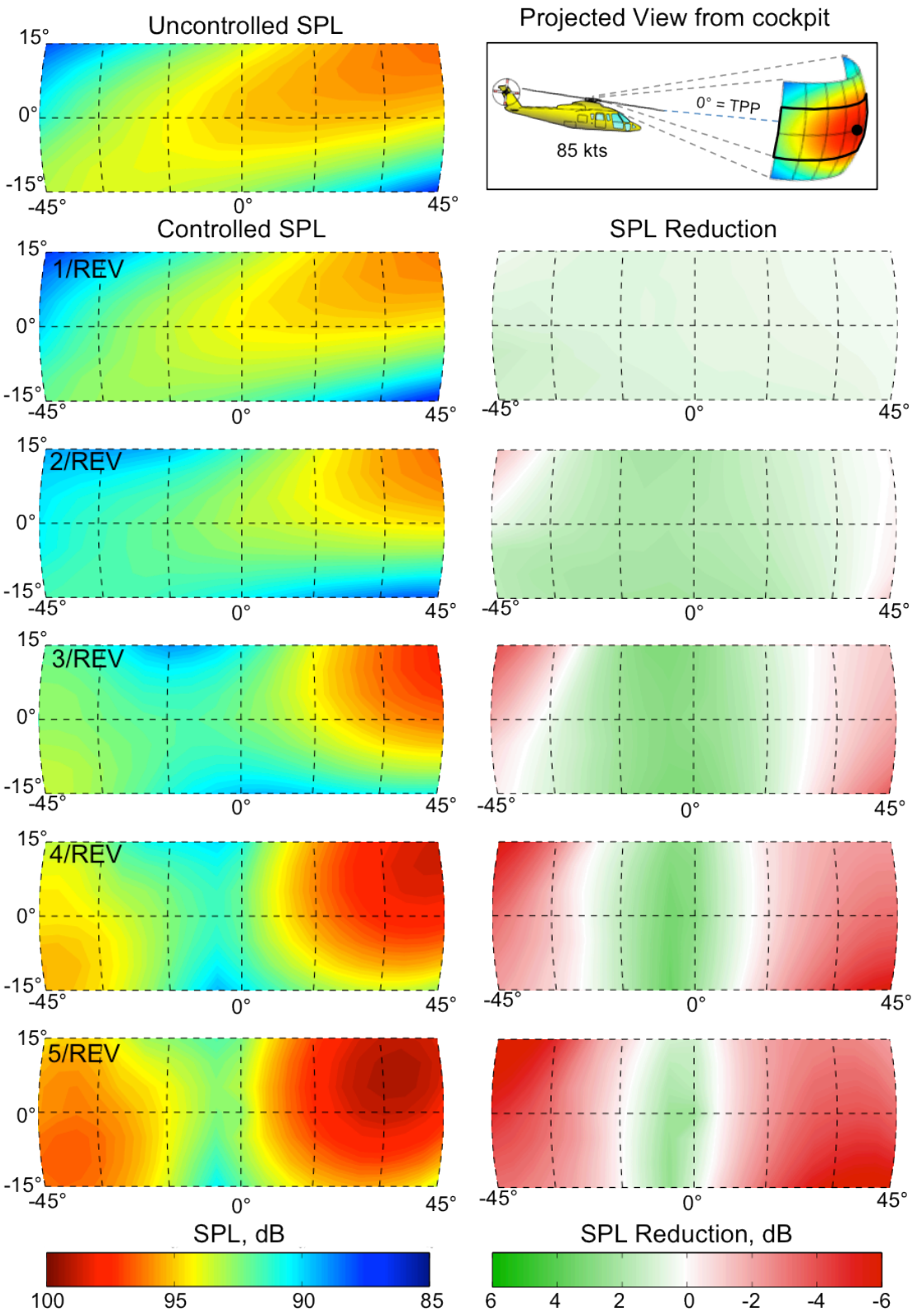

Figure 2-30: Directivity contours for harmonic blowing acoustic control.

2.5.2 Single Pulse Blowing

Single pulse per revolution controllers are now evaluated. The jet velocity is prescribed using a single cycle of the pure harmonic control,

$$V_{JET}(\psi)=\begin{cases}0 & :\ \psi-(90^\circ+\Delta\psi)\le-\dfrac{90^\circ}{n}\\ \dfrac{1}{2}V_{MAX}\left[1-\cos\left(n(\psi-\Delta\psi)-(n-1)\dfrac{\pi}{2}\right)\right] & :-\dfrac{90^\circ}{n}<\psi-(90^\circ+\Delta\psi)<\dfrac{270^\circ}{n}\\ 0 & :\ \psi-(90^\circ+\Delta\psi)\ge\dfrac{270^\circ}{n}\end{cases} \tag{2.29}$$

The jet Mach number as a function of rotor azimuth for a single cycle of the 2/REV, 3/REV and 4/REV is shown below in Figure 2-31. The frequency content of the single pulse blowing profiles is also shown in Figure 2-32. Once again the phase is adjusted as needed to yield the best target peak-to-peak reduction ($\Delta\psi$ = 14°, 12° an 11° degrees).

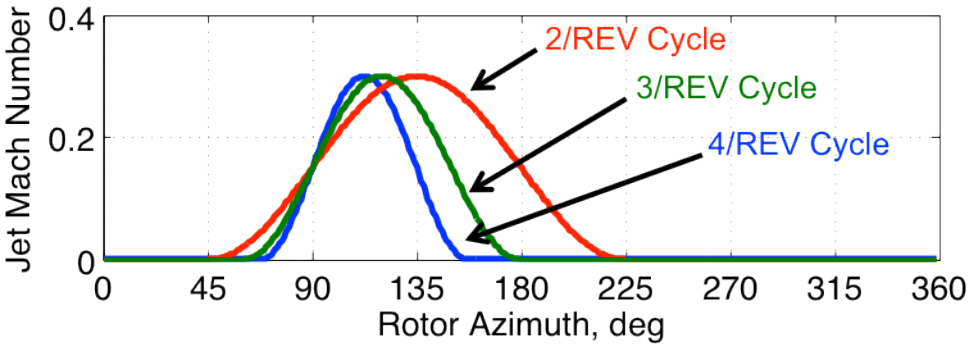

Figure 2-31: Jet velocity for single pulse blowing.

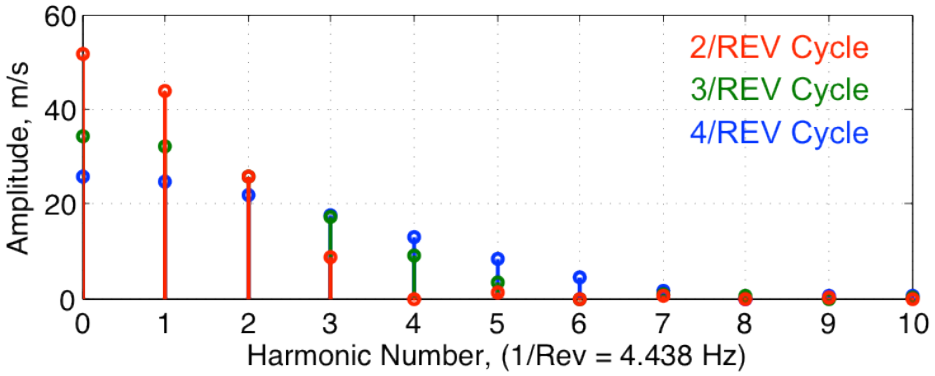

Figure 2-32: Frequency spectra for single pulse blowing.

In addition to its effect on off-target noise levels, the single pulse blowing also yields smaller net requirements for blowing mass flow which would likely have a positive effect on the vibration and performance penalties associated with an active jet acoustic control system. The acoustic pressure (a), frequency content (b) and frequency specific SPL reduction (c) is shown for the 2P, 3P and 4P based single pulse controllers in Figure 2-33, Figure 2-34 and Figure 2-35 respectively. The results are quite similar as those seen for the pure harmonic controller. However the anti-noise symmetry is somewhat diminished as the initial negative peak is entirely reduced to zero in all three cases.

For all three cases, the single pulse control has a different impact on the higher frequency content of the rotor noise. In general however, the single pulse controller is as effective if not more effective than the pure harmonic controller at reducing peak-to-peak SPL and the LF-IPH. More interesting is the directivity associated with these single pulse controllers. In Figure 2-30 the off-target noise indicated that higher frequency pure harmonic controllers result in a more narrowly focused zone of reduction and in some case, significant increases in SPL at observers relatively close to the target.

Figure 2-36 indicates that a single pulse control affects the off-target peak-to-peak levels less than the pure harmonic control, particularly for observers to the right of the target. These locations are those in which the source strength before ~90 degrees rotor azimuth is most important. For the pulse control, the source strength in this region is small and has a lower rate of change that its pure harmonic counterpart. The contours do however still show a significant increase in SPL for observers to the left of the target observer. This region is largely related to the source strength after ~90 degrees.

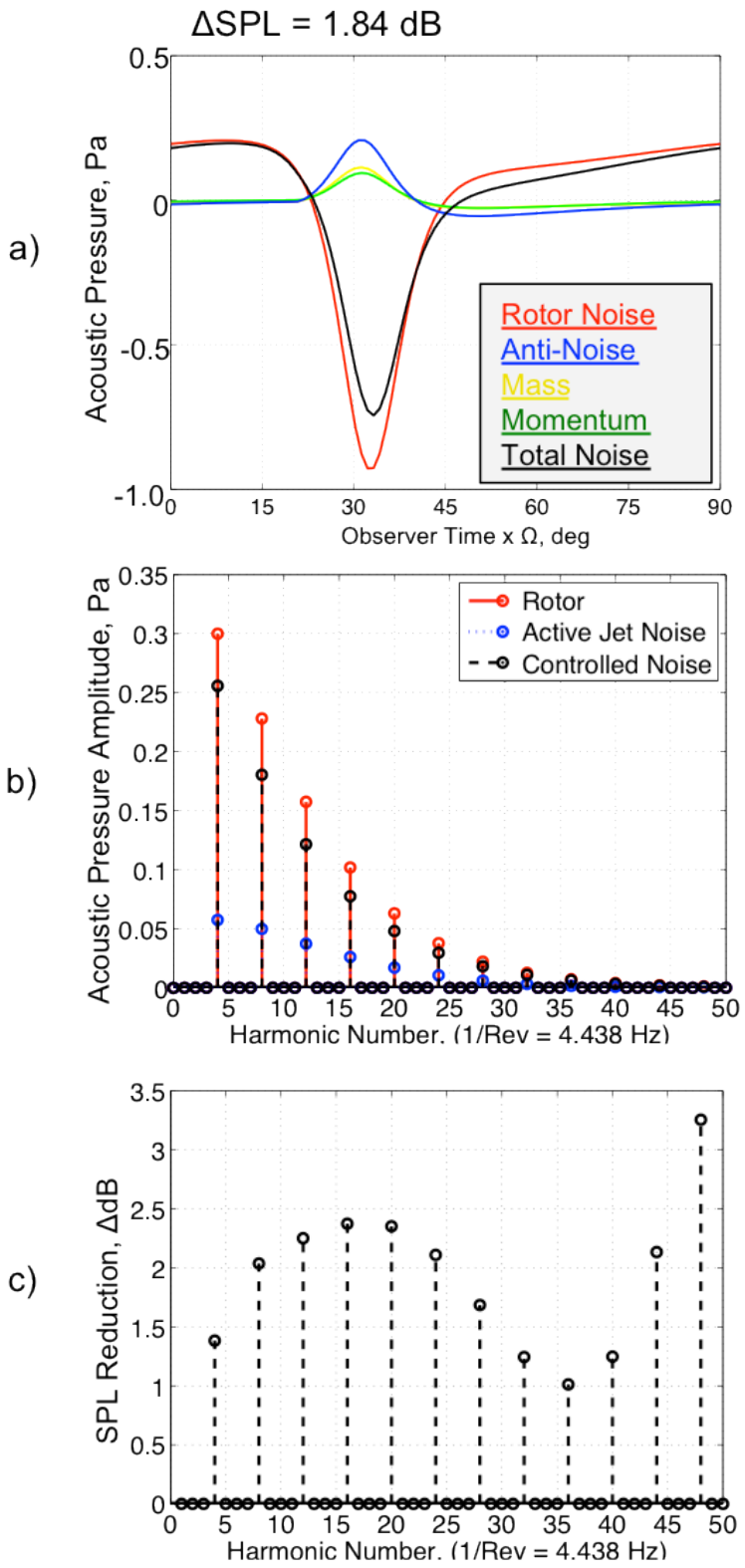

Figure 2-33: 2/REV base control a) pressure, b) frequency, and c) ΔSPL.

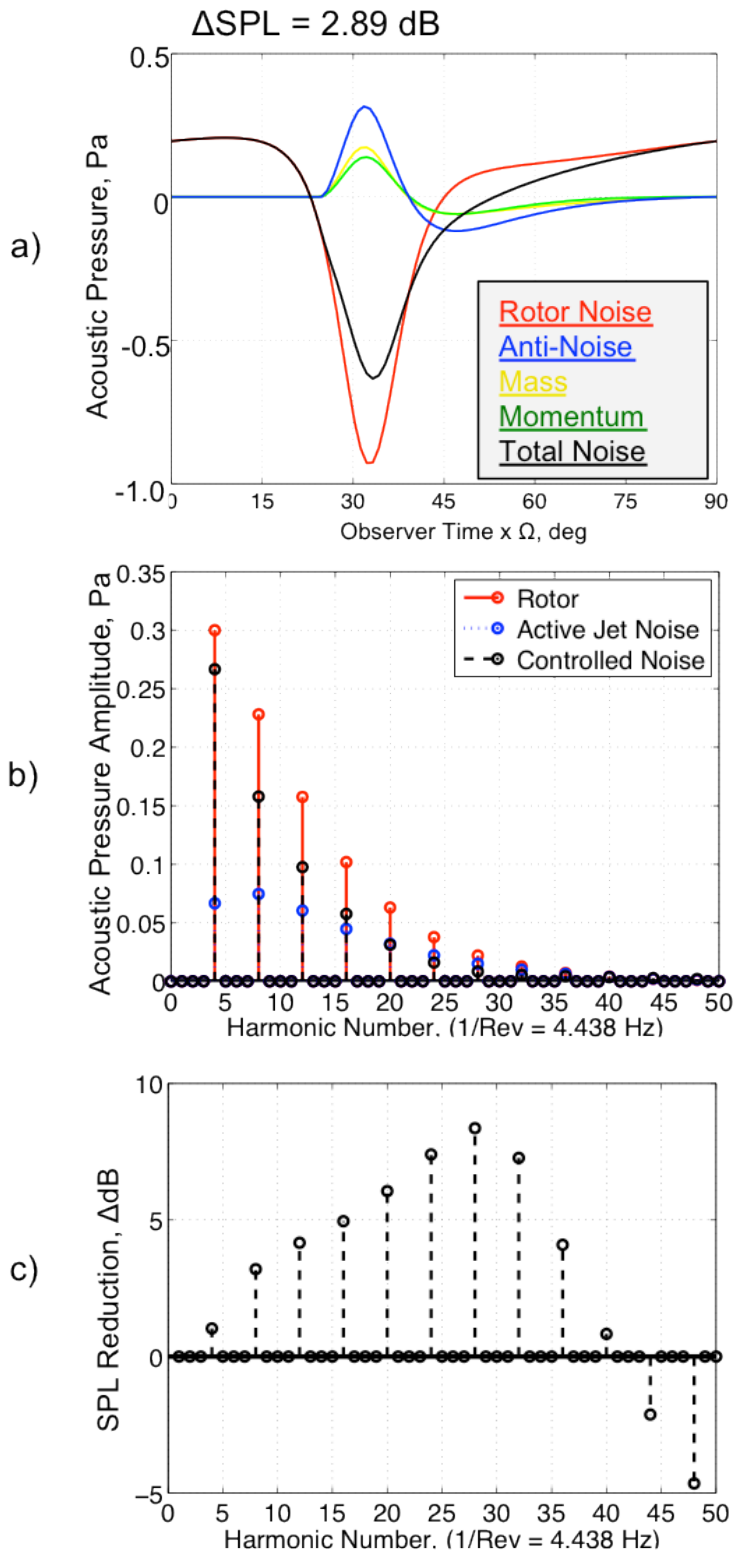

Figure 2-34: 3/REV base control a) pressure, b) frequency, and c) ΔSPL.

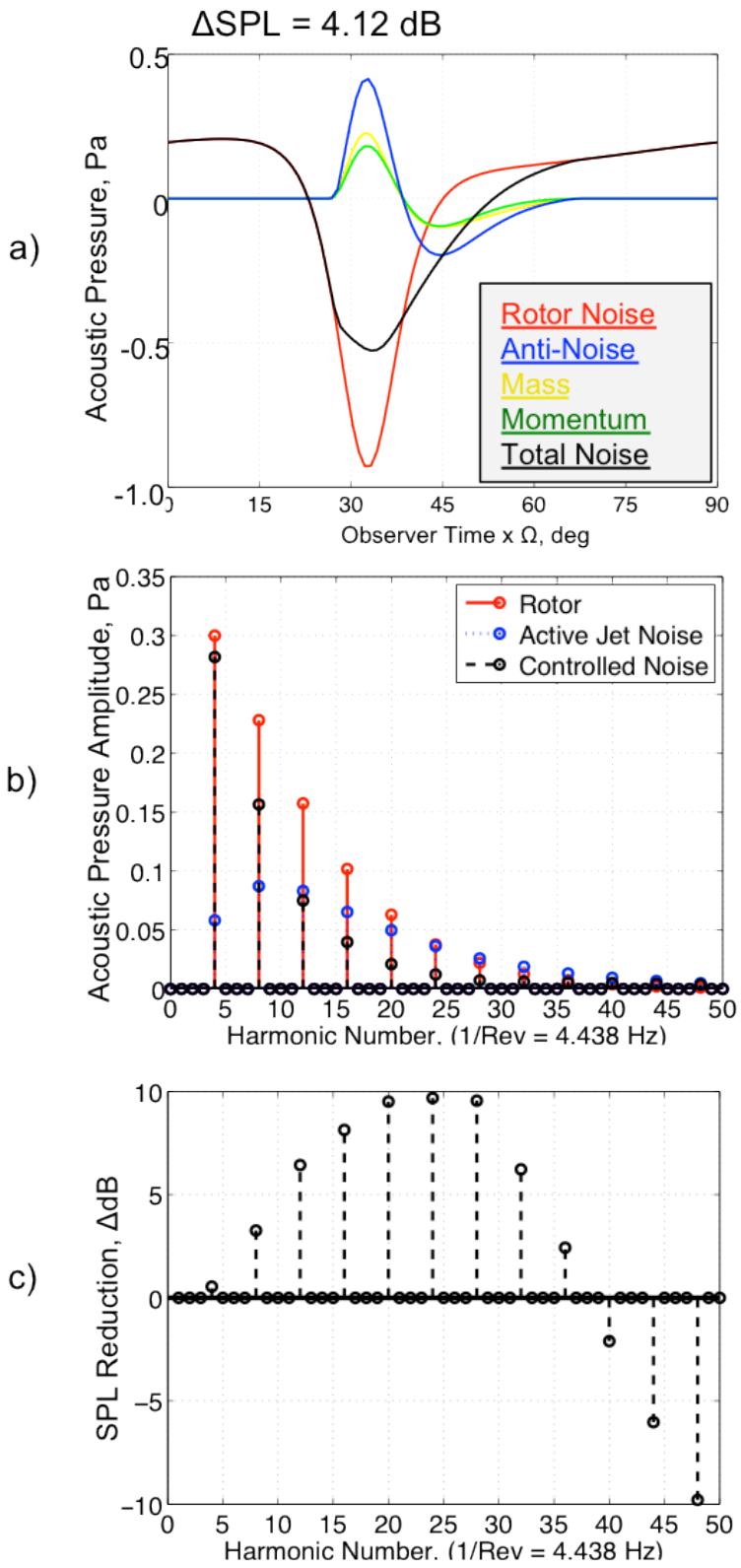

Figure 2-35: 4/REV base control a) pressure, b) frequency, and c) ΔSPL.

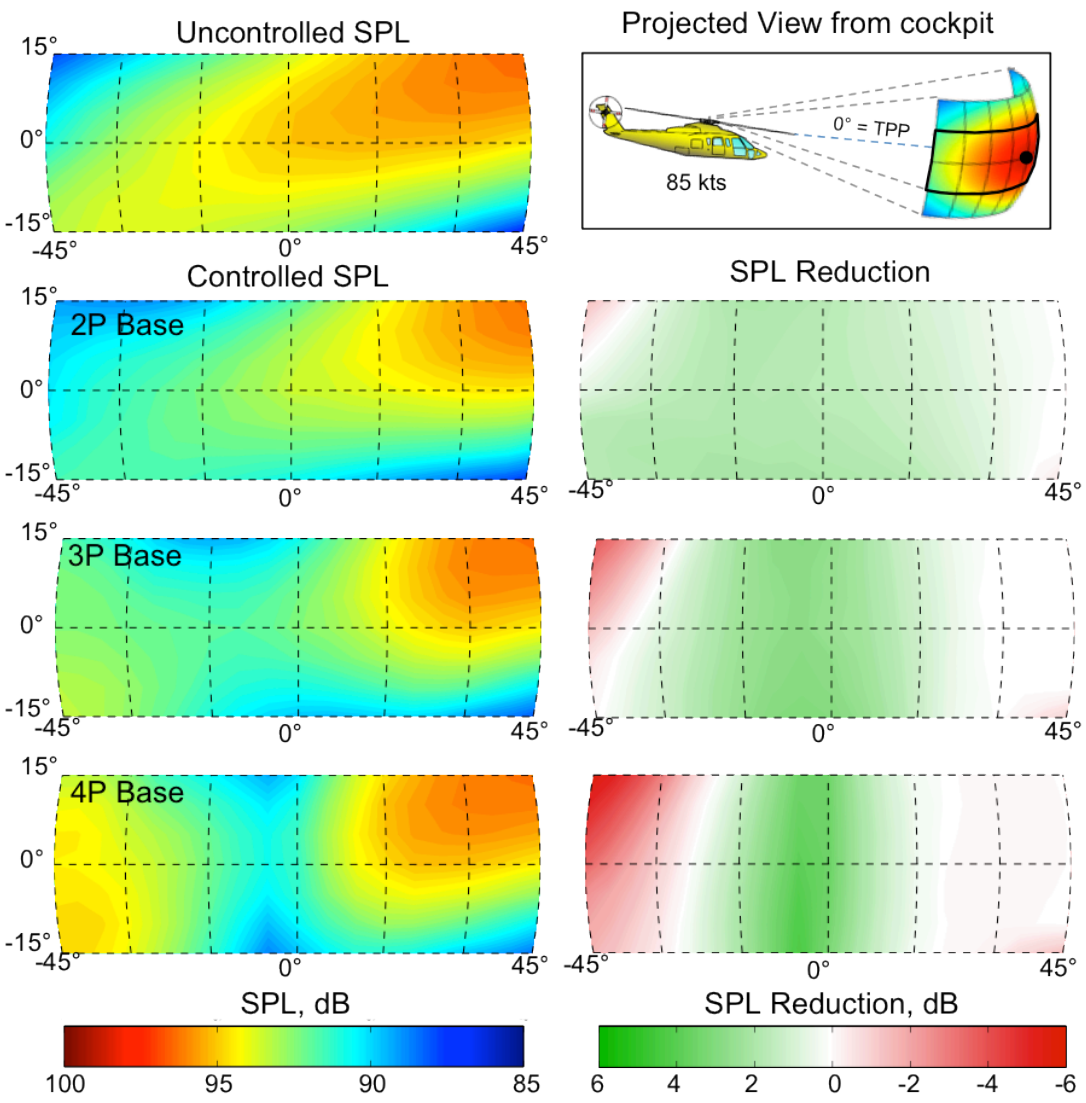

Figure 2-36: Directivity contours for single pulse blowing acoustic control.

2.5.3 Additional Blowing Profiles

To reduce the additional noise generated to the left of the target, which occurs even when using a single pulse blowing profile, the falling edge of the waveform can be further manipulated. One way of doing this is to use a specific shape for the rising edge (4/REV base) and another less steep change for the falling edge (1.5/REV base). This

case is shown in Figure 2-37. The goal in this case is to reduce the anti-noise peak amplitude at observers to the left of the target while maintaining reductions at the target.

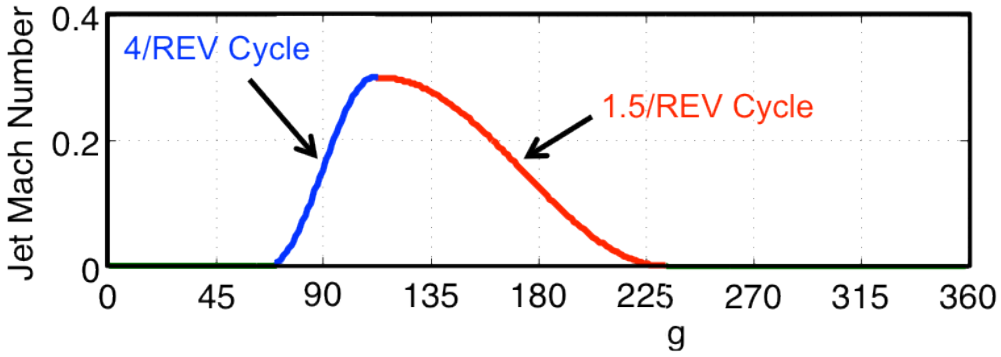

Figure 2-37: Blowing profile for improved directivity.

The target acoustic pressure and frequency content are shown in Figure 2-38. The acoustic anti-noise waveform is quite similar to those for the 4P base single pulse controller except that the second negative peak of the anti-noise is now reduced in amplitude. The resultant pulse width is narrower than the original 4P single pulse controlled result.

The directivity contour, shown in Figure 2-39, has similar characteristics to the 4P case in Figure 2-36 surrounding and to the right of the target. The control is also relatively benign to the left of the target, indicating that tailoring of the falling edge of the waveform can be an effective means of reducing the controller's global acoustic effectiveness.

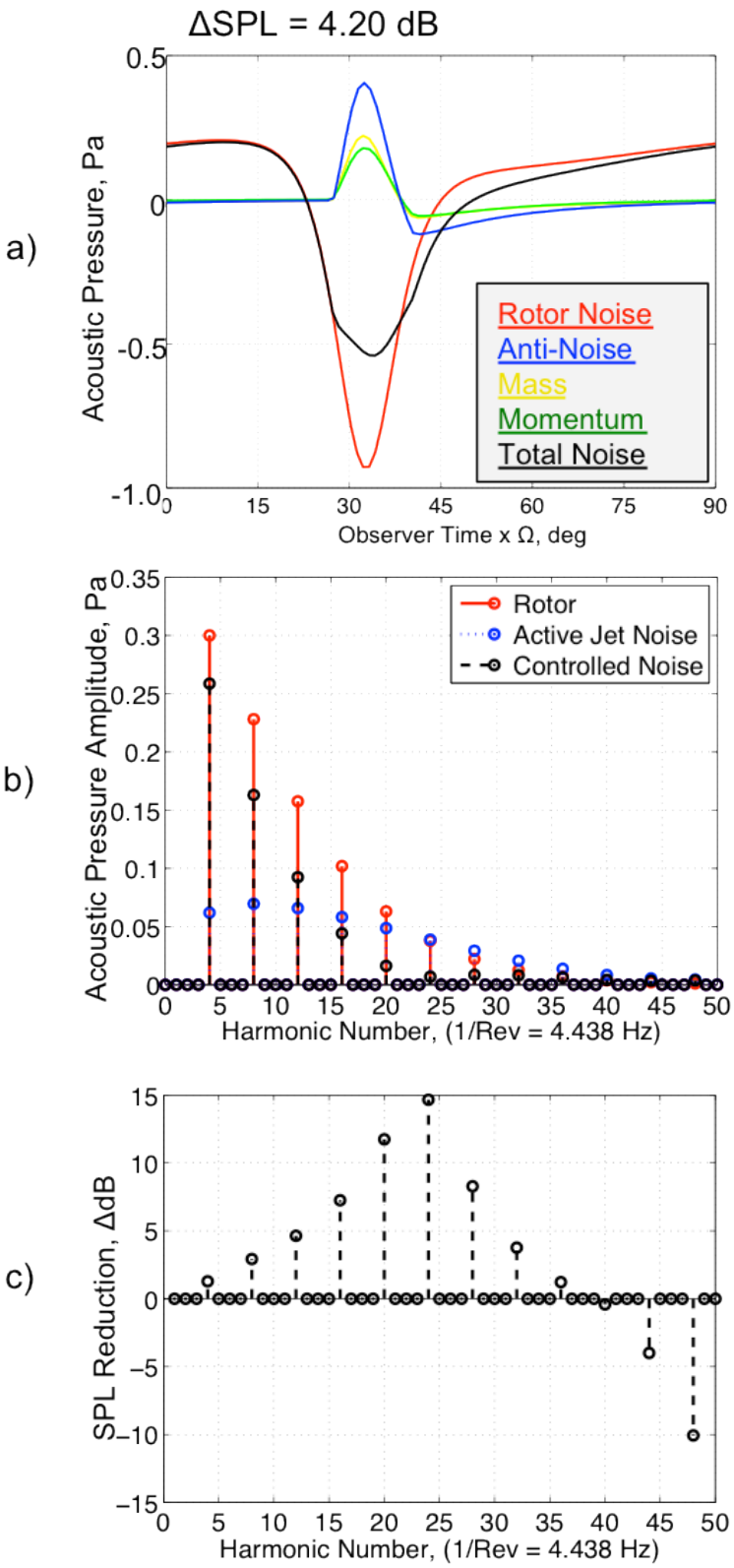

Figure 2-38: Improved control a) pressure, b) frequency, and c) ΔSPL.

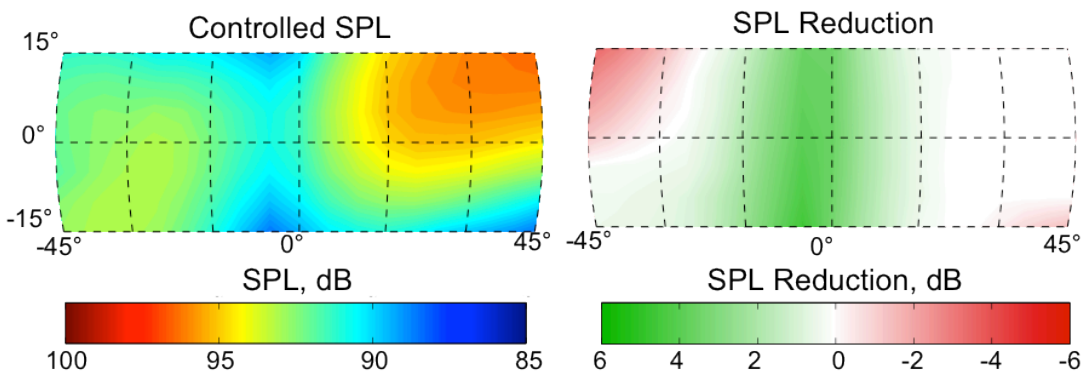

Figure 2-39: Directivity contour for improved directivity blowing.

2.6 Model-Scale Hovering Rotor Acoustic Testing

Throughout this chapter the focus has been on how active jet acoustic control can be applied to a full-scale rotor system in forward flight. This is the most likely scenario in which active acoustic control might be used. However, experimental acoustic testing of a full-scale rotor in forward flight is very difficult due the large acoustic chamber requirements and high cost of full-scale wind tunnel and/or flight-testing.

The experiment described in chapter 3 and used to validate the theoretical model is a model-scale, non-lifting hover experiment. Fortunately the active jet acoustic control methodology is scalable and can be applied to both a hovering and cruising rotor system. To show this, an active acoustic control case (a single pulse per revolution case shown in Figure 2-40) for the full-scale baseline rotor and a $1/7^{th}$ scale baseline rotor in forward flight are shown in Figure 2-41 for an observer 10R from the hub in the direction of flight. The tip and cruise speeds of both rotors are the same and so they have the same advancing tip Mach number and the period of a single revolution is much shorter for the scale rotor (~$1/31^{st}$ sec instead of ~$1/4^{th}$ sec). The area of the jet is also scaled so that the

orifice area remains 43% of the blade cross-sectional area so that the mass flow is 1/7th scale.

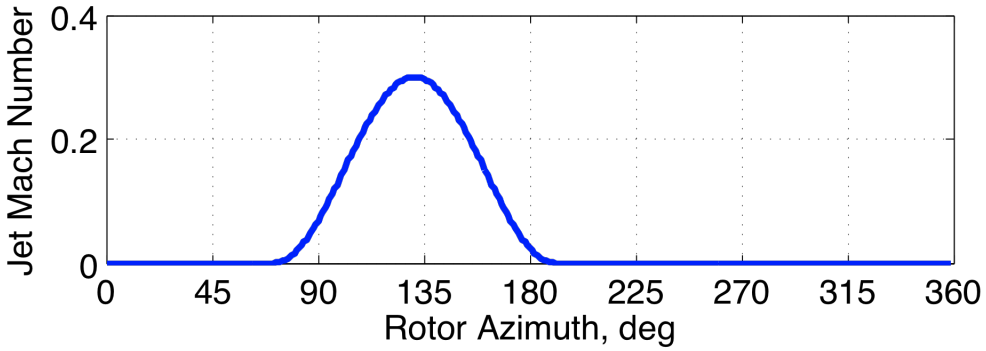

Figure 2-40: Control case for scalability study

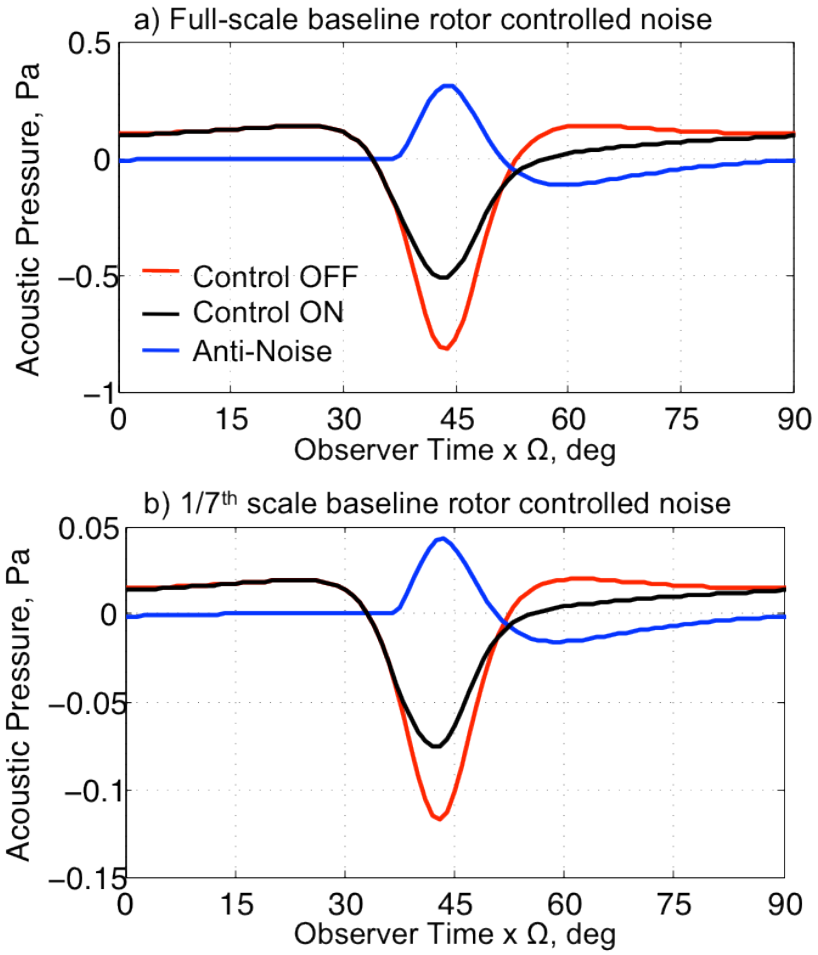

Figure 2-41: Pressure for full-scale (a) and 1/7th scale (b) rotor at 10R.

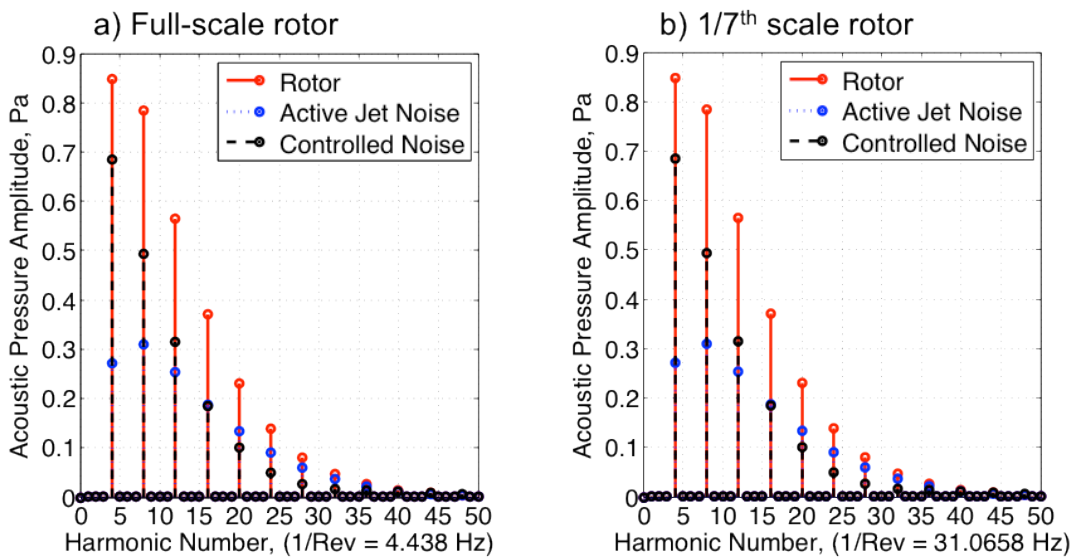

Figure 2-42: Frequency spectra for full-scale (a) and 1/7th scale (b) rotor at 10R.

The thickness noise (red), which is the dominant source of LF-IPH, produced by both rotors is identical in terms of shape, amplitude and frequency content relative to the rotor harmonic (Figure 2-42). While the frequency distributions are equivalent with respect to rotor harmonic number, the corresponding frequencies of the model-scale rotor are much higher. For both cases the controlled noise is also identical and shows that the AJAX methodology scales well for a cruising rotor. However, the UMAC facility is also limited to a hovering rotor experiment.

The control noise of the 1/7th scale baseline rotor is once again shown in Figure 2-43. Figures (a) through (b) show the calculated acoustic pressure as a function of advance ratio for a constant advancing tip Mach number of 0.7. The hover tip Mach number changes as $M_H = M_{AT}/(1+\mu)$. For all three cases the same jet velocity time history was used, shown in Figure 2-40. The general pulse shape and width of the uncontrolled, controlled and anti-noise for all three cases are very similar but the amplitudes decreases as advance ratio is increased (and the hover tip Mach number is decreased).

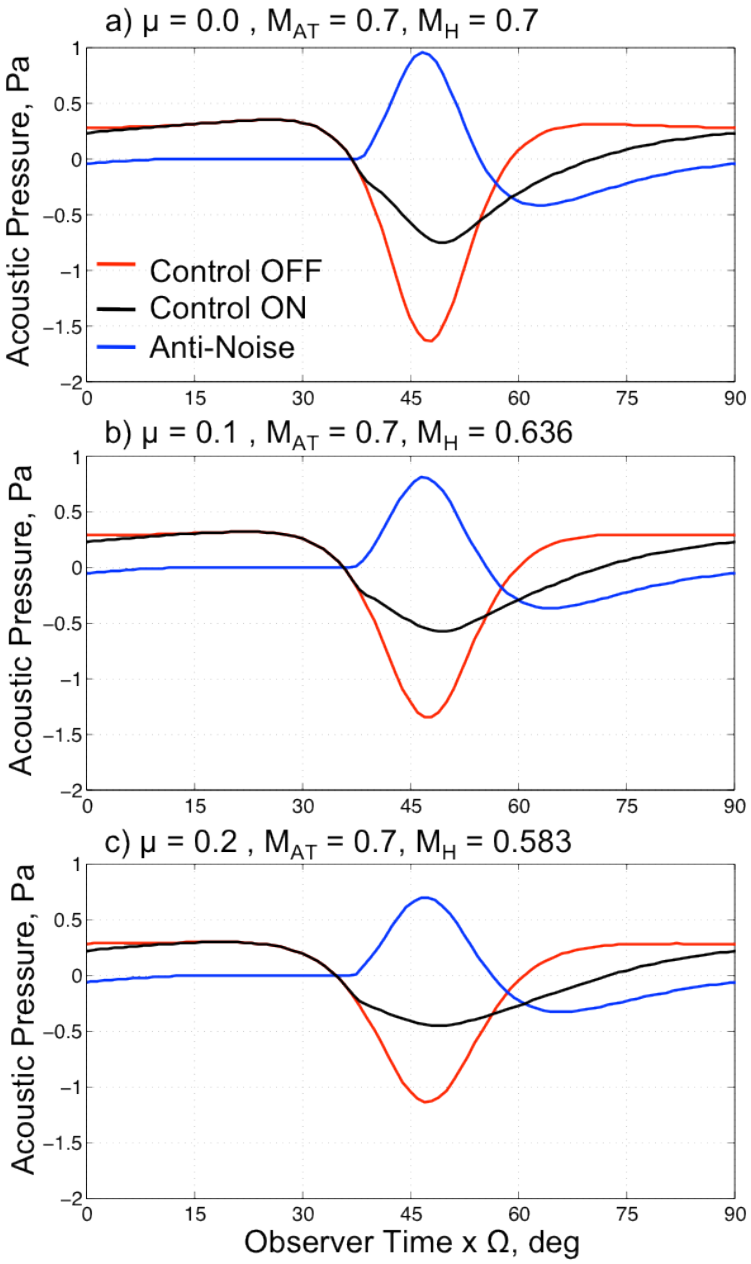

Figure 2-43: 1/7th scale AJAX rotor as a function of advance ratio for M_{AT} = 0.7.

What this shows is that the AJAX problem is actually more difficult for a hovering rotor than one in forward flight. For the same advancing tip Mach number, the peak amplitude of a hovering rotor is larger. However, the AJAX methodology can be

applied to both conditions and it is this fact that justifies the experimental approach taken for this dissertation.

2.7 Summary of Theoretical Modeling

In this chapter a new theoretical acoustic model for a subsonic tip located air jet has been developed. The governing aeroacoustic equation, in the form the Ffowcs Williams and Hawkings equation for permeable surfaces, has been extended to include both the addition of mass and momentum that occurs when a tip located air jet is used.

This model was then applied to a baseline, medium weight helicopter rotor system and the effect of steady and unsteady blowing was explored. It was determined that the chord-wise location of a steady jet can be used to induce an effective phase adjustment. Further, it was shown that the preferred jet, from an acousticians point of view, would be located at the tip, near the trailing edge, pointed in the radial or forward direction, with a jet orifice that is as large as possible. Steady blowing (constant velocity) is however a relatively inefficient method of reducing LF-IPH.

The unsteady blowing cases examined in this chapter include pure sinusoidal, harmonic based single pulse, and tailored waveforms. Higher frequency controllers yielded larger peak-to-peak amplitudes but there is a point of diminishing returns at which the pulse width of the anti-noise becomes narrower than the LF-IPH. This occurs when the frequency of the control noise exceeds that of the rotor noise, resulting in additional high frequency content to the total controlled noise and a less effective reduction in peak LF-IPH amplitude. The sinusoidal results show that higher frequency controls also result in a more narrowly focused zone of noise reduction and can actually increase the noise for off-target locations. This effect is reduced by using a single pulse

blowing profile and even further reduced by tailoring the falling edge of the waveform to return to zero less rapidly.

Finally, a study of the scalability of active jet acoustic control has been conducted. The methodology has been show to work for both the full-scale and a $1/7^{th}$ model-scale rotor system. AJAX has also been applied to a hovering rotor, which is actually a more difficult problem than a cruising rotor. However, the defining source mechanisms remain the same paving the way for the experimental work described in the following chapters.

This work provides a basis of understanding on which future optimization of the blowing profiles and the design of actual pneumatic valve systems can be conducted. Due to the nature of the mathematical model, unconstrained optimization of the control noise problem can be quite difficult. If however, the general features of a desirable solution are known, the problem can be constrained to a point that makes it far more tractable.

Chapter 3: Experimental Approach

In order to validate the active jet acoustic control theoretical model a model-scale experiment was conducted in the University of Maryland Acoustic Chamber (UMAC). LF-IPH is difficult to measure and full-scale testing requires very large facilities to place a microphone at sufficient distance from the rotor to be in the acoustic far-field. The testing space is normally covered with absorbing material (acoustic wedges) to avoid reflections from the surrounding surfaces so that only the noise generated by the rotor is measured. An example of this type of acoustic measurement, taken in the DNW anechoic open jet wind tunnel for a hovering "Model 360" model rotor, is given in reference [76]. The difficulty of capturing the true pulse shape of LF-IPH noise can be seen by comparing the pulse shape changes of two in-plane microphones – one in the part of the facility where no reflective surfaces were present and one near the inadequately treated nozzle of the DNW's open jet. The measured pulse shapes recorded near the nozzle are significantly distorted.

Measuring LF-IPH noise in the UMAC, which is considerably smaller than the DNW and has less effective acoustic treatment, is a challenge. However, the use of a single-bladed rotor minimizes the reflections normally associated with multiple rotor blades. Additionally, microphones are positioned so that the pulse time history reflections are separated from the measurement pulse of interest. Finally, strategic placement of additional absorbing material at key reflection surfaces enables quantitative LF-IPH noise measurements to be made in the UMAX. To date, several studies examining the nature of BVI have been successfully conducted using this facility [77,78].

3.1 The Active Jet Acoustic Control Experimental Setup

Testing was conducted using an approximately 1/7th scale Active Jet Acoustic Control Experimental Test Rotor (AJAX ETR) installed on the Rotor Test Stand (RTS) in the UMAC. The AJAX ETR, shown in Figure 3-1, includes a single bladed, internally ducted, non-lifting rotor, and a fixed-frame pneumatic valve system used to control airflow at the blade tip. This setup provides the unique ability to study the fundamental nature of the AJAX concept and compare experimental results directly with theoretical predictions for a variety of flow profiles.

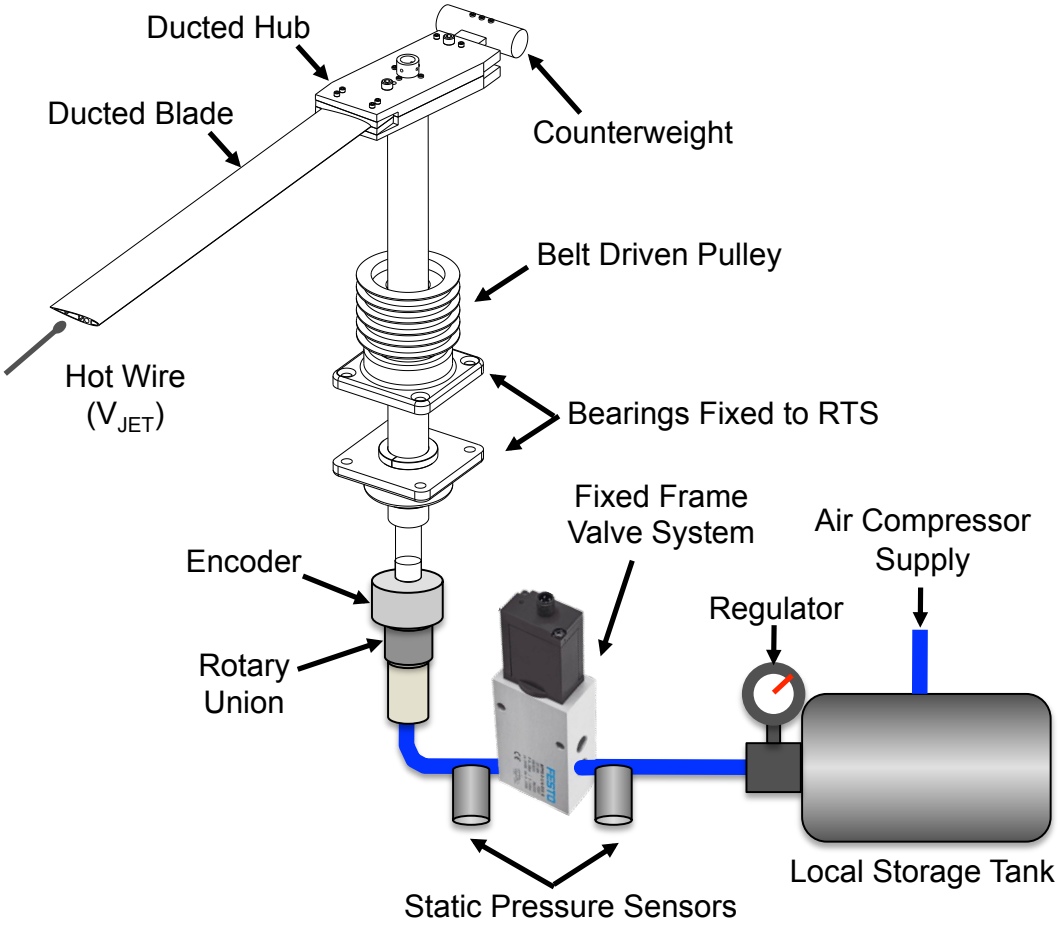

Figure 3-1: Active Jet Acoustic Control Experimental Test Rotor.

3.1.1 Experimental Test Rotor and Rotor Test Stand

The AJAX ETR was designed and constructed in 2009 and is compatible with the rotor test stand (RTS). The system is a single bladed, counterweighted, rigid rotor with a 2° downward collective pitch. This produces a very small amount of downward thrust in order to push the rotor wake above the rotor plane and provide as clean an acoustic environment as possible. Unique to the AJAX ETR are a pneumatic slip ring, an internally ducted hub and an internally ducted composite rotor blade that allows air to be transferred from the fixed frame pneumatic control system to the blade tip.

3.1.1.1 Rotor Test Stand

The RTS is belt driven by a 15 hp variable RPM electric motor, chosen for its relatively quiet operation. A 10-bit incremental quadrature encoder (BEI HS-45) that provides 1024/REV and 1/REV signals allows for precise measurement of the rotor angular position. It also is critical for accurately maintaining a phase-lock relationship between the pneumatic valve control system and rotor angular position. This is discussed in further detail in Section 3.1.2. The RTS is also equipped with several accelerometers, eddy sensors, and thermocouples for careful monitoring and balancing during testing.

3.1.1.2 AJAX ETR Shaft Design

A hollow rotor shaft, shown in Figure 3-2, is used to supply air to the blade root for the active jet acoustic controller. The hollow shaft has an outer diameter of 2.75”, and inner diameter of 1.00” and is made from 6061-T651 Aluminum. The major diameter is reduced to 1.50” for the top 3.00” of the shaft, which is compatible with previous hub designs. The shaft has two different hole patterns with ¼”-20 threaded holes that can be used for legacy and current hub designs (1.125” and 1.063” from the axis of rotation).

Four ¼”-20 threaded holes in the shaft body 0.50” from the top edge. These hold the shaft air plug in place and provide a useful point of attachment for additional sensors or equipment. A 3/8” wide, 1” long oval shaped orifice near the top of the shaft allows air to be transferred to the rotor hub as shown in Figure 3-3. The bottom 4.50” of the shaft has a reduced diameter of 1.75” making it compatible with the encoder.

Air is transferred from the fixed-frame pneumatic valve system to the rotating shaft through a Deublin 1205-000-025 pneumatic slip ring. It then travels down the length of the shaft, through the shaft orifice to the hub and finally to the blade itself as illustrated in Figure 3-2. The lower attachment point of the shaft, including the pneumatic slip ring and encoder, is shown in Figure 3-4.

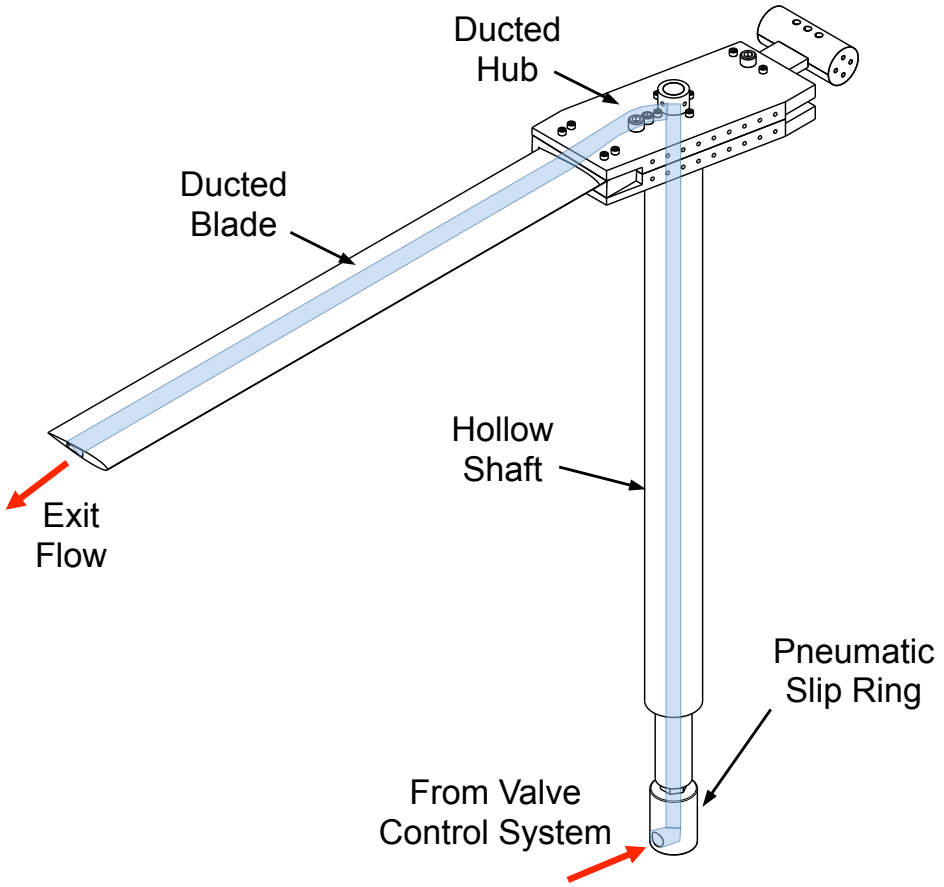

Figure 3-2: Pneumatic flow path through AJAX ETR.

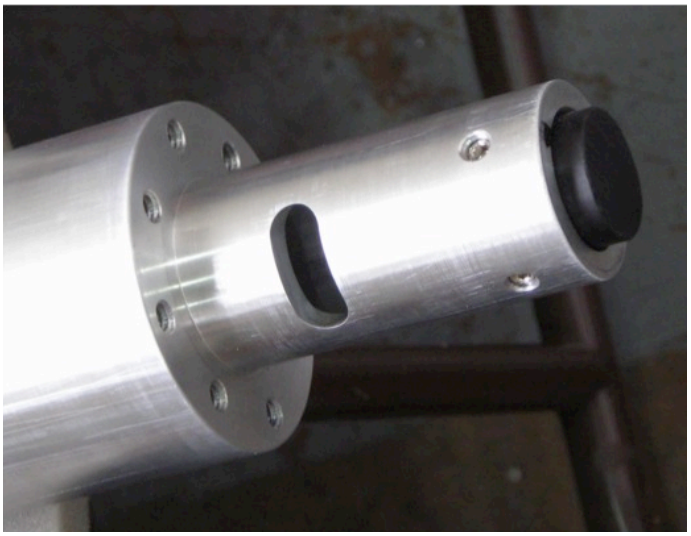

Figure 3-3: Top of the ETR shaft with pneumatic orifice and plug.

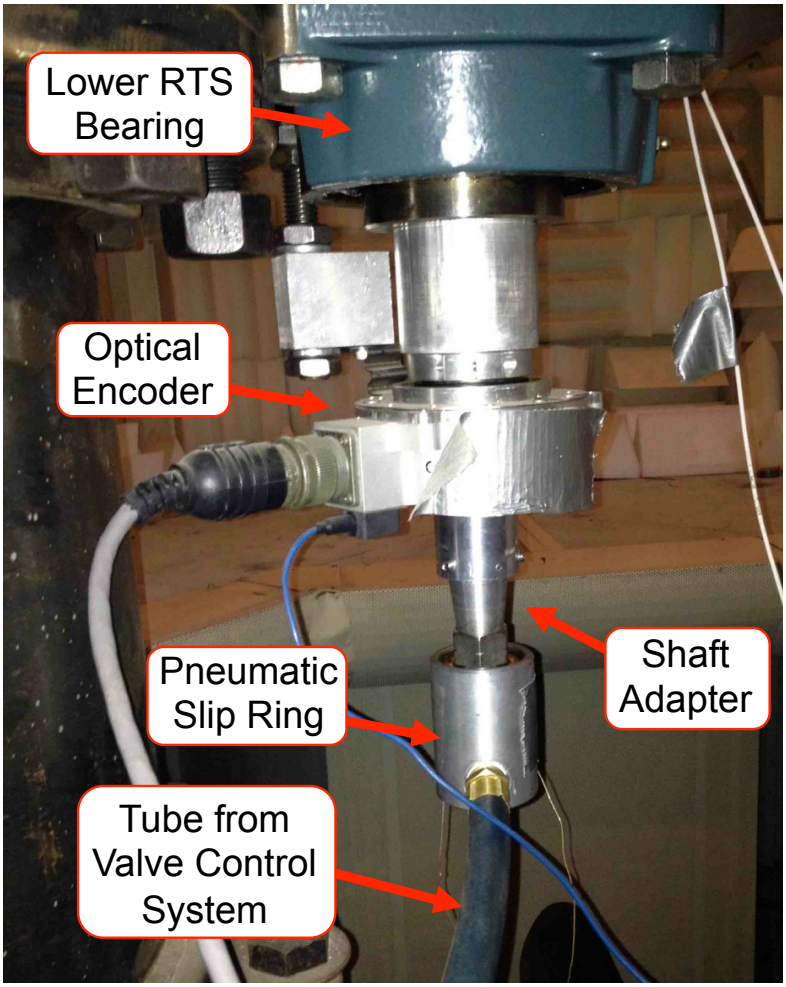

Figure 3-4: AJAX ETR Pneumatic Slip Ring and Encoder.

3.1.1.3 AJAX ETR Hub Design

The hub provides a robust and stiff platform that can be used for current and future pneumatic blade designs. It is constructed from two 1.00” thick plates of high strength 7075-T6 Aluminum. The outer radial edge extends 6.00 inches from the axis of rotation. A 1” wide by 0.2” deep channel allows air to be transferred from the shaft to the blade, as highlighted in blue in Figure 3-5, which shows the bottom half of the hub. Tight tolerances and silicon caulk provide an airtight passage. The manufactured hub plate is shown in Figure 3-6. The hub is also outfitted with a counterweight (two ¼” and one ½” shoulder bolts) and a variety of attachment points to aid in the balancing process as shown in Figure 3-7.

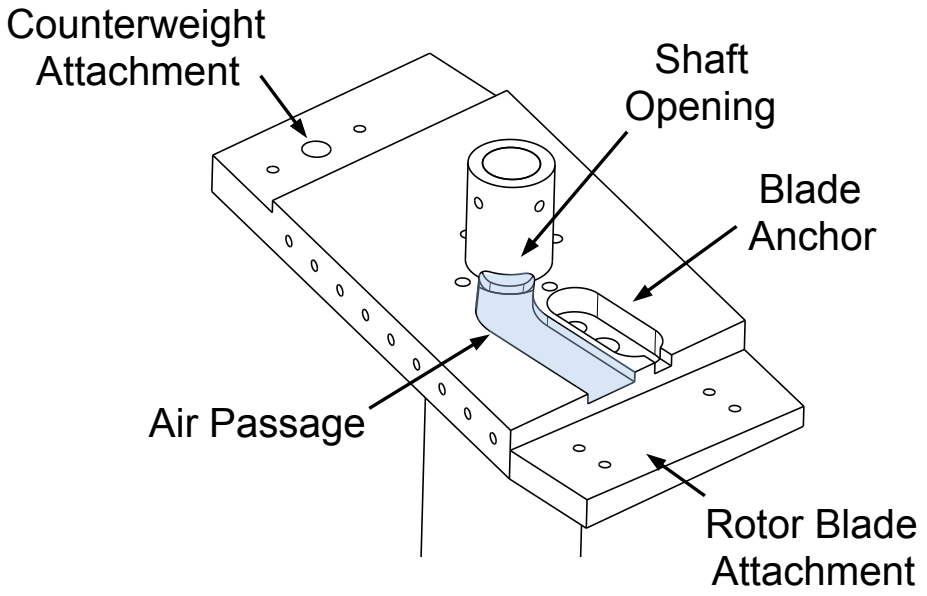

Figure 3-5: Hub plate at shaft interface with highlighted pneumatic flow path.

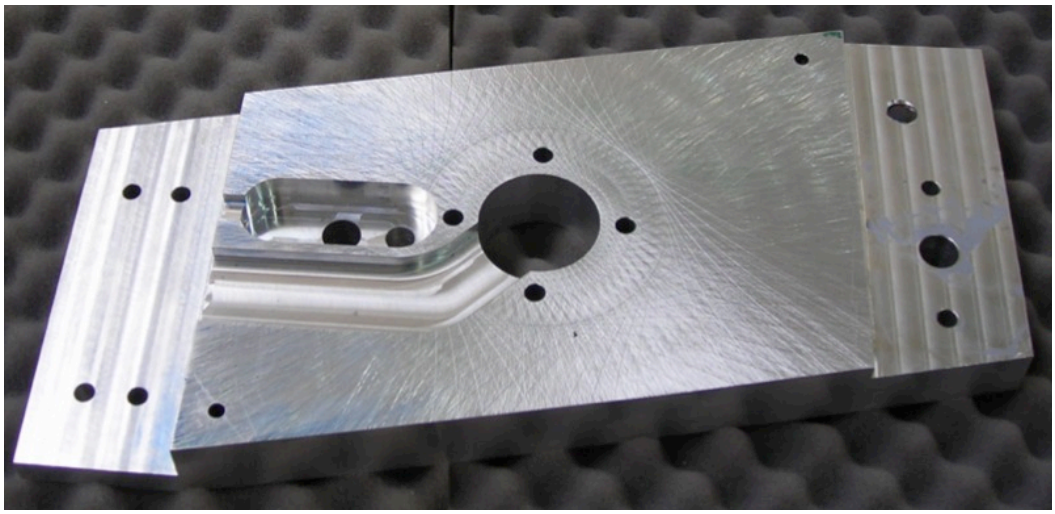

Figure 3-6: Manufactured AJAX ETR hub plate.

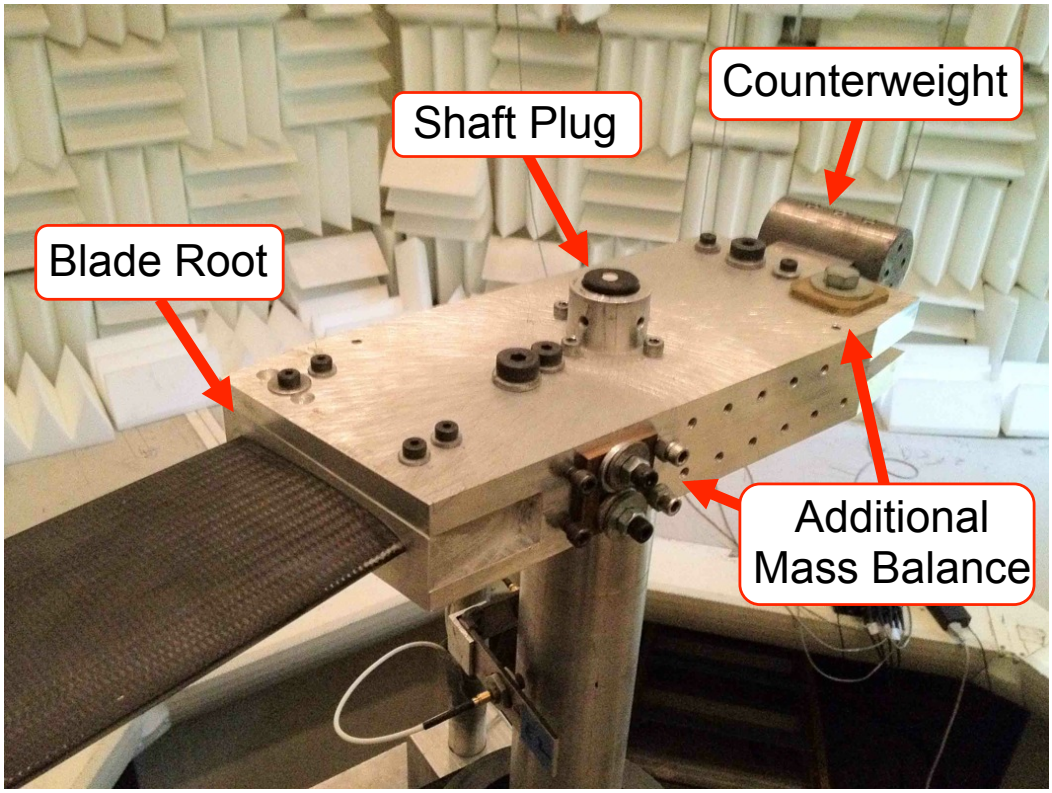

Figure 3-7: AJAX ETR Hub attachment points.

One disadvantage of this hub design is that it is not symmetric about the shaft axis. This net weight imbalance results in large 1/rev vibratory loads if not dealt with. To balance the hub independently, the hub and shaft were taken to The House of Balance in

Baltimore Maryland and dynamically balanced. Additional dynamic balancing was then conducted using test stand mounted eddy sensors to measure shaft vibratory deflection and a trial weight balancing procedure..

3.1.1.4 AJAX ETR Rotor Blade Design

The AJAX ETR rotor blade allows air to be transferred from the blade root to the tip and can withstand the large forces exerted upon it in full-scale Mach number testing. A new composite construction process was conceived to provide these capabilities and is summarized in Appendix A.

The blade has an extruded aluminum rub-structure as the main spar and shape template. The extrusion is made from 6063 Aluminum with a 4.00" chord and symmetric NACA 0012 profile, shown in Figure 3-8. The area outlined in red is used as the air duct to pass air from the hub to the tip and has an area of 0.333 in^2 (~25% of the total blade cross-sectional area).

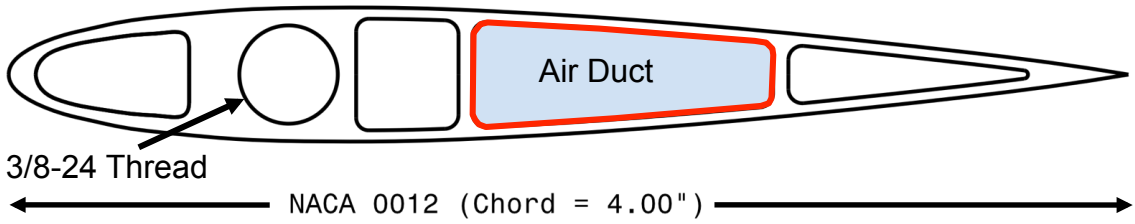

Figure 3-8: Extruded aluminum blade profile and pneumatic duct.

The majority of the centrifugal load exerted on the hub is transmitted through a threaded rod (3/8-24) connected to the blade quarter chord. The thread engagement is approximately 4.0". The opposite end of the rod is attached to an oval shaped anchor that fits securely in the hub. As an additional measure, the outer surface of the blade is bonded

to an aluminum block that conforms to its external surface which is attached to the hub using four ¼" shoulder bolts. The blade root attachment is shown below in Figure 3-9.

One problem associated with the extruded blade design is that the baseline chord-wise center of gravity is located at ~50% c. Previous rotors operated on the UMCP RTS have shown signs of flutter instabilities when operated at high tip speeds. In order to mitigate this possibility and properly balance the fully extruded structure, a powdered tungsten/epoxy composite is used. While effective for lower tip Mach number cases, this blade was too heavy for safe operation at higher rotational rates. Additional discussion of this is in Appendix B.

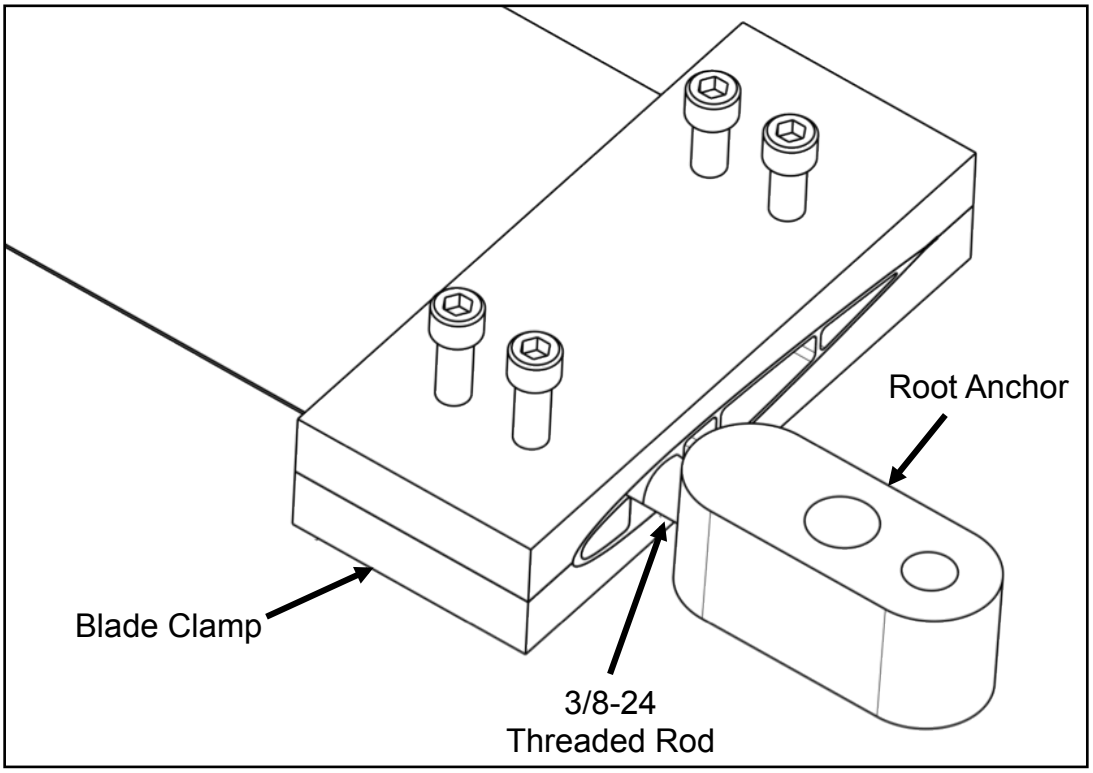

Figure 3-9: Blade root attachment diagram.

To facilitate high-speed operation of the rotor and reduce the overall blade weight, the aluminum extrusion is removed aft of the square duct (third from leading

edge) and replaced with a lightweight foam core. The entire structure, shown in Figure 3-10, is then covered with a woven carbon fiber biaxial sleeve (2.5” 6K/Aerospace Soller Composites) and hardened after a wet-layup and vacuum bagging. The inner pneumatic duct geometry is maintained using a silicon mandrel during the layup process.

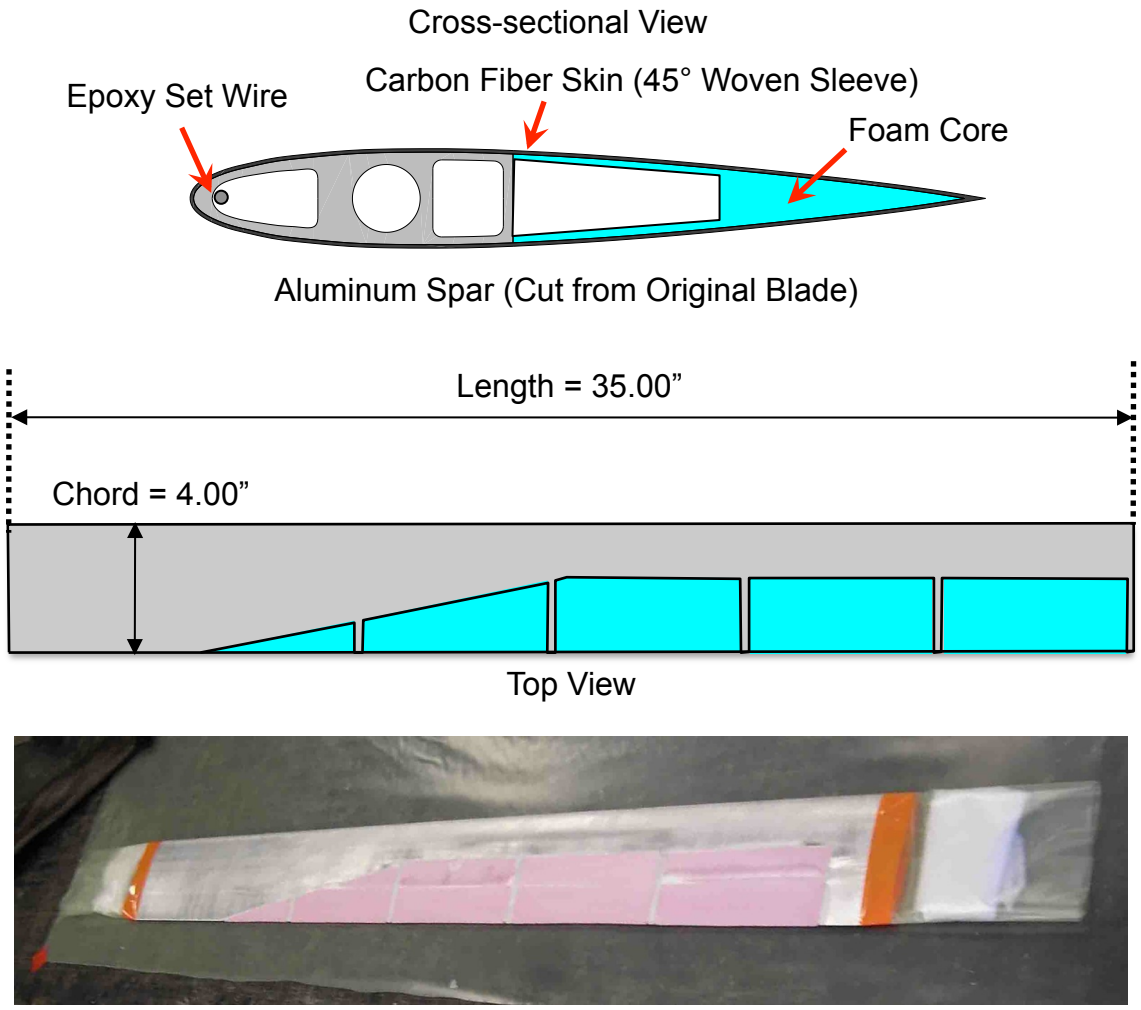

Figure 3-10: AJAX ETR composite rotor blade schematic and layup.

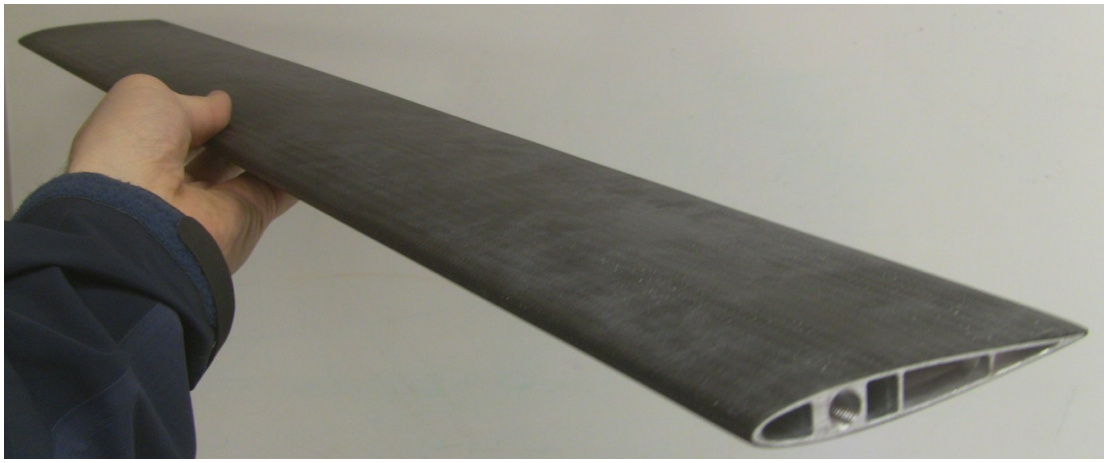

Figure 3-11: AJAX ETR composite rotor blade.

Table 3.1: AJAX ETR composite rotor blade parameters

Characteristic	English	Metric
Length (Root to Tip)	35.00 in	0.889 m
Length (Axis of Rotation to Tip)	39.00 in	0.9906 m
Chord	4.00 in	0.1016 m
Aspect Ratio	9.75	
Airfoil Shape	NACA 0012	
Weight	1.616 lb	733.01 gm

The resultant composite structure weighs only 1.616 lb, 47% less than the original balanced aluminum extrusion blade. All holes at the blade tip are sealed with the exception of the air duct. The final blade is shown in Figure 3-11 and its parameters are summarized in Table 3.1.

3.1.2 Pneumatic Valve Control System

The pneumatic valve control system is used to control the amount and rate of airflow at the blade tip. Due to the physical constraints imposed by testing on sub-scale rotors, a fixed frame valve is used. This makes control and measurement of the valve feasible and also allows for the use of an off the shelf proportional valve.

Air is supplied to the valve control system from the building compressor at 100 psia, stored locally in a regulated 20-gallon tank, and passed through a 5-gallon surge tank. The valve is connected to one end of the surge tank, with absolute static pressure measurements (Kulite HKL-375-100A & 200A) up and downstream of the valve. The downstream end of the valve is connected to the pneumatic slip ring (attached to the shaft) by a flexible rubber tube. The system is shown in Figure 3-12 and summarized in Table 3.2.

Due to the high rotational frequencies associated with sub-scale testing at full-scale tip Mach numbers, a valve that can open and close at a high rate and still supply a significant amount of peak air flow is required. A proportional spool valve manufactured by FESTO is used (MPYE-5-1/4-010-B). The valve spool is controlled using an analog voltage signal from 0-10 V DC. The steady state flow diagram supplied by FESTO is shown in Figure 3-13 (a). The valve has an approximate response time of 4.8 msec, an operating range of 0-10 bar, and a peak flow rate of 1400 std. liters/min. A schematic of the flow paths through the valve are shown in Figure 3-13. Flow from the air supply system (port 1) is routed through the valve to port 4 and attached to the ETR pneumatic slip ring. The flow between ports 1 and 4 is controlled using a 5-10 V DC signal.

Figure 3-13(a) does not take the unsteadiness of the flow through pneumatic system into account. The flow through the AJAX ETR pneumatic duct is in reality non-linear due to the internal geometry and fast actuation of the valve.

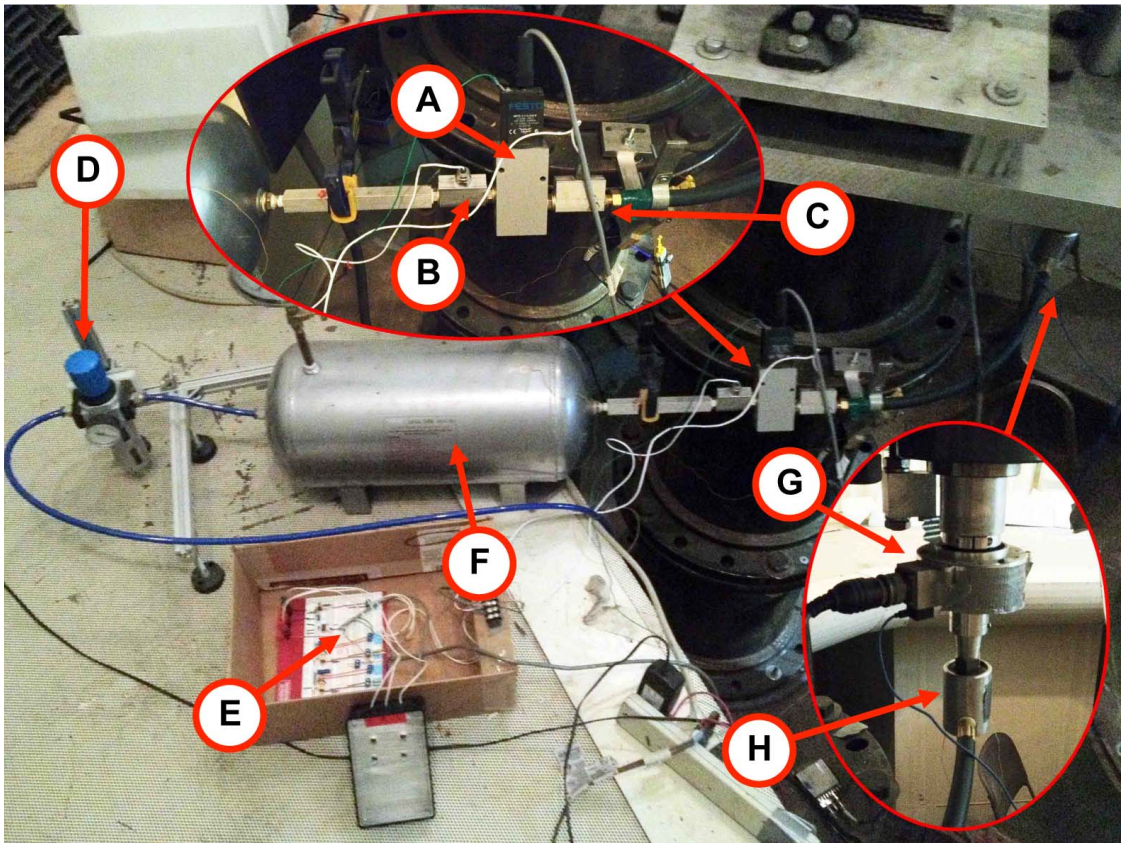

Figure 3-12: Pneumatic valve control system.

Table 3.2: Pneumatic valve control system items

Item	Description
A	Festo Proportional Spool Valve (MPYE-5-1/4-010-B)
B	Upstream Static Pressure Port (Kulite HKL-375)
C	Downstream Static Pressure Port (Kulite HKL-375)
D	Regulator/Filter
E	Pressure Sensor Signal Conditioning
F	5 gallon Surge Tank
G	Incremental Quadrature Encoder (BEI HS-45)
H	Pneumatic Slip Ring (Deublin 1205-000-025)

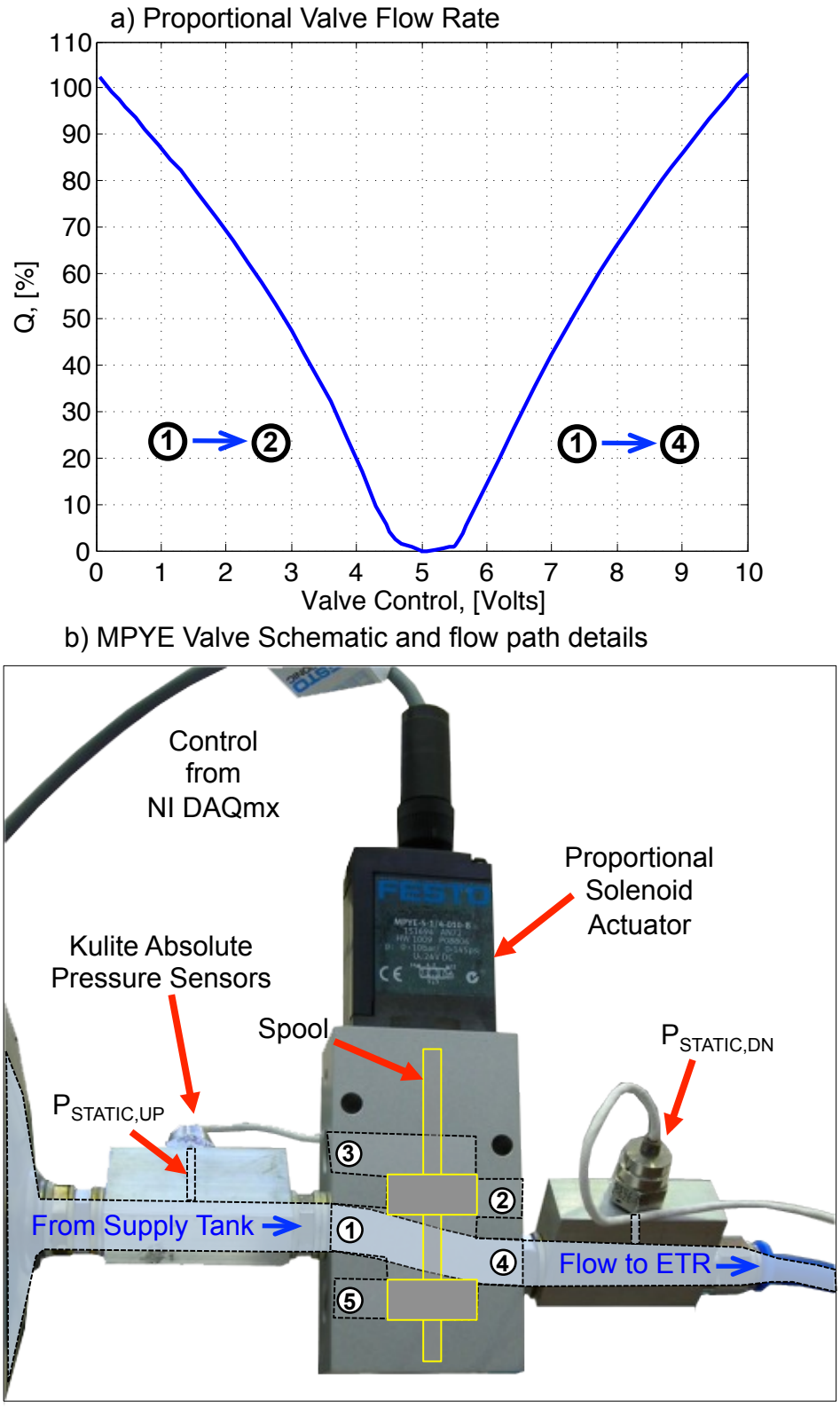

Figure 3-13: FESTO Proportional valve flow diagram (a) and schematic (b).

The valve is controlled using a National Instruments PXI-6281 Multi-function data acquisition system and LabVIEW. The PXI-6281 has two 2.8 MHz 16-bit analog outputs (+/- 10 VDC) which can be timed using an external clock signal and start trigger. To maintain the phase relationship between a given valve control and the rotor angular position, the sample clock of the analog output is triggered using the 1024/REV signal from the incremental encoder. The valve is also initially triggered using the 1/REV and occasionally reset so that small shifts in phase do not propagate over time. The desired valve voltage is divided into 1024 discrete pieces and updated on the leading edge of every cycle of the 1024/REV clock. At $M_H = 0.661$, this corresponds to valve update rate of approximately 37.5 kHz. This process is depicted in Figure 3-14.

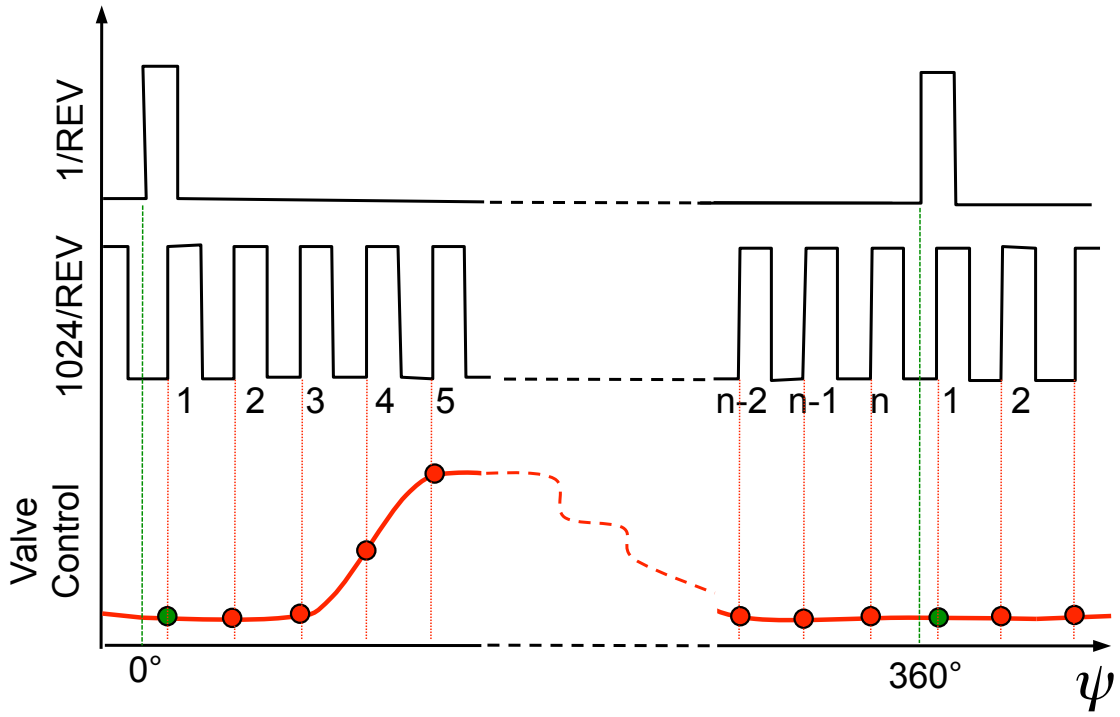

Figure 3-14: Valve control sampling process.

Accurately modeling the unsteady flow through the rotor system is complicated by the duct geometry and the non-linear nature of the high-frequency fixed-frame pneumatic controller. The flow is also subject to the natural centrifugal pumping of the rotating blade. Therefore, thermal anemometry measurements are used to quantify the exit airflow associated with a given prescribed control to the valve. The velocity data is then used as input to the theoretical acoustic model so that direct comparisons with experimental data can be made in Chapter 5.

To measure the jet exit flow velocity, a pre-calibrated, single component, hot-film thermal anemometer is used (TSI Model 1201). The probe is positioned at the jet exit of the non-rotating blade tip at the centroid of the jet orifice, and the velocity is measured for a given valve control (Figure 3-16). A chord-wise sweep of the velocity across the jet exit was also conducted for several control cases and the integrated volumetric flow is compared to the flow calculated using a single measurement at the orifice centroid. The result for a single pulse valve control is shown in Figure 3-15.

Measurements for the multi-point volumetric flow were made at 24 points spanning the jet exit. The difference between the integrated volume flow and the single point measurement is very small, particularly on the rising edge of the waveform. All velocity measurements included in the following sections are based on single point data assuming constant velocity distribution across the jet orifice.

Measurement of the jet velocity for this dissertation is conducted using the non-rotating rotor system. Blade rotation results in a pressure gradient within the blade due to centrifugal forces exerted on the fluid medium. This influences the exit flow to some extent but these effects are assumed to be small compared to the losses of the internal

duct. Additionally, no other effective means of measuring the flow through the rotating system was available. In the future, an embedded flow sensor inside the blade tip, capable of measuring jet velocity while the blade is rotating, should be explored.

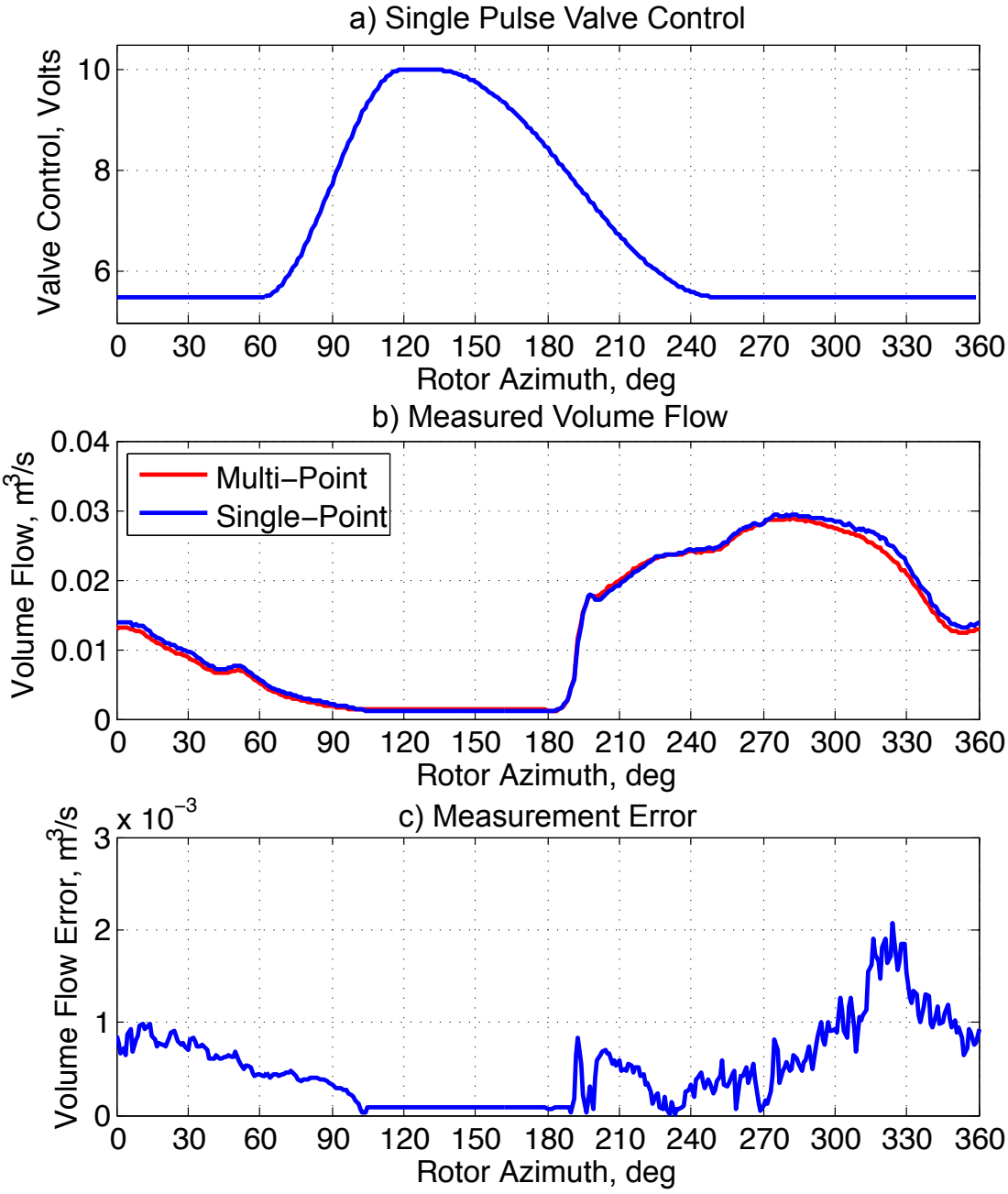

Figure 3-15: Valve control (a), multi-point and single-point flow (b) and error(c).

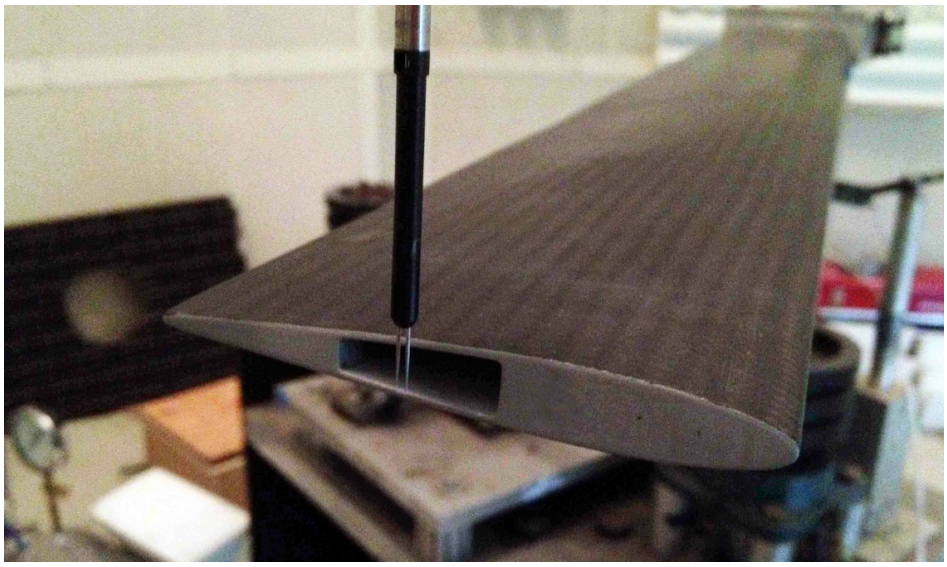

Figure 3-16: Hot file thermal anemometer probe positioned at jet exit.

3.1.3 University of Maryland Acoustic Chamber

The University of Maryland Acoustic Chamber (UMAC) (also referred to as the Free-Field Rotor Test Chamber (FFRTC) in some works) is an octagonal 20 ft by 20 ft wide, 30 ft tall acoustically treated facility. The chamber walls are composed of 8-inch thick fiberglass sandwiched between metal plates (perforated on the interior), preventing external noise contamination and reducing interior wall reflections. The original facility was calibrated and found to be adequate for sound measurements above the low-end cutoff frequency of ~200 Hz [79]. The room has since been treated with strategically place 6-inch deep melamine foam wedges that provide favorable absorption characteristics for harmonic noise produced by rotors of this size [77]. Though reflections of the low frequency noise radiated by the rotor still exist, a discussion in Chapter 4 shows that when examining time domain data, the pulse width of the rotor noise is narrow enough to separate the main pulse and the reflected pulses. The fact that a single bladed rotor is used makes this possible. A schematic of the acoustic chamber and installed experimental equipment is shown in Figure 3-17.

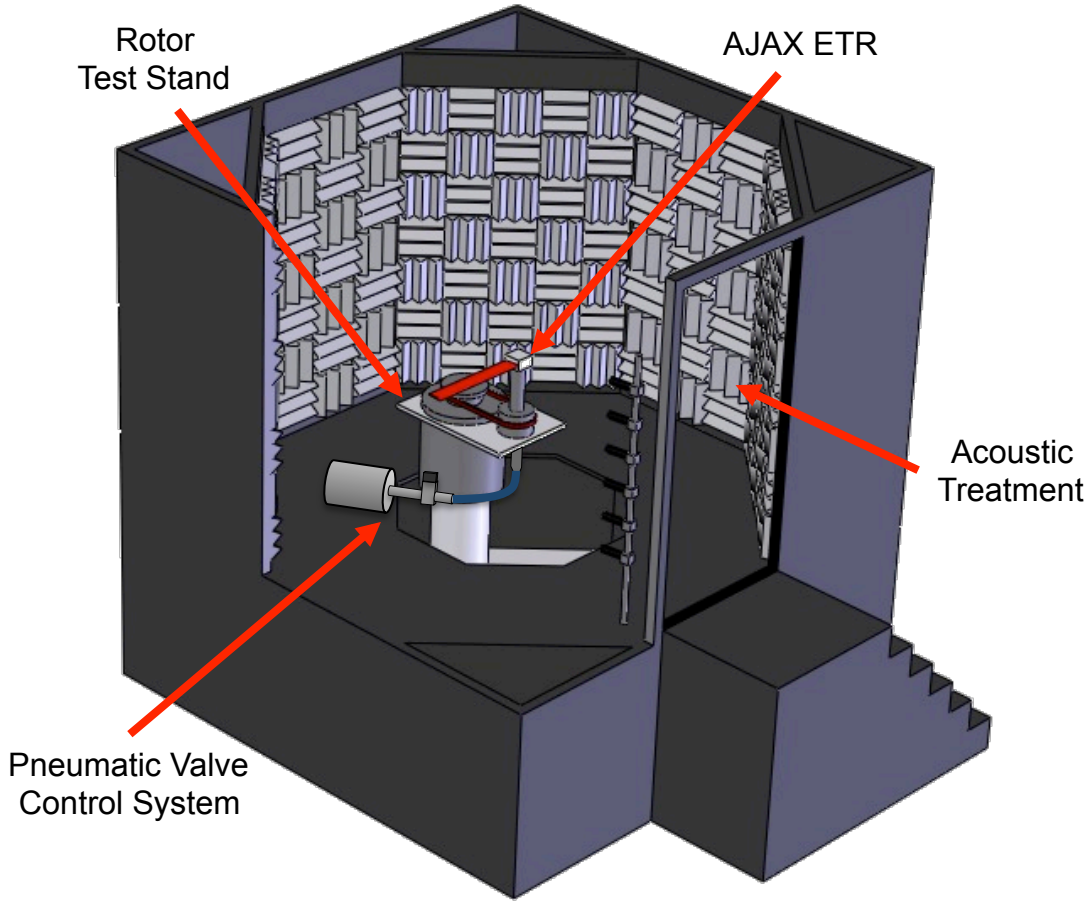

Figure 3-17: University of Maryland Acoustic Chamber.

3.1.4 Microphone Measurement System

The chamber is equipped with three in-plane and one near-plane microphones (1/2" Brüel & Kjær Type 4191) placed at angle intervals of approximately 15° to the left (M2), right (M3) and above (M4) the target microphone (M1), shown in Figure 3-18. The precise locations of the four microphones are summarized below in Table 3.3 in both polar and Cartesian coordinates with the origin at hub center and $\psi = 0°$ representing the encoder 0° reading.

Though the distance from the microphones to the hub center is slightly less than desired for true acoustic far-field measurements of LF-IPH, Chapter 4 shows that the near

field rotor noise does not significantly alter the LF-IPH pulse shape or amplitude. The AJAX noise near-field component is very small at these distances. The assembled experiment and rotor are shown in Figure 3-19.

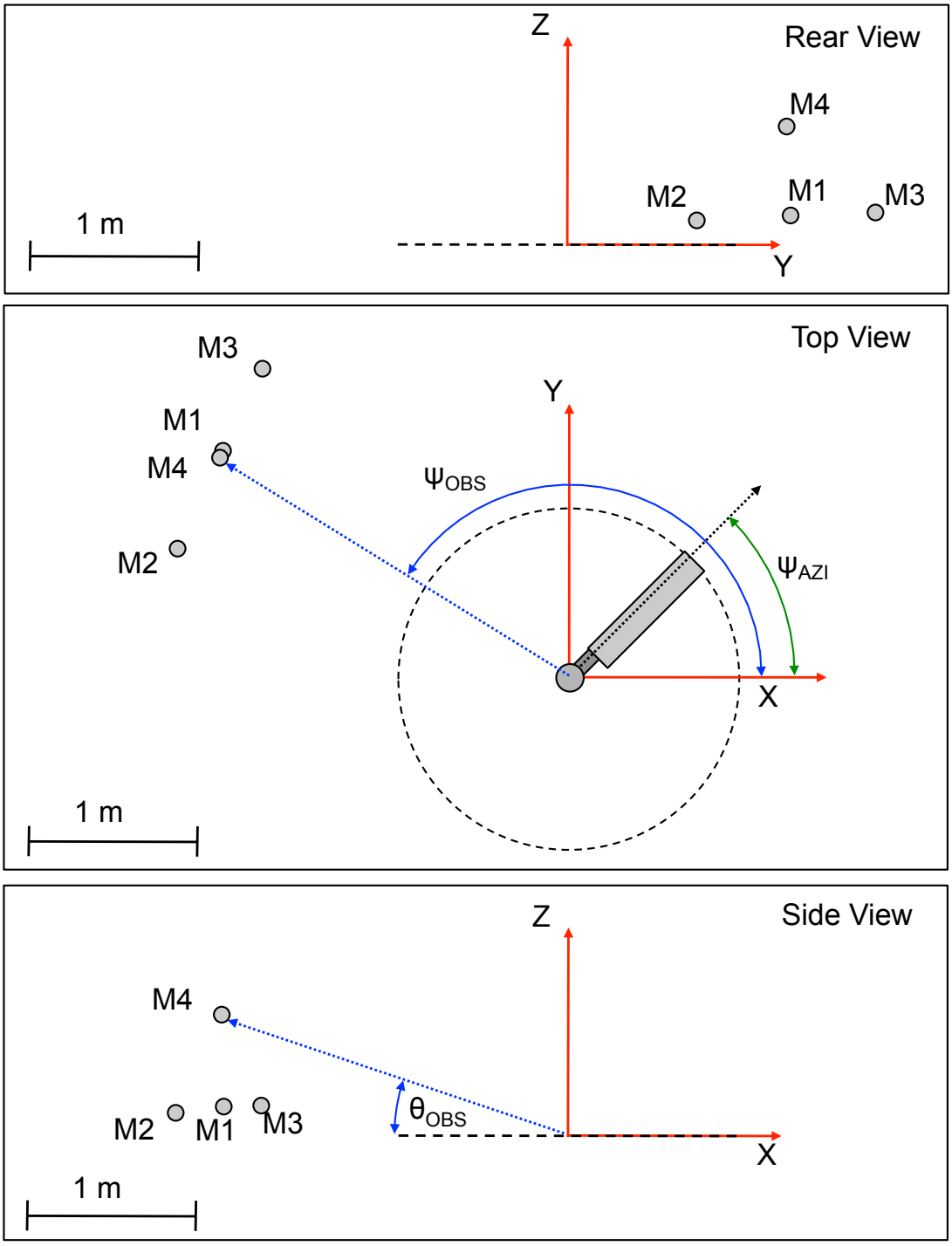

Figure 3-18: Microphone positions.

Table 3.3: Microphone coordinates

MIC	D [m]	ψ_{OBS}	θ_{OBS}	X [m]	Y [m]	Z [m]
M1	2.3832	146.7°	3.99°	-1.9873	1.3049	0.1657
M2	2.3847	161.7°	3.40°	-2.2596	0.7490	0.1415
M3	2.5195	134.4°	4.23°	-1.7571	1.7961	0.1859
M4	2.4704	147.4°	16.51°	-1.9952	1.2765	0.7020

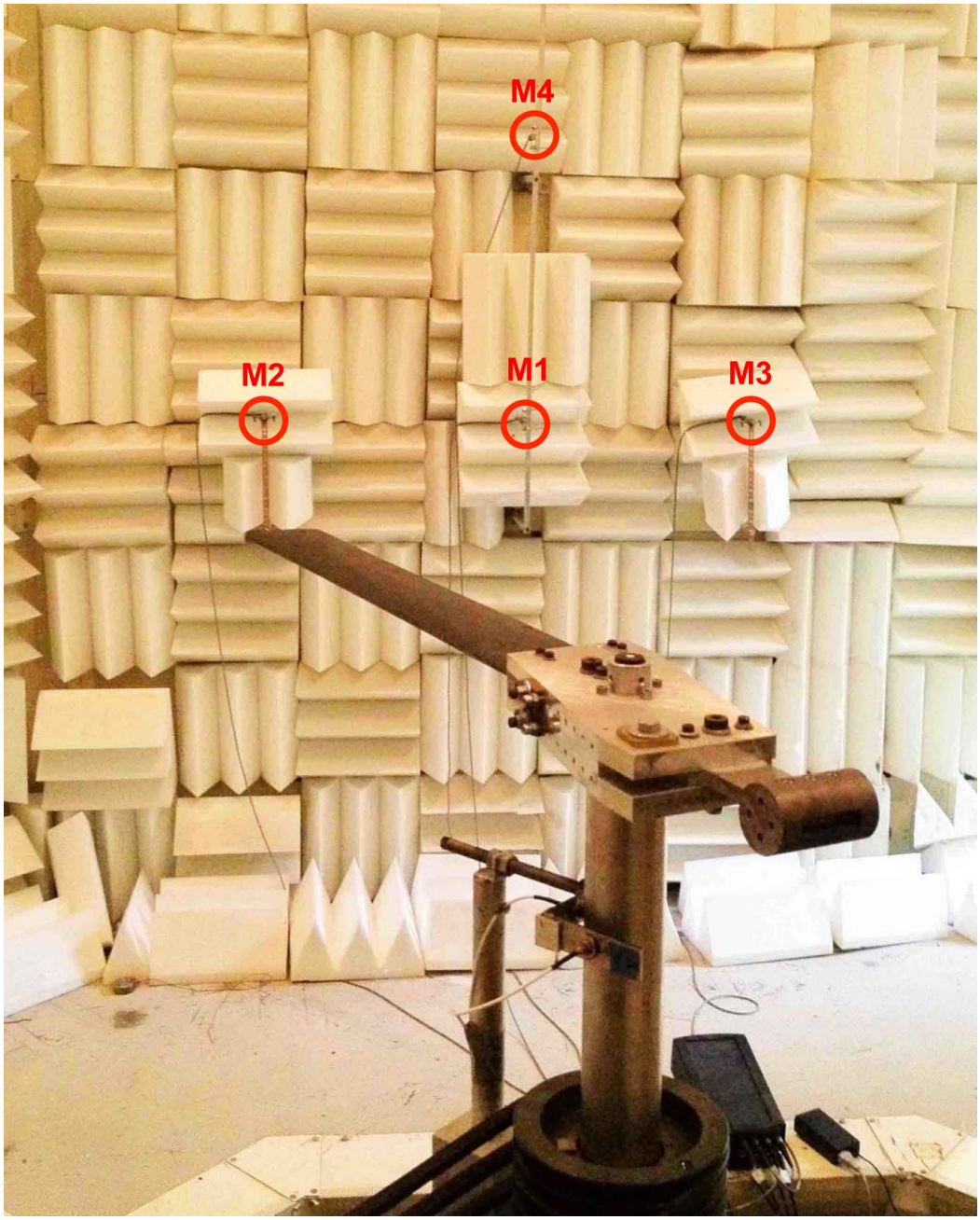

Figure 3-19: ETR and microphone positions in acoustic chamber.

3.1.5 Data Acquisition and Reduction Technique

Data is acquired using National Instruments multi-function data acquisition hardware and LabVIEW software. Microphone and pneumatic system sensors are sampled simultaneously using NI PXI-6281 and PXI-6123 multi-channel systems at 100 kHz. Data is synchronized with the encoder 1/rev (which is recorded as an isolated analog signal on each device). Acoustic and pneumatic data displayed in the following chapters are time averaged over 64 revolutions and post-processed to 2048 samples/revolution.

Chapter 4: Model Rotor Acoustic Measurement and Prediction

In this chapter, acoustic measurements of the uncontrolled experimental test rotor (ETR) described in Chapter 3 are examined and compared with theoretical rotor noise predictions made using the FW-H equation described in Chapter 2. Results at four microphones are examined in both the time and frequency domain. The presence of some low frequency discrepancies between the measured and predicted noise and an exploration of their possible cause is also conducted. The goal of this chapter is to show that the University of Maryland Acoustic Chamber is suitable for measuring the LF-IPH of the experimental test rotor.

4.1 Experimental Test Rotor Noise Modeling Summary

The noise radiated by the experimental test rotor is predicted using an "on-surface", retarded time formulation (1A) of the FW-H equation, as described in Chapter 2. The number of blade and time elements used for both the loading and thickness noise calculations are summarized below in Table 4.1. A discussion of these choices is made in Appendix C.

Table 4.1: Rotor noise modeling parameters

Parameter	Value
p'_T radial sections	95
p'_T chord-wise elements	60
Total Thickness noise elements	5700
p'_L radial sections	95
p'_L chord-wise elements	1 (at ¼ c)
Total Loading noise elements	95
Time steps per revolution	360

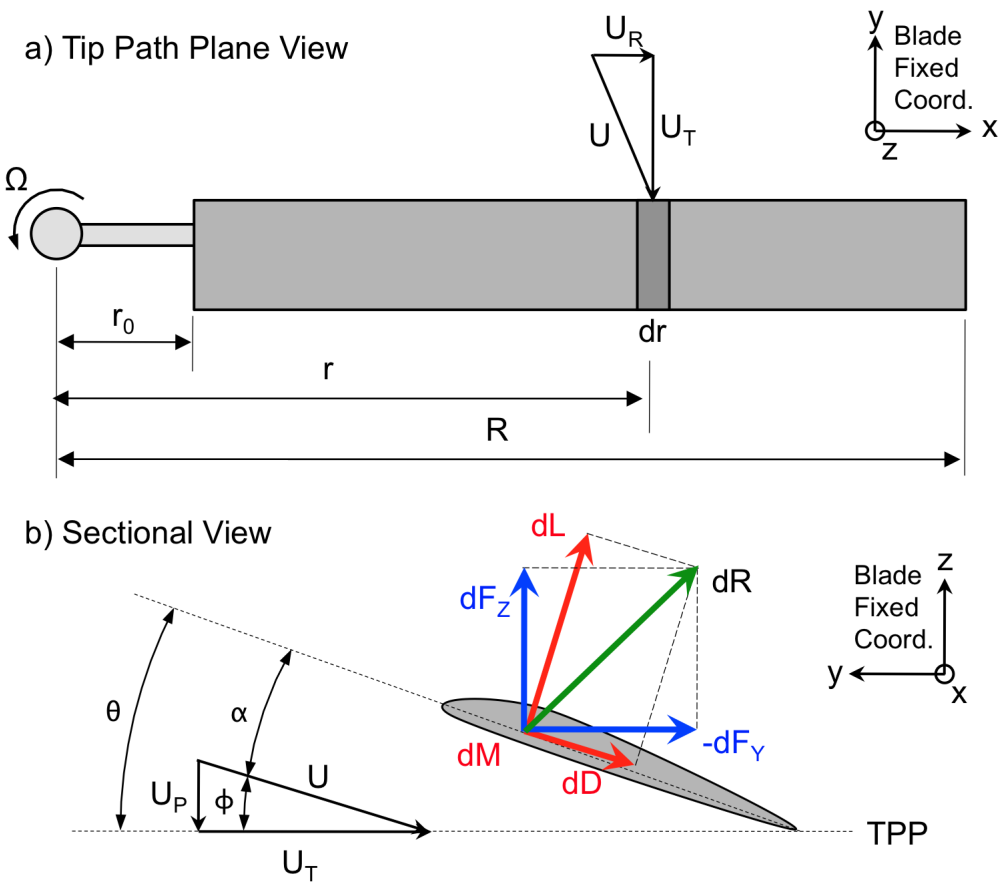

Figure 4-1: Velocities and blade loads of blade element momentum theory model.

The blade loads can be predicted any number of ways. For the theoretical rotor system in Chapter 2, the loads are calculated using a comprehensive rotor analysis code, UMARC. Because the ETR produces very little thrust (-2° fixed collective) and is a hover experiment, a more simple method of predicting the loading noise is used; a lifting line, blade element, momentum theory (BEMT) calculation [80]. A sketch of the flow velocities and aerodynamic forces of a blade element are shown in Figure 4-1. The radial component of the incident velocity U_R is ignored. Therefore the resultant velocity at a blade element for the hovering rotor is,

(4.1) $U = \sqrt{U_T^2 + U_P^2}$ where $U_T = \Omega r$ and $U_P = v_i$

Using small angle assumptions, the relative inflow angle and effective AoA are then,

$$(4.2) \quad \phi \approx \frac{U_P}{U_T} \quad \text{and} \quad \alpha = \theta - \phi \approx \theta - \frac{U_P}{U_T}$$

The blade elements lift and drag then are,

$$(4.3) \quad \mathrm{dL} = \frac{1}{2}\rho U^2 c C_l dr \quad \text{and} \quad \mathrm{dD} = \frac{1}{2}\rho U^2 c C_d dr$$

where the lift and drag coefficients are,

$$(4.4) \quad C_l = C_{l\alpha}\alpha \quad \text{and} \quad C_d = C_{d0}$$

The tip path plane normal and in-plane forces are,

$$(4.5) \quad \mathrm{dF_z} = \mathrm{dL}\cos\phi - \mathrm{dD}\sin\phi \quad \text{and} \quad -\mathrm{dF_y} = \mathrm{dL}\sin\phi + \mathrm{dD}\cos\phi$$

Assuming that ϕ and dD are very small for the one bladed rotor,

$$(4.6) \quad \mathrm{dF_z} = \mathrm{dL} \quad \text{and} \quad -\mathrm{dF_y} = \phi\mathrm{dL} + \mathrm{dD}$$

The nondimensional inflow for the hovering rotor can be written as,

$$(4.7) \quad \lambda = \frac{\mathrm{v_i}}{\Omega \mathrm{R}} = \frac{\mathrm{v_i}}{\Omega \mathrm{r}}\left(\frac{\Omega \mathrm{r}}{\Omega \mathrm{R}}\right) = \phi\bar{r}$$

which is calculated as a function of radial location as,

$$(4.8) \quad \lambda(\bar{r}) = \frac{\sigma C_{l\alpha}}{16F}\left(\sqrt{1 + \frac{32F}{\sigma C_{l\alpha}}\theta\bar{r}} - 1\right)$$

where the Prandtl Tip-Loss function is,

$$(4.9) \quad F = \frac{2}{\pi}\cos^{-1}\left(\exp\left(-\frac{1}{2}\left(\frac{1-\bar{r}}{\lambda}\right)\right)\right)$$

and the sectional thrust and power coefficients are,

$$(4.10) \quad dC_T = \frac{\sigma}{2}C_{l\alpha}\left(\theta\hat{r}^2 - \lambda\hat{r}\right)dr$$

$$(4.11) \quad dC_P = \lambda dC_T + \frac{\sigma}{2}C_{d0}\hat{r}^3 dr$$

resulting in the sectional in and out of plane forces,

$$dF_z = \rho A(\Omega R)^2 dC_T \tag{4.12}$$

$$-dF_y = \rho A(\Omega R)^2 \frac{dC_P}{r} \tag{4.13}$$

For these calculations $M_H = 0.661$, $\theta = -2°$, $\sigma = 0.0329$, $C_{l\alpha} = 2\pi$ and $C_{d0} = 0.015$ are used. The value of zero lift drag coefficient is chosen due to the somewhat blunt trailing edge of the composite rotor blade and correspondingly high level of profile drag [81]. Viscous drag has been assumed to be zero in these calculations because it does not directly influence the pressure over the airfoil surface and therefore cannot contribute to the radiated noise through the surface pressure terms of the FWH equation. A compact chord form of this loading is applied at the ¼ chord of the blade. For the ETR, the resultant thrust and power coefficients are $C_T = 0.000432$ and C_P=6.9E-5.

The predicted noise at microphone M1 is shown in Figure 4-2. Plot (a) shows the total, thickness and loading noise in black, red and blue. The loading noise is small compared to the thickness noise as expected for the in-plane microphone. It does however add to the amplitude of the leading rising peak of the thickness noise.

Due to the acoustic chamber dimensions, the microphones can only be placed approximately 2.5 R from the hub. Therefore the near-field noise affects the noise measurements to some extent. Plots (b) and (c) show the near-field and far-field components of thickness and loading noise respectively. Though the near-field component is not insignificant, it does not change the pulse shape or amplitude of the characteristic negative peak of LF-IPH that the AJAX methodology is aimed at reducing. Regardless, both the near and far field components of the predicted noise are included in all subsequent theoretical calculations.

The frequency content of the predicted total, thickness and loading (both near and far-field) is shown below in Figure 4-3. Thickness noise dominates the entire frequency spectrum except for the first few harmonics where the loading noise also contributes significantly.

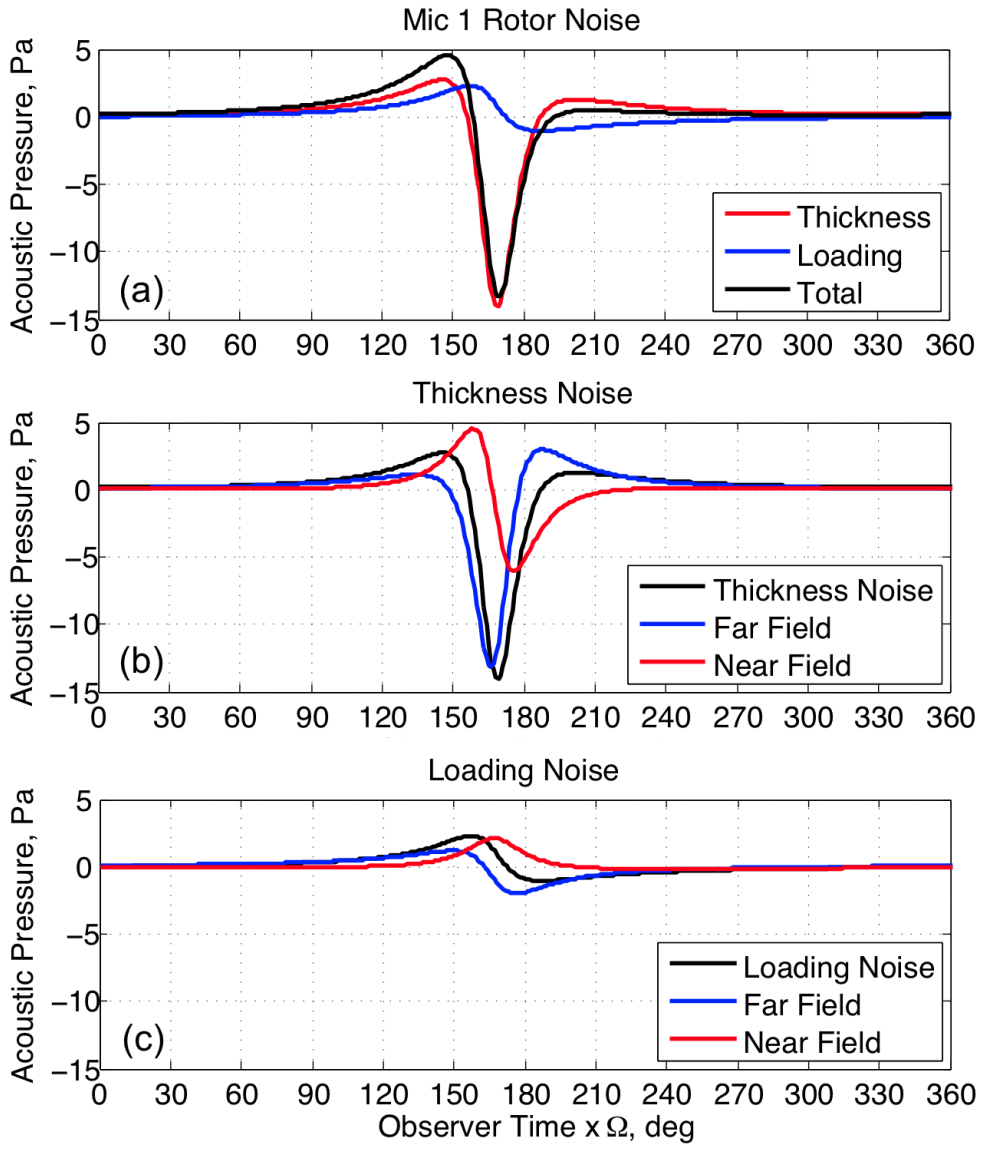

Figure 4-2: Predicted near and far field IPH for ETR at M1 at M_H=0.661.

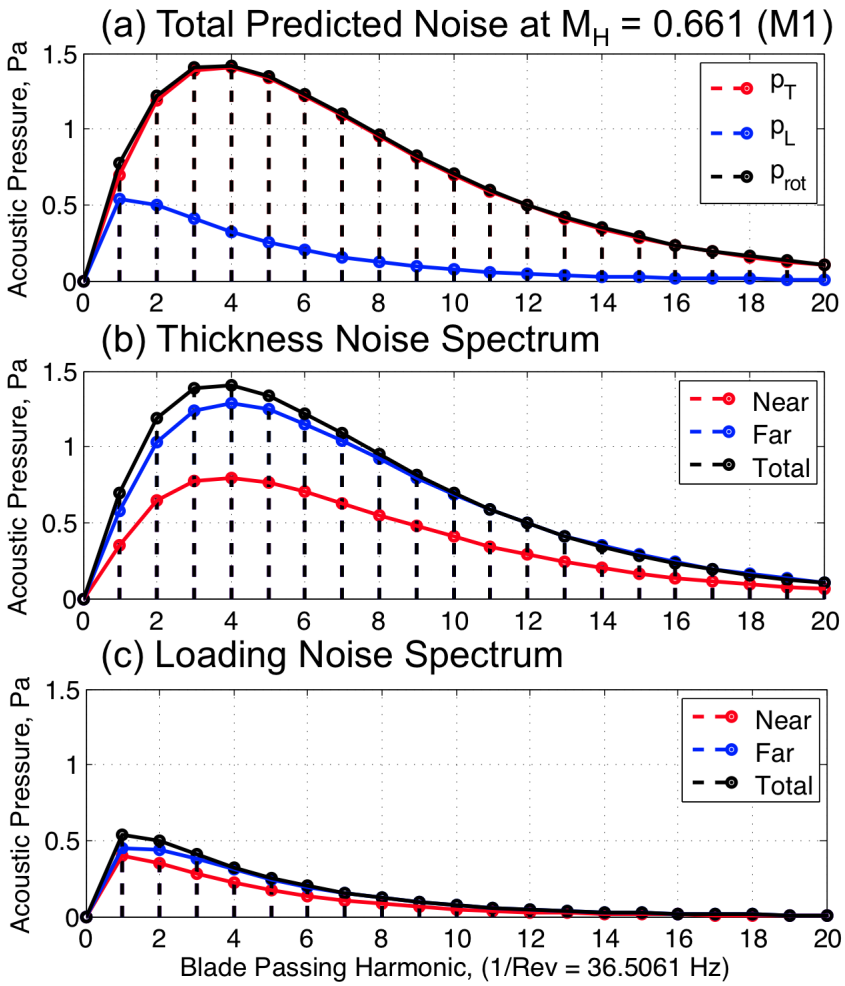

Figure 4-3: Predicted noise frequency spectra for ETR at M1 at M_H=0.661.

4.2 Low Frequency In-Plane Harmonic Noise Measurements

Verifying that the experimental setup provides clean and repeatable low frequency in-plane harmonic noise measurements is an important and necessary step when choosing an operational tip Mach number for research of this nature. The uncontrolled rotor noise at microphone M1 was measured as a function of hover tip Mach number and the resultant time-averaged acoustic pressures (blue) are compared directly with predicted values of rotor thickness noise (red) in Figure 4-4.

At low tip Mach numbers ((a) and (b)), the comparison between theory and experiment is quite poor. In these cases the pulse width of the recorded noise is substantially larger than the predicted pulse. A considerable discrepancy in pulse amplitude is also present. This difference can be attributed to a combination of effects which are illustrated in the predicted waveforms shown in Figure 4-5 and Figure 4-6 at hover tip Mach numbers of $M_H = 0.45$ and $M_H = 0.65$. In both figures, plot (a) shows the total predicted noise at microphone M1. Plot (b) and (c) show the near and far-field components of the predicted thickness and loading noise. Finally (d) shows a crude estimate of what a reflected measurement might look like for an incident wave (black) that is reflected by a wall 1.5 feet behind the microphone. The magnitude of the reflected wave (red) is assumed to be half that of the incident wave and the total measured acoustic pressure is shown in blue.

At $M_H = 0.45$, the ratio between in-plane loading and thickness noise is quite low resulting in a total waveform that is wider than the thickness noise alone. The thickness noise is composed of approximately half far-field and half near-field noise. Because of the wide pulse, the wave reflected by the wall merges with the incident wave, further widening the appearance of the measured waveform. As the Mach number is increased to $M_H = 0.65$ in Figure 4-6, the thickness noise becomes increasingly dominant and the net waveform pulse width becomes narrower. The far-field content is also more dominant. Because of the more narrow pulse width, the reflected waveform separates from the oncoming incident wave and the comparison between predicted thickness noise and experiment improves. This highlights very clearly that a hover tip Mach number of 0.661 is sufficient.

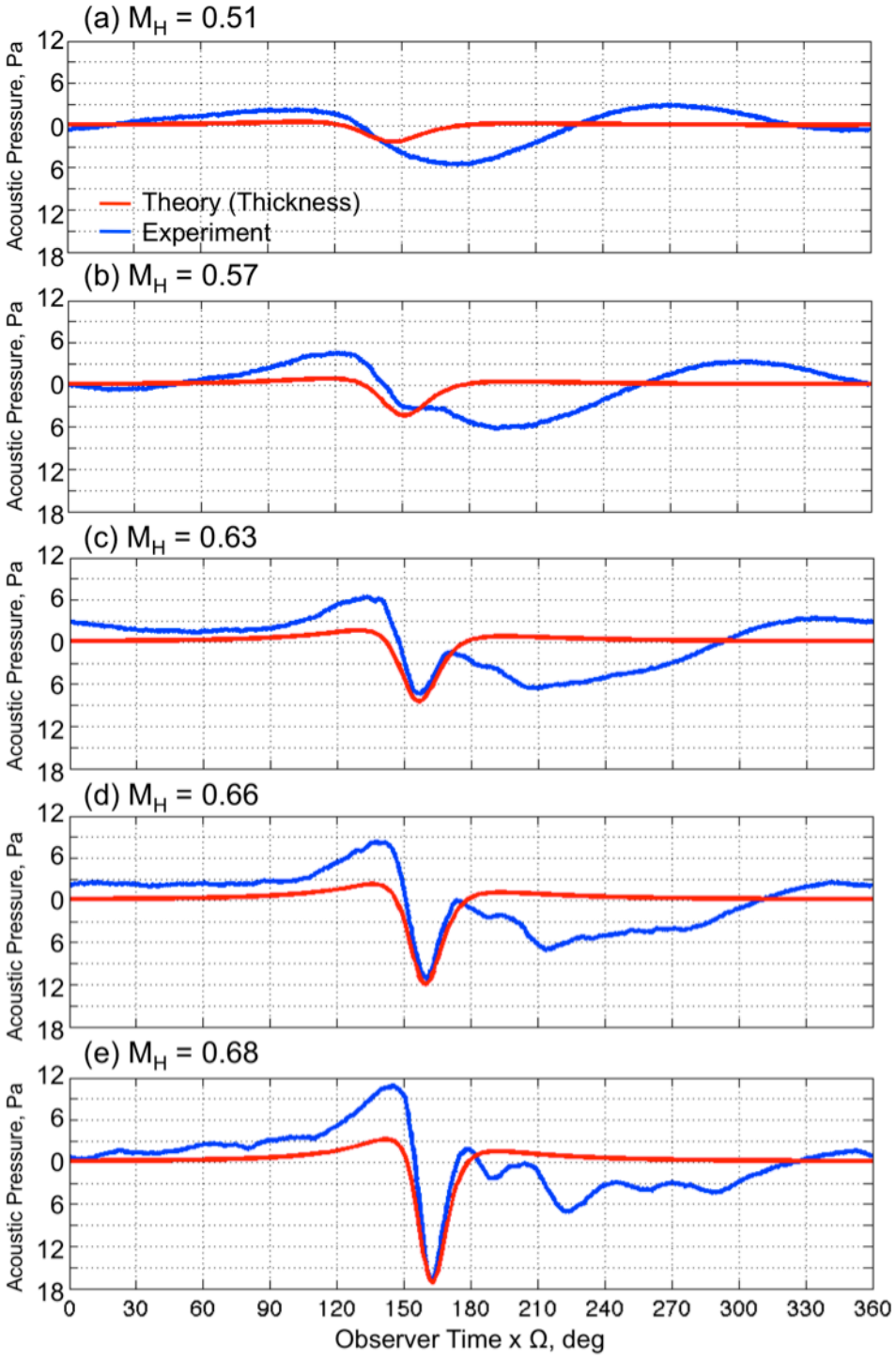

Figure 4-4: Measured and predicted noise at M1 as a function of M_H.

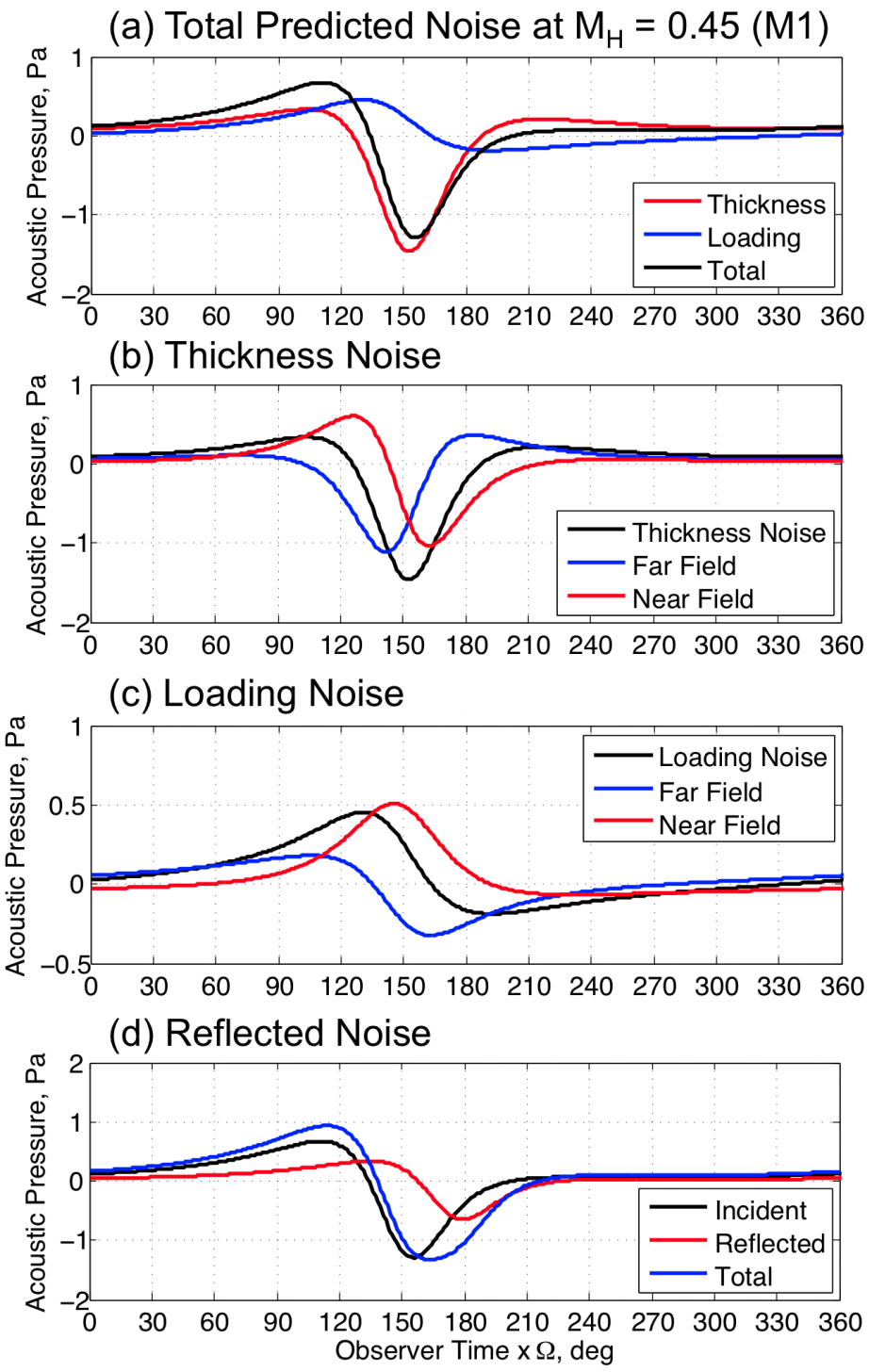

Figure 4-5: Total (a), thickness (b), loading (c) & reflected (d) noise (M_H = 0.45).

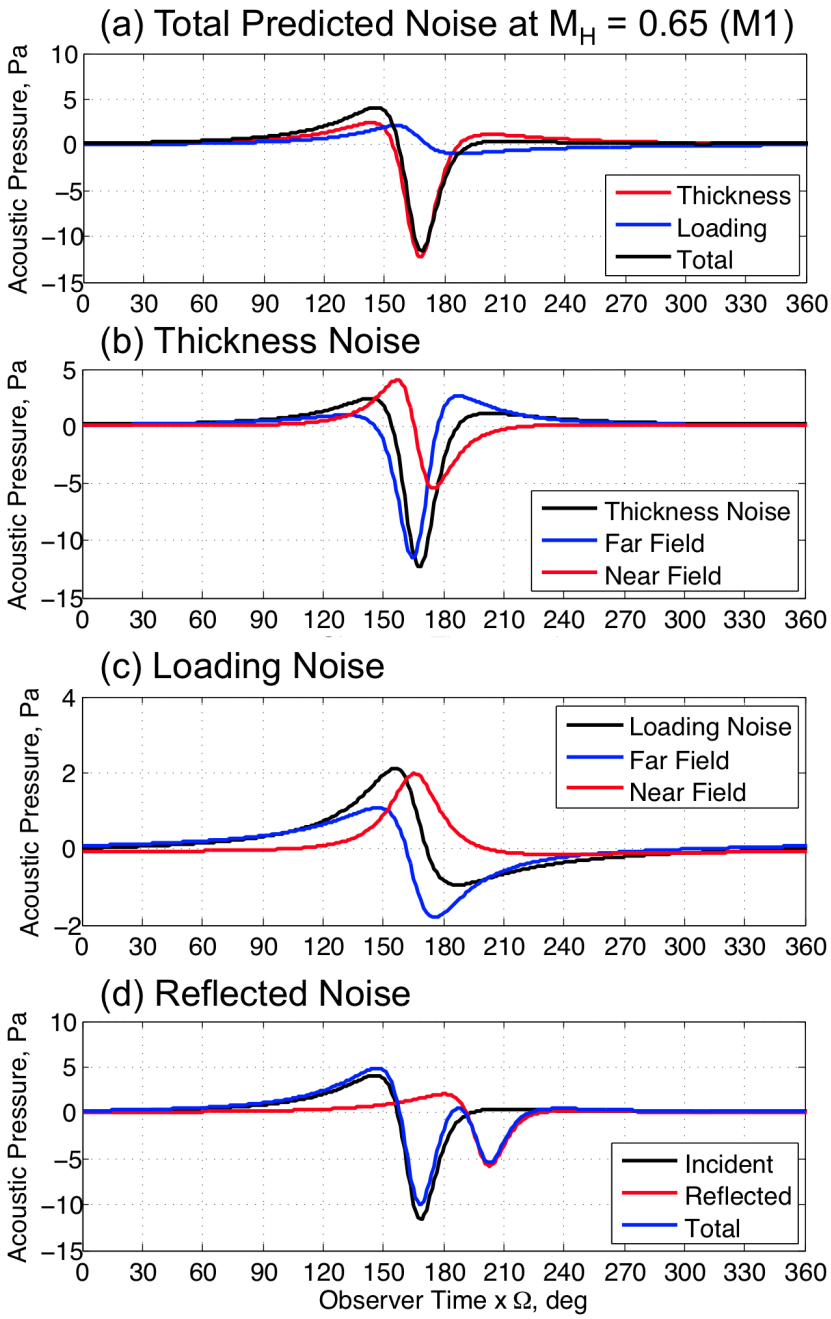

Figure 4-6: Total (a), thickness (b), loading (c) & reflected (d) noise (M_H = 0.65).

Referring again to Figure 4-4, the leading positive peak of the waveform and the time history after the main thickness negative pulse remains present at higher tip Mach numbers. To better understand these differences the measured data at a hover tip Mach number of M_H = 0.661 at all microphone positions is examined and compared with a predicted waveform that also includes an estimate of the loading noise.

Figure 4-7 shows the predicted (black) and measured (blue) waveforms. The red dashed line represents the standard deviation in the measurements used to generate the averaged time history and shows the data to be highly repeatable.

The pulse width and amplitude of the main LF-IPH pulse at microphone M1 are well captured by the theory. The leading, rising edge peak is however under predicted. In section 4.1 it was shown that the main contributors to this leading positive peak are the loading and near-field thickness noise. The discrepancy in this region is likely due to an under prediction of the loading noise.

The acoustic pressure after the main negative peak is also poorly predicted due to low frequency reflections occurring in the acoustic chamber. Figure 4-6 (d) shows similar behavior for a simplified reflective boundary condition. In reality, multiple reflections of varying magnitudes are likely to occur. Though undesirable, the Mach number is high enough to separate most of the reflected pulses from the main LF-IPH negative pulse, resulting in acceptable comparisons in the region of interest.

Microphone M2 shows similar behavior to M1. This is unsurprising given that they are approximately the same distance from the hub. Microphone M3 shows a slightly larger discrepancy in SPL. This may be due to an error in the calculated distance for M3 or due to differences in acoustic reflections at that microphone location. However, the negative peak amplitude and width remain well captured.

Finally, microphone M4 shows the measured and predicted noise 16° below the rotor plane where lower levels of thickness noise and a larger contribution from loading noise is expected. Once again the general shape amplitude of the measured noise is well captured by the theory.

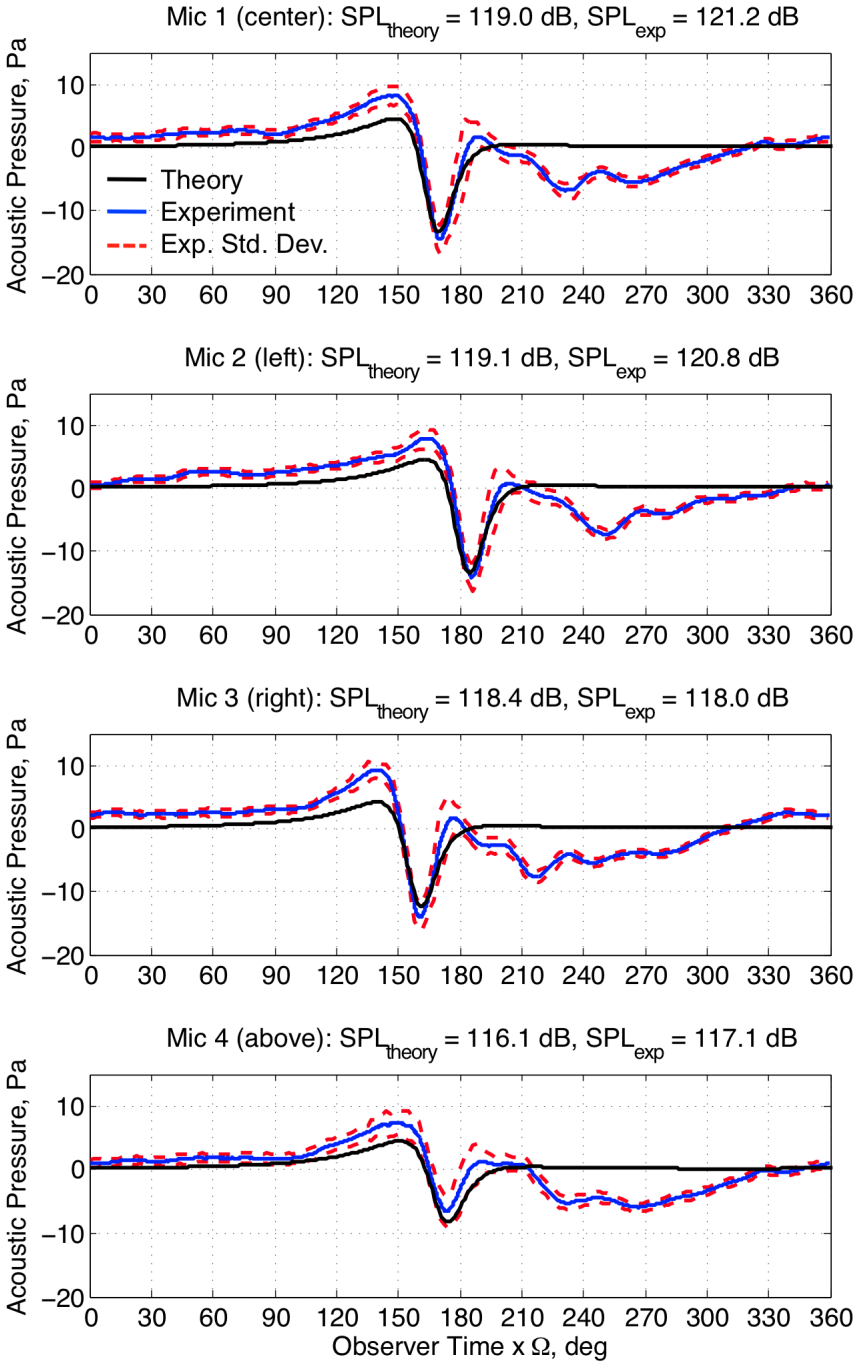

Figure 4-7: Pressure of ETR rotor noise theory and experiment (M_H=0.661).

Figure 4-9 shows the frequency spectra of the measured and predicted acoustic waves. The measured data (blue) contains a large 1/REV component and scalloping in the frequency content is likely representative of reflections within the chamber confirming the earlier hypothesis based on the time domain results. A time domain window can be applied to the measured waveform such that the acoustic pressure after the main negative peak is set to zero (Figure 4-8). This removes the majority of the reflected energy from the measured waveform. The frequency spectrum of the windowed data (red) then matches the predicted spectra more favorably.

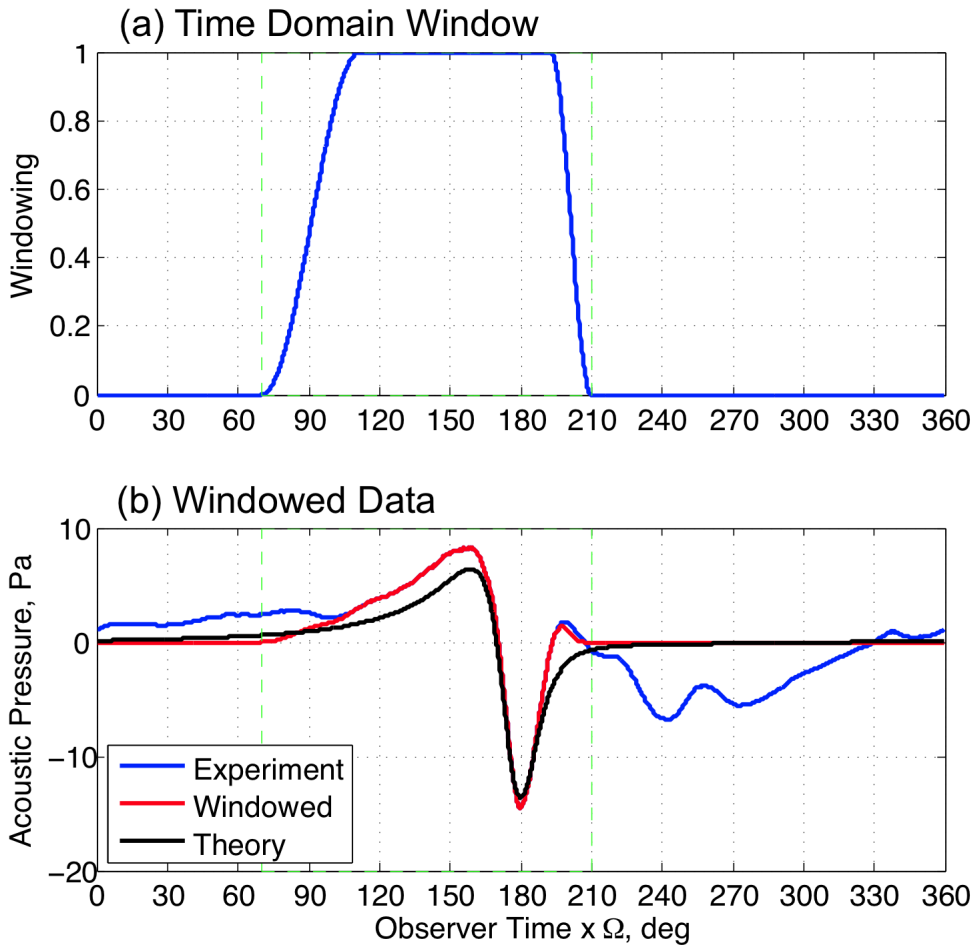

Figure 4-8: Windowed acoustic measurements.

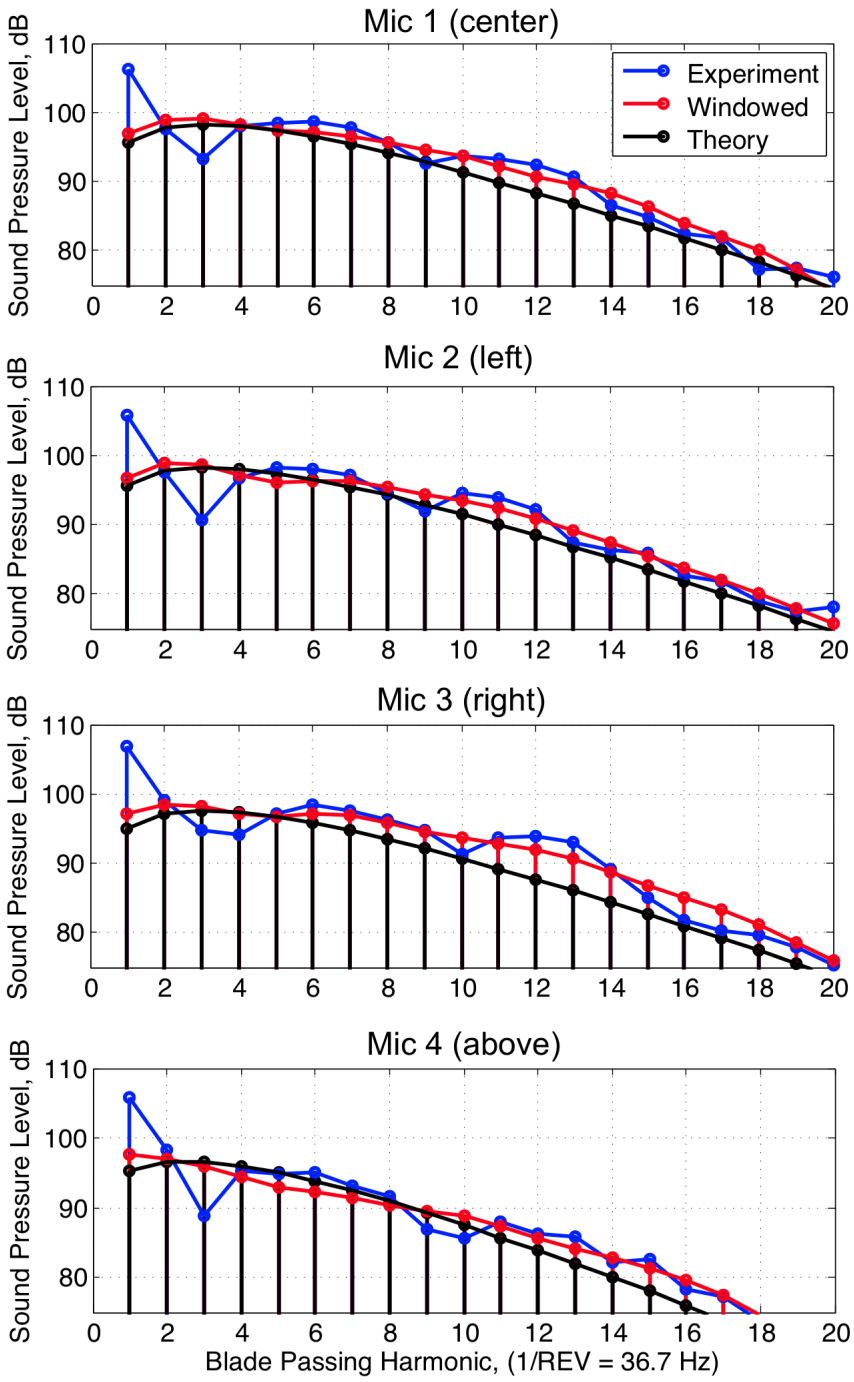

Figure 4-9: Frequency spectra of uncontrolled ETR noise theory and experiment.

4.3 Acoustic Measurement Quality Summary

The UMAC facility and AJAX ETR have been shown to produce repeatable and predictable levels of LF-IPH at a hover tip Mach number of 0.661. Though acoustic reflections and discrepancies in the leading positive peak of the LF-IPH are still visible at $M_H = 0.661$, the major features of the negative IPH peak correlate well with the predicted values. This result means that the UMAC facility and AJAX ETR can be used to explore the use of active jet acoustic control.

Chapter 5: AJAX Measurement and Prediction

In this chapter, acoustic measurements of the controlled experimental test rotor (ETR) are examined and compared with theoretical rotor noise predictions made using the model described in Chapter 2. The acoustic results for four active jet acoustic control cases are studied at a hover tip Mach number of 0.661. These cases include three single harmonic sinusoidal controls of the valve (2/REV, 3/REV and 4/REV) and a single pulse per revolution case. Results at four microphones are examined in both the time and frequency domain.

5.1 Active Jet Acoustic Control Modeling Summary

The anti-noise radiated by the active jet acoustic controller is predicted using the retarded time formulation (1A) of the FW-H equation, as described in Chapter 2. The jet, shown in Figure 5-1, is modeled as a single point source located at the non-dimensional chord-wise position of -0.28125 (2.125 inches from the leading edge) at the tip of the blade (r_{jet} = < 39.0”, -1.125”, 0 >). The jet is assumed to act at as a purely radial jet so α_{jet} = 0° with an orifice area of 0.333 in^2. The jet velocity is prescribed relative to the blade using hot-wire measurements of the exit flow through the non-rotating ETR as discussed in Chapter 3. Additional details on the jet model are found in Appendix C.

Table 5.1: ETR Active Jet Acoustic Control modeling parameters

Parameter	Value
r_{jet} (blade fixed)	< 39.0”, -1.125”, 0 >
α_{jet}	0°
A_{jet}	0.333 in^2

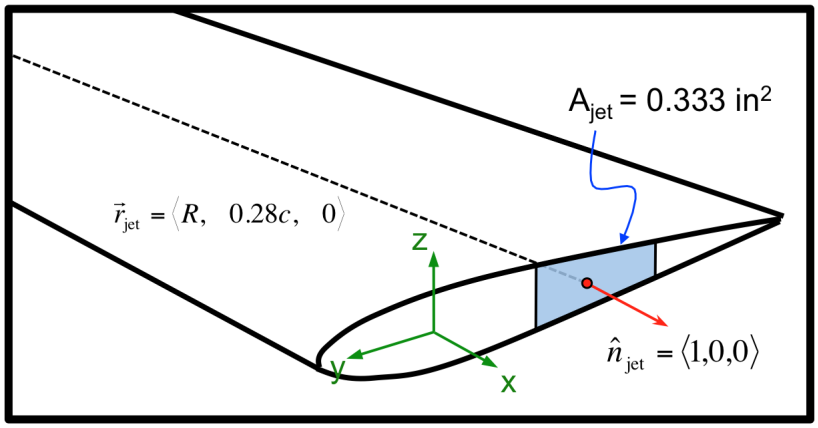

Figure 5-1: AJAX model discretization

5.2 Sinusoidal Valve Control

5.2.1 Pneumatic Valve Control System Output

Sinusoidal control of the valve is first evaluated. 2/REV, 3/REV and 4/REV sinusoidal controls of the valve (minimum at 5.5V and maximum at 10 V) are investigated at a rotor tip speed of M_H = 0.661 (1P = 36.6 Hz). For a steady state pneumatic system operating in its linear range, the application of 10 volts would open the valve orifice completely and the application of 5 volts would close the orifice. This was shown in the steady-state flow diagram in Section 3.2.2. The exit flow would respond linearly and instantaneously as a sinusoidal variation in jet exit velocity. However the dynamic behavior of the valve spool and unsteady effects of the air flowing through the AJAX ETR yield a markedly different result at the jet exit.

Figure 5-2 shows the valve control signal (a) and resultant hot-film velocity measurements (b) through the non-rotating AJAX ETR for all three sinusoidal control cases. The nonlinearity of the system is clearly evident. All three cases exhibit significant phase, amplitude, and pulse shape discrepancies between the voltage input and the

velocity output. The end result is that the duration of the rising edge of the waveform, which is largely responsible for determining the pulse width and amplitude of the anti-noise pulse, is shorter than desired. The acoustic implications of this shortened duration are evident in the following discussion.

The phase relationship between the jet control and output indicates that in order to aim the controller to produce a positive peak at the target microphone (M1), a phase adjustment is required. It was shown in Chapter 2 that an increase in jet velocity occurring at a phase angle corresponding to the position at which the radiation vector (jet to observer) and source vector (hub to source) are nearly perpendicular is desirable. For each controller this angle was used as a starting point during testing. The phase was then adjusted until the control noise positive peak and rotor noise negative peak were in phase with each other.

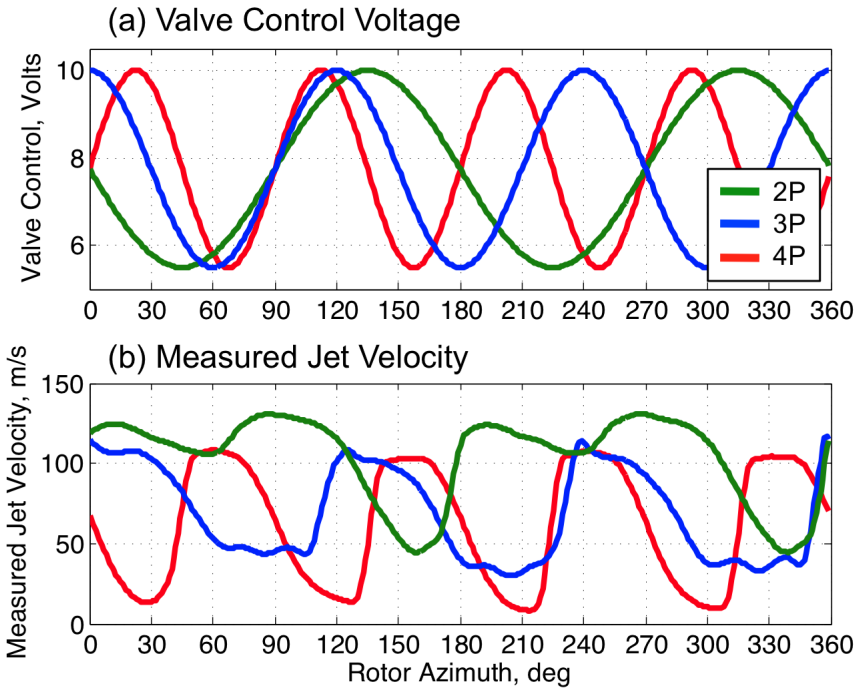

Figure 5-2: Sinusoidal valve control (a) and measured output (b).

5.2.2 2/REV valve control acoustic results

The voltage control signal and measured jet exit velocity of the 2/REV valve control is shown in Figure 5-3 with the same phase that was used during acoustic testing. The control was shifted by -75 degrees in order to move the peak velocity time rate-of-change into a desirable location (ψ_{azi} = 90° - 100°) for maximum effectiveness at the target microphone, M1.

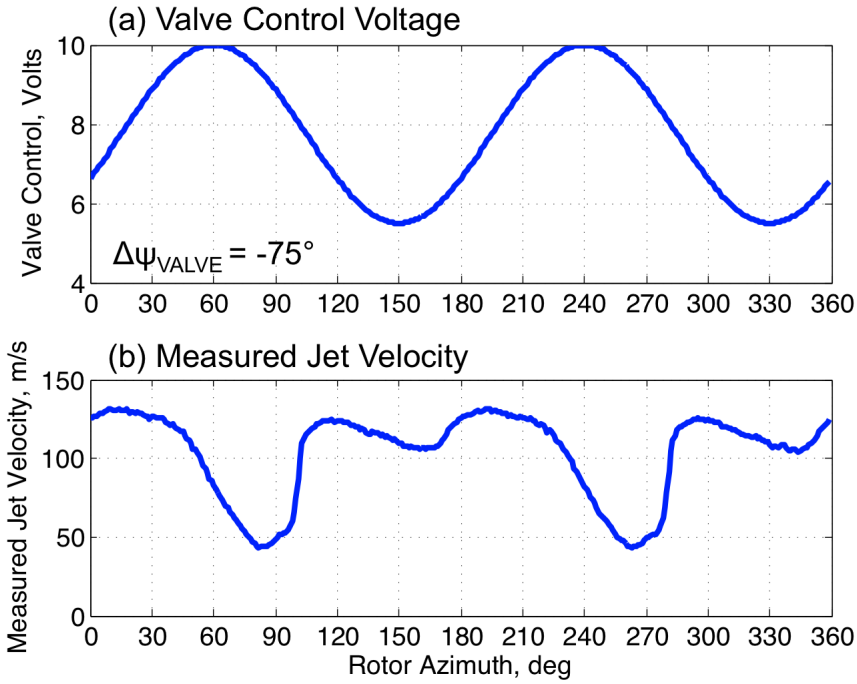

Figure 5-3: 2/REV sinusoidal valve control and measured velocity.

Though this control isn't ideal for large LF-IPH noise reductions (due to the short duration of increasing velocity), Figure 5-4 shows that the 2/REV control does result in a change to the measured acoustic time history at all four microphones. The anti-noise pulse, shown in blue, is calculated by subtracting the measured noise of the baseline uncontrolled rotor (red) from the measured noise of the controlled rotor (black).

At the target microphone, M1, the control noise pulse width is wide enough to reduce the negative peak amplitude by approximately 5 Pa. At M2 and M3 the signal has shifted off of the peak center, occurring earlier in M2 and later in M3. This is because the control was phased to be most effective at M1. Since M2 is to the left of M1, the resulting anti-noise occurs too early in observer time. Similarly, since M3 is to the right of M1, the control occurs after the main negative peak in observer time.

The primary purpose of the acoustic testing is to validate the theoretical model. The velocity measurement shown in Figure 5-3 is used as the prescribed jet velocity input for the analytical model and compared to the measured data. Figure 5-5 shows this comparison to be quite good. The model captures the anti-noise pulse width and amplitude well at all four microphones, including the near-plane M4. A slight over prediction of the peak amplitude may be due to the averaging process used for the measured data or smoothing of the jet flow (due to blade rotation).

In both the measured and predicted time histories it is apparent that the pneumatic system output isn't ideally suited for large reductions in LF-IPH. Despite reducing the peak amplitude slightly at M1, the controller generally increases the high frequency content of the waveform. This is evident in the frequency spectra of the measured and predicted waveforms (Figure 5-6 and Figure 5-7). Once again the data is windowed to reduce the scalloping associated with reflections. The un-windowed spectra can be found in Appendix D. The red and black data points represent the frequency amplitudes of the uncontrolled and controlled noise respectively. The blue shows the frequency spectrum of the anti-noise waveform itself.

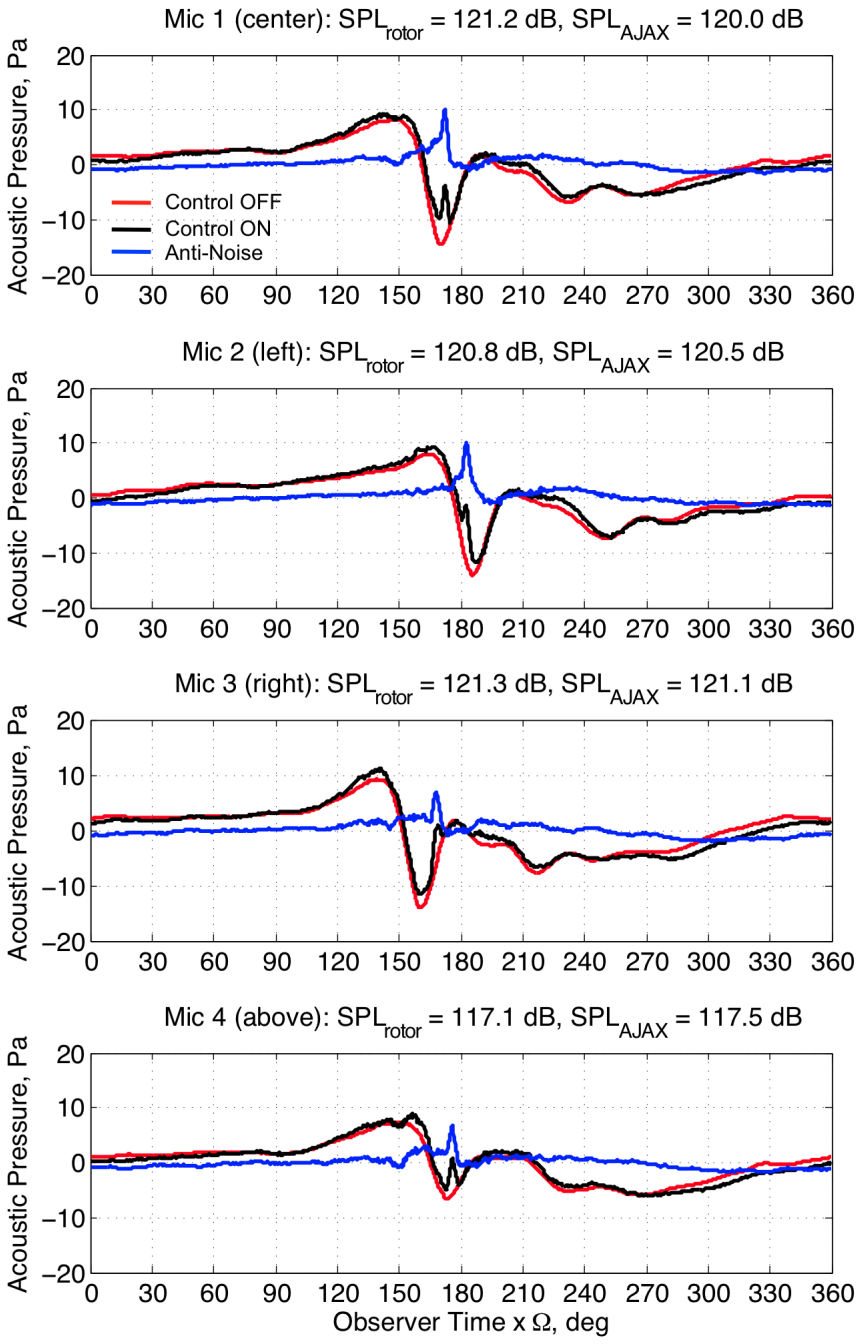

Figure 5-4: 2/REV control measured acoustic time history at M_H=0.661.

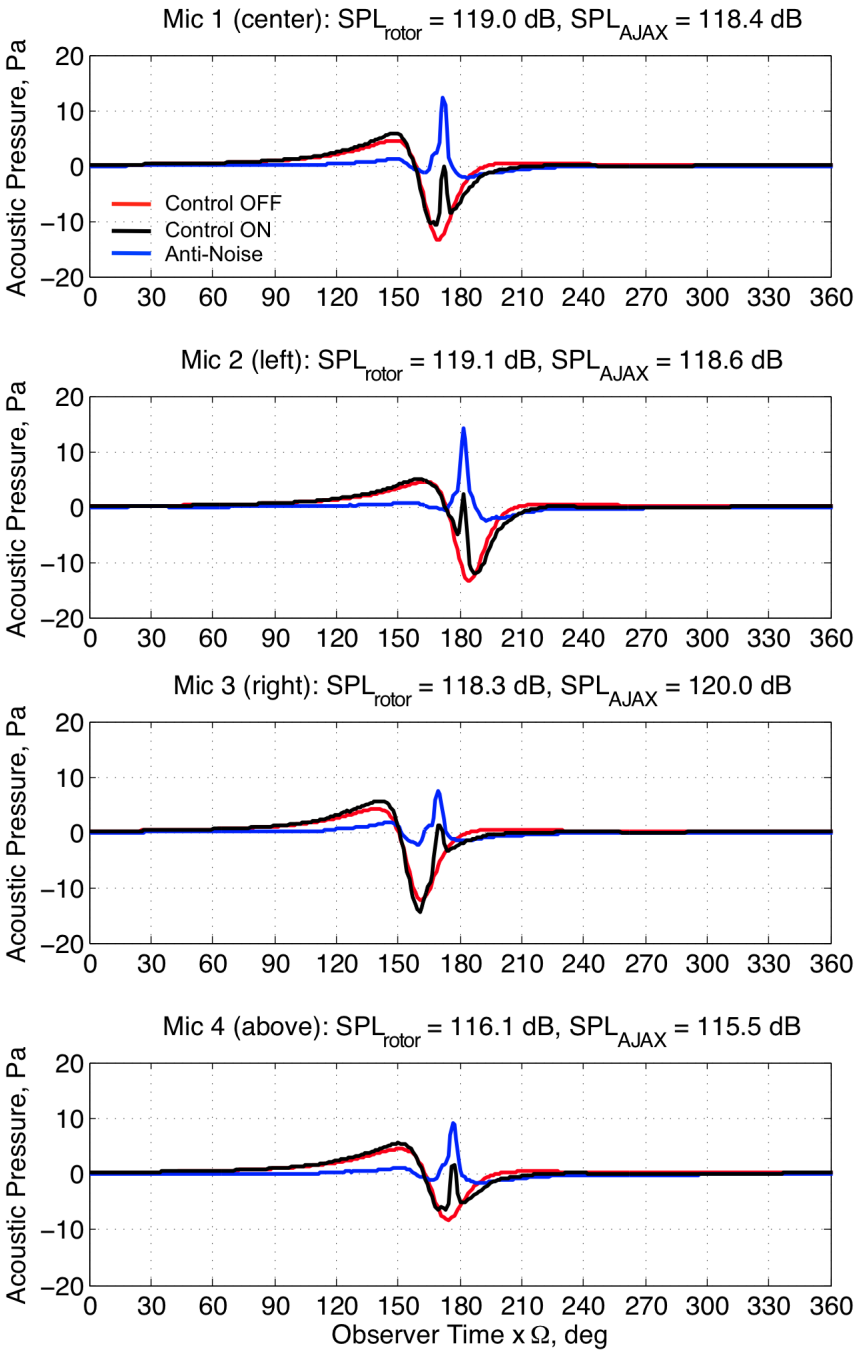

Figure 5-5: 2/REV control predicted acoustic time history at M_H=0.661.

The trends in frequency content between the predicted and measured waveforms for the anti-noise are similar at all four microphones. The first harmonic amplitude is increased slightly and the 2nd and 3rd harmonics exhibit almost no change at all. The harmonic amplitude is decreased by 1 to 6 dB for the 4th through 20th harmonics at microphone M1 in the measured data. A smaller impact is observed at M2 and M3. For all four microphones the cross over point between the controlled and uncontrolled noise occurs at a lower frequency in the prediction than in the measurement. This is possibly due to existing artifacts from acoustic reflections and the averaging process.

One of the more important lessons learned from examining the frequency spectrum is that time domain analysis is significantly more useful in determining a controller's effectiveness as it allows for a fast and easy visual inspection of the phase relationship between the anti-noise and rotor noise peak amplitudes. Despite this, frequency analysis does highlight how a controller can be designed to manipulate certain frequency ranges instead of the peak value and has important ramifications for decreasing the detection distance of aircraft.

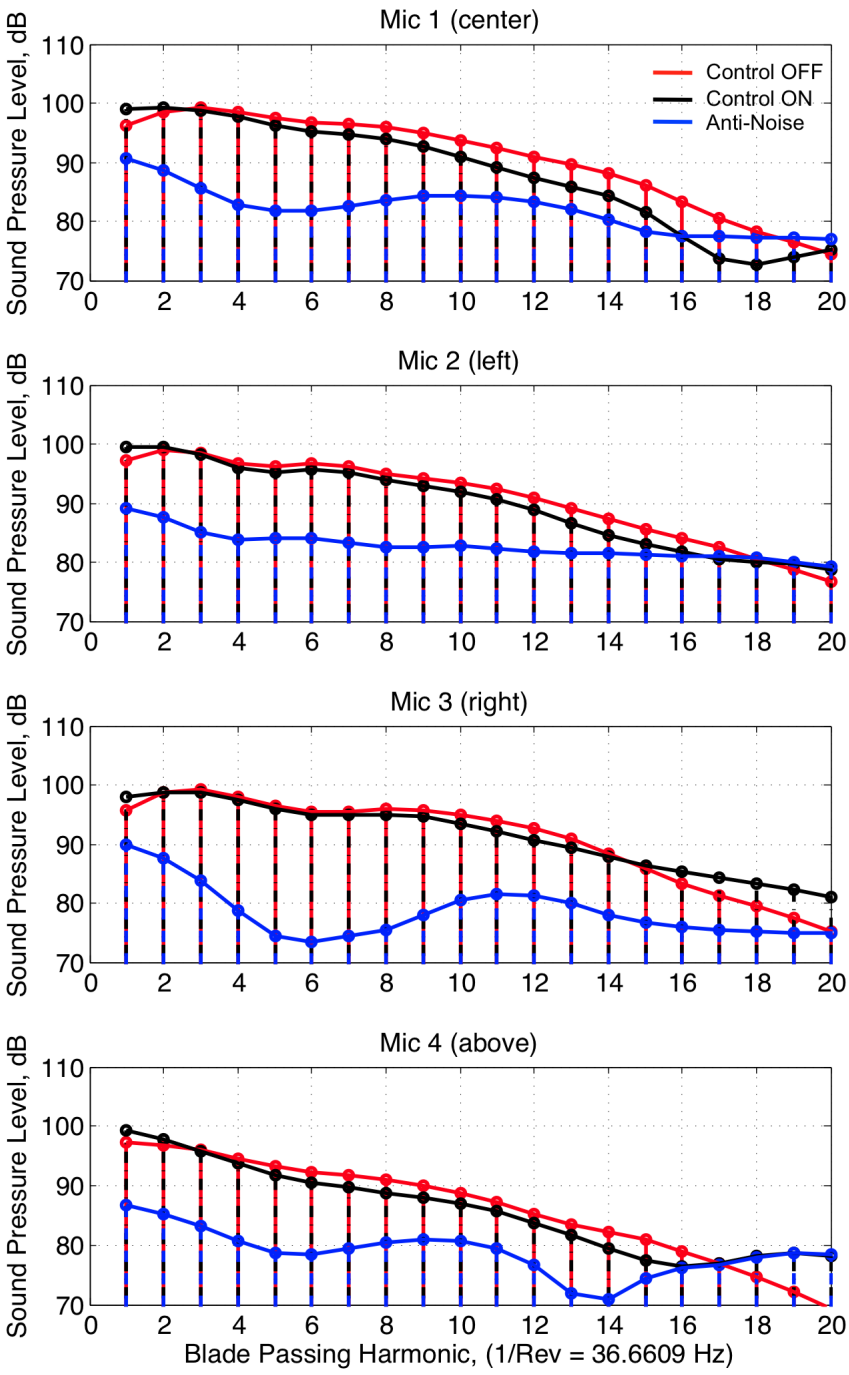

Figure 5-6: 2/REV control measured frequency spectra.

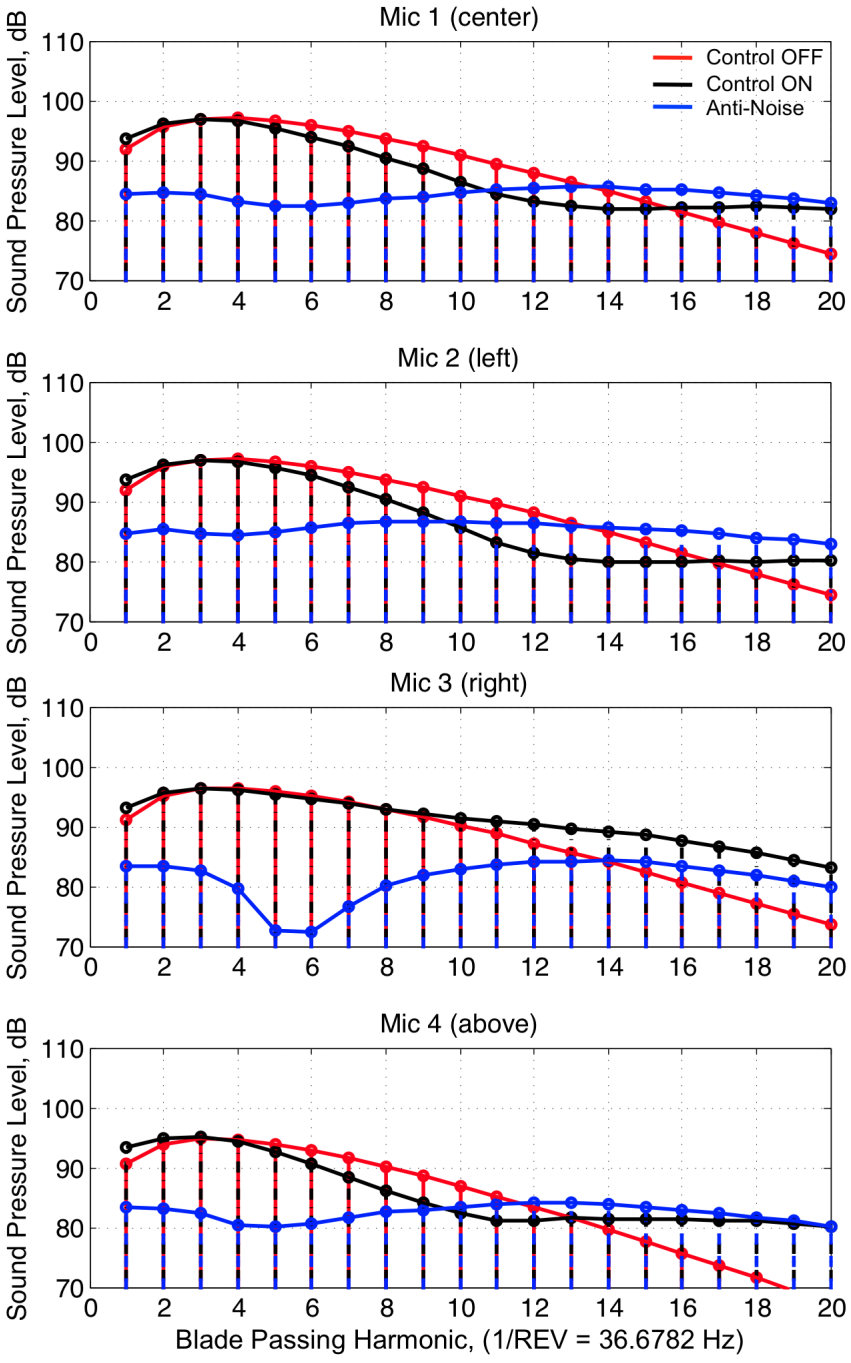

Figure 5-7: 2/REV control predicted frequency spectra.

5.2.3 3/REV valve control acoustic results

The 3/REV valve voltage control and measured jet exit velocity are shown in Figure 5-8 with the same phase that was used during acoustic testing. The control was shifted by -10 degrees.

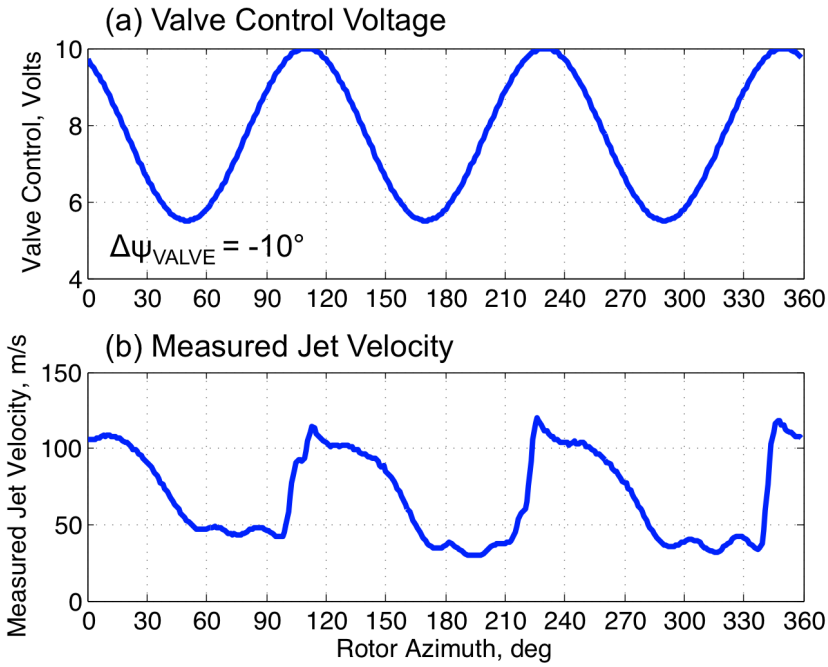

Figure 5-8: 3/REV control and measured velocity.

For the remainder of this chapter only relevant time and frequency domain data are presented. The full set of data for all microphones can however be found in Appendix E. The primary focus is on the target (M1) acoustic measurements and predictions, as shown in Figure 5-9. Once again the theory is well correlated with the measured data. The peak amplitude of the anti-noise pulse is larger than the 2/REV case. Similarly, the pulse width has been reduced. The frequency content, shown in Figure 5-10, is also well correlated though the measured data shows larger reductions in the 4^{th} through 20^{th} harmonics. Decreases of approximately 9 dB are seen at some of the higher frequencies. Once again very little change is made to the first 3 harmonics. Altering these harmonics for a single bladed rotor is very difficult.

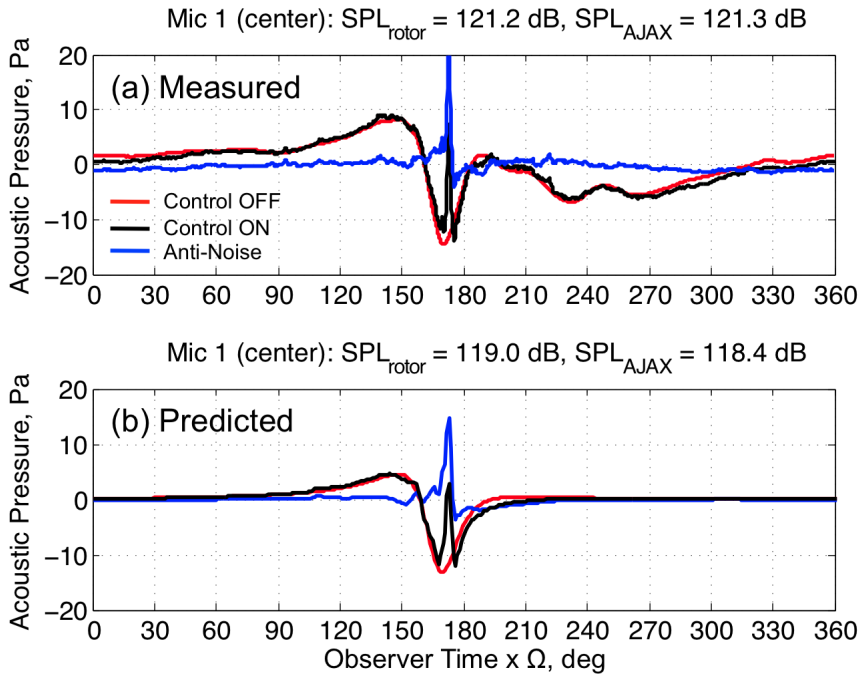

Figure 5-9: 3/REV control experiment (a) and theory (b) acoustic pressure (M1).

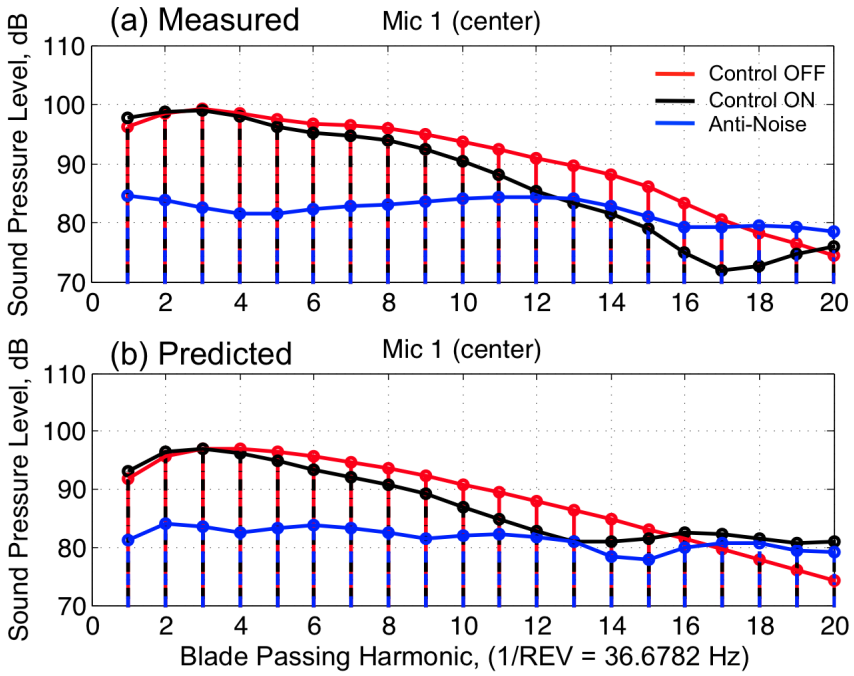

Figure 5-10: 3/REV control experiment (a) and theory (b) frequency spectra (M1).

5.2.4 4/REV valve control acoustic results

The 4/REV valve voltage control and measured jet exit velocity are shown in Figure 5-11. The control was shifted by -30 degrees for this case.

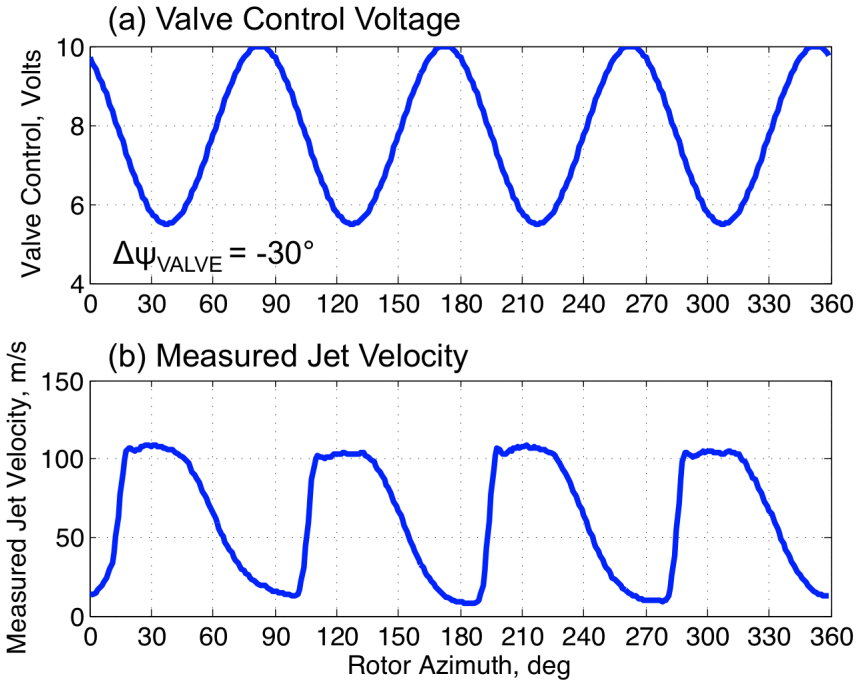

Figure 5-11: 4/REV sinusoidal valve control and measured velocity.

Figure 5-12 shows that the theory is once again well correlated with the measured data. The peak amplitude of the main anti-noise pulse is now bigger than for the 2/REV and 3/REV cases due to the increase in velocity time-rate-of-change on the advancing side of the rotor. In addition to the main pulse, off-target perturbations in the waveform are present before and after (Ωt_{obs}=130° and 270°) the main IPH pulse. These small peaks are associated with increases in jet velocity occurring at ψ_{azi} = 15° and ψ_{azi} = 200° (in Figure 5-12 (b)). The frequency content, shown in Figure 5-13, is well correlated. Once again, the measured data shows larger reductions in the 4th through 20th harmonics than is evident in the predicted data.

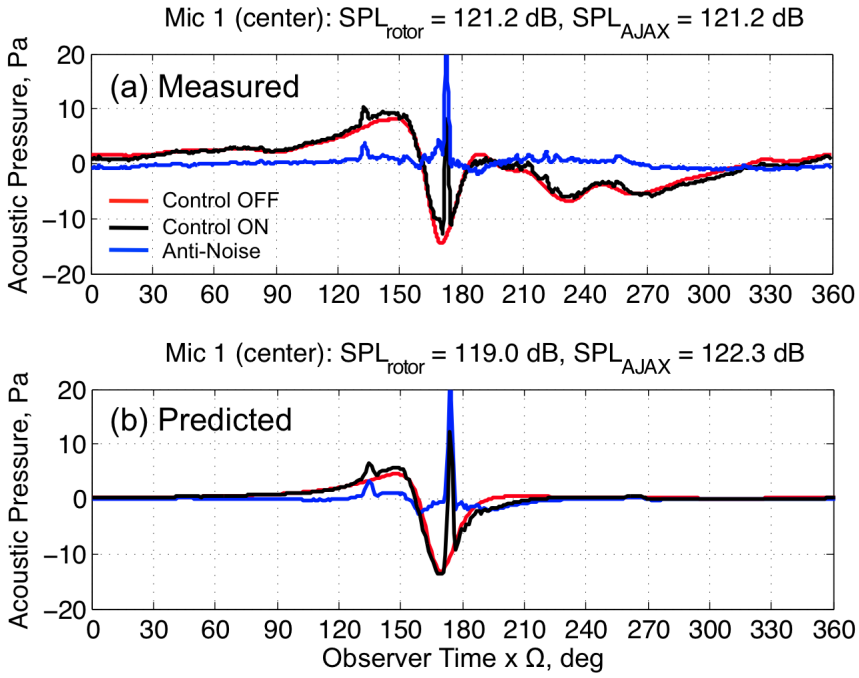

Figure 5-12: 4/REV control experiment (a) and theory (b) acoustic pressure (M1).

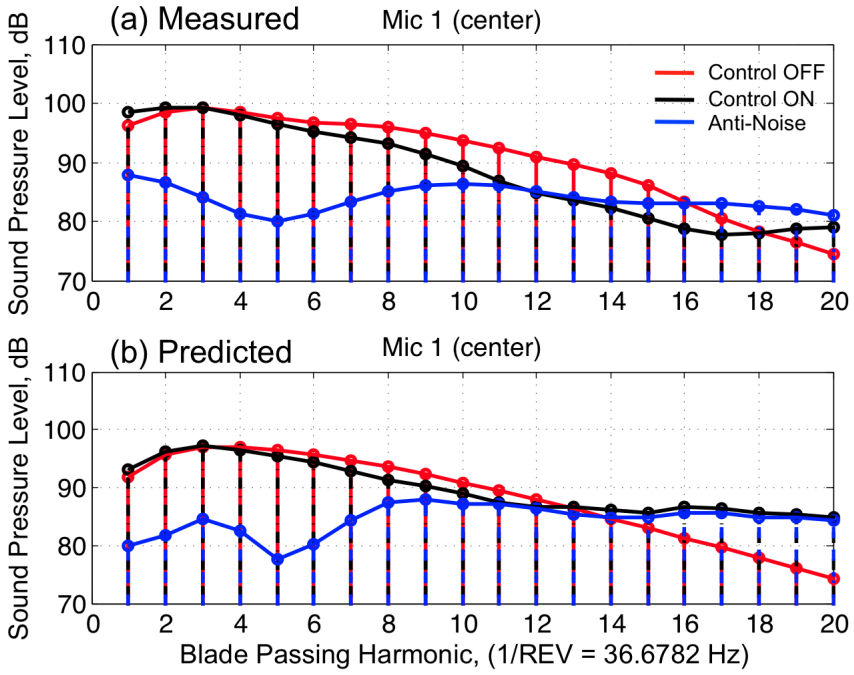

Figure 5-13: 4/REV control experiment (a) and theory (b) frequency spectra (M1).

5.2.5 Sinusoidal Valve Control Summary

The sinusoidal valve control cases examined in this section have indicated that the theoretical model described in Chapter 2 does a good job of predicting the anti-noise in both the time and frequency domain. To further highlight how good this comparison is, Figure 5-14 shows a close-up of the predicted and measured anti-noise for all three cases along with the standard deviation of the measured dataset. The theory captures not only the main pulse but also any acoustic perturbations before and after. As the time-rate-of-change of the jet velocity is increased, the amplitude of the anti-noise pulse becomes larger while the pulse width reduces. However, despite having larger peak amplitudes, the 3/REV and 4/REV controllers are outperformed by the 2/REV control in terms of LF-IPH peak reduction. This highlights the fact that large peak amplitudes do not always provide the largest noise reduction but rather that a careful compromise between amplitude and pulse width must be made when choosing a controller.

These cases also show that the 4^{th} through 20^{th} harmonics exhibit the largest reductions at the target microphone. Due to the sharp pulse width of the anti-noise, increases in the higher frequencies are also observed. For all cases very little change in the first 3 harmonics are evident. This is revisited briefly at the end of this chapter.

The higher frequency sinusoidal controls also indicate that the periodic nature of the control does affect off-target noise levels. This was seen in Chapter 2 for the theoretical rotor and is manifested in the measured data as the small bumps in acoustic pressure before and after the main IPH pulse. In order to minimize this effect, it was proposed in Chapter 2 that a single pulse per revolution control be used.

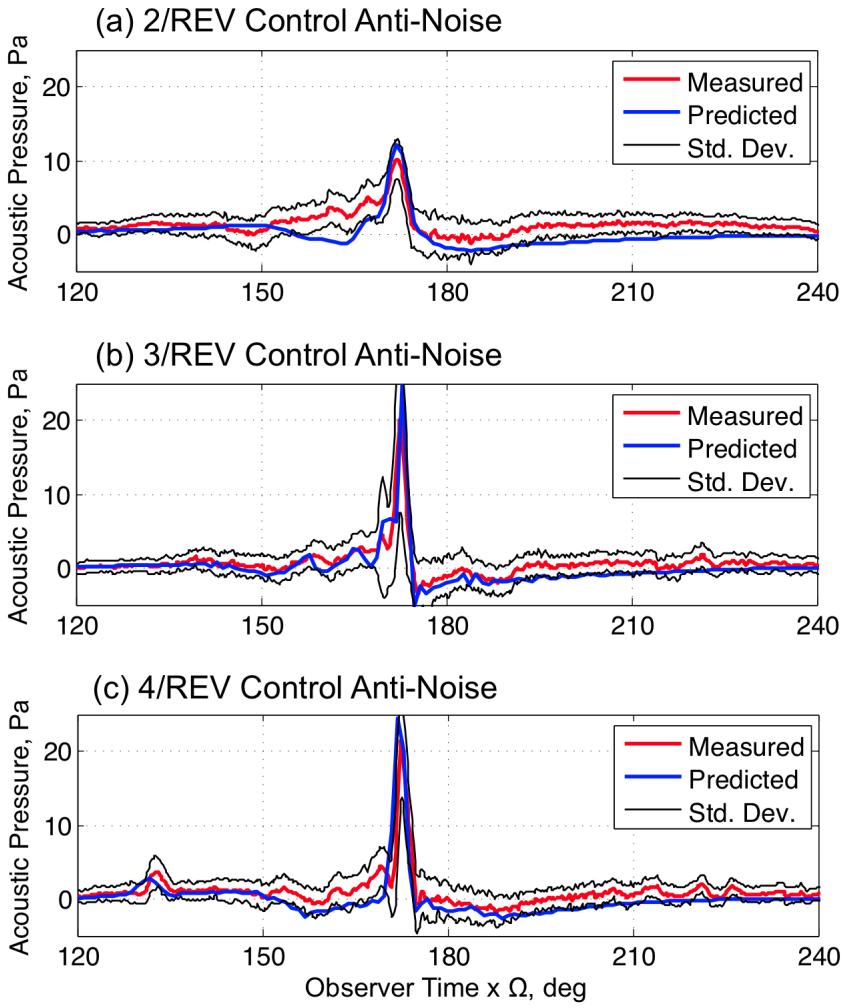

Figure 5-14: Measured and predicted anti-noise for 2/REV, 3/REV, and 4/REV.

5.3 Single Pulse Valve Control

5.3.1 Pneumatic Valve Control System Output

The acoustic affect of a control in which a single pulse of air is released once per revolution is now explored. This control would be preferred in a real world implementation of the AJAX concept because of the reduced affect on off-target in-plane noise levels and the reduction in the total amount of required airflow. The valve is driven with a voltage signal that opens over 60 degrees of rotor azimuth (as would a 3/REV

sinusoidal control), remains open for 10 degrees of rotor azimuth and closes slowly over 120 degrees (as would a 1.5/REV sinusoid). The resultant control and measured jet exit velocity is shown in Figure 5-15. Once again, the phase of the control shown in the plot is the same as was used for the experiment and prediction (-90 deg.).

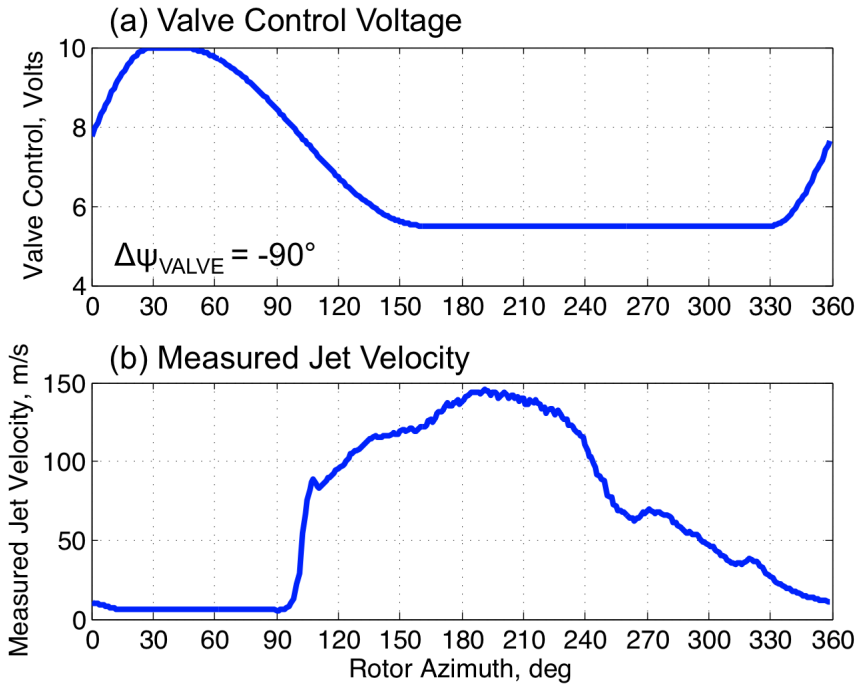

Figure 5-15: Single pulse valve control and measured velocity.

5.3.2 Single pulse valve control acoustic results

The measured and predicted acoustic pressures at M1 are shown in Figure 5-16. The peak amplitude and width are similar to that seen for the 3/REV sinusoidal control, as expected since the rising edge slope of the jet velocity for both controls is similar. The frequency content of the radiated noise is also quite similar, as seen in Figure 5-17. Reductions in the 4th through 20th harmonics of between 1 and 4 dB are observed. A slight increase in the first harmonic and very little change to the 2nd and 3rd harmonics are also once again present.

The time and frequency data at M2 is also shown (Figure 5-18 and Figure 5-19). Though the control has very little effect on the peak amplitude of the noise in the time domain at this location, the frequency spectrum shows that large reductions (up to 10 dB) in the higher frequency content (8^{th} to 18^{th} harmonics) are observed. This interesting result shows the importance of examining both the time history and frequency spectrum when evaluating the performance of acoustic controllers in future work.

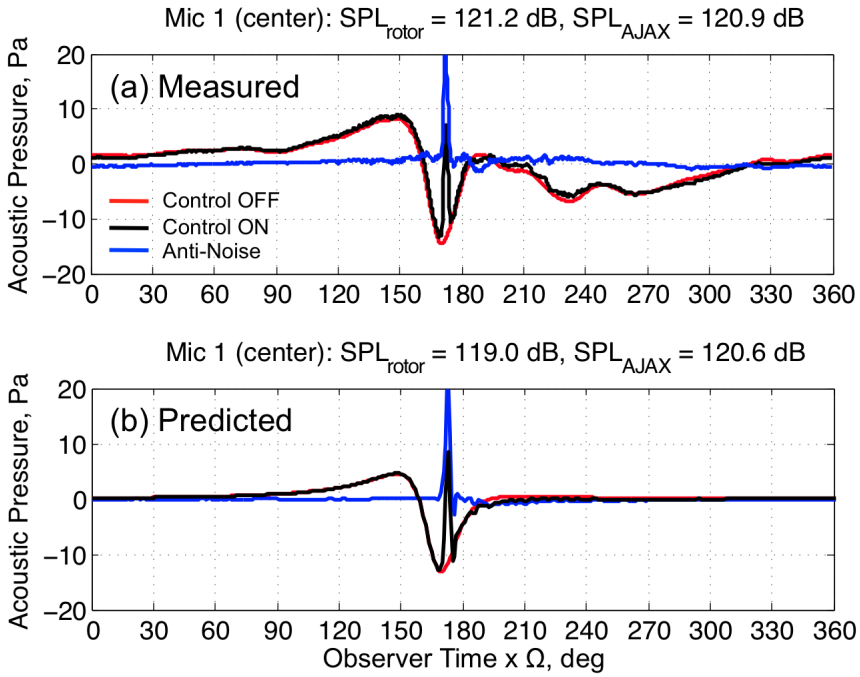

Figure 5-16: Pulse control experiment (a) and theory (b) acoustic pressure (M1).

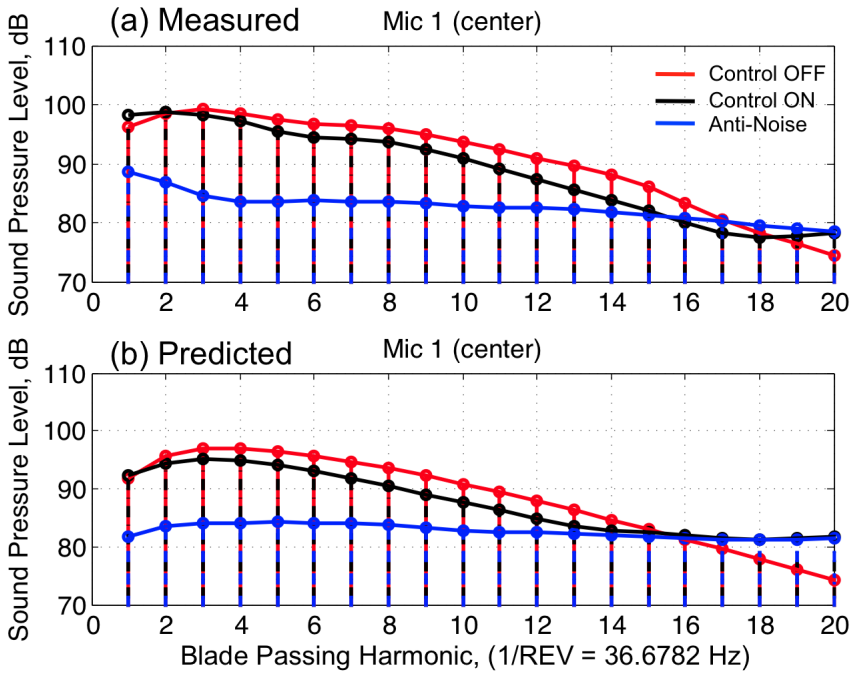

Figure 5-17: Pulse control experiment (a) and theory (b) frequency spectra (M1).

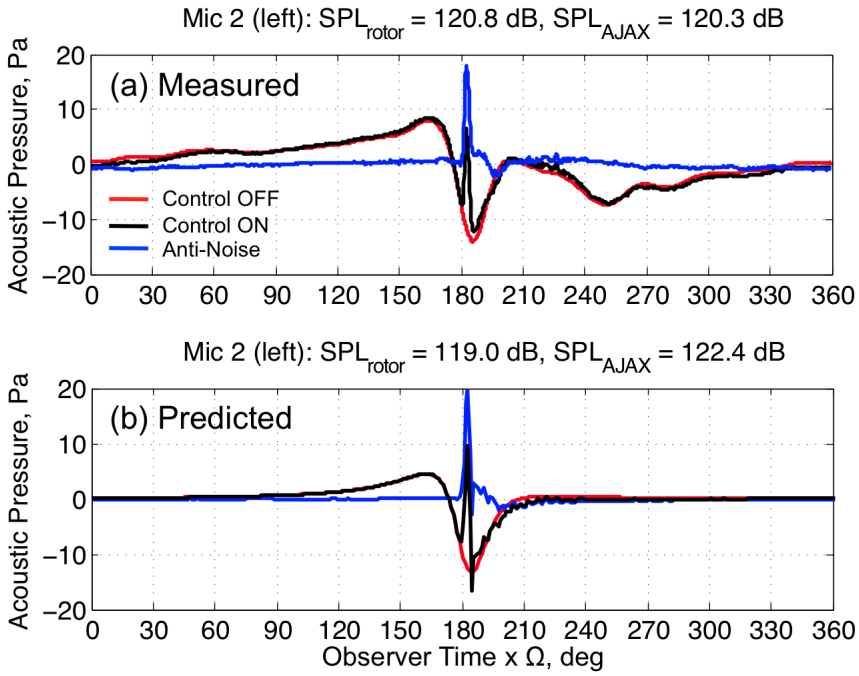

Figure 5-18: Pulse control experiment (a) and theory (b) acoustic pressure (M2).

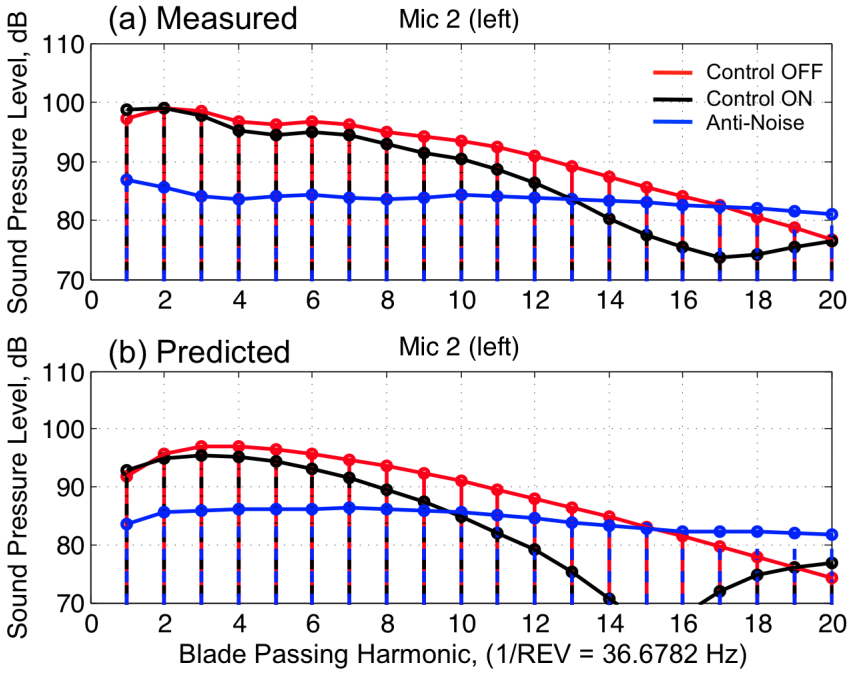

Figure 5-19: Pulse control experiment (a) and theory (b) frequency spectra (M2).

5.3.3 Single pulse valve control summary

A close up of the comparison between theory and experiment is shown below in Figure 5-20 with the standard deviation of the measured dataset (in black). The pulse width and amplitude are once again well predicted by the theory.

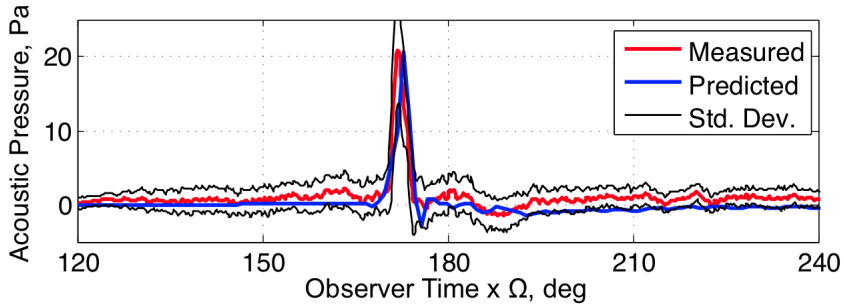

Figure 5-20: Measured and Predicted anti-noise for single pulse control.

The largest benefit that a single pulse valve control has over the sinusoidal control is that it has less of an effect on off target noise levels. Due to the acoustic chambers physical limitations, measuring the off-target noise over a wide range is difficult. Instead the predicted in-plane anti-noise for the 3/REV sinusoidal and single pulse controls is

compared. The same phase as used during testing is once again used. Figure 5-21 and Figure 5-22 show the peak-to-peak amplitude of the anti-noise as a function of observer location (a) and the corresponding observer time at which the anti-noise peak occurs (blue) (b) for the two controllers. Also shown in figure (b) is the observer time at which the negative peak of the rotor IPH occurs. When the two lines interest the controller can be thought of as "in phase" at that location.

Both cases exhibit similar behavior near the target location (M1). However the 3/REV control continues to generate a significant amount of noise away from the target. The single pulse control alleviates this to a large extent. The off-target peak values are reduced and the control becomes more localized.

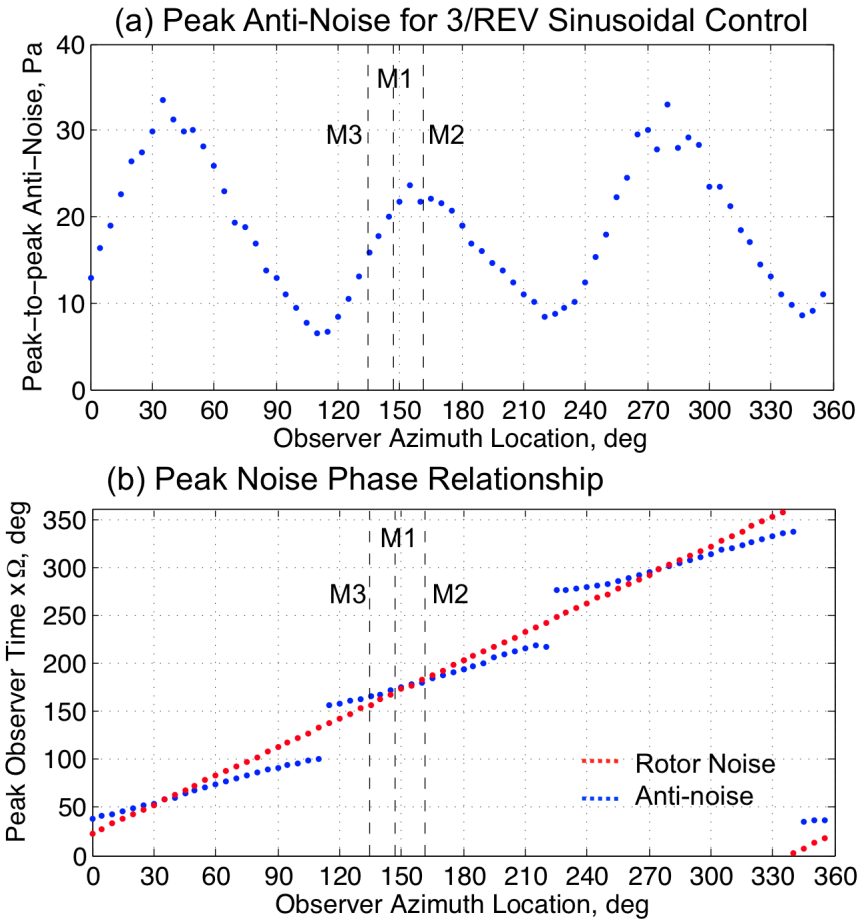

Figure 5-21: Predicted 3/REV anti-noise characteristics versus observer location.

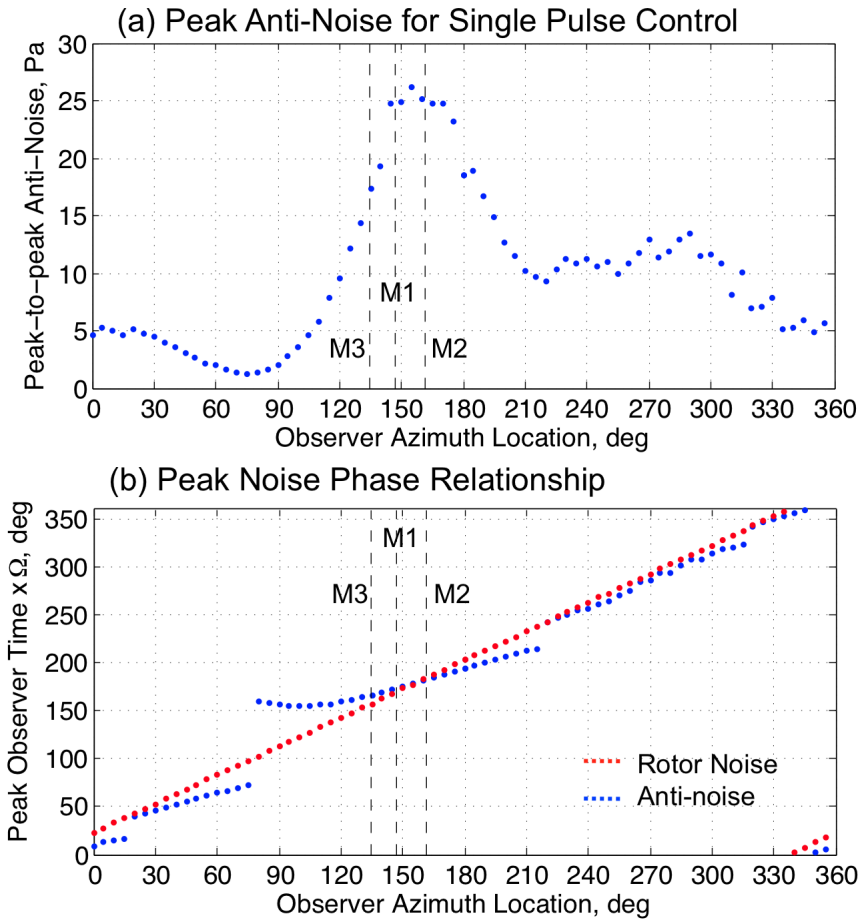

Figure 5-22: Predicted single pulse anti-noise characteristics.

5.4 Additional Observations and Comments

5.4.1 Mass and momentum source contributions to anti-noise

The theoretical model developed in this work includes both the mass and momentum source mechanisms associated with the subsonic air jet. Though it is impossible to separate these effects from one another in the measured data, their relative importance can be seen using the predicted waveforms. Figure 5-23 shows the theoretical mass (a) and momentum (b) source noise at microphone M1 for the 2/REV sinusoidal

valve control. Both the near and far-field terms are included and indicate that the near-field control noise is negligible at this distance. The amplitudes of both pulses are also similar and their relative phasing results in a total anti-noise waveform that benefits almost equally from both sources. This highlights the importance of using both terms when modeling the acoustic performance of active jet acoustic controllers.

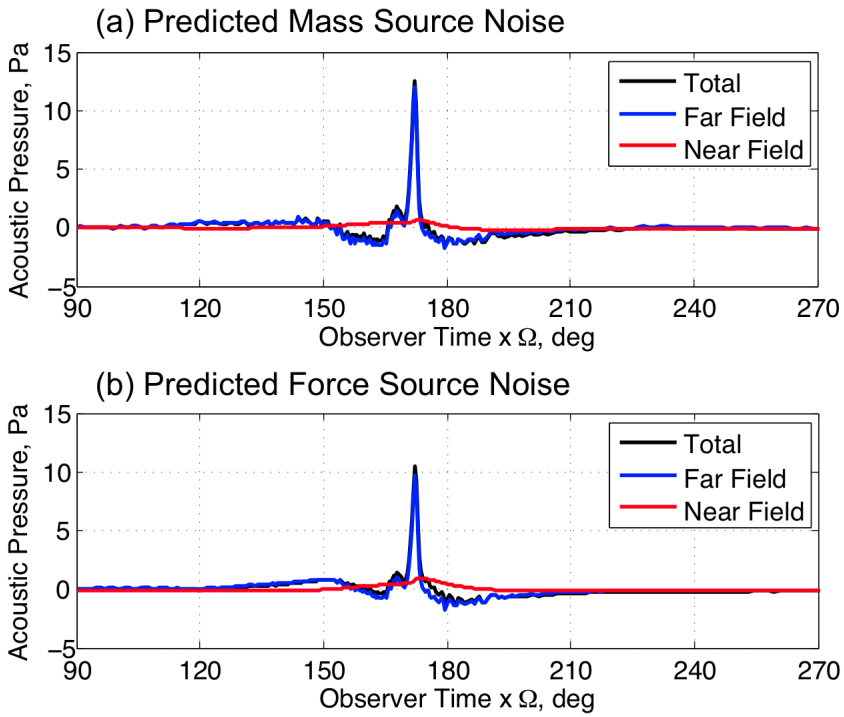

Figure 5-23: 2/REV control mass (a) and momentum (b) source noise (M1) .

5.4.2 Limitations of the pneumatic valve control system

The failure to produce an acoustic control anti-noise that dramatically reduces the LF-IPH of the ETR was largely due to difficulties associated with the sub-scale pneumatic valve system and the inability to generate sustained periods of rapidly increasing flow. Due to the dynamic limitations of the valve and pneumatic systems in general, obtaining perfect exit flow profiles is very difficult. In each of the control cases explored it is evident that as the jet velocity approaches 100 m/s, the nature of the flow

rate changes abruptly due to both choking of the valve and compressibility effects within the system. The net acoustic result of this is a narrow anti-noise pulse. Considerable effort was made to improve the system output but desirable waveform could not be achieved. In future work, improvements the pneumatic valve control system should be made. The incorporation of PID control, additional valves or larger capacity valves will result in improved jet velocity time histories. It should also be noted that in larger scale testing, valve complications might be reduced due to lower actuation frequency requirements.

As a final point, an example of what might be achieved experimentally with an improved pneumatic controller is shown in Figure 5-24. The predicted result for a pure 3/REV sinusoidal control with similar peak flow rates as obtained in the experiment is show in Figure 5-24 (a). The resultant anti-noise pulse has roughly 50% mass and 50% momentum source noise contributions (Figure 5-24 (b)). The resultant reduction in noise (ΔSPL = 5.5 dB) is shown in Figure 5-24 (c) and finally, the frequency spectra is shown in Figure 32(d). The increase in the period of time during which the velocity is increasing results in a wider pulse that more effectively reduces the peak negative amplitude of the LF-IPH. The frequency spectra also show that dramatic reductions in the lower frequencies may be realized if a control profile of this nature can be produced in the laboratory.

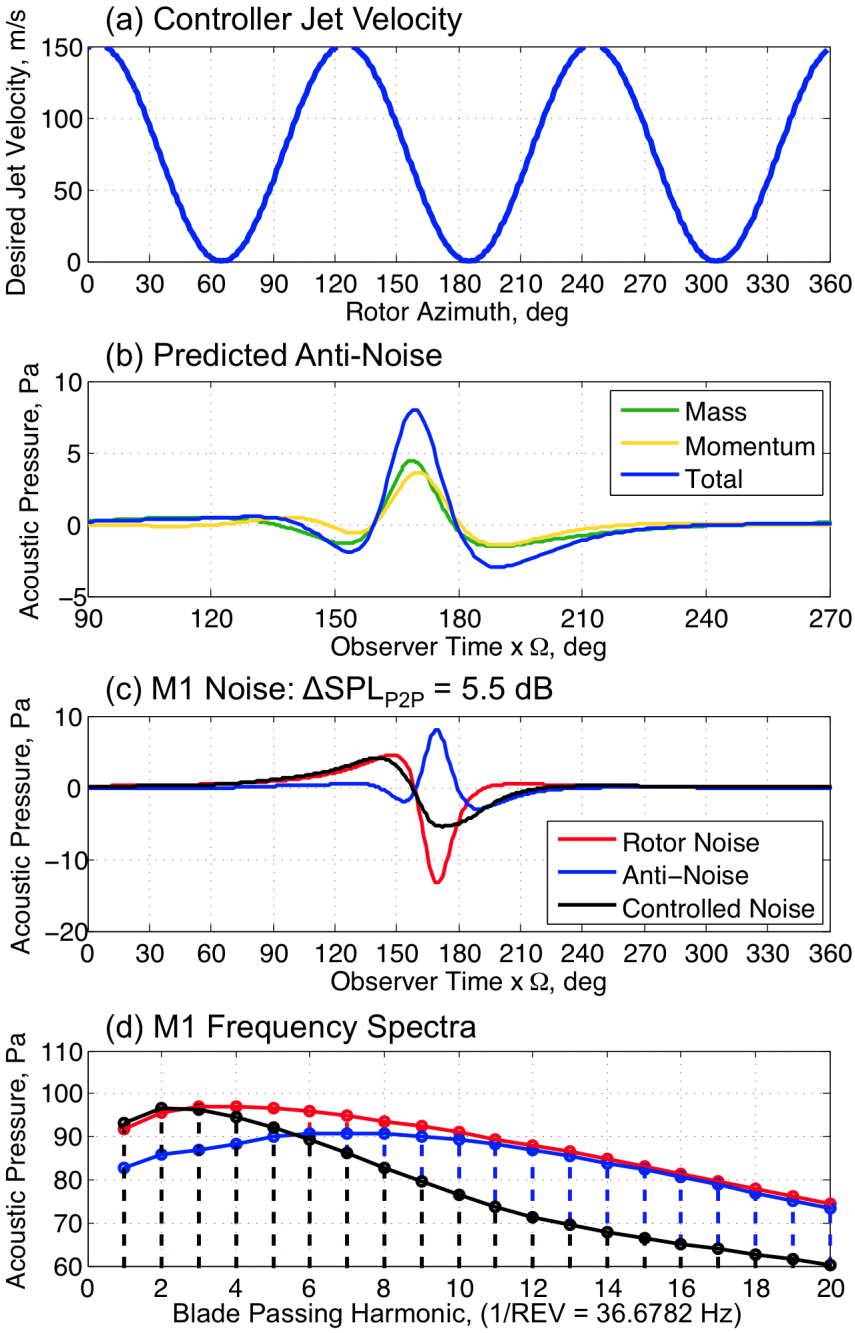

Figure 5-24: Predicted AJAX capability at M1 with 3/REV control.

Chapter 6: Summary and Conclusions

The reduction of low frequency in-plane harmonic rotor noise using an actively controlled on-blade tip air jet has been investigated theoretically and experimentally for a non-lifting hovering model-scale rotor. Acoustic measurements taken in the University of Maryland Acoustic Chamber using the Active Jet Acoustic Control Experimental Test Rotor have shown, for the first time, that the AJAX methodology is a novel and promising method for reducing low frequency in-plane harmonic noise. Using the same correlated theoretical model, a study of how the active jet acoustic control methodology can be applied to a full-scale helicopter was shown. The directivity and acoustic performance of a variety of controller configurations and jet velocity profiles were explored. This chapter summarizes these achievements in further detail and discusses recommendations for future research.

6.1 Summary of Conclusions

- **AJAX Theoretical Model and Application to a Full-Scale Helicopter**

  A theoretical model of the active acoustic jet has been developed. It includes the mass and momentum contributions of the unsteady, subsonic air jet controller and an "on-porous surface", retarded time formulation of the Ffowcs Williams and Hawkings equation that was derived in Chapter 2. The jet is assumed to be incompressible, at ambient pressure, and closed when no flow is passing through the orifice.

  A parametric study of how the AJAX concept can be applied to a full-scale helicopter rotor was conducted. The influence on the relative magnitudes of

the mass and momentum source terms due to the various jet parameters under steady blowing conditions were examined and the two terms were found to be of nearly equal importance. The study shows that *steady blowing* can reduce noise if placed towards the trailing edge of the blade, effectively introducing a phase shift, but that *the required flow rates are prohibitively high*.

Time-varying "tailored" blowing profiles are shown to be the most likely candidates for effectively reducing LF-IPH. For the baseline medium weight helicopter, 3/REV and 4/REV controllers are quite effective and reduce the peak SPL by 3-6 dB depending on the peak jet velocity amplitude. Higher frequency controllers result in increases to the high frequency content of the control and more localized zones of noise reduction.

Single pulse per revolution control cases, with tailored falling edge flow rates, are found to be an effective method for improving the directivity characteristics and performance penalties associated with future control designs.

- **AJAX ETR and Pneumatic Valve Control System**

The design details of the new AJAX Experimental Test Rotor were discussed in detail in Chapter 3. The rotor generates a significant amount of LF-IPH in the UMAC at full-scale tip Mach numbers. Further, it allows time-varying air to be transferred from the fixed-frame pneumatic valve control system to the blade tip. *The AJAX ETR and UMAC facility provide the unique opportunity to take high quality acoustic measurements of an AJAX equipped rotor system and serve as the first system of this kind*.

The pneumatic control system was shown to produce precise and repeatable flow profiles. However some limitations of the system were evident, as sustained durations of high exit velocity time rate-of-change could not be achieved during testing. This results in anti-noise pulses that are narrower than desired for large reductions in SPL. These complications are attributed in large part to the requirements imposed by high frequency, model scale testing at full-scale tip Mach numbers – a complication that is not expected to be as severe on a full-scale helicopter main rotor.

- **Measurement of IPH in the UMD Acoustic Chamber**

A direct comparison between the uncontrolled ETR noise measured in the UMAC and the noise predicted using Formulation 1A of the FW-H equation shows *that linear acoustic theory captures the pulse width and negative amplitude of the thickness noise dominated LF-IPH measurement well at moderate tip Mach numbers*. The time histories included in Chapter 4 show that reflections of the main LF-IPH pulse do occur in the chamber. However, when the rotor is operated at a sufficiently high hover tip Mach number ($M_H > 0.6$), most of the reflected waves arrive in time after the primary event and do not substantially alter the main pulse. The scalloped nature of the frequency spectra of the measured noise confirms the presence of these acoustic reflections. This is particularly evident when the reflected waveform is removed from the measured data using time domain windowing and the frequency spectra are once again examined.

- **AJAX Theoretical Model Validation**

The new theoretical model described in Chapter 2 has been validated with acoustic measurements of a non-lifting, model-scale rotor, operated at a full-scale hover tip Mach number of 0.661, in an acoustically treated and properly sized hover test facility. The model confirms that both mass and momentum terms are important contributors to the LF-IPH noise, each accounting for approximately 50% of the peak amplitude of the resultant anti-noise pulse.

A comparison between theory and measurement, at three in-plane and one near in-plane microphone, has also been shown for several active jet acoustic control valve profiles. *Theory and experiment agree well when the jet flow profile of the rotor under static conditions (i.e. non-rotating hot-film measurements) is used as the active jet acoustic controller source strength. This is the first time that the active jet acoustic control theory has been validated with experimental data.*

- **The Active Jet Acoustic Control Concept**

A comparison of the controlled and uncontrolled model scale rotor acoustic measurements has demonstrated that active jet acoustic control does reduce LF-IPH. The lower frequency 2/REV sinusoidal control reduces the peak negative amplitude of the test rotor's radiated noise by 35% (5 Pa from a peak of -14 Pa) at the target microphone. Smaller reductions are observed at the off-target microphone locations.

The single pulse per revolution control case has a smaller effect on off-target noise levels. Control profiles of this type should be the primary focus of future studies. *This experimental work serves as the first time that the Active Jet*

Acoustic Control concept has been proven and paves the way for a wide array of future research endeavors.

6.2 Recommendations for Further Research

This dissertation opens the door to a variety of theoretical and experimental work that can continue in this new and exciting area of research.

- **Higher Tip Mach Number Experimental Cases:** The active jet acoustic control concept should be evaluated at higher tip Mach number than explored experimentally for this dissertation. Operating at higher tip Mach numbers will likely introduce additional non-linear effects to the problem that can then be evaluated.
- **Theoretical Jet Flow Profile Optimization:** The theoretical study conducted for this dissertation aimed to provide an understanding of how varying jet parameters and flow profiles affect the LF-IPH reduction capability of the AJAX system. Though the conclusions provide insight into what trades are made between the different controllers that were prescribed in this work, they do not shed light on what the "optimal" jet controller might look like. Further, they do not define a criterion for what the optimal acoustic benefit is. For example, is it better to reduce the peak SPL or some other metric of detection or audibility? Determining what these metrics are is a huge undertaking on its own accord.

  In future research that is aimed at implementing the AJAX concept on real helicopters, additional work should be done to better understand what these optimal solutions might look like and what optimization criterion are

most useful in real-world applications. Analytical or numerical solutions to the governing acoustic equations that include both the mass and momentum acoustic control terms should be investigated. Solutions that provide better directivity, frequency selective reductions, or peak noise reductions based on objective performance functions can then be generated through rigorous mathematical means rather than guessed. This work would be similar in nature to the research described in reference [82], which examined performance functions for internal noise reduction.

- **Improved Understanding of Tip Flow Region:** The theoretical model in this work assumes that the blade loading and tip jet blowing are uncoupled. This allowed the blade loads and momentum source terms to be computed independently. Though this proved to be sufficient for the non-lifting AJAX ETR used for this work, it is possible that a full-scale rotor system in forward flight, with a modern tip shape, might be more affected by the coupling between the jet blowing and aerodynamic environment near the blade tip. Further theoretical and ultimately experimental work should be emphasized in this area to evaluate whether it is a significant contributor to the radiated noise. A better understanding of the flow in this region would also provide insight into the acoustic, aerodynamic and pneumatic performance penalties that might be associated with a real AJAX system. Ultimately, an off-surface CFD solution an AJAX equipped rotor should provide invaluable information about this coupling. In this case, the change in pressures on the blade itself

and the quadrupole field of the jet impinging on the ambient fluid will both be included within the computational mesh.

- **Expanded Experimental Measurement Capabilities:** Two additional variables that were not measured during acoustic testing that would provide useful information are the actual jet exit velocity through the rotating ETR and the corresponding time variation in rotor torque. The inclusion of sensors that measure these quantities to the AJAX ETR would add considerable credibility and capability to the entire facility. Both devices require some degree of ingenuity or resourcefulness, since the accurate measurement of these quantities at the model scale is not always as straightforward as it initially appears.
- **Improvement to Pneumatic Valve Control System:** During testing it became evident that the high frequency and small size of the model scale rotor made precise flow control difficult. The single pneumatic valve and its proximity to the blade tip were less than ideal and the net result of this was that only very narrow anti-noise pulses could be generated. Future effort should be made to improve the capabilities of this system. The incorporation of additional valves, connections with fewer flow losses and improved valve control methodologies (PID etc.) would likely result in the ability to generate more desirable control profiles and larger reductions in LF-IPH.
- **Additional Blowing Active Control Methodologies:** The AJAX ETR is a useful platform for testing other active acoustic control methodologies that use

air as the primary source of actuation or noise generation. The rotor system can and should be adapted for additional methods of noise reduction.

- **Full-scale pneumatic design:** The ultimate goal of the AJAX concept is to see use on full-scale operational helicopters. In order to achieve that goal a robust and effective pneumatic control system must be designed. This effort will take considerable investment and time.

Appendix A: AJAX ETR Rotor Blade Design

Acoustic testing for this dissertation was conducted at full-scale hover tip Mach numbers and the rotor diameter had to be small enough such that measurements could still be taken in or near the acoustic far-field of the rotor (D_{obs} > 2.5-3.0R). The diameter was chosen as 78 inches and the maximum operational tip Mach number as 0.7. The resultant rotational rate then was approximately 38.2 Hz. This presented some complications for the design of the internally ducted rotor blade and resulted in two rotor blade designs.

A.1 The Extruded Aluminum AJAX ETR Blade Design

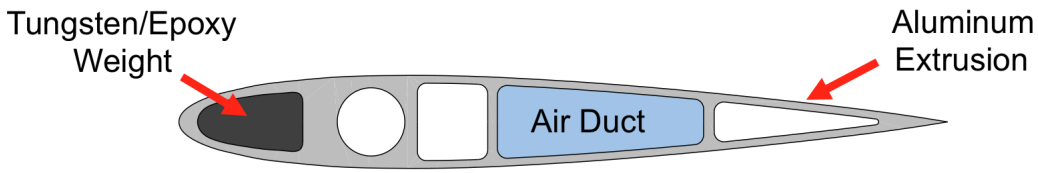

Figure A-1: Extruded Aluminum AJAX ETR blade cross-section.

The first rotor blade that was constructed was an extruded aluminum (6063) blade with 4 inch chord and NACA 0012 profile, the cross section of which is shown in Figure A-1. In order to balance the blade and avoid any possible flutter instability issues a tungsten/epoxy composite material obtained from Tungsten Heavy Powder Inc. in San Diego, CA was used. This material uses a fine grained Tungsten powdered contained in a high strength epoxy matrix and can be tailored to densities of up to 11.5 g/cm^3 and then poured or injected. This material and two 1/8" tungsten filaments are used to fill the leading edge cavity of the blade thus moving the blade CG to very near the quarter chord.

The blade was sealed at the tip (all cavities except for the large air plenum) using a small amount of epoxy that was cured with the blade in a vertical position, and painted flat black to reduce reflections from the stroboscope used in the Acoustic Chamber. The blade dimensions are summarized in Table A-1.

Table A-1: Extruded Aluminum AJAX ETR Blade Parameters

Characteristic	English	Metric
Length (Root to Tip)	35.00 in	0.889 m
Length (Axis of Rotation to Tip)	39.00 in	0.9906 m
Chord	4.00 in	0.1016 m
Aspect Ratio	9.75	
Airfoil Shape	NACA 0012	
Weight	3.043 lb	1380.08 gm

As mentioned in Chapter 2, this blade was ultimately too heavy for safe operation at full-scale hover tip Mach number. The centrifugal force exerted by the blade is,

$$F_{CF} = M\Omega^2 R = (3.043 \text{ lb})(17.42 \text{ in})(38 \text{ Hz} \times 2\pi)^2 \approx 8000 \; lbf$$

A series of tests was conducted to establish whether the aluminum blade could withstand this load with a satisfactory margin of safety.

The MTS Tensile test setup tested three lengths of thread engagement (0.5", 1.0" and 1.75") and is shown in Figure A-2. A similar analysis was also conducted with CATIA Simulation, as shown in Figure A-3. The resulting failure points for both cases are summarized in Figure A-4. FEA Analysis, using CATIA Finitie Element Analysis, and tensile testing of the extruded aluminum structure, indicated that it could withstand tensile loads due to centrifugal loading on the order of 11,000 lbf.

Figure A-2: Test setup for MTS tensile test.

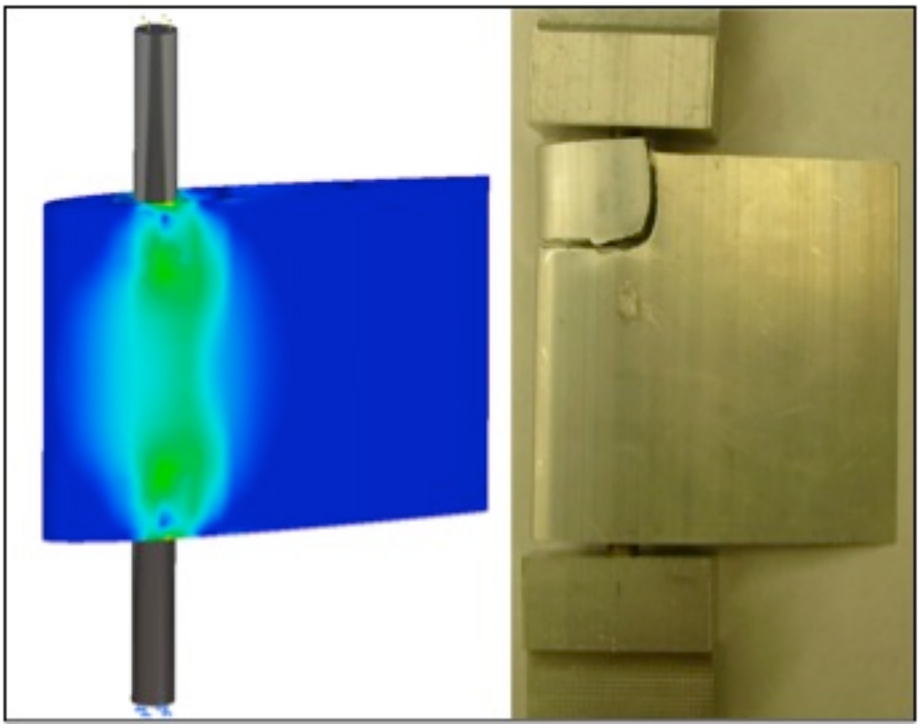

Figure A-3: CATIA FEA simulated stress and failed MTS section.

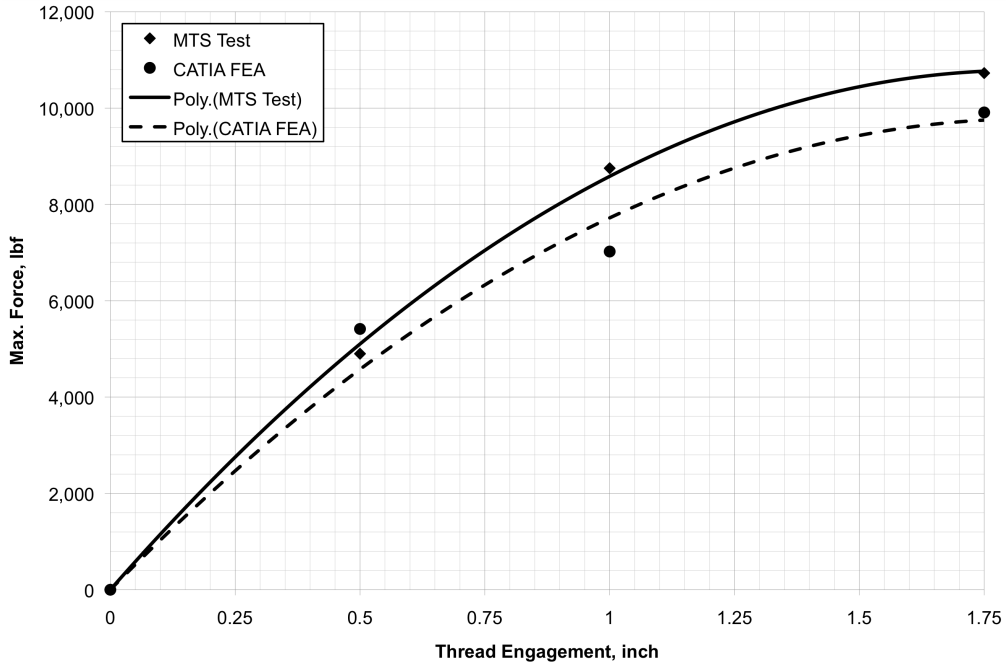

Figure A-4: Failure analysis from MTS and FEA.

The margin of safety was deemed to be too small for the extruded aluminum blade and so additional measures were taken to reduce the total blade weight.

A.2 The Composite AJAX ETR Blade Design

In order to facilitate high-speed operation of the rotor and reduce the overall blade weight, the aluminum extrusion was removed aft of the square duct (third from leading edge) and replaced with a lightweight foam core. A cross section of the blade is shown in Figure A-5. The entire blade spar was trimmed so that the root section maintained full structural integrity. Full sections of the extrusion (0.25” width) were also kept approximately every six inches to maintain the blade trailing edge and shape. The structure, shown in Figure A-6, was then covered with a woven carbon fiber biaxial sleeve (2.5” 6K/Aerospace Soller Composites) and hardened after a wet-layup and vacuum bagging. The blade specifications are summarized in Table A-2.

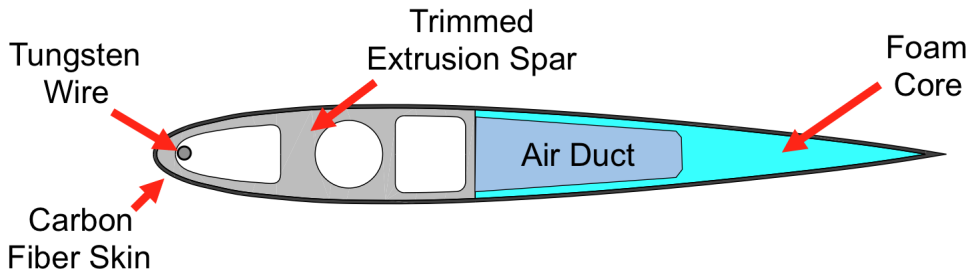

Figure A-5: Composite AJAX ETR Blade cross-section.

Table A-2: Composite AJAX ETR blade parameters.

Characteristic	English	Metric
Length (Root to Tip)	35.00 in	0.889 m
Length (Axis of Rotation to Tip)	39.00 in	0.9906 m
Chord	4.00 in	0.1016 m
Aspect Ratio	9.75	
Airfoil Shape	NACA 0012	
Weight	1.616 lb	733.01 gm

The resultant composite structure weighs only 1.616 lb, 47% less than the original balanced aluminum extrusion blade. Due to the manufacturing process the radial CG was also moved inboard, and so the resultant centrifugal force exerted by the blade is,

$$F_{CF} = M\Omega^2 R = (1.616\text{ lb})(15.0\text{ in})(38\text{ Hz} \times 2\pi)^2 \approx 3600\ lbf$$

This blade is deemed safe for high-speed operation up to $M_H = 0.7$ though testing was conducted at 0.661.

A.3 Composite AJAX ETR Blade Manufacturing Process

A description of the construction process of the Composite AJAX ETR blade is now presented step by step.

1. **Blade Spar Preparation:** In order to cut the extruded aluminum blade to the require dimensions shown in Figure A-6 several steps were taken, as illustrated in Figure A-7(a) – (e).

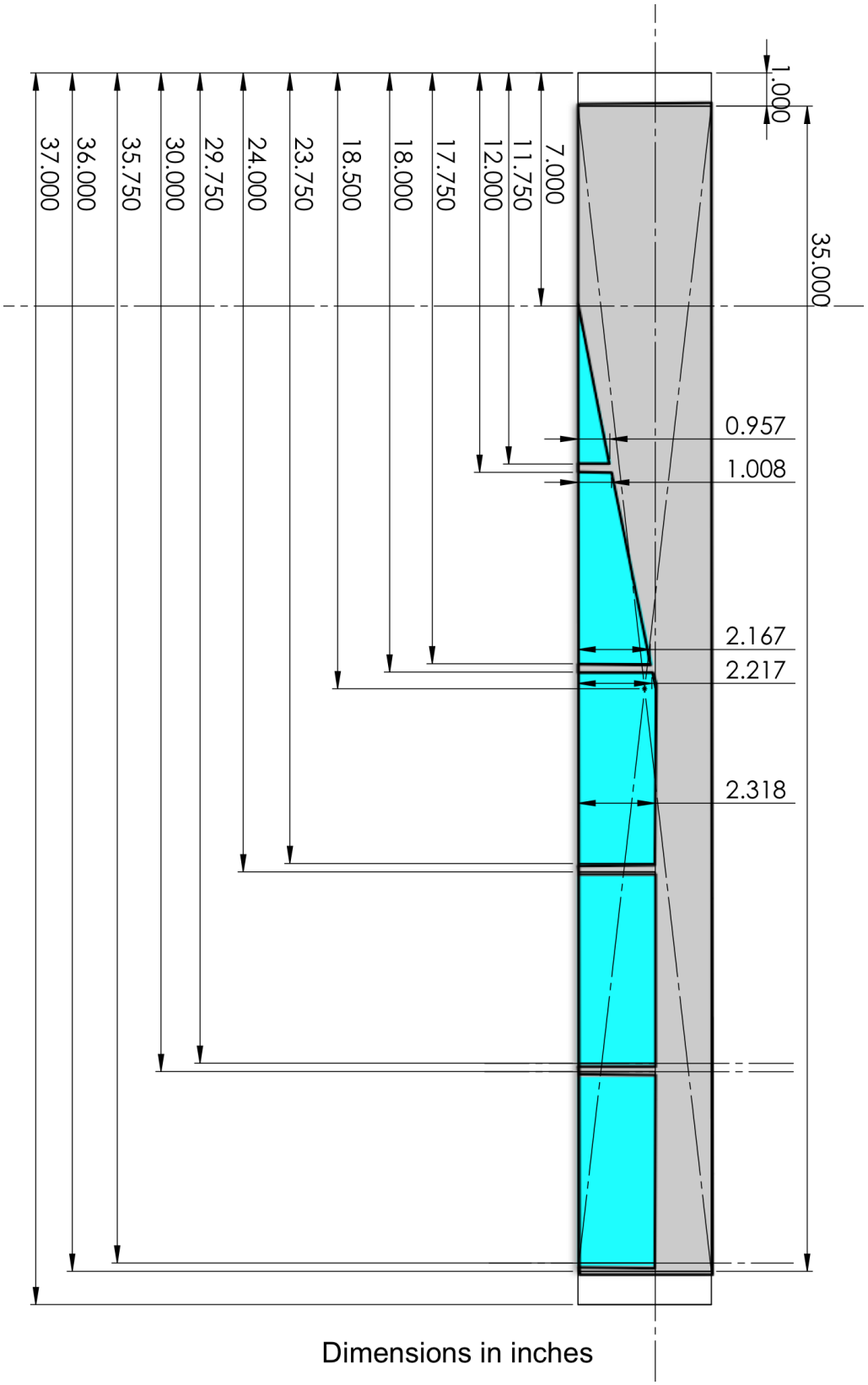

Figure A-6: Composite AJAX rotor blade spar dimensions.

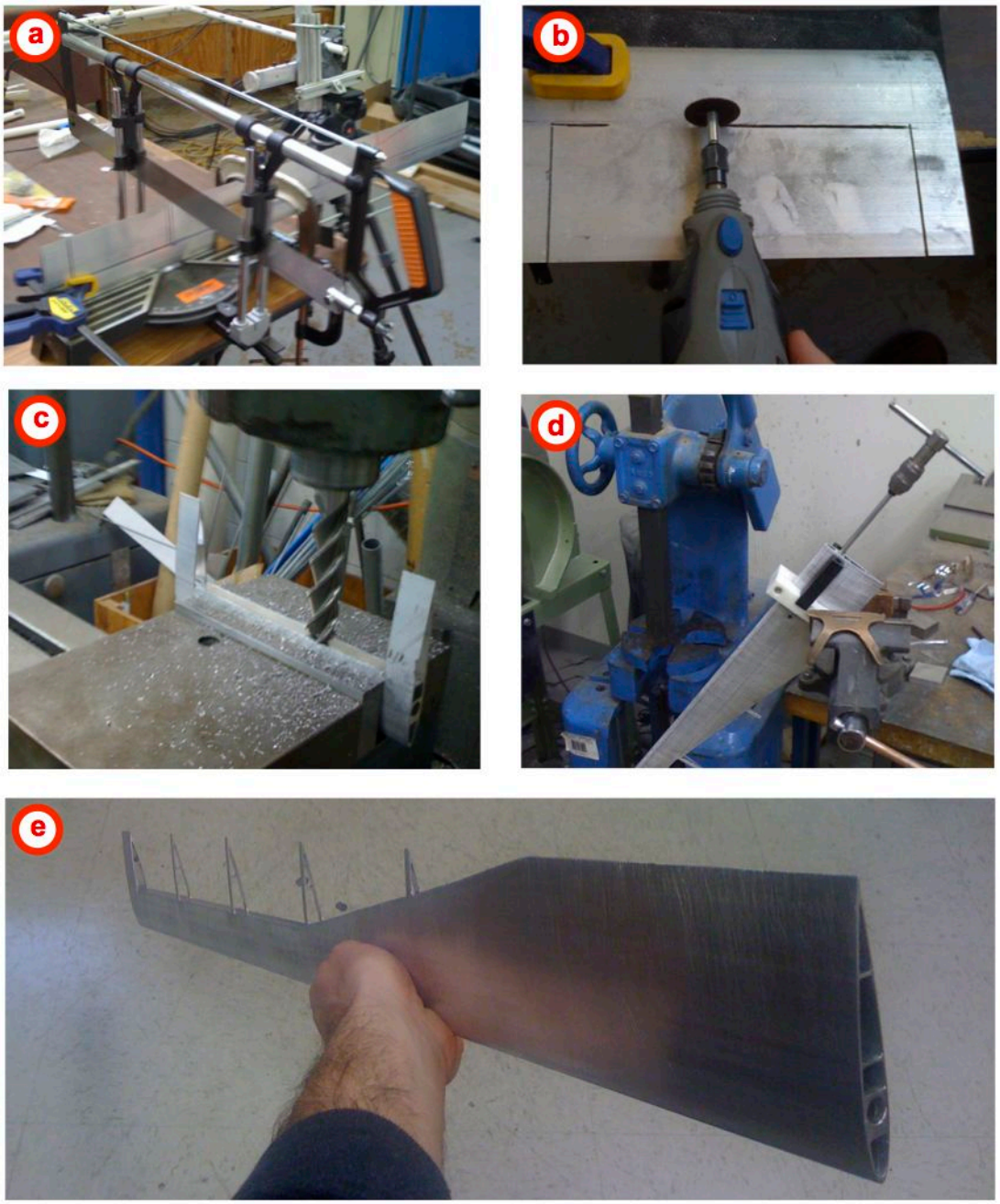

Figure A-7: Blade spar preparation.

(a) After tracing spar pattern on the blade surface, make chord-wise cuts in blade spar (parallel to blade chord) using manual miter saw to required depth.

(b) Remove aft aluminum sections using Dremel tool equipped with high-speed cutting wheel along trailing edge of square conduit. Repeat for all sections that are to be replaced with foam.

(c) Smooth flat edge of the trailing edge of the spar using an end mill mounted as shown (LE down). Figure A-7 shows this process on a manual mill for a smaller test section.

(d) Tap ¾-24 thread into quarter-chord hole using extended tap to desired depth, approximately 4 inches (or longer if possible)

(e) Sand blade surface with 80 grit sand paper and prepare for layup.

2. **Foam Core Preparation:** To maintain the duct integrity while reducing the blade weight of the composite blade, lightweight foam inserts are used in place of the removed aluminum structure.

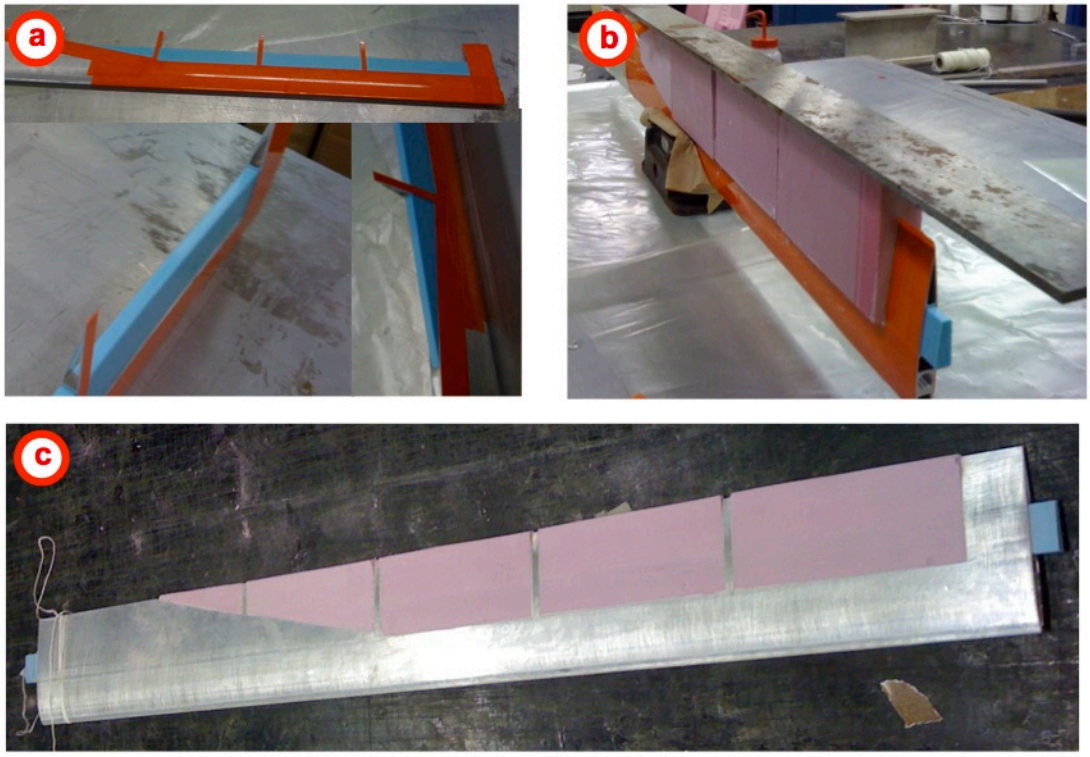

Figure A-8: Foam core preparation.

(a) Tape off exposed aluminum near areas in which foam is to be added. Insert silicon mandrel through air duct leaving 1 inch exposed on either side. Note: The mandrel can be made using a full-length blade and pourable silicon rubber. Cut foam blocks to size for each of the five removed sections with inner slot cutout (in the shape of the duct). This can be done with the wire foam cutter and precision saw and then smoothed with sand paper and file.

(b) Fill inner foam duct with thickened epoxy and fit in appropriate aft section. Clamp the blade in place and place weight on top of foam blocks. Let the epoxy dry for required time.

(c) Remove tape and file/sand additional foam to conform to the blade cross section. A sanding bar wider than 6 inches can be used for this purpose.

3. **Blade Layup and Cleanup:** The final step in the composite AJAX blade construction process is to adhere the carbon fiber skin to the blade surface and trim and sand the external surface.

(a) Tape up blade ends (you should have 1 in of extra aluminum on both sides) so that silicon inner mandrel and other orifices are sealed off. Use additional sealant as needed. Place the blade on one layer of peel ply. Prepare flexible plastic outer mold. Note: This is made two pieces of flexible plastic

connected with a strip of flashbreaker tape. The soft outer mold ensures a smooth finish during curing.

(b) Pull carbon fiber sleeve (2.5” 6K/Aerospace Soller Composites) over the blade surface. Pull tight at ends and trim excess material. Apply two-part epoxy resin to entire surface and cinch peel ply tight. Using flat edge, remove as much excess resin as possible by scraping along blade surface. Insert peel ply covered blade in flexible plastic outer mold.

(c) Insert blade in vacuum bag and place breather strip along the trailing edge and near the blade root. This allows resin to flow smoothly. Seal the vacuum bag and attach required fittings. Push blade mold up against the edge of the vacuum bag and apply vacuum suction. Place a long weight along the blade trailing edge to maintain a straight edge. Allow the blade to cure for required time under suction.

(d) Once the blade has been cured carefully remove from the bag and trim excess carbon fiber sleeve material from the edges. Take care not to destroy the silicon mandrel. Remove the mandrel and check inner duct surface for smoothness.

(e) Sand the blade surface as required and trim root and tip aluminum excess material (approximately 1 inch). The blade is complete.

Figure A-9: Blade layup and cleanup.

Appendix B: AJAX ETR Dynamics

The rotational resonance frequencies associated with the AJAX ETR are calculated in this appendix. An Impact Hammer test (PCB Modal Analysis Kit shown in Figure B-1) was performed to ascertain the first few non-rotating flapping and torsion frequencies. The rotational frequencies of the ETR were predicted using an analogy to a cantilevered beam. An additional frequency analysis was conducted using CATIA's frequency analysis package. Both the predicted and experimental non-rotating modal frequencies are summarized below in Table B-1.

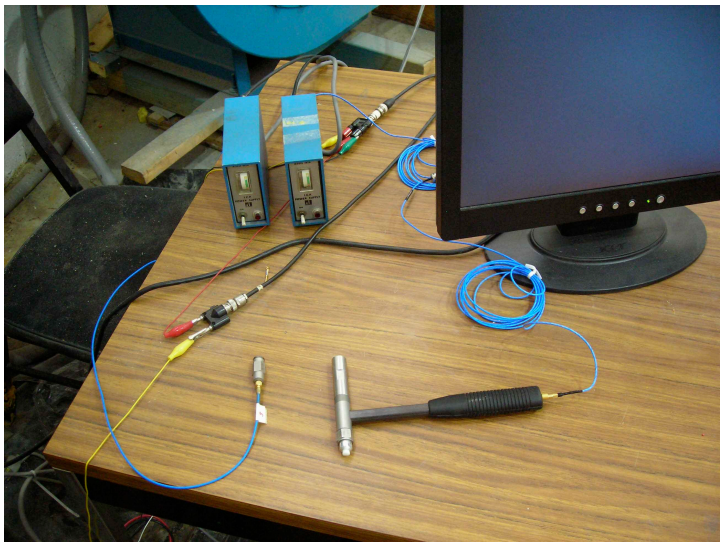

Figure B-1: Impact Hammer PCB modal analysis kit.

Table B-1: Non-rotating modal frequencies of AJAX ETR.

Mode	Predicted	Experiment (Hz ± 0.4)	Error
1st flap	10.97	10.40	0.57
2nd flap	68.55	65.20	3.35
3rd flap	190.7	193.2	2.50
1st torsion	205.94	211.0	5.06

The increase in error at higher frequencies is due to both discretization of the model and a rough estimate for the net modulus of elasticity, E, and moment of inertia, I, of the extruded aluminum blade with a tungsten composite leading edge. An error in the blade EI results in a linearly increasing error with increasing frequency.

The fan plot generated using the measured frequencies is plotted in Figure B-2. The non-rotating frequencies are converted to rotating frequencies and plotted versus RPM.

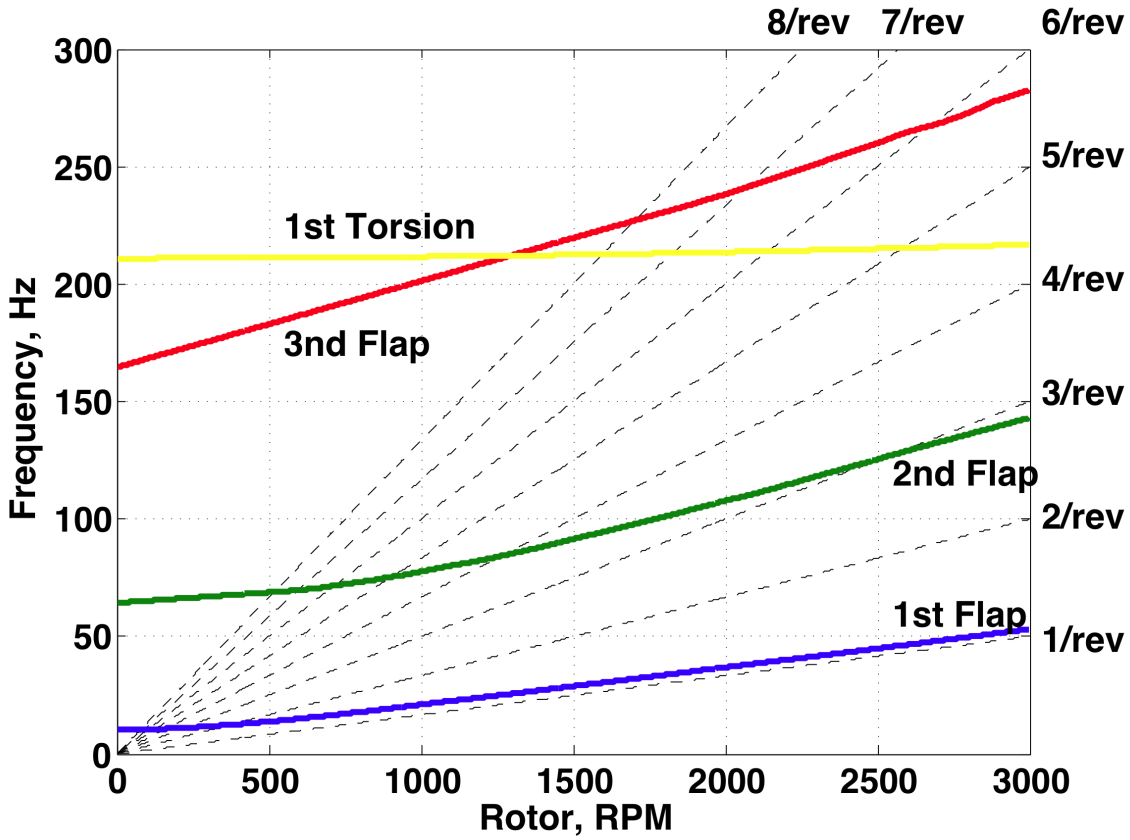

Figure B-2: Natural rotational frequencies of the AJAX ETR.

To avoid operating the rotor at resonance frequencies, rotational speeds above or below 2500 RPM are preferable so as to not excite the 1st or 2nd flapping frequencies. The operational hover tip Mach number of 0.661 corresponds to a rate of 2200 RPM.

Appendix C: AJAX ETR Theoretical Model Discretization

The computational discretization used in the theoretical work for this dissertation is discussed in this appendix. Both the full-scale and model-scale predictions of thickness noise calculations discretize the blade as 95 radial sections, each containing 60 chord-wise elements, for a total of 5700 elements. The loading noise calculations are made using a compact chord assumption and each blade is discretized as 95 radial section elements, with the loads acting at the blade quarter chord. These choices are evaluated here.

The numerical convergence of the thickness noise acoustic pressure as a function of radial and chord-wise elements is shown in Figure C-1. The radial and chord-wise elements are evenly distributed across the blade radius and chord respectively. Convergence is sensitive to the number of chord-wise elements but does not improve dramatically after 16 elements. Blades with more than 60 radial sections also do not show improvement.

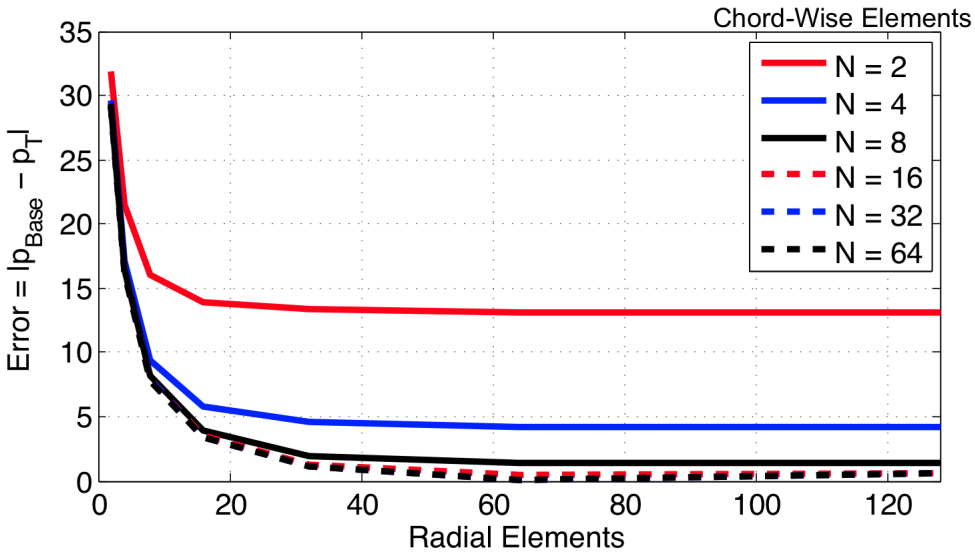

Figure C-1: Chord-wise and radial discretization of thickness noise.

The blade tip cap (in the y-z plane of the blade fixed coordinates) is not included in the theoretical predictions in this dissertation but can be included as shown in Figure C-2. Though the tip cap can produce significant levels of thickness noise for contoured or tapered tips, Figure C-3 shows that the thickness noise associated with the flat, rectangular tip of the ETR is very small (a). The shape of the pulse is similar to a drag dipole and the near-field thickness term, as shown in Figure C- 3 (b).

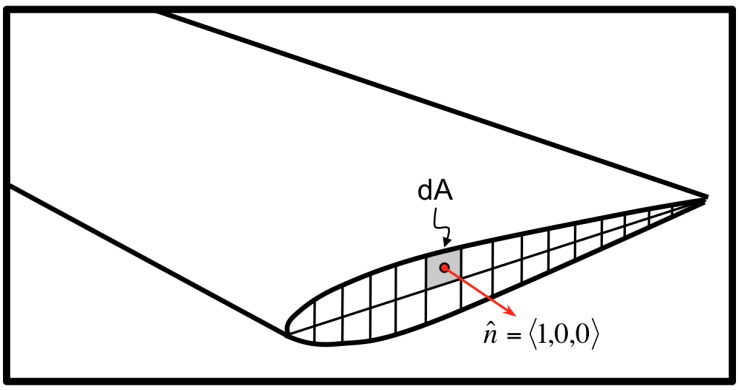

Figure C-2: Tip cap discretization for thickness noise calculation.

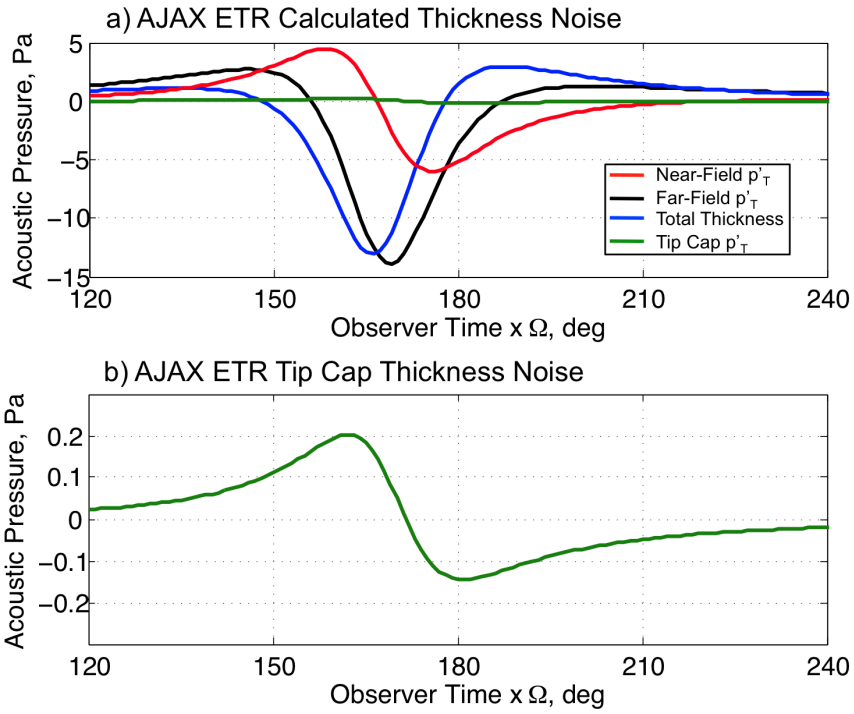

Figure C-3: Thickness noise calculation for tip cap and ETR blade at M1.

The loading noise calculations made in this dissertation used either UMARC or a simple BEMT lifting line approach to predict the loads. A compact chord assumption was then used. In order to show that this is a reasonable assumption for the non-lifting ETR, a pressure distribution was assumed based on the result for a flat plate in classical thin airfoil theory. The pressure distribution across the blade chord then is,

$$\Delta C_P = 4\alpha\sqrt{\frac{1-\bar{x}}{\bar{x}}} \quad \text{where} \quad \bar{x} = \frac{x}{c} \tag{A.1}$$

The effective angle of attack calculated using the BEMT approach is used with this approximation. The distributed loading noise is calculated using 10 and 100 chord-wise elements with 95 radial sections and compared directly with the compact chord BEMT assumption as shown in Figure C-4.

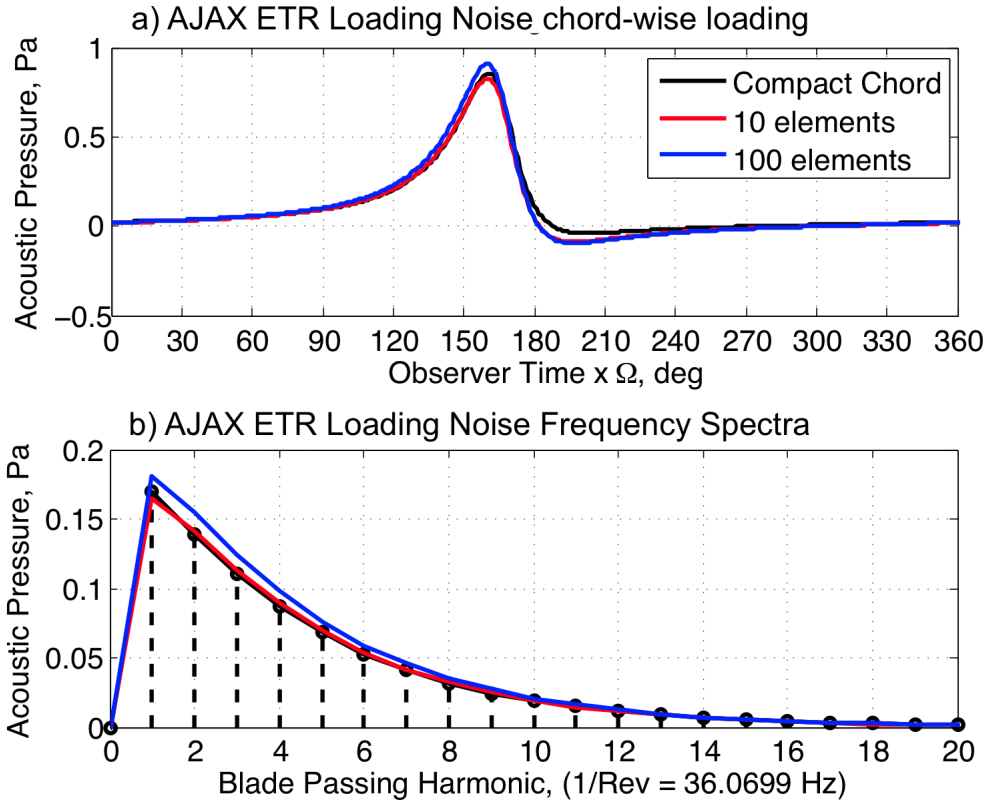

Figure C-4: Compact chord in-plane loading noise assumption at M1.

A discrepancy in the positive and negative peak amplitudes exists but the majority of the loading noise is captured using the compact chord assumption. Further, the relative amplitude of the thickness and loading noise justifies the use of the less time consuming compact chord calculation.

Finally, the number of elements used to model the active jet acoustic controller is evaluated. The full-scale jet controller was modeled using two elements and the model scale jet was discretized as a single source. The calculated anti-noise acoustic pressure as a function of increasing the number of jet orifice elements (as shown in Figure C-5) for a 3/REV sinusoidal jet velocity variation applied to the AJAX ETR, is shown in Figure C-6. The error in peak-to-peak pressure is summarized in Figure C-7. For the AJAX ETR jet, the anti-noise is insensitive to the number of chord-wise elements and so a single source is adequate. This does assume that both jets act simultaneously and so for a very long chord-wise jet, additional care should be made to evaluate how important the jet discretization is.

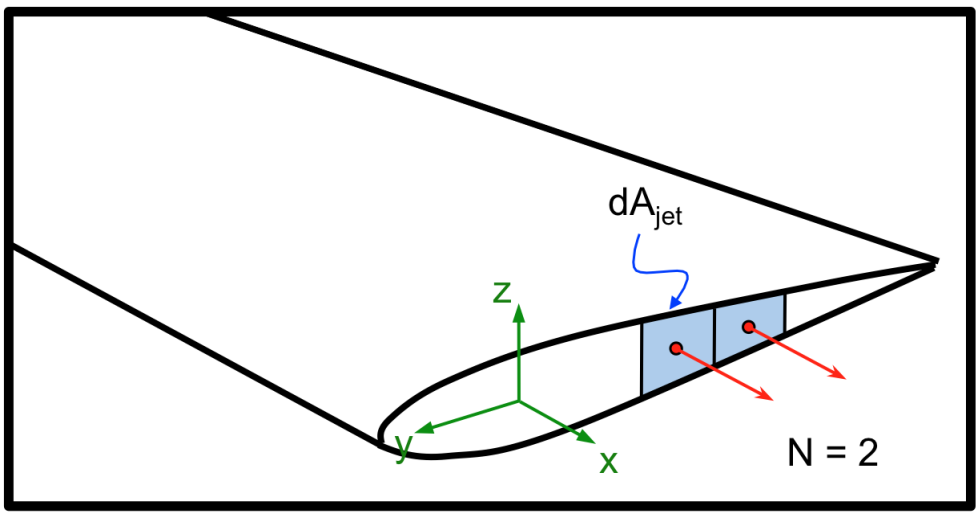

Figure C-5: Jet orifice discretization.

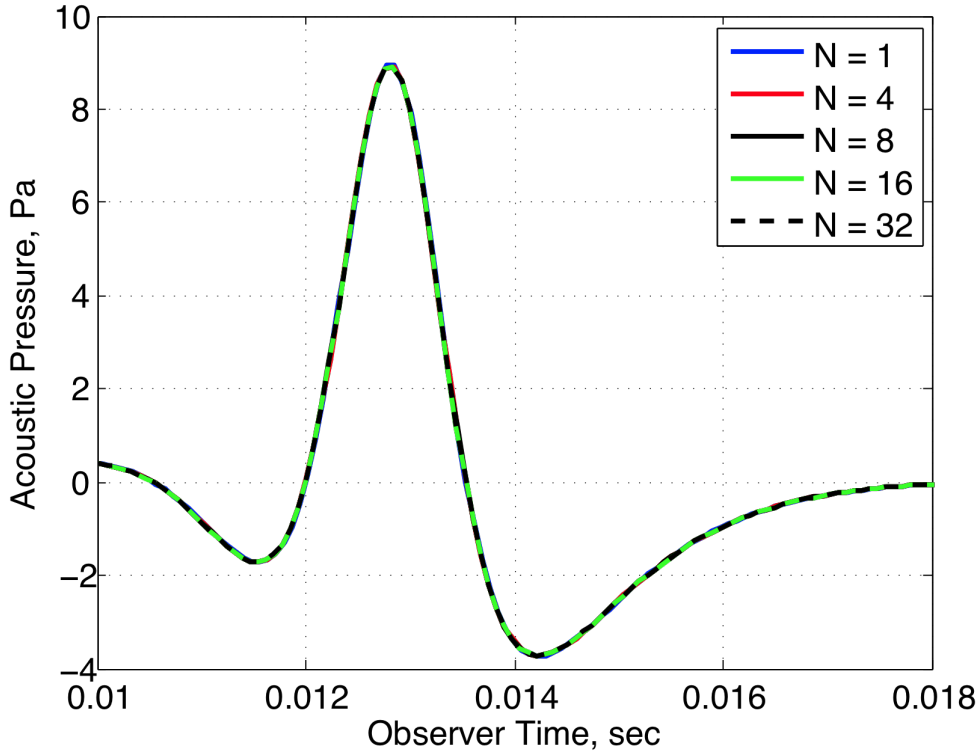

Figure C-6: Calcualted anti-noise for 3/REV control of AJAX ETR

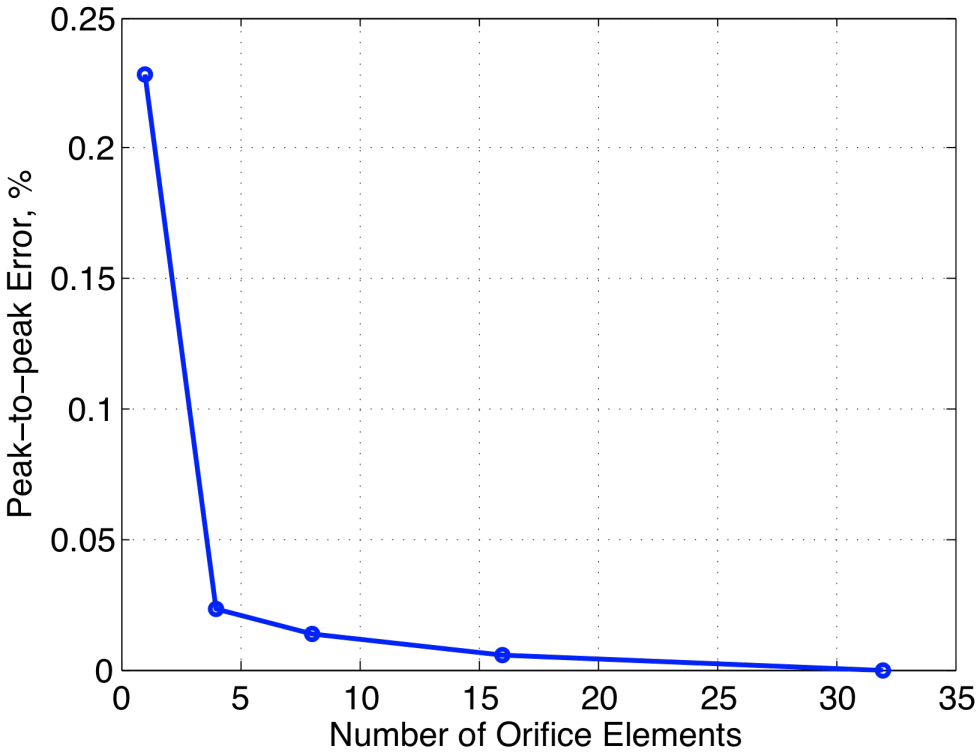

Figure C-7: Peak-to-peak pressure error for 3/REV control of AJAX ETR.

Appendix D: AJAX ETR Measured Data (Frequency)

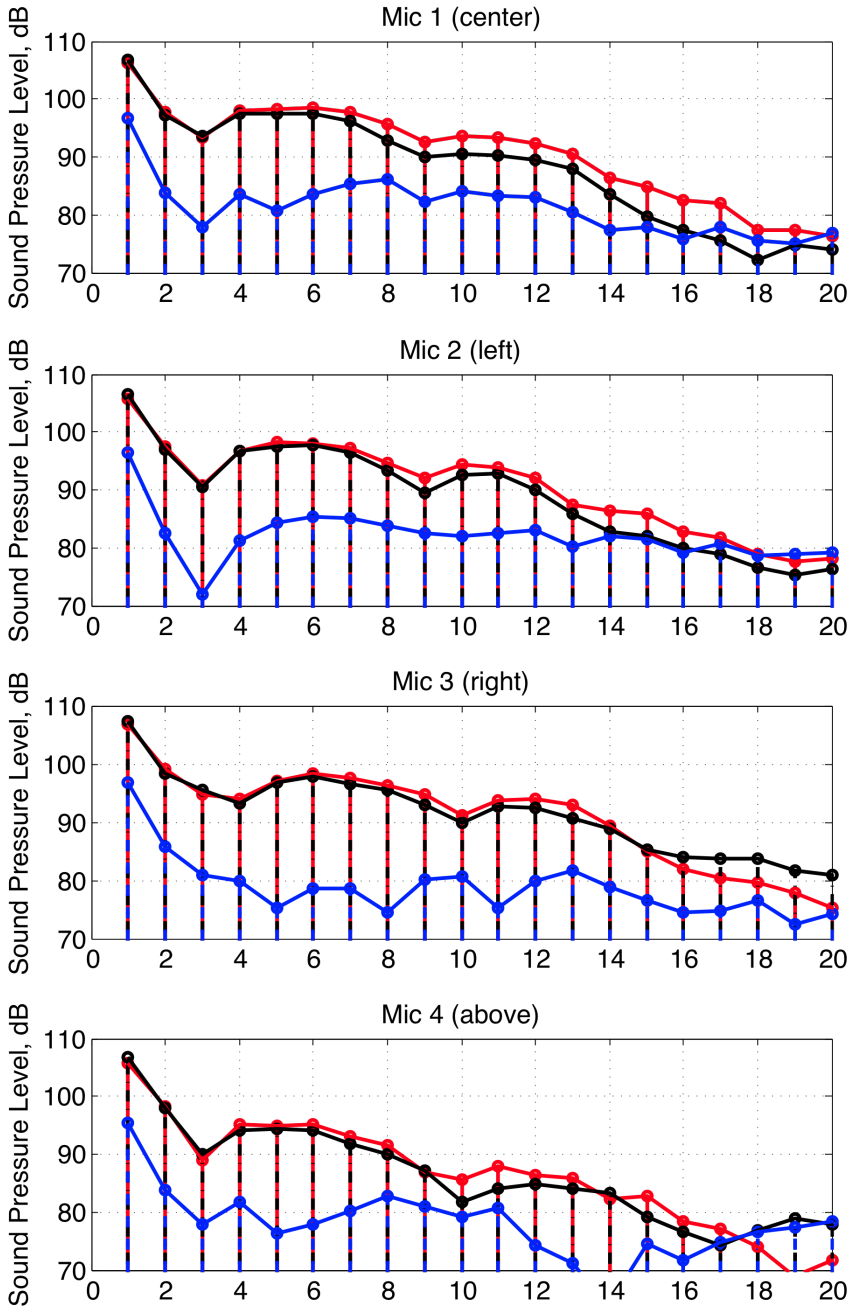

Figure D-1: 2/REV control measured frequency content (1/REV = 36.7 Hz).

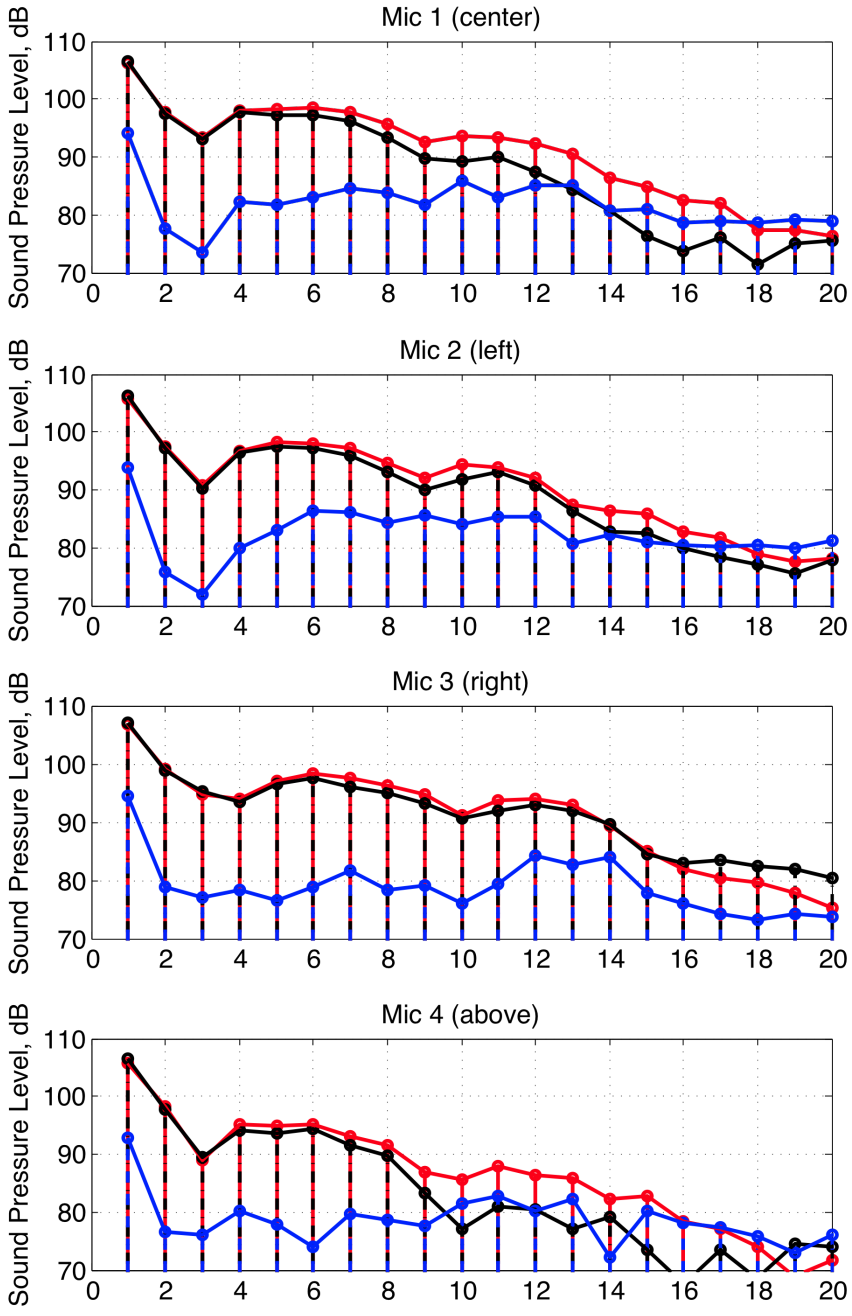

Figure D-2: 3/REV control measured frequency content (1/REV = 36.7 Hz).

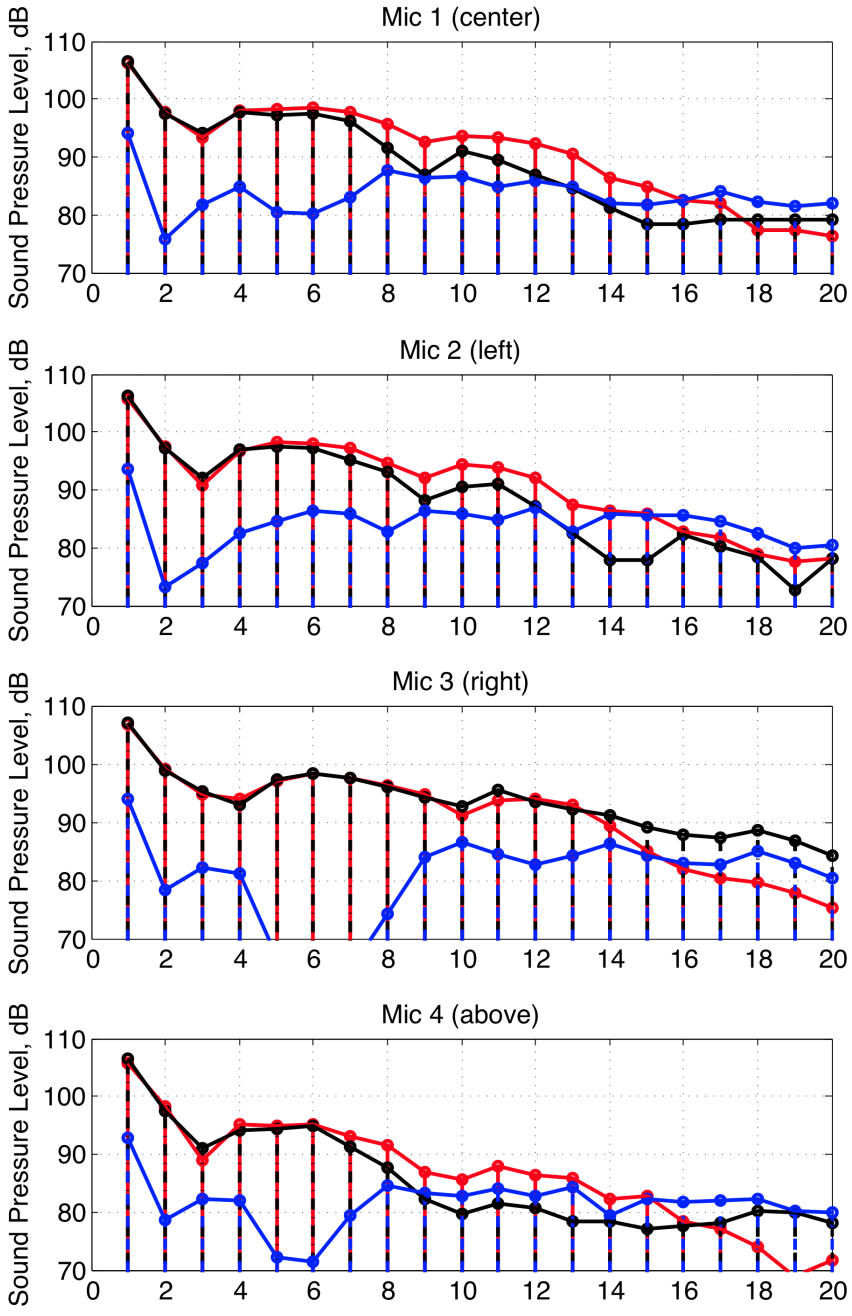

Figure D-3: 4/REV control measured frequency content (1/REV = 36.7 Hz).

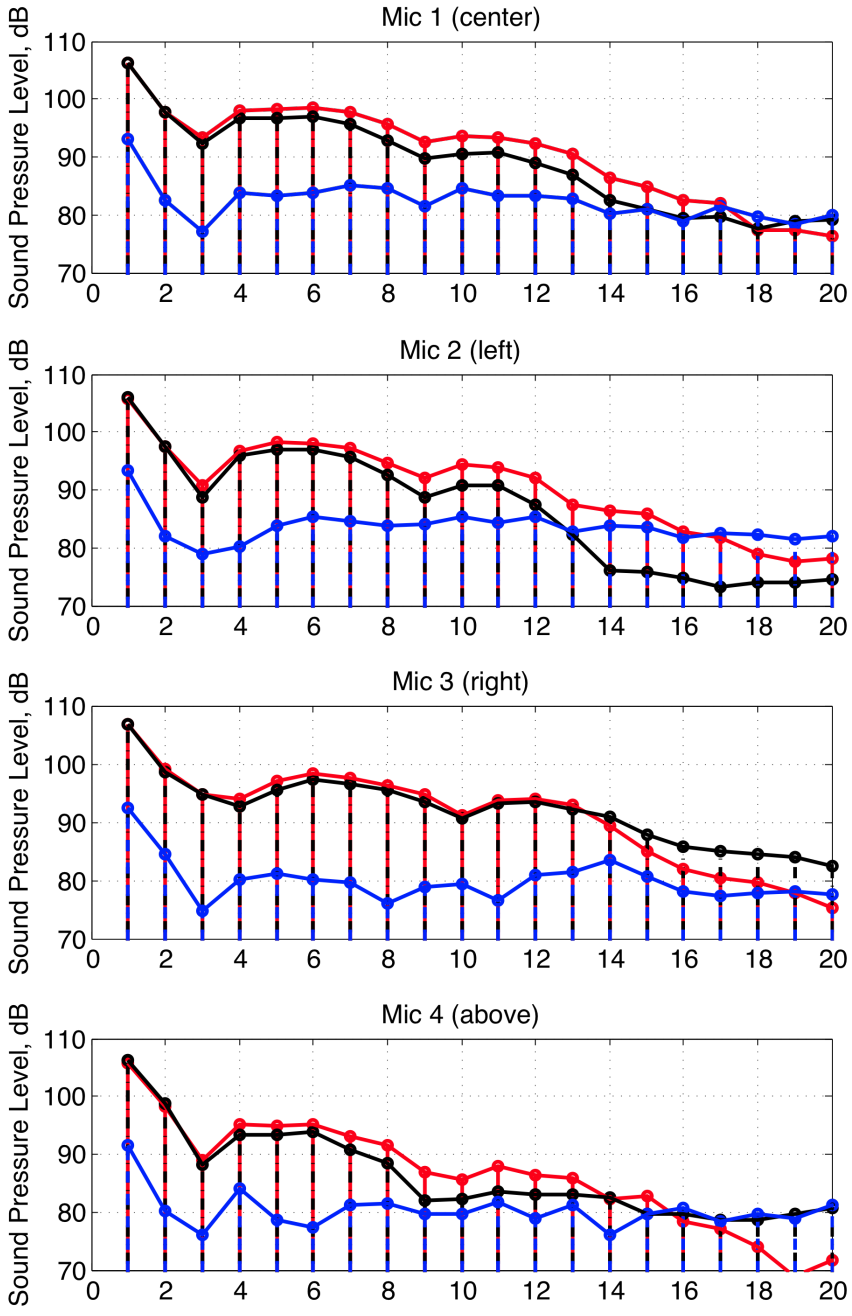

Figure D-4: Single pulse per revolution control measured frequency content (1/REV = 36.7 Hz)

Appendix E: AJAX ETR Measured Data (Time)

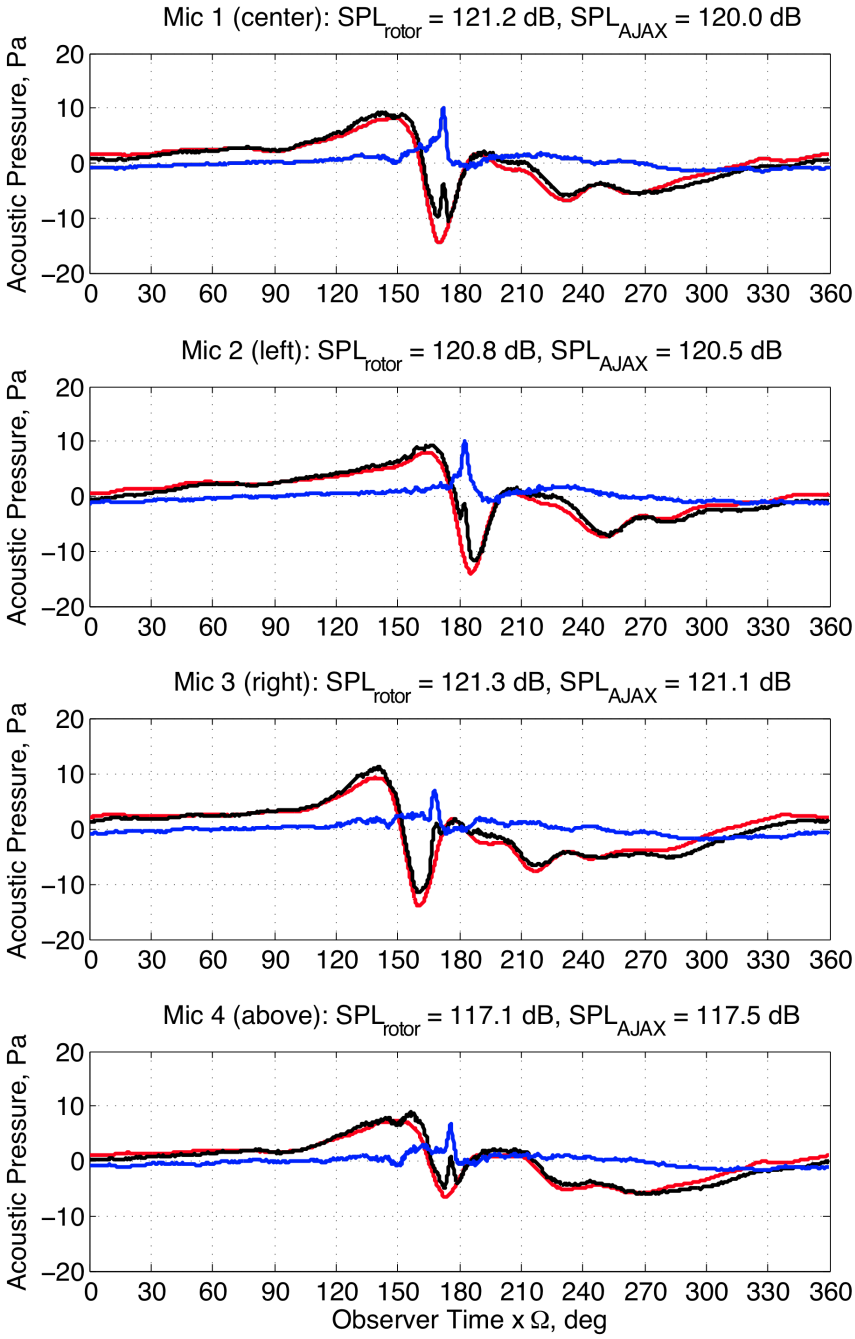

Figure E-1: 2/REV control measured time history (1/REV = 36.7 Hz).

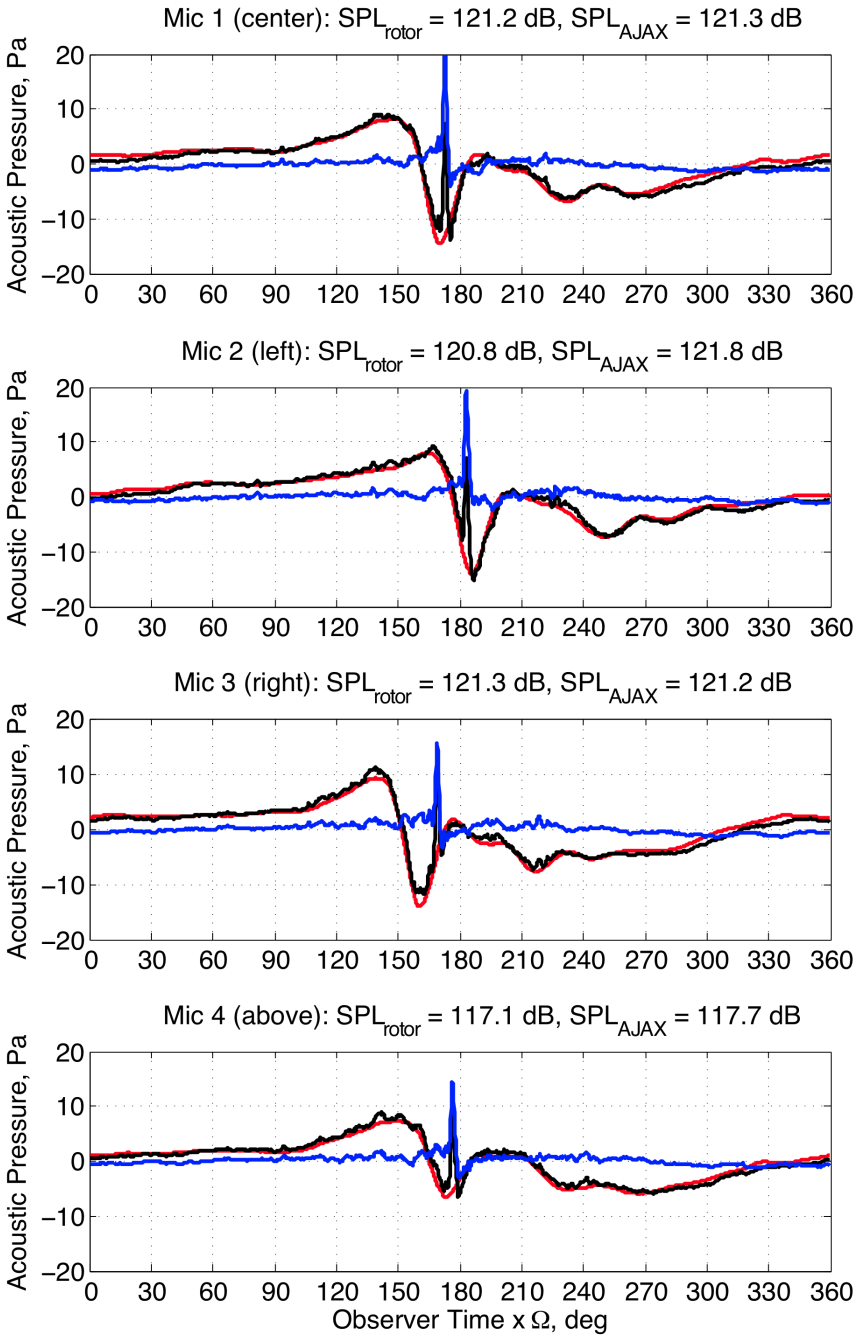

Figure E-2: 3/REV control measured time history (1/REV = 36.7 Hz).

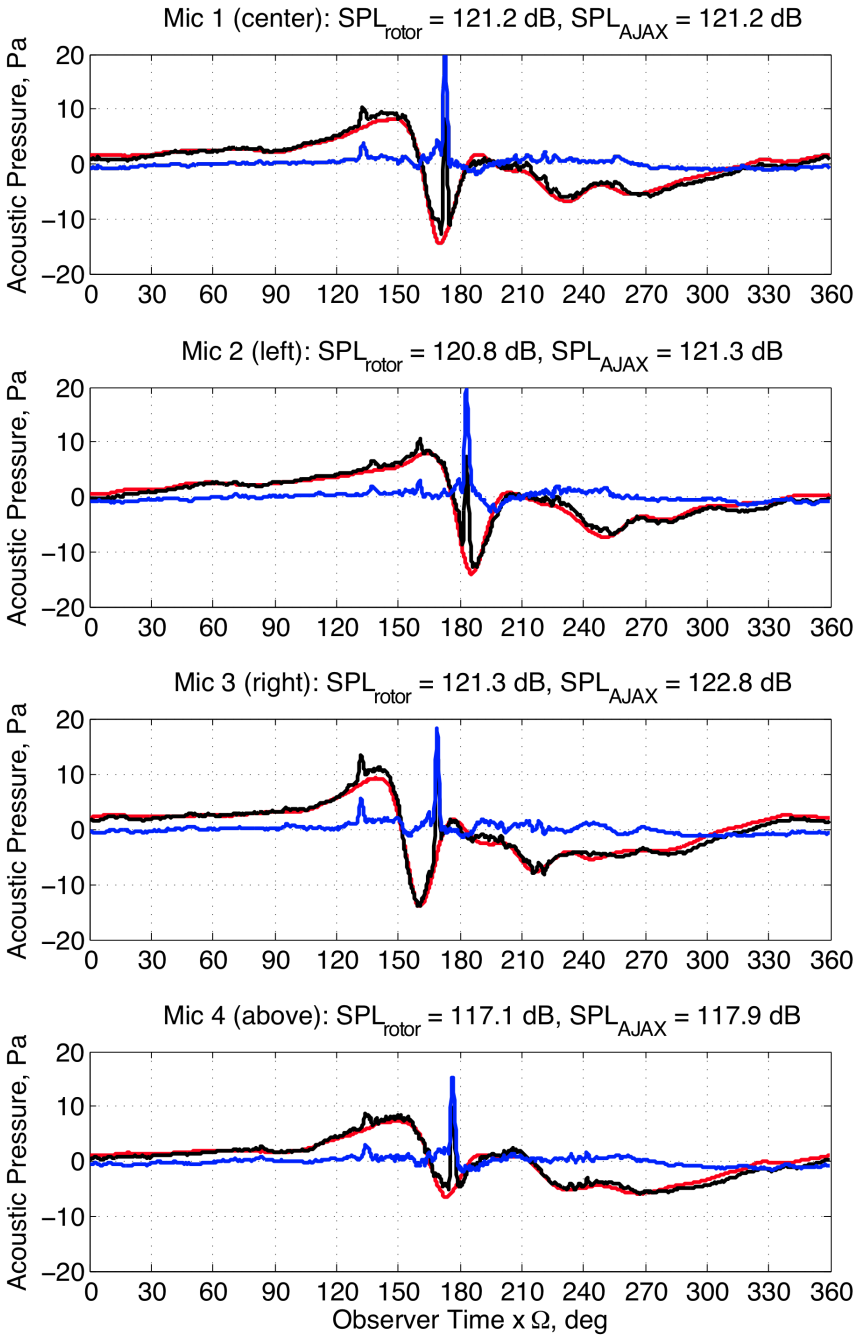

Figure E-3: 4/REV control measured time history (1/REV = 36.7 Hz).

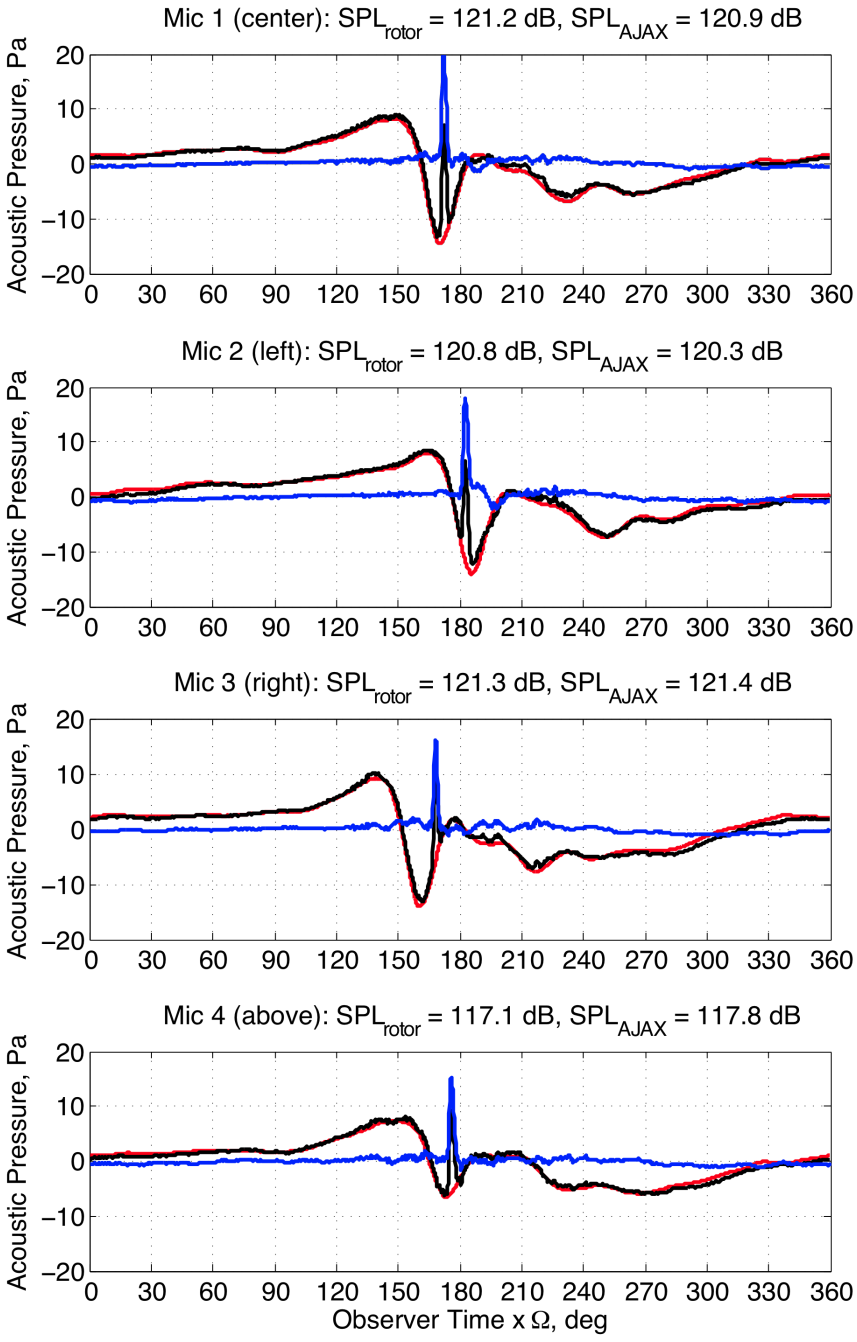

Figure E-4: Single pulse per revolution control measured time history (1/REV = 36.7 Hz).

References

1. Schmitz, F.H., "Rotor Noise," Chapter 2 in book authored by Hubbard, H. H. ,*Aeroacoustics of Flight Vehicles, Theory and Practice, Vol. 1: Noise Sources*, Published for the Acoustical Society of America through the American Institute of Physics, 1995.

2. Schmitz, F. H. and Gopalan, G. "High-Speed Impulsive Helicopter Noise Reduction Possibilities Through On-Blade Control", Invited Paper, presented at the International Forum on Rotorcraft Multidisciplinary Technology Organized by AHS International and the Korean Society for Aeronautical and Space Sciences, Seoul, Korea, October 15-17, 2007.

3. Gopalan, G. and Schmitz, F. H., "Understanding Far Field Near-In-Plane High Speed Harmonic Helicopter Rotor Noise in Hover: Governing Parameters and Active Acoustic Control Possibilities," presented at the American Helicopter Society Specialist's Conference on Aeromechanics, San Francisco, CA, Jan. 23-25, 2008.

4. Gopalan, G. and Schmitz, F. H., "Far-Field Near In-Plane Harmonic Main Rotor Helicopter Impulsive Noise Reduction Possibilities," American Helicopter Society 64th Annual Forum & Technology Display, Montreal, Canada, April 29 – May 1, 2008.

5. Sim, B. W., "*Suppressing In-Plane, Low Frequency Helicopter Harmonic Noise with Active Controls*," American Helicopter Society San Francisco Bay Area Chapter's Aeromechanics Specialist's Meeting, Fisherman's Wharf, CA, January 2008.

6. Sim, B.W., JanakiRam, R.D., Barbely, N.L., and Solis, E., "Reduced In-Plane, Low Frequency Noise of an Active Flap Rotor," American Helicopter Society 65th Annual Forum, Grapevine, Texas, May 27-29, 2009.

7. Lau, B.H., Obriecht, N., Gasow, T., Hagerty, B., Cheng, K.C., and Sim, B.W., "Boeing-SMART Rotor Wind Tunnel Test Data Report for DARPA Helicopter Quieting Program (HQP) Phase 1B," NASA/TM-2010-216404, Sept. 2010.

8. Couch, M. and Lindell, D. "Study on Rotorcraft Survivability." Aircraft Survivability Summer 2010: 9-13.

9. Schmitz, F.H., and Yu, H.Y., "Theoretical Modelling of High-Speed Impulsive Noise," Pro- ceedings of the 3rd European rotorcraft and Powered Lift Aircraft Forum, 1977.

10. Yu, Y.H., Caradonna, F.X., and Schmitz, F.H., "The Influence of Transonic Flow Field on High-Speed Impulsive Noise," Proceedings of the 4th European rotorcraft and Powered Lift Aircraft Forum, Stresa, Italy, 1978.

11. Schmitz, F.H., and Boxwell, D.A., "In Flight Measurement of Helicopter Impulsive Noise," *Journal of the American Helicopter Society,* Vol. 21, No. 4, October 1976, pp. 2–16.

12. Schmitz, F.H., and Yu, Y.H., "Helicopter Impulsive Noise: Theoretical and Experimental Status," *Journal of Sound and Vibration,* Vol. 109, No. 3, 1986.

13. Baeder, J.D., "Passive Design Reductions of High-Speed Impulsive Rotor Noise", Journal of the American Helicopter Society, Volume 43, Number 3, 1 July 1998 , pp. 222-234(13).

14. Cunefare, K., "Active Noise Control", Special Lay-Language Paper for the 75th Anniversary Meeting of the Acoustical Society of America, May 2004.

15. Lueg, P. 1936 US Patent no. 2043416.

16. Bies, D.A., and Hansen, C.H., "Engineering Noise Control: Theory and Practive," Second Edition, 1988.

17. Active control of interior noise in a three-dimensional enclosure
Balachandran, B | Sampath, A | Park, J
Smart Materials and Structures. Vol. 5, no. 1, pp. 89-97. Feb. 1996

18. Brentner, K. S. and Farassat, F. (1992) Helicopter noise prediction: the current status and future direction, In: DGLR/AIAA 14th Aeroacoustics Conf., Aachen, Germany.

19. George, A. R. (1978) Helicopter noise--state-of-the-art, J. Aircraft. 15(1 I), 707 715.

20. Lowson, M. V. (1991, 1992) Progress towards quieter civil helicopters, In: 17th European Rotorcraft Forum, Berlin, Germany, Paper no. 91-59 and Aeronaut. J. 209-223.

21. Marze, H. J. and Philippe, J. J. (1994) A quiet helicopter - a research programme today, a reality tomorrow, In: 20th European Rotorcraft Forum, Amsterdam, Netherlands, Paper no. 9.

22. Schmitz, F. H. and Yu, Y. H. (1986) Helicopter impulsive noise: theoretical and experimental status, J. Sound Vibr. 109(3), 361-422.

23. White, R. P. (1980): The Status of Rotor Noise Technology. J. Am. Helicopter Soc., vol. 25, no. 1, Jan.

24. Yung H. Yu, Bernd Gmelin, Wolf Splettstoesser, Jean J. Philippe, Jean Prieur, Thomas F. Brooks, Reduction of helicopter blade-vortex interaction noise by active rotor control technology, Progress in Aerospace Sciences, Volume 33, Issues 9-10, 1997, Pages 647-687

25. Hardin, J. C. and Lamkin, S. L. (1986) Concepts for reduction of blade vortex interaction noise, J. Airer. 24 (5), pp. 120-125.

26. Splettstoesser, W. R., Lehmann, G. and van der Wall, B. (1990, 1989) Higher harmonic control of a helicopter rotor to reduce blade-vortex interaction noise, Zeitschr!ft Fuer Fluowissenschaften 14, 109--116 and In: 15th European Rotorcraft Forum

27. Brooks, T. F., Booth, E. R., Jolly, J. R., Yeager, W. T. and Wilbur, M. L. (1990) Reduction of blade-vortex interaction noise through higher harmonic pitch control, J. Amer. Helicopter Soc. 35 (1).

28. Richter, P., Eisbreeher, H. D. and KIoeppel, V. (1990) Design and first tests of individual blade control actuators, In: 16th European Rotorcraft Forum, Glasgow, U.K.

29. Jacklin, S. A., Nguyen, K., Blaas, A. and Richter, P. (1994) Full scale wind tunnel test of a helicopter individual blade control (IBC) system, in: 50th Annual Forum of the American Helicopter Society.

30. Jacklin, S. A., Blaas, A., Teves, D. and Kube, R. (1995) Reduction of Helicopter BVI Noise, Vibration, and Power Consumption Through Individual Blade Control. 51st Annual Forum of the American Helicopter Society.

31. Schmitz, F.H., “Reduction of Blade-Vortex Interaction (BVI) Noise through X-Force Control”, J. Am. Helicopter Society 43, Issue 14,1998.

32. Hawles, D. R., “Flight Operations to Minimize Noise,” Proceedings of the American Helicopter Society-AIAA-University of Texas at Arlington Joint Symposium on Environmental Effects of VTOL Designs, Arlington, TX, November, 1970.

33. Rinehart, S.A., "Theoretical Study of Modification of Rotor Tip Vortex by Aerodynamic Means", RASA Report 70-02, ONR Contract N00014-69-C-0i69, January 1970.

34. Balcerak,John C. ; Feller,Raymond F., “Vortex Modification by Mass Injection and by Tip Geometry Variation”, USAAMRDL Tech. Rep 73-74, U.S. Army, June 1973.

35. Pegg, R.J., Hosier, R.N., Balcerak, J.C., and Johnson, H.K., “Design and preliminary tests of a blade tip air mass injection system for vortex modification and possible noise reduction on a full-scale helicopter”, NASA TM X-3314, Dec. 1975.

36. White, R.P., “Wind tunnel tests of a two bladed model rotor to evaluate the TAMI system in descending forward flight”. NASA CR-145195, 1977.

37. Lee, C.C., Tavella, D., Wood, N.J. and Roberts, L., “Flow structure and scaling laws in lateral tip blowing”, AIA Jounral, Vol. 27, No. 8, Paper No. 8601810, 1988.

38. Wu, J.M., Vakili, A.D., Chen, Z.L., and Gilliam, F.T., “Investigation of the effect of discrete wingtip jets, AIAA Paper 83-0546, 1983.

39. Gowanlock, D.K. and Matthewson, C.S., “Control of Rotor Tip Vortices”, AIAA 99-0012, 1999.

40. Han, Y.O., and Leishman, J.G., “ Investigation of Helicopter Rotor-Blade-Tip-Vortex Alleviation Using a Slotted Tip”, AIAA Journal, Vol. 42, No. 3, March 2004.

41. Leishman, J.G., and Han, Y.O., “Rotor blade system with reduced Blade-Vortex Interaction noise,” U.S. Patent 6948906 B2, Sep. 27, 2005.

42. Yang, C., Baek, J., Saito, S., and Aoyama, T., “Numerical Study on the Blade-Vortex Interaction of Helicopter Rotor with Lateral Blowing”, Special Publication by Japanese National Aerospace Laboratory, 2002.

43. Caruso, S.C., Mendenhall, M.R., and Childs, R.E., “Numerical Simulation of Wing Lift Augmentation with Spanwise Tip Blowing”, AIAA 26th Aerospace Sciences Meeting, 1988.

44. Lorber, P. McCormick, D., Anderson, T., Wake, B., MacMartin, D., Pollack, M. Corke, T. & Breuer, K. "Rotorcraft Retreating Blade Stall Control". AIAA Paper 2000-2475. Fluids 2000 Conference, Denver CO. June 2000.

45. Hassan, A. A; Straub, F. K; Charles, B.D.,” Effects of surface blowing/suction on the aerodynamics of helicopter rotor blade-vortex interactions (BVI),” Proceedings of the 52-nd AHS Annual Forum, Washington, DC, June 4-6, 1996.

46. Roos, F.W., “Mr. Mac’s helicopters,” Gateway News, AIAA St. Louis Section publication, September 2006.

47. Cheeseman, I.C., and Seed, A.R., “The application of Circulation Control by blowing to helicopter rotors,” Journal of the Royal Aeronautical Society, Vol. 71, No. 679, July 1967, pp.451-467.

48. Englar, R.J., and Applegate, C.A., "Circulation Control – A bibliography of DTNSRDC Research and Selected Outside References," David W. Taylor Research and Development Center, Rept. DTNSRDC-84/052, Bethesda, MD, Sept. 1984.

49. Uknown Author, "Recent Sikorsky R&D Progress", NASA Document 19880007276, 1988.

50. Fischer, W.C., "X-Wing fly-by-wire vehicle management system", AIAA/IEEE Digital Avionics Systems Conference, San Jose CA, 1988.

51. Mosher, M., "Acoustic Measurements of the X-Wing Rotor", NASA TM 84292, 1983.

52. Healy, G.J., "X-Wing Noise Data Acquisition Program," NASA CR 166454, 1983.

53. Munro, S.E., Ahuja, K.K., and Englar, R.J., "Noise Reduction Through Circulation Control," AIAA 2001-0666, 2001.

54. Ahuja,K.K., Sankar, L.N., Englar, R.J., Munro, S.E., Li,Y., and Gaeta, R.J., "Application of Circulation Control Technology to Airframe Noise Reduction," GTRI Report A5928/2003-1, May 2003.

55. Howe, M.S., "Noise generated by a coanda wall circulation control device," Journal of Sound and Vibration, Vol. 249, No. 4, 2002, pp 679-700.

56. Vasilescu, R., and Dancila, D.S., "Rotor wake modifications in hover using unsteady spanwise blowing," 44th AIAA Aerospace Sciences Meeting and Exhibit, AIAA 2006-1065, 2006.

57. Mitchell, C.A., and Vogel, B.J., "The Canard Rotor Wing (CRW) Aircraft – A new way to fly," AIAA/ICAS International Air and Space Symposium and Exposition, July 2003, AIAA 2003-2517.

58. Morris, Jefferson, "Second X-50A Dragonfly demonstrator lost in crash, Program in Doubt," April 21, 2006, Aviation Week Online Publication.

59. Lorber, P.F., Lord, W.K, "Centrifugal Air Flow Control," US Patent 6203269 B1, Mar 20, 2001.

60. Gopalan,G. and Schmitz, F.H., "Low Harmonic Near-In-Plane Far-Field Helicopter Noise Cancellations Using Distributed On-Blade Controls," Presented at the AHS Southwest Region Technical Specialists' meeting, Dallas-Fort Worth, TX, October 2008.

61. Gopalan, G., and Schmitz, F.H., "Helicopter Thickness Noise Reduction Possibilities through active on-blade acoustic control," Journal of Aircraft,

Vol. 47, No.1, January-February 2010, pp 41-52.

62. Ffowcs Williams, J.E., and Hawkings, D.K., "Sound generation by turbulence and surfaces in arbitrary motion," *Philosophical Transactions of the Royal Society of London, Series A: Mathematical and Physical Sciences,* Vol. A264, No. 1151, 1969, pp. 321-342.

63. Farassat, F., "Linear Acoustic Formulas for Calculation of Rotating Blade Noise," AIAA Journal, Vol. 19, No. 9, Sept 1981, pp. 1122-1130.

64. Farassat, F., "Derivation of Formulatins 1 and 1A of Farassat", NASA TM 214853, 2007.

65. Sargent, D.C., Gopalan, G., Schmitz, F.H., "Acoustic Design and Parametric Variations, Active Acoustic Control and Performance Study of In-Plane Far-Field Helicopter Rotor Noise in Forward Flight," Presented at the 2010 American Helicopter Society Annual Forum, Phoenix, AZ, May 2010.

66. Barbely, N.L., Sim, B.W., Kitaplioglu, C., and Goulding, P., "A Study of Acoustic Reflections in Full-Scale Rotor Low Frequency Noise Measurements Acquired in Wind Tunnels," Presented at the AHS Specialists' Conference on Aeromechanics, San Francisco, CA, January 20-22, 2010.

67. Ffowcs Williams, J.E., "Aeroacoustics", *Annual Review of Fluid Mechanics*, 00 447-468, 1977.

68. Suzuki, T., "A review of diagnostic studies on jet-noise sources and generation mechanisms of subsonically convecting jets," *Fluid Dynamics Research*, Vol. 42, January 18, 2010.

69. Lighthill, M.J., "On sound generated aerodynamically. I. General Theory", *Proceedings of the Royal Society of Aeronautics,* 211, pp 564-587, 1952.

70. Kotake, S., Okazaki, T., "Jet Noise: Far Noise Field of Subsonic Free Air Jet", *Bulletin of the Japan Society of Mechanical Engineers,* Vol. 7, No. 25, 1964.

71. Crighton, D.G., "The Excess Noise Field of Subsonic Jets", *Journal of Fluid Mechanics*, Vol. 56, No. 4, pp 683-684, 1972.

72. Ffowcs Williams, J.E. and Hawkings, D.L., "Sound Generated by Turbulence and Surfaces in Arbitrary Motion," *Philosophical Transactions of the Royal Society,* A264, pp 321-342, 1969.

73. Crigthon, D.G., Dowling, A.P., Ffowcs Williams, J.E., Heckl, M. and Leppington, F.G., *Modern Methods in Analytical Acoustics,* Chap. 11, Pringer-Verlag, London, pp 334-342, 1992.

74. Lockard, D.P. and Casper, J.H., "Permeable Surface Corrections for Ffowcs

Williams and Hawkings Integrals," 11th AIAA/CEAS Aeroacoustic Conference, AIAA Paper 2005-2995, 23-25 May, 2005.

75. Phillips, J.D., "An Efficient Tip Jet Drive," AIAA Aircraft Design Systems and Operations Meeting, Baltimore, MD, Sept. 23-25 1991, AIAA-91-3124.

76. Schmitz, F. H., Aggarawal H. R., Boxwell D. A., "Prediction and Measurement of Low-Frequency Harmonic Noise of a Hovering Model Helicopter Rotor", *Journal of Aircraft*, Vol. 37, Number 5, Pages 786-795, Sept.– Oct., 2000.

77. Koushik, Sudarshan. "A New Experimental Approach to Study Helicopter Blade-Vortex Interaction Noise." University of Maryland Dissertation 2007.

78. Feinerman, J., Koushik, S., and Schmitz, F.H., "Effect of Leading-Edge Serrations on Helicopter Blade-Vortex Interaction Noise", Presented at the American Helicopter Society 67th Annual Forum, Virginia Beach, VA, May 3-5, 2011.

79. Sim, B.W., "The design and anechoic assessment of the free-field rotor test chamber (FFRTC), University of Maryland internal report, Nov. 10th, 1998.

80. Leishman, J. Gordon. Principles of Helicopter Aerodynamics. Cambridge University Press, New York, 2006, pp 457-489.

81. Smith, H.A., and Schaeder, R.F., "Aerodynamic characteristics at Reynolds numbers of 3.0×10^6 and 6.0×10^6 of three airfoil sections formed by cutting off various amounts from the rear portion of the NACA 0012 airfoil section," NACA TN 2074, April 1950.

82. Sampath, A., and Balachandran, B., "Studies on performance functions for interior noise control," Smart Material Structures No. 6, 1997.